Characterization and modelling of microstructural evolutions and mechanical properties during the thermal treatments of Dual-Phase steels

Alexandre Mathevon

▶ **To cite this version:**

Alexandre Mathevon. Characterization and modelling of microstructural evolutions and mechanical properties during the thermal treatments of Dual-Phase steels. Materials. Université de Lyon, 2020. English. NNT : 2020LYSEI120 . tel-03186693

HAL Id: tel-03186693

https://theses.hal.science/tel-03186693v1

Submitted on 31 Mar 2021

HAL is a multi-disciplinary open access archive for the deposit and dissemination of scientific research documents, whether they are published or not. The documents may come from teaching and research institutions in France or abroad, or from public or private research centers.

L'archive ouverte pluridisciplinaire **HAL**, est destinée au dépôt et à la diffusion de documents scientifiques de niveau recherche, publiés ou non, émanant des établissements d'enseignement et de recherche français ou étrangers, des laboratoires publics ou privés.

N°d'ordre NNT : 2020LYSEI120

THESE de DOCTORAT DE L'UNIVERSITE DE LYON
opérée au sein de
L'Institut National des Sciences Appliquées de Lyon

Ecole Doctorale N° ED 34
Matériaux de Lyon

Spécialité de doctorat :
Matériaux

Soutenue publiquement le 11/12/2020, par :
Alexandre MATHEVON

Characterization and modelling of microstructural evolutions and mechanical properties during the thermal treatment of cold-rolled Dual-Phase steels

---

Devant le jury composé de :

Van Der ZWAAG, Sybrand	Professeur	TU Delft	Examinateur
ZUROB, Hatem	Professeur	McMaster	Rapporteur
JACQUES, Pascal	Professeur	UCLouvain	Rapporteur
OLLAGNIER, Arnaud	Docteur	Fives KEODS	Examinateur
MASSARDIER, Véronique	Maitre de conférence	INSA LYON	Directrice de thèse
FABREGUE, Damien	Professeur	INSA LYON	Directeur de thèse
PEREZ, Michel	Professeur	INSA LYON	Invité
ROCABOIS, Phillipe	Docteur	Fives KEODS	Invité

Cette thèse est accessible à l'adresse : http://theses.insa-lyon.fr/publication/2020LYSEI120/these.pdf
© [A. MATHEVON], [2020], INSA Lyon, tous droits réservés

Cette thèse est accessible à l'adresse : http://theses.insa-lyon.fr/publication/2020LYSEI120/these.pdf
© [A. MATHEVON], [2020], INSA Lyon, tous droits réservés

Département FEDORA – INSA Lyon - Ecoles Doctorales – Quinquennal 2016-2020

SIGLE	ECOLE DOCTORALE	NOM ET COORDONNEES DU RESPONSABLE
CHIMIE	**CHIMIE DE LYON** **http://www.edchimie-lyon.fr** Sec. : Renée EL MELHEM Bât. Blaise PASCAL, 3e étage **secretariat@edchimie-lyon.fr** INSA : R. GOURDON	**M. Stéphane DANIELE** Institut de recherches sur la catalyse et l'environnement de Lyon IRCELYON-UMR 5256 Équipe CDFA 2 Avenue Albert EINSTEIN 69 626 Villeurbanne CEDEX **directeur@edchimie-lyon.fr**
E.E.A.	**ÉLECTRONIQUE, ÉLECTROTECHNIQUE, AUTOMATIQUE** **http://edeea.ec-lyon.fr** Sec. : M.C. HAVGOUDOUKIAN **ecole-doctorale.eea@ec-lyon.fr**	**M. Gérard SCORLETTI** École Centrale de Lyon 36 Avenue Guy DE COLLONGUE 69 134 Écully Tél : 04.72.18.60.97 Fax 04.78.43.37.17 **gerard.scorletti@ec-lyon.fr**
E2M2	**ÉVOLUTION, ÉCOSYSTÈME, MICROBIOLOGIE, MODÉLISATION** **http://e2m2.universite-lyon.fr** Sec. : Sylvie ROBERJOT Bât. Atrium, UCB Lyon 1 Tél : 04.72.44.83.62 INSA : H. CHARLES **secretariat.e2m2@univ-lyon1.fr**	**M. Philippe NORMAND** UMR 5557 Lab. d'Ecologie Microbienne Université Claude Bernard Lyon 1 Bâtiment Mendel 43, boulevard du 11 Novembre 1918 69 622 Villeurbanne CEDEX **philippe.normand@univ-lyon1.fr**
EDISS	**INTERDISCIPLINAIRE SCIENCES-SANTÉ** **http://www.ediss-lyon.fr** Sec. : Sylvie ROBERJOT Bât. Atrium, UCB Lyon 1 Tél : 04.72.44.83.62 INSA : M. LAGARDE **secretariat.ediss@univ-lyon1.fr**	**Mme Sylvie RICARD-BLUM** Institut de Chimie et Biochimie Moléculaires et Supramoléculaires (ICBMS) - UMR 5246 CNRS - Université Lyon 1 Bâtiment Curien - 3ème étage Nord 43 Boulevard du 11 novembre 1918 69622 Villeurbanne Cedex Tel : +33(0)4 72 44 82 32 **sylvie.ricard-blum@univ-lyon1.fr**
INFOMATHS	**INFORMATIQUE ET MATHÉMATIQUES** **http://edinfomaths.universite-lyon.fr** Sec. : Renée EL MELHEM Bât. Blaise PASCAL, 3e étage Tél : 04.72.43.80.46 **infomaths@univ-lyon1.fr**	**M. Hamamache KHEDDOUCI** Bât. Nautibus 43, Boulevard du 11 novembre 1918 69 622 Villeurbanne Cedex France Tel : 04.72.44.83.69 **hamamache.kheddouci@univ-lyon1.fr**
Matériaux	**MATÉRIAUX DE LYON** **http://ed34.universite-lyon.fr** Sec. : Stéphanie CAUVIN Tél : 04.72.43.71.70 Bât. Direction **ed.materiaux@insa-lyon.fr**	**M. Jean-Yves BUFFIÈRE** INSA de Lyon MATEIS - Bât. Saint-Exupéry 7 Avenue Jean CAPELLE 69 621 Villeurbanne CEDEX Tél : 04.72.43.71.70 Fax : 04.72.43.85.28 **jean-yves.buffiere@insa-lyon.fr**
MEGA	**MÉCANIQUE, ÉNERGÉTIQUE, GÉNIE CIVIL, ACOUSTIQUE** **http://edmega.universite-lyon.fr** Sec. : Stéphanie CAUVIN Tél : 04.72.43.71.70 Bât. Direction **mega@insa-lyon.fr**	**M. Jocelyn BONJOUR** INSA de Lyon Laboratoire CETHIL Bâtiment Sadi-Carnot 9, rue de la Physique 69 621 Villeurbanne CEDEX **jocelyn.bonjour@insa-lyon.fr**
ScSo	**ScSo*** **http://ed483.univ-lyon2.fr** Sec. : Véronique GUICHARD INSA : J.Y. TOUSSAINT Tél : 04.78.69.72.76 **veronique.cervantes@univ-lyon2.fr**	**M. Christian MONTES** Université Lyon 2 86 Rue Pasteur 69 365 Lyon CEDEX 07 **christian.montes@univ-lyon2.fr**

*ScSo : Histoire, Géographie, Aménagement, Urbanisme, Archéologie, Science politique, Sociologie, Anthropologie

Cette thèse est accessible à l'adresse : http://theses.insa-lyon.fr/publication/2020LYSEI120/these.pdf
© [A. MATHEVON], [2020], INSA Lyon, tous droits réservés

Cette thèse est accessible à l'adresse : http://theses.insa-lyon.fr/publication/2020LYSEI120/these.pdf
© [A. MATHEVON], [2020], INSA Lyon, tous droits réservés

Remerciements

Il est temps pour moi après ces 3 ans de thèse de remercier l'ensemble des personnes que j'ai eu l'occasion de croiser et qui ont su m'accompagner et me prodiguer de précieux conseils au cours de cette expérience aussi bien scientifique qu'humaine. Je ne peux que remercier l'ensemble du laboratoire MATEIS et de FIVES KEODS qui ont su être une véritable famille tout au long de ces 3 ans et je vais tenter de n'oublier aucune des personnes rencontrées.

Tout d'abord, je tiens à remercier tous les membres de mon jury d'avoir accepté de prendre le temps d'évaluer mon travail en participant à ma soutenance et par la même occasion d'enrichir l'échange via leurs remarques et commentaires avisés. Je remercie Pascal JACQUES pour son regard critique concernant les microstructures étudiées et le modèle de prédiction des propriétés mécaniques développé. Je tiens également à remercier l'ensemble des membres de la conférence ALEMI notamment, Hatem ZUROB et Sybrand van der ZWAG, qui m'auront introduit au monde des transformations de phase, ce qui m'a permis de développer un nouvel outil pour la prédiction des transformations thermodynamiques des aciers. Je retiendrais également l'échange privilégié avec l'université de Delft grâce à Sybrand et Hussein qui m'auront permis de découvrir les Pays-Bas, la gare de Bruxelles pour nos différentes réunions et surtout le GEB !

Je suis obligé de souligner que la qualité du travail réalisé n'a pu être possible que grâce à un formidable trio d'accompagnement (Véronique MASSARDIER, Michel PEREZ et Damien FABREGUE). Je vais commencer par Damien FABREGUE grâce à qui tout a commencé, car c'est toi qui a su me convaincre de me lancer dans ce projet de thèse, ce qui n'était pas couru d'avance. Bien que réussir à fixer des réunions n'a jamais été une mince affaire (je ne compte plus les échanges sur le pas d'une porte ou en mouvement en direction de tes multiples activités), tu as toujours su être là pour échanger sur mes questionnements scientifiques et personnels et me donner des pistes à suivre. Et puis ma plus grande réussite aura été de t'emmener faire de l'escalade. Difficile de décrire en quelques lignes tout ce que l'on aura échangé durant ces 3 ans Michel, mais je me souviens que dès l'entretien de thèse, tu t'es plus intéressé à ma personne qu'à mes compétences. Je pense que ce sont tes qualités humaines, ton optimisme et ton écoute envers les différents membres de l'équipe que je retiendrais par-dessus tout. Je ne peux que te remercier pour m'avoir épaulé lors du développement et de l'acceptation du GEM aux yeux de tous, mais également pour toutes les expéditions sportives de ces 3 dernières années (baptême de parapente dans le plus haut village de France, escalade dans la neige, saut de ruisseau à ski et tes fameux raccourcis après 140 km de vélo). Je te remercie également pour tes questionnements sur l'impact environnemental de nos recherches qui m'aura permis d'approfondir cet aspect

Cette thèse est accessible à l'adresse : http://theses.insa-lyon.fr/publication/2020LYSEI120/these.pdf
© [A. MATHEVON], [2020], INSA Lyon, tous droits réservés

de ma thèse. Véronique, merci pour ton soutien constant durant cette thèse, qui a permis d'aboutir au manuscrit actuel malgré les quelques problèmes expérimentaux que l'on aura rencontrés. Ta disponibilité pour la réalisation des différentes expériences, des discussions pour établir une explication convaincante du revenu de la martensite et ta rigueur sur la rédaction des articles et du manuscrit ont été une vraie chance que la plupart des doctorants rêveraient d'avoir.

Cette thèse n'aurait pas eu lieu sans l'accompagnement et la confiance de FIVES KEODS. Merci Philippe pour ton suivi régulier durant ces 3 ans à MATEIS et l'ensemble de tes connaissances pratiques du terrain et des aciéries qui nous a souvent permis de nous recentrer sur l'essentiel et d'éclairer certaines parts d'ombres. Bien que l'échange a été plus court, je tiens à remercier Eric BUSCARLET et Arnaud OLLAGNIER pour leurs échanges. Pour finir merci à (Jean-Paul, Shervin, Fanny, Yvan, Maxime, Carlos, Raphael, Damien, Guillaume, Denys, Etienne, Vianney, Gohkan, Myriam, Alexis), pour nos échanges durant les séminaires à MATEIS et les deux séminaires chez FIVES qui m'ont permis de découvrir tout l'univers professionnel de FIVES KEODS.

Je tiens également à remercier plus particulièrement l'ensemble des personnes m'ayant aidé au cours de ma thése. Merci Patrice pour tes connaissances de résolution numérique qui m'auront permis au cours des nombreux échanges avec Michel d'aboutir au modèle GEM qui semble bien parti pour continuer à exister après moi. Florian pour m'avoir formé sur la Gleeble, ce qui suivant les jours n'a pas toujours été une mince affaire ! Sophie pour cet essai de traction in-situ, qui m'aura permis d'approfondir et d'appuyer mon modèle de simulation numérique. Thierry pour ton expérience de microscopie FIB qui nous auront permis de percer un peu plus les mystères du revenu de la martensite. Merci à Yves Bréchet, Hugo van Landeghem pour leurs conseils et nos discussions. Je remercie également Ce Xiao et Callum d'avoir effectué leur stage à l'INSA en lien avec mon projet de thèse.

Plus que son côté scientifique, cette thèse a été une expérience de vie grâce aux différents membres du laboratoire et notamment l'ambiance de l'équipe Métal. Je tiens à remercier tout d'abord, Frida notre incroyable secrétaire pour nos différentes discussions et ta bonne humeur, Jonathan pour notre découverte du Japon et de toute sa richesse (on retiendra notre coup de coeur pour Kyoto), Jérome pour ta bonne humeur, nos sorties sportives et ta fameuse blague sur les toilettes japonais, Christophe et Joel L. pour vos échanges modélisations et l'ensemble des outils mis en place pour l'équipe, Stéphanie pour ta bonne humeur, Eric pour tes conseils et les brins de pailles que je retrouve encore aujourd'hui, Sylvain pour ton appétit digne des plus grands, Jean-Yves "Guide du XXIème siècle, Grand homme descendu du ciel et commandant à la volonté de fer invaincu depuis 1903" pour ta gentilesse même envers tes "esclaves" et de nos aventures à l'armentier été comme hiver (PS : nous n'avons toujours pas fait officiellement les 21 virages), Joel C. pour ton animation quotidienne, Carole pour nos discussions lors des différents aléas expérimentaux, Pierre-antoine pour tes conseils sur le Phase-Field et nos soirées escalade. Patrice pour m'avoir secouru avec du pain d'épice maison lors de mes premières sorties ski de fond. Laurent pour ta gentillesse et tes connaissances des implants lors de mon PFE. Sophie pour nos échanges et ta connaissance de la microscopie et Xavier pour tes très bons conseils scientifiques.

La force de cette équipe métal repose notamment sur son dynamisme et le renouvelle-

Cette thèse est accessible à l'adresse : http://theses.insa-lyon.fr/publication/2020LYSEI120/these.pdf
© [A. MATHEVON], [2020], INSA Lyon, tous droits réservés

ment de ces doctorants que je compte aujourd'hui pour la plupart en tant qu'ami !

Merci aux anciens que je n'ai pu qu'apercevoir pour la plupart (Josselin, Thibaud, Sebastien, Mélanie). Mélanie, merci pour tes précieux conseils qui m'ont convaincu de me lancer dans cette aventure et pour le temps que tu m'as accordé sur la fin de ta thèse.

Merci à Gwen, Sib, Victor, Oriane, Justine, Alethea, Morgane, Yassin, Théo et Fanfan pour la vie que vous avez su insuffler à l'équipe à travers divers événements ("Recettes pompettes", Week-end doctorants et autres). Sib et Victor pour ces 3 ans de grimpe et j'espère que l'on aura l'occasion de partager ca à nouveau une fois qu'aucun de vous ne sera au Canada ! Gwen pour t'avoir aidé indirectement dans ta thèse. Théo pour ta motivation notamment sportive et je ne retiendrai que notre sortie hivernale à vélo de route ou nous aurions mieux fait d'amener nos skis de fond (PS : L'idée est toujours d'actualité mais choisit mieux la date cette fois). Oriane pour m'avoir accepté au sein du meilleur bureau, pour ton magnifique accent indien jamais égalé en France, ta soif de victoire sur les pauses music quiz et ce merveilleux surnom que tu auras laissé bien après ton départ. Morgane pour ta simplicité et ton courage pour cette thèse en bi-appartenance avec le Japon. Alethea pour ta gentillesse et ton attention quotidienne envers tout le monde et Yassin pour ton imagination débordante.

Merci à mes ainés partis un an plus tôt, Alexis, Francois, Gabriel, Julie, Amin. Alexis pour notre directeur sportif en commun et nos nombreuses discussions bainite. Francois pour ta transformation sportive durant ta thèse (grimpeur, cycliste et coureur émérite) et toutes ces heures de discussions sur nos thèses respectives et l'univers fantaisie. Je retiendrai notre pause quotidienne de mots croisés et c'est un grand plaisir d'apprendre ton retour dans la région. Gabriel fan inconditionnel de Totoro, merci pour ces deux ans de joie et de problèmes quotidiens partagés. Je retiendrai tes pulsions de chanteur partagé avec baubau et tes envies de mobilité interne du bureau régulière. Julie pour ce magnifique panier de basket toujours sur mon bureau. Amin pour ta discrétion.

Merci à tous les doctorants de ma promotion (Marion, Arnaud, Lucile, Quentin, Qin Qin) pour nos belles réussites collectives (Repas de Noel et Team Building). Marion pour toutes ces discussions durant ces 3 années "notre porte de bureau est restée grande ouverte" et surtout tes qualités humaines envers les gens qui t'entourent. Je n'oublierai pas les magnifiques surnoms gravés sur mon bureau et les petites citations qui égayaient le quotidien. Je retiendrai surtout que l'on a réussi tous ensemble à se lancer dans des défis que l'on n'aurait pas tenté seul (Impossible de traverser le vercors jusqu'à Glandage tu m'avais dit) et Matthieu pour ce doublé du Mont Ventoux. Arnaud, je peux dire que depuis mon arrivée à l'INSA on ne s'est pas quitté et je ne perds pas espoir de voir Ana nous accompagner bientôt dans nos sorties sportives futures ! Cette route commune a été si longue parce que notre travail nous tient tous les deux à coeur et nos centres d'intérêts ont souvent convergés jusqu'au choix de la thèse. Merci pour tes questionnements sur notre environnement et pour tous ces à côtés sportifs (Tu m'en auras fait baver les premières fois à vélo). Lucile, je retiendrais ta gentillesse et ta force tranquille qui n'a jamais été affectée par les difficultés. Pionnière dans le groupe de course à pied, on a finalement réussi à faire souffrir ton vélo dans les monts du lyonnais. Quentin le chat noir des doctorants, on commencait à avoir peur que le labo explose avec toutes tes péripéties (PS : certains avaient déjà essayé avant toi). Musicien du groupe, je retiendrai ta bonne

Cette thèse est accessible à l'adresse : http://theses.insa-lyon.fr/publication/2020LYSEI120/these.pdf
© [A. MATHEVON], [2020], INSA Lyon, tous droits réservés

humeur et tes équipements disproportionnés lors des sorties sportives. Qin qin pour tes efforts d'intégration lors des sorties collectives.

Merci également à toute la relève plus ou moins jeune qui sauront conserver cet esprit familial au sein de l'équipe : Arnaud pour ta bonne humeur avec ton binôme célèbre "tic et tac", Maxime pour ta persévérance à l'apprentissage de la modélisation et ta patience pour l'arrivée de ton four ("Tout vient à point a qui sait attendre"), Manon la reine des ampoules pour ton aide précieuse et pour ton implication permanente à aider les autres, Laurabelle pour ta bonne humeur et la lecon de rigueur que tu as donné à tout le monde pour ta rééducation plus proche d'un entrainement olympique, Ce pour ton optimisme malgré les complications de ton projet, Théophile pour nos échanges et courage tu vas finir par percer les mystères de l'émission acoustique, Justine pour ta découverte du ski de fond, Mathilde pour ton implication envers tout les doctorants du laboratoire, Masato, Lucas, Louis, Theotim, Mael, Florian.

Je tiens également à remercier tous mes amis de promotion de l'INSA, Nassim et Julie pour leur soutien et encouragement durant cette thèse.

Finalement, je tiens également à remercier ma famille et mes proches qui ont toujours su être là pour moi au fil des années dans ce parcours qui n'a pas toujours été régulier, mais qui a permis d'aboutir à ce travail.

Pour finir merci à Justine qui a su être à mes côtés tout au long de cette thèse et à Oriol qui m'aura fait une place dans cette colocation que je n'ai jamais quittée. Merci pour tout ce que tu m'apportes au quotidien et j'espère que comme je te l'avais déjà dit lors de ta thèse notre route ensemble ne fais que commencer. Merci de m'avoir permis de découvrir l'univers du vélo et les nombreux souvenirs que l'on aura partagés.

Cette thèse est accessible à l'adresse : http://theses.insa-lyon.fr/publication/2020LYSEI120/these.pdf
© [A. MATHEVON], [2020], INSA Lyon, tous droits réservés

Résumé en français

Cette partie est un résumé étendu en français, donnant le contexte et les objectifs des travaux, les principaux résultats et conclusions de chaque chapitre, ainsi que les principales perspectives. Pour accéder à l'intégralité des travaux, le lecteur est prié de se référer au reste du manuscrit, rédigé en anglais.

Introduction et contexte industriel

Le transport apparait aujourd'hui comme l'un des secteurs principaux d'émission de CO2. C'est pourquoi, les constructeurs automobiles se retrouvent confrontés à de nouvelles contraintes du point de vue de la sécurité et de la diminution des émissions de gaz à effet de serre. L'amélioration du système de propulsion, de l'aérodynamisme et la réduction de la résistance au roulement a permis de réduire drastiquement l'émission moyenne des véhicules tout en conservant un poids de véhicules constant sur la même période temporelle. Une comparaison sur le remplacement des aciers standards par des aciers à haute résistance mécanique, de l'aluminium et des composites a été menée dans ce travail de thèse (voir la préface) afin de déterminer le matériau le plus approprié pour optimiser les émissions globales de CO2. La forte croissance de production d'acier et d'aluminium conduit à un taux de matériau recyclé faible ($\approx 30\%$) par rapport à la production totale de ces deux matériaux. L'étude complète du cycle de vie pour un chassis de véhicule permet de conclure sur la pertinence environnementale du développement des aciers à haute résistance mécanique (AHSS).

De nombreux types d'aciers AHSS ont été mis au point ces dernières années. On peut tout d'abord citer la 1ère génération d'acier à base ferritique (aciers Dual-Phase (DP), Ccomplex-Phase et Transformed Induced Plasticity). Ensuite, la 2ème génération d'acier à base austénitique a vu le jour (aciers inox austénitiques, aciers Lightweight with Induced Plasticity and Twinning Induced Plasticity) permettant de palier le manque de ductilité des premiers mais engendrant en contre-partie des problèmes de soudage et une fragilité face à l'hydrogène. La 3ème génération se base quant à elle, sur le développement d'aciers à base bainitique et l'optimisation des procédés de fabrication des aciers de la 1ère génération (Dual-Phase).

Le bon compromis entre haute résistance mécanique et ductilité des aciers DP provient de la présence d'une phase ferritique molle (α) dans laquelle est insérée une phase martensitique dure (α'). Le cycle thermique industriel classique d'un acier DP est composé de 3 étapes permettant d'aboutir à la microstructure ferrite-martensite voulue.

Cette thèse est accessible à l'adresse : http://theses.insa-lyon.fr/publication/2020LYSEI120/these.pdf
© [A. MATHEVON], [2020], INSA Lyon, tous droits réservés

Tout d'abord, une étape de chauffage suivie d'un maintien dans le domaine intercritique ($Ae_1 < T < Ae_3$, ∼720-830 °C) pendant 1-3 min permet la transformation de la structure ferrito-perlitique initiale en une microstructure homogène recristallisée grâce au phénomène de restauration et de recristallisation. Dans la même étape, la formation d'austénite a lieu pouvant conduire à une interaction entre recristallisation et transformation de phase en fonction de la vitesse de chauffe, du taux de déformation et de la composition chimique de l'acier. Ensuite, une phase de refroidissement permet de transformer la fraction d'austénite préalablement formée durant le maintien intercritique en martensite si la vitesse de refroidissement (∼30 °C/s) est suffisante. Pour finir, une étape de revenu de la martensite (aux alentours de 460 °C) est induite par le processus de gavanisation de l'acier consistant à plonger l'acier dans un bain de zinc liquide.

Bien que les aciers DP soient apparus dans les années 1970, de nombreuses incertitudes demeurent à propos de leur fabrication. En effet, le nombre important de paramètres de fabrication (vitesse de chauffe et de refroidissement ainsi que le temps et la température de maintien intercritique) et les nombreux phénomènes mis en jeu (recristallisation, transformation de phase et revenu) rendent quasiment impossibles une prédiction précise des propriétés mécaniques finales de l'acier en fonction de sa composition chimique et de ses paramètres de fabrication.

Cette thèse s'inscrit dans le cadre d'un projet lancé par Fives KEODS en 2014 qui vise à développer et optimiser les méthodes de production des aciers avec les objectifs suivants:

- Développement de nouvelles routes métallurgiques adaptées aux contraintes de production des différents secteurs en adaptant la teneur des éléments d'alliages par rapport à un souci d'optimisation du coût final du produit.
- Optimisation de l'énergie totale consommée durant la production de l'acier en ajustant la puissance de chauffage et de refroidissement en accord avec la composition chimique et les paramètres de la ligne.
- Rationalisation du nombre de produits d'entrées permettant de réaliser la différentiation des produits finaux le plus tard possible sur la ligne de production en jouant sur les paramètres de la ligne de production.
- Optimisation des contrôles de la ligne de production en ajustant les paramètres de fabrication pour chacune des bobines dans le but d'atteindre les propriétés mécaniques visées (SmartLine).

Pour mener à bien ces objectifs, le développement de différents outils de prédiction à base physique permettant de prédire les évolutions microstructurales et les propriétés mécaniques finales de l'acier est nécessaire.

La précédente thèse de M. OLLAT, lancée en 2014, s'est principalement focalisée sur l'étude des phénomènes de recristallisation et de transformation de phase ainsi que leurs potentielles interactions lors du traitement thermique d'un acier micro-allié DP1000.

La présente thèse démarée en 2017 vise à proposer des outils de modélisation prédictifs permettant de prévoir l'évolution de la microstructure des aciers Dual-Phase à partir des compositions chimiques, du taux de réduction, de la taille de grains initiales et des paramètres du traitement thermique. Les grandeurs caractéristiques de la microstructure sont ensuite utilisées comme données d'entrée pour le modèle de prédiction des propriétés mécaniques.

Cette thèse est accessible à l'adresse : http://theses.insa-lyon.fr/publication/2020LYSEI120/these.pdf
© [A. MATHEVON], [2020], INSA Lyon, tous droits réservés

Organisation du manuscrit

Le manuscrit de thèse est composé de 6 chapitres organisés selon l'avancement du procédé de fabrications des aciers DP comme illustré dans la Figure 1:

- **Le chapitre 1** s'attache à décrire l'état initial des différents aciers utilisés durant cette thèse (Composition chimique présentée dans le Tableau 1): (i) 4 aciers ternaires Fe-C-Mn issus de coulées de laboratoire et utilisés pour calibrer les différents modèles et comprendre les effets de la composition chimique et (ii) deux aciers industriels permettant de valider les différentes approches proposées.

Nuances acier	Composition chimique (en % massique)						
	C	Mn	Cr	Si	Nb	Ti	N
Aciers ternaires	0.17	0.5	-	-	-	-	-
	0.17	1.7	-	-	-	-	-
	0.17	2.5	-	-	-	-	-
	0.08	1.7	-	-	-	-	-
DP600	0.09	1.5	0.5	0.3	-	-	-
DP1000	0.17	1.7	0.4	0.3	0.03	0.03	0.006

Table 1: Composition chimique des aciers ternaires et industriels étudiés dans cette thèse.

- **Le chapitre 2** est consacré au développement d'un modèle de recristallisation couplé à un modèle de précipitation étendant le formalisme des modèles JMAK existants. La prédiction des cinétiques décrivant la fraction recristallisée (f_α^{ReX}) a été couplée aux différents paramètres physiques du système tels que la composition chimique et le taux de réduction pendant le laminage pour des cycles isothermes et non-isothermes.
- **Le chapitre 3** est axé sur le développement d'un nouveau modèle de prédiction de la transformation de phase $\alpha \leftrightarrow \gamma$ basé sur la minimisation de l'énergie de Gibbs du système. Il permet de définir la fraction d'austénite (f_γ) lors d'un cycle industriel comprenant une rampe de chauffage et un maintien intercritique pour un système quaternaire en prenant en compte la dissolution de la cémentite.
- **Le chapitre 4** traite de la prédiction de la température de début de transformation martensitique (M_S) et de la fraction martensitique ($f_{\alpha'}$) dans le cas des aciers bi-phasés (présentant une microstructure avant refroidissement partiellement austénitique) . Un modèle thermodynamique couplé à la taille des grains austénitiques D_γ et à l'enrichissement des éléments de substitution à l'interface a permis d'expliquer la chute expérimentale de la température M_S dans le cas des aciers bi-phasés par rapport à celle des aciers totalement austénitiques avant refroidissement.
- **Le chapitre 5** propose d'apporter des modifications au modèle de prédiction des propriétés mécaniques: prise en compte (i) du rôle de la taille des grains austénitiques et (ii) des conditions d'interaction entre la ferrite et la martensite. Ce modèle a été ensuite validé pour une large gamme de compositions chimiques et de fractions de martensite sur les différents aciers de cette étude.

Cette thèse est accessible à l'adresse : http://theses.insa-lyon.fr/publication/2020LYSEI120/these.pdf
© [A. MATHEVON], [2020], INSA Lyon, tous droits réservés

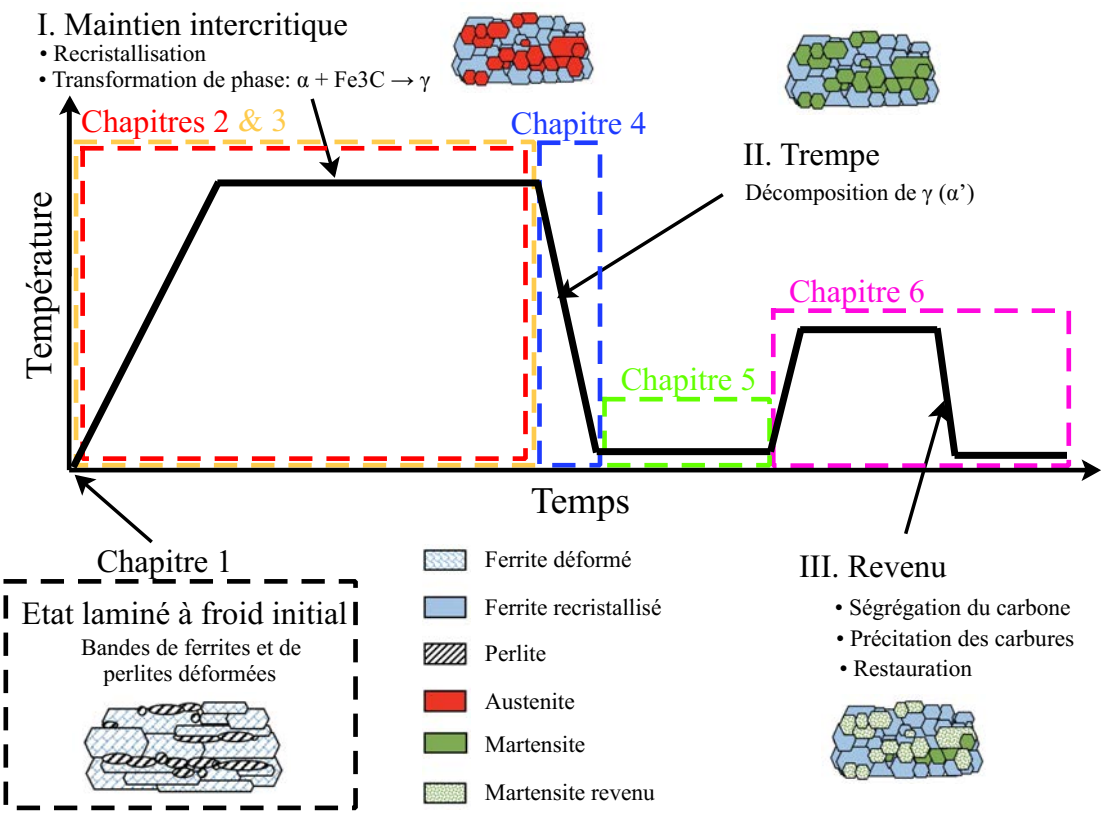

Figure 1: Cycle thermique classique utilisé pour la fabrication d'aciers DP composés d'un traitement de chauffage intercritique suivi d'une trempe et d'un revenu. La structure du manuscrit suit les différentes étapes de fabrication du cycle thermique.

- **Le chapitre 6** étudie les évolutions microstructurales qui se produisent pendant l'étape de revenu du cycle thermique des aciers DP. L'adoucissement des propriétés mécaniques de la martensite a été reproduit par la modification de la teneur en carbone en solution solide suivi par mesures de pouvoir thermoélectrique (PTE) et dureté. Les propriétés de la martensite après revenu sont ensuite intégrés au modèle précédent de prédiction des propriétés mécaniques dans la cas des aciers bi-phasés.

Chapitre 2: Développement d'un modèle à base physique pour la prédiction des cinétiques de recristallisation pour des aciers Dual-Phase

Ce chapitre est consacré au paramétrage d'un modèle à base physique de prédiction des cinétiques de recristallisation d'acier Dual-Phase prenant en compte plusieurs paramètres physique (composition chimique, température, vitesse de chauffe, taux de réduction et état de précipitation). Le contrôle des cinétiques de recristallisation est primordial pour les aciers avancés à haute résistance afin de garantir une recristallisation suffisante lors du début de la formation d'austénite permettant d'obtenir une microstructure finale ho-

Cette thèse est accessible à l'adresse : http://theses.insa-lyon.fr/publication/2020LYSEI120/these.pdf
© [A. MATHEVON], [2020], INSA Lyon, tous droits réservés

mogène.

La modélisation des cinétiques de recristallisation des aciers DP prend en compte l'effet des différents éléments chimiques (Mn, Si, Cr, Mo, Nb). Chaque élément d'alliages est supposé ralentir la cinétique de recristallisation en raison d'un effet de trainage dû à la ségrégation des éléments au sein de l'interface. Les données (coefficient de diffusion, énergie de liaison aux joints de grains) de chaque élément ont été extraites de la littérature. Les cinétiques prédites par le modèle MiReX ont été réalisées sans aucun paramètre ajustable et comparées à un large éventail de cinétiques expérimentales.

Une validation du modèle a d'abord été effectuée sur des alliages ternaires Fe-Mn-C afin de confirmer l'influence de la composition chimique et du taux de réduction sur la cinétique de recristallisation. Il a été observé que le Mn, en raison de sa concentration assez élevée dans les aciers DP, joue un rôle majeur sur la cinétique de recristallisation, qui est considérablement retardée par rapport à celle des aciers Fe-C binaires.

Le modèle a ensuite été confronté aux résultats expérimentaux de la littérature sur des systèmes plus complexes de type Fe-C-Mn-X, représentatifs de la composition chimique des aciers DP ou TRIP, notamment pour valider l'influence de l'addition de Si, Mo et Cr. Contrairement au silicium, le molybdène peut avoir une forte influence sur la recristallisation en raison de son faible coefficient de diffusion et de sa forte énergie de liaison aux joints de grains. Un bon accord entre le modèle MiReX et l'expérience a été noté dans un large domaine de la composition chimique ainsi que pour des rapports de réduction standard par laminage à froid sans paramètres d'ajustement.

Dans le cas de l'acier micro-allié DP1000, un couplage avec un logiciel de modélisation de la précipitation a été utilisé pour inclure l'effet des carbo-nitrure de (Ti,Nb)C. Il a été souligné que le Ti et le Nb ont un rôle crucial dans la cinétique à la fois en tant que solution solide et sous forme de précipités en raison de leur effet d'épinglage sur les joints des grains. L'intégration des précipités dans le modèle MiReX a permis de reproduire l'interaction de la précipitation et de la recristallisation pour les aciers micro-alliés.

Enfin, le modèle MiReX a été utilisé pour prédire la recristallisation lors d'un chauffage continu nécessaire pour analyser la possibilité d'interaction de ce phénomène avec la formation d'austénite. Pour les aciers DP600, ce type d'interaction est attendu pour des vitesses de chauffage supérieures à 3 °C/s et il conduit à une accélération de la cinétique de formation de l'austénite.

Chapitre 3: Modèle GEM de minimisation de l'énergie de Gibbs pour la transformation de phase austénite-ferrite dans les alliages Fe-C-X-Y

Le chapitre 3 vise à modéliser la cinétique de transformation $\alpha \leftrightarrow \gamma$ dans le cas des systèmes quaternaires pendant un cycle thermique industriel comprenant une chauffe continue suivie d'un maintien isotherme. L'originalité du modèle provient du fait que, pour chaque élément d'alliage, le profil de concentration est calculé en résolvant une équation de diffusion *unique* (incluant les 3 phases et les interfaces). L'interface est décrite en supposant une variation linéaire des potentiels chimiques, ce qui permet d'accélérer le

Cette thèse est accessible à l'adresse : http://theses.insa-lyon.fr/publication/2020LYSEI120/these.pdf
© [A. MATHEVON], [2020], INSA Lyon, tous droits réservés

temps de calcul. Le mouvement de l'interface est piloté par la minimisation de l'énergie de Gibbs du système. Cette nouvelle description permet de traiter des systèmes contenant plusieurs interfaces, nécessaires pour prendre en compte la dissolution de la cémentite lors de traitements non-isothermes dans les systèmes quaternaires Fe-C-X-Y.

Tout d'abord, les effets des paramètres numériques du système ainsi que les paramètres physiques (coefficient de diffusion de l'interface, longueur du système) ont été analysés. L'effet de la dissolution de la cémentite et de l'enrichissement en cémentite a ensuite été étudié dans le cas d'un alliage ternaire Fe-C-Mn. Par la suite, des cycles complexes reproduisant des cycles industriels ont été utilisés pour valider la précision du modèle sur une large gamme d'aciers Fe-C-Mn. Il a ainsi été possible d'utiliser le demi-espacement entre les zones perlitiques et l'enrichissement en cémentite des éléments d'alliage pour mettre en évidence la sensibilité du modèle à la température de maintien intercritique et à la composition chimique de l'alliage.

La nécessité d'introduire le chrome dans la simulation afin de stabiliser la cémentite pour la prédiction de la cinétique de transformation dans le cas des nuances industrielles a été soulignée. L'interaction entre la recristallisation et le modèle de transformation de phase a permis de reproduire la sensibilité des différents états initiaux du DP1000 à la vitesse de chauffage pendant le traitement de recuit.

Enfin, le modèle a été testé sur un cycle thermique cyclique et sur des tests de décarburation qui ont permis de prouver la réversibilité du modèle pour les transformations $\gamma \rightarrow \alpha$.

Chapitre 4: Modèle thermodynamique couplée au modèle GEM pour prédire la température M_s des aciers bi-phasés

Suite au développement de modèles pour la prédiction de la température de début de transformation martensitique M_S ces dernières années, basés sur des modèles thermodynamiques permettant de prendre en compte l'effet de la taille des grains austénitiques, il est maintenant possible de prédire avec précision la température du M_S et la cinétique de formation de martensite pour les aciers entièrement austénitiques avant refroidissement. Cependant, très peu d'études ont examiné le cas des aciers bi-phasés sur la transformation martensitique, même si la plupart des aciers à haute résistance de nouvelle génération comportent plusieurs phases et une forte teneur en éléments d'alliage. L'objectif des travaux présentés dans ce chapitre a donc été de modéliser la baisse considérable des températures expérimentales M_S observée dans les états bi-phasés qu'aucun modèle dans la littérature n'a pu saisir. Dans certaines situations, cette baisse ne peut pas être expliquée en prenant en compte uniquement l'enrichissement de l'austénite en carbone et l'affinement de la taille des grains austénitiques. On a donc supposé que l'enrichissement des éléments de substitution au niveau de l'interface γ/α pouvait être partiellement responsable de la baisse du M_S. Le modèle GEM a donc été utilisé pour prédire l'enrichissement au niveau de l'interface après le maintien intercritique permettant de prédire avec succès la température M_S des aciers biphasés. Ces hypothèses ont permis de conforter les fondements thermodynamiques du modèle développé initialement pour les états 100% austénitiques et

Cette thèse est accessible à l'adresse : http://theses.insa-lyon.fr/publication/2020LYSEI120/these.pdf
© [A. MATHEVON], [2020], INSA Lyon, tous droits réservés

de l'appliquer au cas des aciers bi-phasés grâca à un couplage avec le modèle de prédiction de transformation de phase développé dans le chapitre précédent.

Chapitre 5: Investigation et modélisation en champ moyen des mécanismes microstructuraux régissant les propriétés mécaniques des aciers DP

Le chapitre 5 concerne le développement d'un modèle mécanique (Hy-MFC) nécessaire pour reproduire les propriétés mécaniques d'aciers DP, ce modèle étant basé sur les paramètres microstructuraux (*i.e.* composition chimique, fraction de martensite et taille de grains ferritique initiale)

Pour les aciers entièrement martensitiques, une nouvelle dépendance des propriétés mécaniques avec la taille de grains austénitiques avant trempe a permis la calibration du modèle sur l'ensemble des aciers de cette étude. Un bon accord expérimental a été obtenu pour différentes compositions chimiques d'acier et pour différentes tailles de grains (mesurées sur des aciers issus de coulées de laboratoire et sur des aciers industriels). Le carbone présente un rôle primordial sur l'évolution des propriétés des aciers entièrement martensitiques contrairement au manganèse qui semble uniquement contribuer en tant que solution solide.

Dans le cas des aciers DP, des observations EBSD sur des zones sélectionnées à différentes valeurs de déformation lors d'un essai de traction nous ont permis de détecter des décohésions locales et des zones de désorientation dans les grains de ferrite en contact avec de la martensite. Ces localisations de déformation au niveau des interfaces ferrite/martensite indiquent l'interêt d'étudier l'effet composite de la microstructure, validant l'hypothèse d'ajouter des dislocations géométriquement nécessaires dans la ferrite pour accomoder le changement de volume lors de la transformation austénite → martensite pendant la trempe et les incompatibilités de déformation entre les deux phases. Une nouvelle loi d'interaction entre les deux phases a été proposée au cours de l'étude, supposant une transition linéaire entre une loi iso-déformation et une loi iso-travail. Cette loi permet une description plus précise du durcissement à faible déformation observé dans les structures DP bi-percolantes.

Chapitre 6: Evolutions microstructurales et prédiction des propriétés mécaniques lors du revenu d'aciers DP.

Le chapitre 6 présente la caractérisation des évolutions microstructurales et des propriétés mécaniques des aciers 100% martensitiques durant un revenu isotherme effectuée dans la gamme (100-550 °C). A l'aide d'un suivi des évolutions microstructurales de la martensite revenue par mesures de dureté et de PTE, 3 mécanismes principaux ont été identifiés durant la phase de revenu grâce à une équivalence temps-température. A très basse température (<150 °C) et potentiellement durant la trempe, une partie du carbone ségrège sur les défauts intrinsèques de la martensite sans effet sur les propriétés

Cette thèse est accessible à l'adresse : http://theses.insa-lyon.fr/publication/2020LYSEI120/these.pdf
© [A. MATHEVON], [2020], INSA Lyon, tous droits réservés

mécaniques. Par la suite, une première chute des propriétés mécaniques est due à une précipitation intra-latte de cémentite. Celle-ci se fait à partir de la fraction de carbone n'ayant pas ségrégé sur les défauts avec une énergie d'activation de l'ordre de 80 kJ/mol. Le deuxième adoucissement des propriétés mécaniques est attribué à un réarrangement des défauts de la microstructure et à la diminution de la densité de dislocations associée à une énergie d'activation de 210 kJ/mol proche de l'auto-diffusion du fer. Cette réorganisation permet au carbone piégé dans les défauts de précipiter afin d'atteindre la fraction prévue par l'équilibre thermodynamique pour un revenu supérieur à 500 °C.

Par la suite, un modèle "composite" à champ moyen permettant de prédire les propriétés mécaniques de la martensite revenue a été proposé en utilisant plusieurs lois JMAK pour reproduire les différents mécanismes identifiés à l'aide d'énergies d'activation expérimentales. Une validation du modèle a d'abord été effectuée dans le cas d'aciers ternaires Fe-C-Mn entièrement martensitiques trempés dans diverses conditions. Enfin, l'introduction de l'adoucissement de la martensite revenue au sein du modèle composite global a permis de valider sa capacié à prédire les propriétés mécaniques de plusieurs aciers bi-phasés revenus. Cette dernière étape assure la base physique du modèle qui ne nécessite aucun paramètre d'ajustement pour combiner tous les paramètres physiques de la microstructure (*i.e.* composition chimique, fraction de martensite et taille des grains) ainsi que la durée et la température de revenu appliqué.

Perspectives: Couplage des différents modèles sur une route métallurgique industrielle

Actuellement, tous les modèles ont été développés au sein d'une architecture globale permettant de coupler les différents modèles de prédiction des évolutions microstructurales et des propriétés mécaniques des aciers DP. La Figure 2(a) présente l'approche à suivre pour le couplage des différents modèles. Pour les différents modèles, la composition chimique de l'acier et les paramètres du cycle thermique sont nécessaires pour la prédiction des différents phénomènes. Un exemple des résultats qui peuvent être obtenus à partir des différents modèles est détaillé dans le cas d'un acier Fe-0.17C-1.7Mn.

La première étape du chauffage continu consiste à déterminer la cinétique de recristallisation avant la formation de l'austénite en fonction de la composition chimique de l'acier et du taux de réduction. Une recristallisation complète assure une microstructure homogène, tandis qu'une forte interaction avec le phénomène de transformation de phase peut être observée lorsque la recristallisation n'a pas pu avoir lieu. Dans l'exemple étudié, une vitesse de chauffage de 5 °C/s conduit à une recristallisation presque complète au début de la formation de l'austénite, ce qui entraîne une faible interaction, comme le montre la Figure 2.(b).

Le modèle de transformation de phase est basé sur le demi-espacement des zones perlitiques généralement lié à l'affinement de la microstructure ainsi qu'à l'enrichissement des éléments d'alliage dans la cémentite résultant du processus de bobinage. Le modèle de transformation de phase est capable de prédire la fraction d'austénite obtenue à la fin du chauffage intercritique pendant 3 min à différentes températures (100%α', 67%α' et 50%α'

Cette thèse est accessible à l'adresse : http://theses.insa-lyon.fr/publication/2020LYSEI120/these.pdf
© [A. MATHEVON], [2020], INSA Lyon, tous droits réservés

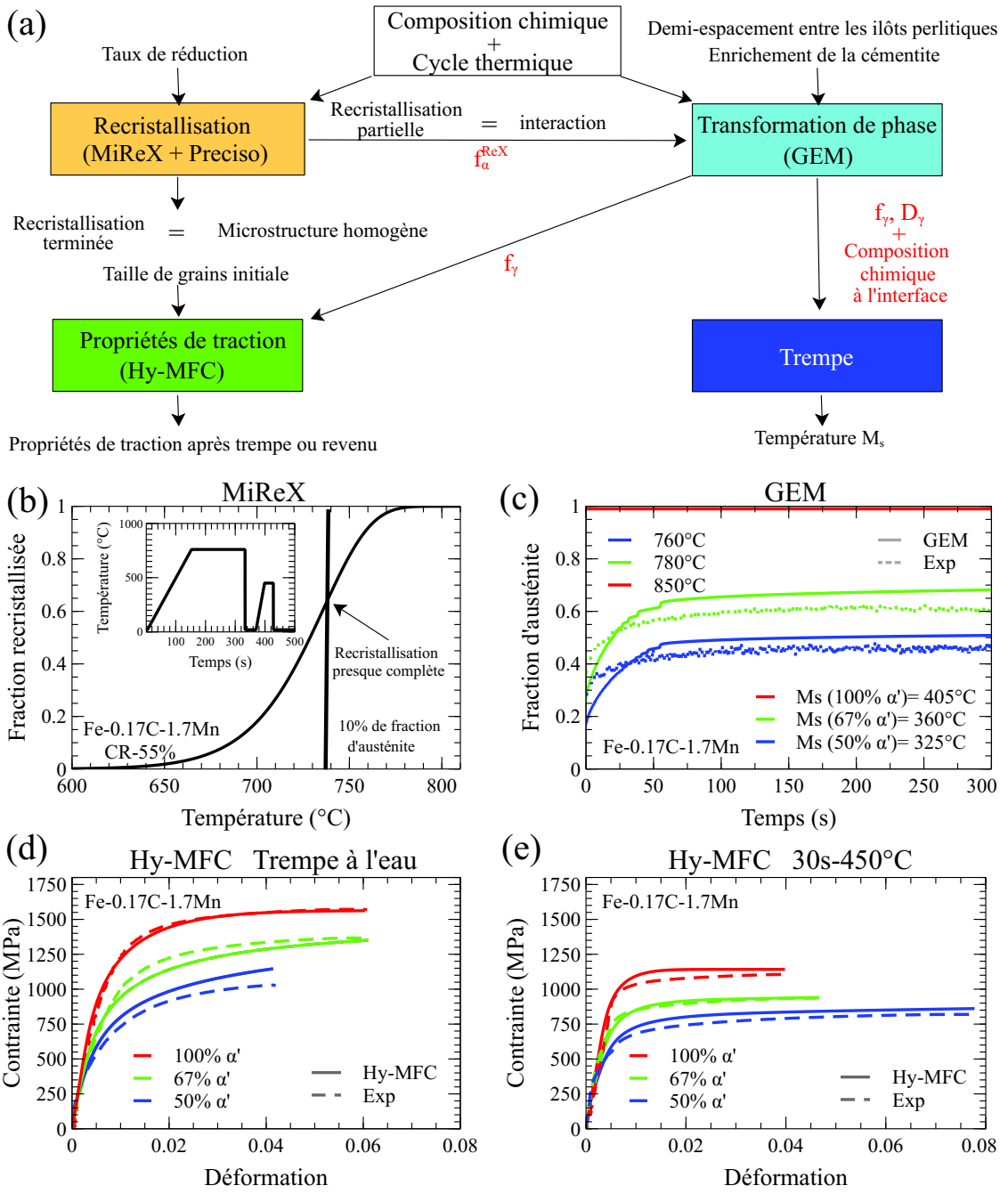

Figure 2: (a) Aperçu de l'approche de couplage des différents modèles développés dans la thèse. (b) Présentation de la cinétique de recristallisation dans le cas de l'acier Fe-0.17C-1.7Mn lors d'un chauffage continu avec une vitesse de chauffage de 5 °C/s. (c) Comparaison de la cinétique de formation austénitique expérimentale et modélisée pendant le recuit intercritique et la température M_s pour différentes fractions de martensite. (d-e) Comparaison des propriétés de traction des aciers DP trempés et revenus pour différentes fractions de martensite.

Cette thèse est accessible à l'adresse : http://theses.insa-lyon.fr/publication/2020LYSEI120/these.pdf
© [A. MATHEVON], [2020], INSA Lyon, tous droits réservés

pour une température de 850 °C, 780 °C et 760 °C) sur l'acier Fe-0.17C-1.7Mn (voir la Figure 2.(c)).

À partir du modèle de transformation de phase, il est possible de déterminer la fraction d'austénite à la fin du recuit intercritique et d'estimer à la fois le diamètre des grains austénitiques à partir de la taille initiale des grains et l'enrichissement des différents éléments de substitution à l'interface. Ces différents paramètres sont nécessaires pour évaluer l'évolution de la température M_s en fonction du cycle thermique appliqué et de la composition chimique. La Figure 2.(c) présente les résultats obtenus dans le cas de l'acier Fe-0.17C-1.7Mn où l'on note une diminution de M_S due à l'affinement de la taille des grains et à l'enrichissement supplémentaire en éléments d'alliage lorsque la fraction austénitique diminue.

Enfin, les propriétés de traction des aciers DP après la trempe ou le revenu sont définies à partir du modèle Hy-MFC en utilisant la composition chimique de l'acier, la taille initiale des grains ferritiques et les paramètres du processus de revenu. La Figure 2.(d-e) présente les résultats obtenus pour l'acier Fe-0.17C-1.7Mn avec différentes fractions de martensite calculées par le modèle GEM des aciers DP trempés ou revenus. Dans les deux cas, un bon accord est obtenu sur les propriétés finales de l'acier malgré la petite erreur commise sur l'estimation de la fraction d'austénite.

À l'avenir, une validation plus complète de cette approche et des résultats des différents modèles sur une chaîne de production industrielle pour une large gamme de composition chimique sera nécessaire afin de fixer les limites d'utilisation et d'explorer les difficultés supplémentaires rencontrées lors du passage de l'échelle de laboratoire à l'échelle industrielle. Cette démarche pourra également être étendue pour d'autres types d'aciers multiphasés.

Cette thèse est accessible à l'adresse : http://theses.insa-lyon.fr/publication/2020LYSEI120/these.pdf
© [A. MATHEVON], [2020], INSA Lyon, tous droits réservés

Contents

Cette thèse est accessible à l'adresse : http://theses.insa-lyon.fr/publication/2020LYSEI120/these.pdf
© [A. MATHEVON], [2020], INSA Lyon, tous droits réservés

Cette thèse est accessible à l'adresse : http://theses.insa-lyon.fr/publication/2020LYSEI120/these.pdf
© [A. MATHEVON], [2020], INSA Lyon, tous droits réservés

Cette thèse est accessible à l'adresse : http://theses.insa-lyon.fr/publication/2020LYSEI120/these.pdf
© [A. MATHEVON], [2020], INSA Lyon, tous droits réservés

Cette thèse est accessible à l'adresse : http://theses.insa-lyon.fr/publication/2020LYSEI120/these.pdf
© [A. MATHEVON], [2020], INSA Lyon, tous droits réservés

Cette thèse est accessible à l'adresse : http://theses.insa-lyon.fr/publication/2020LYSEI120/these.pdf
© [A. MATHEVON], [2020], INSA Lyon, tous droits réservés

Cette thèse est accessible à l'adresse : http://theses.insa-lyon.fr/publication/2020LYSEI120/these.pdf
© [A. MATHEVON], [2020], INSA Lyon, tous droits réservés

List of Figures

Cette thèse est accessible à l'adresse : http://theses.insa-lyon.fr/publication/2020LYSEI120/these.pdf
© [A. MATHEVON], [2020], INSA Lyon, tous droits réservés

Cette thèse est accessible à l'adresse : http://theses.insa-lyon.fr/publication/2020LYSEI120/these.pdf
© [A. MATHEVON], [2020], INSA Lyon, tous droits réservés

Cette thèse est accessible à l'adresse : http://theses.insa-lyon.fr/publication/2020LYSEI120/these.pdf
© [A. MATHEVON], [2020], INSA Lyon, tous droits réservés

Cette thèse est accessible à l'adresse : http://theses.insa-lyon.fr/publication/2020LYSEI120/these.pdf
© [A. MATHEVON], [2020], INSA Lyon, tous droits réservés

Cette thèse est accessible à l'adresse : http://theses.insa-lyon.fr/publication/2020LYSEI120/these.pdf
© [A. MATHEVON], [2020], INSA Lyon, tous droits réservés

Cette thèse est accessible à l'adresse : http://theses.insa-lyon.fr/publication/2020LYSEI120/these.pdf
© [A. MATHEVON], [2020], INSA Lyon, tous droits réservés

Cette thèse est accessible à l'adresse : http://theses.insa-lyon.fr/publication/2020LYSEI120/these.pdf
© [A. MATHEVON], [2020], INSA Lyon, tous droits réservés

Cette thèse est accessible à l'adresse : http://theses.insa-lyon.fr/publication/2020LYSEI120/these.pdf
© [A. MATHEVON], [2020], INSA Lyon, tous droits réservés

Cette thèse est accessible à l'adresse : http://theses.insa-lyon.fr/publication/2020LYSEI120/these.pdf
© [A. MATHEVON], [2020], INSA Lyon, tous droits réservés

Cette thèse est accessible à l'adresse : http://theses.insa-lyon.fr/publication/2020LYSEI120/these.pdf
© [A. MATHEVON], [2020], INSA Lyon, tous droits réservés

Cette thèse est accessible à l'adresse : http://theses.insa-lyon.fr/publication/2020LYSEI120/these.pdf
© [A. MATHEVON], [2020], INSA Lyon, tous droits réservés

Cette thèse est accessible à l'adresse : http://theses.insa-lyon.fr/publication/2020LYSEI120/these.pdf
© [A. MATHEVON], [2020], INSA Lyon, tous droits réservés

List of Tables

Cette thèse est accessible à l'adresse : http://theses.insa-lyon.fr/publication/2020LYSEI120/these.pdf
© [A. MATHEVON], [2020], INSA Lyon, tous droits réservés

Cette thèse est accessible à l'adresse : http://theses.insa-lyon.fr/publication/2020LYSEI120/these.pdf
© [A. MATHEVON], [2020], INSA Lyon, tous droits réservés

General introduction

Development of Advanced High Strength Steels (AHSS)

In response to the increasing demand from automobile manufacturers for steel grades with higher mechanical properties, many grades of AHSS were developed from the mid-1970s to the present day as shown in Figure 3.

The first generation brings together different types of steels, based on a ferritic structure. This family includes Martensitic (MART) and multiphase (Complex Phase (CP), Transformation Induced Plasticity (TRIP) and Dual-Phase) steels. They have a wide range of mechanical properties but nevertheless present a lack of ductility often leading to forming problems [BOU 13].

To overcome the formability problems of first generation steels, the second generation of AHSS was developed in the 1990s based on a fully austenitic structure giving it a good combination of strength and ductility. Austenitic Stainless Steels (AUST. SS), Lightweight steels with Induced Plasticity (L-IP) and Twinning Induced Plasticity (TWIP) steels are part of this family for which a considerable addition of alloying elements (Manganese, Nickel,...) has been made in order to stabilize austenite. This results in a high production cost in addition to poor welding quality and a risk of delayed fracture due to hydrogen and zinc [HIL 15, NAN 16]. These drawbacks explain why few examples of industrial applications were developped and today's production is close to zero.

The third generation is still in the development phase. It is based on the improvement of the first generation steels following the development of knowledge and production means (for example 980 XG3 Concept of US Steel). In particular, the increase in heating and cooling speeds allowing more complex cycles and the consideration of material properties in the design of parts (roll forming with more simple geometry and new assembling techniques to overcome welding issue) were used to optimize their mechanical properties. We can note the development of new metallurgical routes such as Quenching and Partitioning (Q&P) and new ultra-fine bainite microstructures or the improvement of existing processing lines of TRIP and DP steels [MAT 12, MAT 09, NAN 16].

DP steels studied during this PhD-work appear promising from an industrial point of view, particularly in the manufacture of Body In White (BIW), thanks to their high mechanical properties but also low manufacturing cost (few alloying elements) and a good adaptation to different industrial processes such as welding, forming and coating. The objective today is therefore to understand in detail the various mechanisms involved in their manufacture in order to be able to optimize and predict their properties.

Cette thèse est accessible à l'adresse : http://theses.insa-lyon.fr/publication/2020LYSEI120/these.pdf
© [A. MATHEVON], [2020], INSA Lyon, tous droits réservés

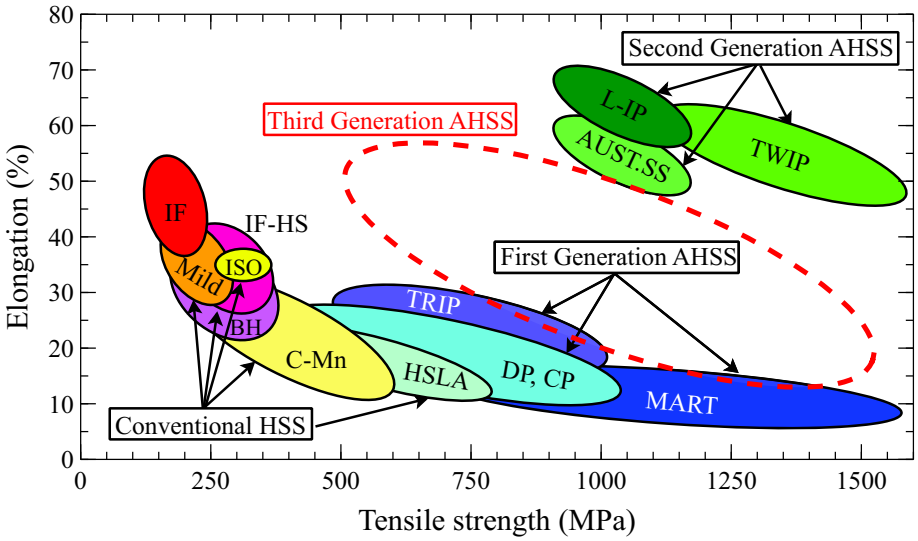

Figure 3: Overview of tensile strength and total elongation for various High Strength Steels (HSS) and Advanced High Strength Steels (AHSS) grades. Based on data extracted from [KWO 10, MAT 12, NAN 16]

Dual-phase steels: Processing step and microstructure

The mechanical properties of DP steels are due to the particularity of their microstructure, which is composed of two phases consisting of a soft ferritic phase (α) in which a hard martensitic phase (α') is inserted. The martensite fraction used industrially is in the range of 5-70 % in order to guarantee sufficient ductility and formability properties. An example of a classical thermal cycle used industrially to obtain a ferrite-martensite microstructure is shown in Figure 4, starting from a cold-rolled ferritic-pearlitic microstructure obtained after hot rolling and coiling. The evolution of the microstructure then takes place in 3 steps detailed below:

- **Intercritical annealing stage:** In order to form a two-phase microstructure made up of austenite and ferrite grains, the first step is to heat the steel sheet in the intercritical annealing range ($Ae_1 < T < Ae_3$, $\sim$ 720-830 °C) for 1-2 minutes. During heating, recovery and recrystallization phenomena will take place to transform the cold-rolled deformed microstructure into a homogeneous recrystallized microstructure. Then, austenite nucleation and growth will occur. Nevertheless, in some cases, an interaction between the two phenomena may occur depending on the chemical composition and for high heating rates. The Radiant Tube Furnace (RFT) and the Direct Flame Furnace (DFF) lead to an average heating rate of 5 and 30 °C/s respectively. More recently, Induction Furnaces have been developed with heating rates of the order of 100 °C/s. Hence, it is necessary to understand the effect of the heating rate on the possible interaction of the two phenomena.
- **Cooling stage:** Once the ferrite-austenite mixture has been obtained during intercritical annealing, austenite has to be decomposed into martensite. For this purpose, a sufficiently high cooling rate ($\sim$ 30 °C/s) must be guaranteed to avoid other decomposition products (bainite, ferrite-pearlite).

Cette thèse est accessible à l'adresse : http://theses.insa-lyon.fr/publication/2020LYSEI120/these.pdf
© [A. MATHEVON], [2020], INSA Lyon, tous droits réservés

- **Tempering stage:** Industrially it is necessary to carry out an additional treatment on DP steels either to protect them from corrosion or to guarantee sufficient formability. There are 2 main types of coating methods: GalvanIzation (GI) consists of depositing a Zn protective film by immersing the steel sheet in a liquid zinc bath (about 460 °C) and the GalvAnnealing (GA) step consists of alloying the Zn film deposited by GI with a holding of 10-20 s at $\sim$ 500 °C. In parallel, it is possible to carry out independently or following the protective treatments, an over-ageing allowing to soften the properties of martensite and thus to increase the formability of the whole steel.

Although DP steels emerged in the 1970s and many studies have been carried out into their development, many shadows still exist during their manufacture. Indeed, due to the numerous processing parameters (such as the heating rate, intercritical annealing temperature and time or cooling rate) and the numerous phenomena taking place (recrystallization, phase transformations and tempering), it is still impossible to accurately predict the steel final properties and the microstructure as a function of the steel chemical composition and other process parameters (rolling, reduction ratio).

Global objectives of PhD-projects launched by Fives KEODS since 2014

The project launched in 2014 by Fives KEODS aimed at developing and optimizing steel production methods through the following objectives:

- Development of new metallurgical routes adapted to each sector based on the constraints of their production line while adjusting the alloying elements content used in terms of the final product cost.
- Optimization of the total energy consumption during steel production by adjusting the heating and cooling power of the production lines according to the chemical compositions and the rolling process.
- Rationalization of the number of input products and achievement of differentiation as late as possible in the production line.
- Optimization of the production line control by adjusting the manufacturing process parameters for each coil in order to reach the targeted mechanical properties (SmartLine project).

To successfully carry out these objectives, it was important to develop reliable physically-based prediction tools to accurately predict the microstructural evolutions and the final mechanical properties of the steel.

To this end, Mélanie OLLAT's previous thesis, launched in 2014, has been used to study the recrystallization and phase transformation phenomena and their interactions involved in the heat treatment of a micro-alloyed DP1000 steel. Predictive modelling solutions and microstructural characterization of phase transformations during intercritical annealing were considered. Finally, a prospective study was carried out on quenching and tempering.

The present thesis launched in 2017 aims at proposing predictive modelling tools to forecast the microstructure evolution of Dual-Phase (DP) steels with various chemical

Cette thèse est accessible à l'adresse : http://theses.insa-lyon.fr/publication/2020LYSEI120/these.pdf
© [A. MATHEVON], [2020], INSA Lyon, tous droits réservés

compositions, reduction ratios and grain sizes throughout the heat treatment in order to use them as input data for a mechanical property prediction model.

PhD-manuscript outline

The current PhD-manuscript is composed of 6 chapters organized in the following manner and illustrated in Figure 4:

- **Chapter 1** describes the initial state of the different materials used during this PhD thesis: (i) 4 laboratory ternary Fe-C-Mn steels used to calibrate the different models and understand the effect of the chemical composition and (ii) 2 industrial steels (DP600 and DP1000) allowing to validate the different approaches in an industrial context. Experimental methods used for characterization are then presented.

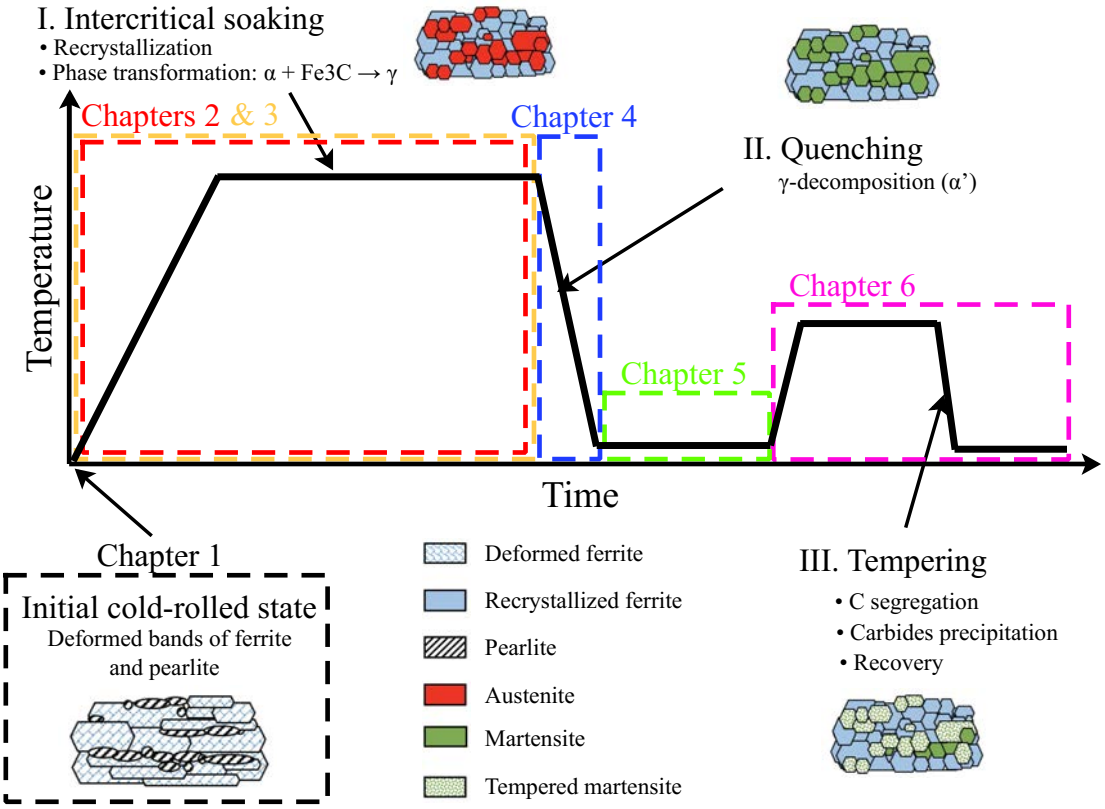

Figure 4: Typical thermal cycle used for the processing of DP steels composed of an intercritical annealing treatment followed by a cooling stage and a tempering stage. Structure of the PhD manuscript with respect to the different stages of the DP process is illustrated.

- **Chapter 2** is devoted to the development of a recrystallization model coupled with a precipitation model by extending the formalism of the existing JMAK models. The prediction of the recrystallization phenomenon (f_{α}^{ReX}) was coupled to the different physical parameters of the system such as chemical composition and reduction ratio during cold-rolling for isothermal and non-isothermal cycles. It was calibrated on

Cette thèse est accessible à l'adresse : http://theses.insa-lyon.fr/publication/2020LYSEI120/these.pdf
© [A. MATHEVON], [2020], INSA Lyon, tous droits réservés

ternary compositions before being validated on industrial compositions. Finally, a discussion on the interaction of the recrystallization phenomenon of industrial steels with the austenite formation is addressed.

- **Chapter 3** is focused on a new model developed to predict the ferrite to austenite transformation kinetics in steels including austenite fraction (f_γ) after intercritical annealing and the chemical composition profiles in the sample enabling to determine chemical compositions at the α/γ interface ($C^{\alpha/\gamma}_{C,Mn,Cr}$). For each alloying element, the concentration profile is computed solving a *unique* diffusion equation (including the 2 phases and the interface) within the system. The system length (L) is equal to the average half-spacing between pearlitic zones containing all cementite. The interface is described assuming linear variation of chemical potentials, saving thus computational time. Interface motion is driven by the minimization of Gibbs energy (GEM). The model naturally reproduces the transition between thermodynamic equilibria (Para equilibrium, Local equilibrium with negligible partitioning, Local equilibrium) during heating. The model integrates the cementite (M_3C) dissolution during non-isothermal heating with the determination of its initial alloying element enrichment ($C_{(C,Mn,Cr),M_3C}$). The validity of the model has been performed for the austenite formation over complex thermal cycles and compared to DICTRA sofware. For reverse transformation, validation has been carried out on ternary and quaternary systems Fe-C-(Mn-Si-Mo) on decarburization experiments and on cyclic phase transformations in intercritical domain.
- **Chapter 4** deals with the prediction of the martensitic transformation start temperature (M_S) and martensite fraction ($f_{\alpha'}$) in the case of two-phase steels. A coupling between an existing thermodynamic M_S prediction model and the phase transformation model of the previous chapter ($C^{\alpha/\gamma}_{C,Mn,Cr}$) with prior austenite grain size D_γ has been carried out to explain the error committed by the literature models for two-phase states.
- **Chapter 5** proposes an improvment of existing models for predicting the mechanical properties of existing DP steels. Various modifications such as the role of prior austenitic grain sizes and the interaction conditions between ferrite and martensite in the case of two-phase steels were added. Experimental validation has been performed on the different steels available in this PhD.
- **Chapter 6** finally investigates microstructural evolutions occurring during the tempering stages of DP thermal cycle. The tempering effect on the martensite mechanical property has been added to the global prediction model. Finally the mechanical property prediction model could be performed on pure martensite and on different two-phase states.

Figure 5 presents the general algorithm combining the different metallurgical models developed during the PhD to allow the mechanical property prediction. The input and output parameters of the models enabling their communication are thus summarized. The explanation of all these parameters has been detailed in the chapter descriptions.

Cette thèse est accessible à l'adresse : http://theses.insa-lyon.fr/publication/2020LYSEI120/these.pdf
© [A. MATHEVON], [2020], INSA Lyon, tous droits réservés

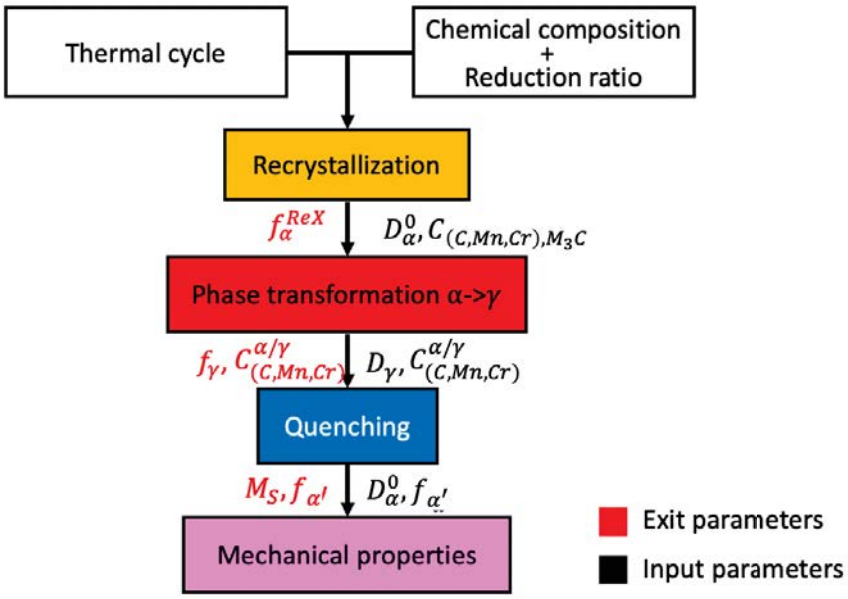

Figure 5: General algorithm combining the different models allowing the prediction of the DP steels mechanical properties. Input data are shown in black while output data are shown in red.

Cette thèse est accessible à l'adresse : http://theses.insa-lyon.fr/publication/2020LYSEI120/these.pdf
© [A. MATHEVON], [2020], INSA Lyon, tous droits réservés

Preface

Steel in car industry: environmental context

The aim of this preface is to propose a discussion on the environmental impact of Dual-Phase steels in the automotive market and to evaluate the interest of this study.

A global awareness of society's environmental problems has been rising, particularly as a result of global warming. For this reason, the Intergovernemental Panel to Climate Change [TAA 19] recommends a real reduction of our CO_2 emissions into the atmosphere to limit global warming to 1.5 °C (see Figure 6.(a)). At the same time, Figure 6.(b) presents the main sectors emitting greenhouse gases. The transport sector appears to be one of the key issues, which has led to the creation of international and European standards compelling car manufacturers to reduce their environmental impacts as shown in Figure 7.(a).

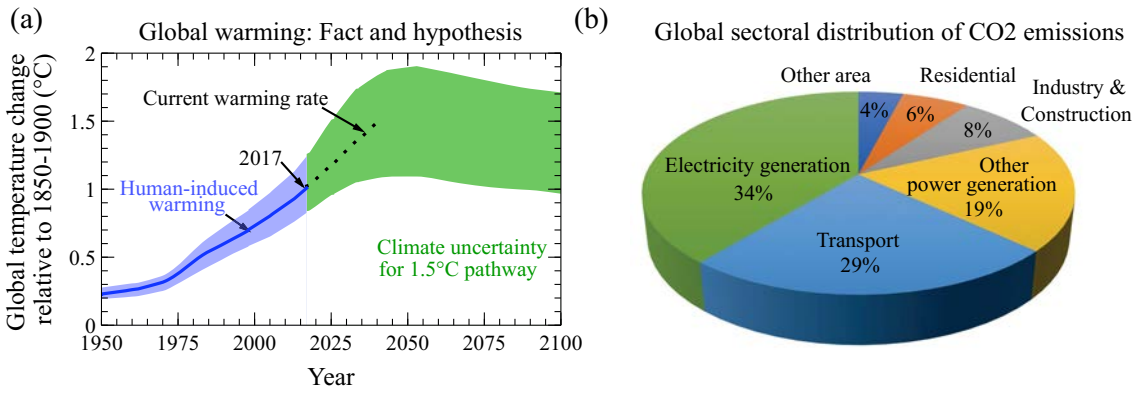

Figure 6: (a) Human-induced warming reached approximately 1 °C in 2017. At the present rate, global temperatures could reach 1.5 °C around 2040. Stylized 1.5 °C pathway shown here involves emission reductions beginning immediately, and CO_2 emissions reaching zero by 2055 [TAA 19]. (b) Sectoral distribution of CO_2 emissions worldwide in 2015. Data are extracted from [BAU 19].

Since the 1990s, in addition to their environmental impact, car manufacturers have been faced with safety and fuel economy constraints. Numerous actions can be taken, including powertrain efficiency improvement, rolling resistance reduction, aerodynamics improvement and vehicle lightweighting. Figure 7.(a) shows that while CO_2 emissions from cars decreased regularly since 2005, the average vehicle weight remained constant. Namely, the overall weight optimisation of the structure was masked by the increase in

Cette thèse est accessible à l'adresse : http://theses.insa-lyon.fr/publication/2020LYSEI120/these.pdf
© [A. MATHEVON], [2020], INSA Lyon, tous droits réservés

the weight of comfort and safety equipment as well as the growing trend towards “sport utility vehicles”.

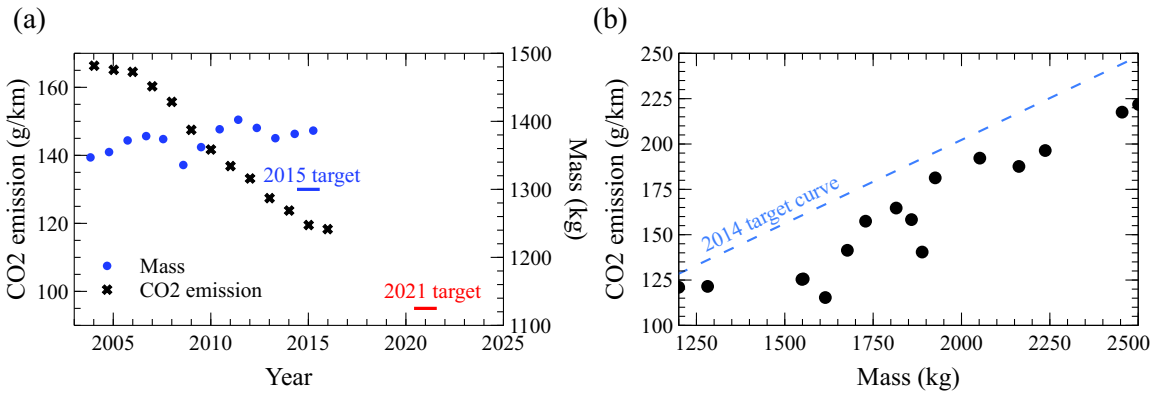

Figure 7: (a) Evolution of the average CO_2 emissions (g/km) and the average mass (kg) of new private cars sold in European Union. (b) Evolution of CO_2 emissions (g/km) as a function of weight for the average of cars sold per manufacturer in 2014 with the target imposed on manufacturers as a function of weight. The data are extracted from [Eur 15] and obtained in normalized tests.

New materials such as advanced high strength steels (AHSS), carbon fiber-reinforced polymer (CFRP), aluminium and magnesium alloys were studied with the aim of replacing standard steel. AHSS steels are expected to improve safety issues and reduce vehicle weight. Their high yield and ultimate tensile strength leads to an improvement in energy absorption and anti-intrusion properties compared to conventional steels. In addition, despite lower stiffness in the case of CFRP, aluminium and magnesium alloys, their low densities allow them to reduce the vehicle’s overall weight after an adjustment of the vehicle design despite a high manufacturing cost. At the same time, the weight reduction of the structure reduces emissions when using the car as illustrated in Figure 7.(b). However, as the manufacturing energy of the materials is not negligible, it is important to carry out a full life cycle assessment in order to know which materials meet both environmental and industrial criteria.

One of the central parts for the lightening of vehicle structures is the body in white (BIW). It often accounts for 1/3 of the overall curb weight and is responsible for passenger safety. Several publications compare the replacement of standard steels by AHSS, aluminium, magnesium or CFRP [TEM 11, STA 12, SUN 19, LIU 12, LEW 14, WIT 11, MAY 12]. Nevertheless for this type of study the hypotheses made have very strong influences on the final results, as shown by the multitude of different conclusions. One of the key points of these studies is generally the hypothesis of new vehicle production exclusively from recycled materials, since car manufacturers announce a recycling rate for steel and aluminium of around 90-95%. Figure 8 presents an assessment of car production from recycled materials in 2020, assuming an average vehicle life of 20 years, a recycling rate of 95% of end-of-life vehicles, and using the real growth in car production of 3% per year over the last 20 years. These choices lead to a proportion of 6.5% for new vehicles to be manufactured in 2021 out of the vehicles total amount produced over the last 20 years. On the contrary, the portion of end-of-life vehicles produced in 2000 to recycle represents

Cette thèse est accessible à l'adresse : http://theses.insa-lyon.fr/publication/2020LYSEI120/these.pdf
© [A. MATHEVON], [2020], INSA Lyon, tous droits réservés

only 3.5% of the total amount produced over the last 20 years. We realize that only **51% of new vehicles are made from recycled material** due to vehicle production growth. The solution to increase this recycled fraction in new vehicle is no longer to improve recyclability but to limit the production growth. The fraction of recycled material in the world production of steel and aluminium is about 30% [ASS 19, ALU 09] due to a higher growth rate and longer immobilization periods as well as lower recycling rates (building and energy production). This is why our own life cycle study was carried out with the main hypothesis (current rate of recycled material in world production) to determine the best candidate to replace the standard steel in BIW.

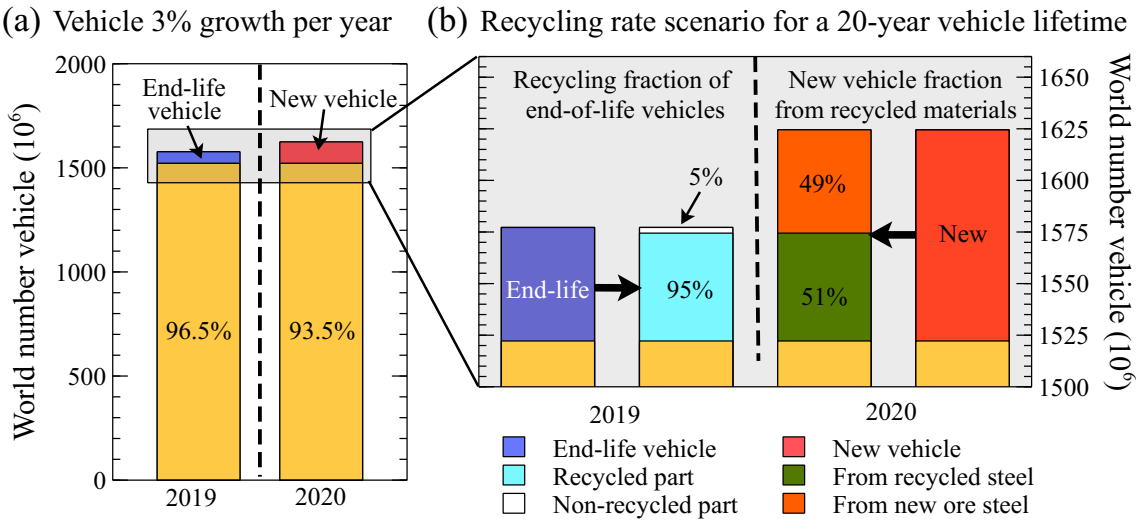

Figure 8: (a) Evolution of the number of vehicles worldwide with a growth of 3% per year and an average lifetime of 20 years, as well as the fraction of end-of-life vehicles and new vehicles produced between 2019 and 2020. (b) Recycling and waste rate of end-of-life vehicles and fraction of new vehicles produced from recycled and new ore materials.

Based on a literature review [EPA 12, SIN 12, MAL 11], three light BIW scenarios are considered. This study selects Scenario I as an AHSS-based lightweight design (98.1% of AHSS steel), Scenario II as an aluminum alloy-based lightweight design (86.1% of aluminium) and Scenario III as a CFRP-based lightweight design (60% of CFRP) to replace the steel baseline (100%). Table 3 summarizes the overall vehicle weight, BIW and the exact proportion of each material used in the scenarios. It is then necessary to evaluate the energy consumed and the amount of CO_2 emitted during the different stages of the vehicle's life cycle, which can be divided into 3 steps in accordance with the following equations:

$$E_{Total} = E_{Mp} + E_S + E_{End} \qquad \text{and} \qquad C_{Total} = C_{Mp} + C_S + C_{End} \tag{1}$$

where E_i and C_i are respectively energy and CO_2 emissions for the different stages of the life cycle analysis, E_{Total} the global energy over the whole lifetime, E_{Mp} the energy required for the production and shaping of the materials, E_S the energy saved in the use

Cette thèse est accessible à l'adresse : http://theses.insa-lyon.fr/publication/2020LYSEI120/these.pdf
© [A. MATHEVON], [2020], INSA Lyon, tous droits réservés

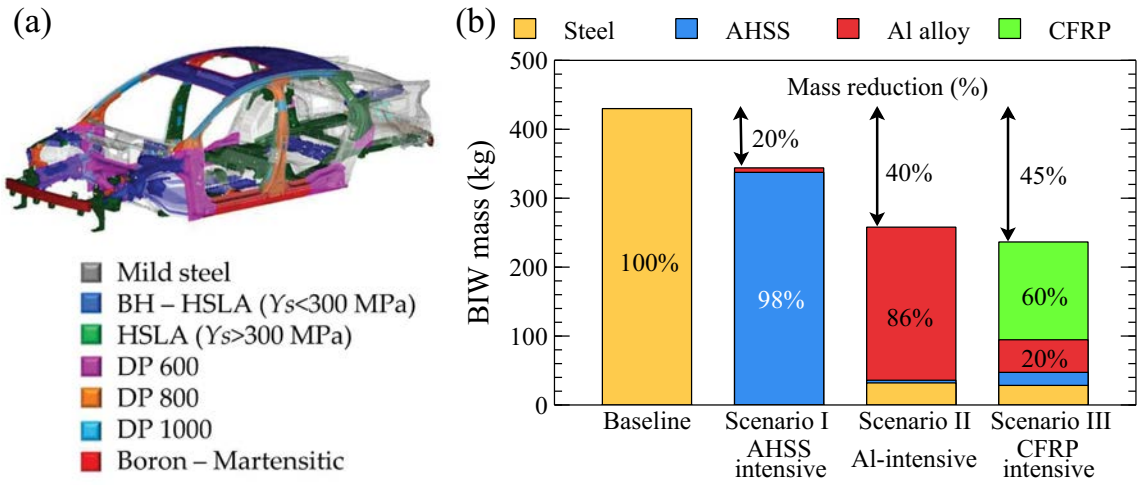

Figure 9: (a) Examples of AHSS used in the body-in-white structure of a commercialized Ford Fusion [AUT]. (b) Body-in-white weight of the four designs containing different materials (Conventional steel, AHSS, Aluminium, CFRP) [SUN 19].

phase compared to the baseline, E_{End} the energy required to process the vehicle at the end of its life.

- **Material production:** The energy required and CO_2 amount emitted to produce the different materials used to manufacture the different BIWs can be broken down as follows:

$$E_{Mp} = (1-\phi)E_{Es} + \phi E_R + E_{Tm} \qquad \text{and} \qquad C_{Mp} = (1-\phi)C_{Es} + \phi C_R + C_{Tm} \quad (2)$$

  where E_{Es} is the energy required to extract, refine and shape from raw material, E_R is the energy required to recycle and re-use the recycled material, E_{Tm} is the energy required to assemble the part (cutting, stamping, joining and painting) and ϕ is the fraction of recycled material in the world production of the considered material (0.28 for steel [ASS 19], 0.32 for aluminium [ALU 09] and 0 for composites).

- **Use phase:** Based on a vehicle fuel economy test conducted, the baseline vehicle's fuel consumption is 6.5 L/100 km. Using the method developed by Koffler and Rohde-Brandenburger [KOF 10], the energy and CO_2 amount saved by the mass-induced fuel consumption (with power train adaptation) can be calculated in the following way for the 3 new BIW lightweight designs compared to baseline state:

$$E_S = -\Delta m F_{RV} D_v H V_g \qquad \text{and} \qquad C_S = -\Delta m F_{RV} D_v F T_g \quad (3)$$

  where Δm the mass saving according to the several BIW scenarios compared to the baseline state, D_v the vehicle lifetime distance (estimated at 200,000 km [SUN 19]),F_{RV} the fuel reduction value (0.38 L/100 kg.100 km [SUN 19]) of the BIWs following the adaptation of the engines in agreement with Koffler and Rohde-Brandenburger [KOF 10] ,HV_g the heating value and FT_g the CO_2 footprint of gazoline (respectively 34.8 MJ/L and 2.36 kg CO_2/L [MAY 12]).

Cette thèse est accessible à l'adresse : http://theses.insa-lyon.fr/publication/2020LYSEI120/these.pdf
© [A. MATHEVON], [2020], INSA Lyon, tous droits réservés

- **End-of-life:** The vehicle's end-of-life energy and CO_2 amount is determined by the way in which they are transformed. The majority of vehicles are sorted and shredded to recover the raw materials. For the CFRPs it is also necessary to take into account the destruction energy (incineration, pyrolysis and fluidized bed process,...) since it is not yet possible to recycle them included in E_{Ss}. At the same time during the life of the vehicle it can happen that parts are defective and replaced which has been evaluated in some studies [MAY 12]. The end-of-life energy of the vehicle is defined as follows:

$$E_{End} = E_M + E_{Ss} \qquad \text{and} \qquad C_{End} = C_M + C_{Ss} \tag{4}$$

with E_M the BIW maintenance energy and E_{Ss} the energy required for sorting and shredding.

	Material	Extraction and shaping	Recycling	Total fabrication	Maintenance	Shredding and sorting
		E_{Es}	E_R	E_{Tm}	E_M	E_{Ss}
Energy (MJ/kg)	Steel	32	9	14.5	7.5	0.4
	AHSS	32	9	15	7.5	0.4
	Al alloy	207	18.7	18.5	7	0.6
	CFRP	272	-	19	7	8.3
		C_{Es}	C_R	C_{Tm}	C_M	C_{Ss}
CO_2 emission (kg)	Steel	2500	700	2600	500	2
	AHSS	2500	700	2800	500	2
	Al alloy	12000	1100	5100	450	2
	CFRP	17250	-	1500	450	1680

Table 2: Values of the energies required and CO_2 emission along the manufacturing process of the vehicle for the different materials [MAY 12]

Table 2 and Table 3 summarize the results and values of the life cycle analysis of the 4 BIW lightweighting designs. From the final results it is clear that from an energetic point of view the **3 BIW structural lightweighting designs are more interesting than the standard steel baseline** as highlighted in Figure 10. CFRP-intensive scenario appears less interesting today than the others because it only becomes interesting from an energetic and CO_2 emission point of view after 200,000 km. On the other hand, it could be promising if a low-energy recycling solution is found. AHSS-intensive and Al-intensive designs appear to be energy and CO_2-equivalent over their lifetime and the recycling rate chosen. **For longer lifetimes** or **an increase in the rate of recycled material in world production** due to a decrease in world production or an increase in the rate of recycled material at the end of life, **aluminium would appear to be more attractive** since it has a higher energy gain and a higher CO_2/BIW gain during the use phase. Nevertheless, at the present time, it seems difficult to imagine the use of aluminium as the only solution in the automotive sector since, with an annual market of 90 million vehicles worldwide always in expansion, scenario II would require 18 million tonnes of

Cette thèse est accessible à l'adresse : http://theses.insa-lyon.fr/publication/2020LYSEI120/these.pdf
© [A. MATHEVON], [2020], INSA Lyon, tous droits réservés

Category	Subcategory	Baseline	Scenario I	Scenario II	Scenario III
Materials (kg)	steel	430	0	32	28.4
	AHSS	0	337.5	3.9	18.9
	Al alloy	0	6.5	222	47.3
	CFRP	0	0	0	141.9
Vehicle information (kg)	Vehicle curb weight	1220	1134	962	768.5
	BIW weight	430	344	258	236.5
	mass gain Δm	-	86	172	193.5
Energy (GJ)	Material production	17.2	14.7	38.2	51
	Use stage	-	-22.7	-45.4	-51.2
	End-of-life	3.4	2.7	1.9	2.9
	Total	20.6	-5.2	-5.4	2.7
CO_2 emission (Tons)	Material production	1.97	1.7	3.19	3.52
	Use stage	-	-1.54	-3.09	-3.47
	End-of-life	0.21	0.17	0.12	0.35
	Total	2.2	0.33	0.22	0.4

Table 3: Information of four body-in-white designs [SUN 19] and the results of the life cycle analysis of the 4 BIW lightweighting designs.

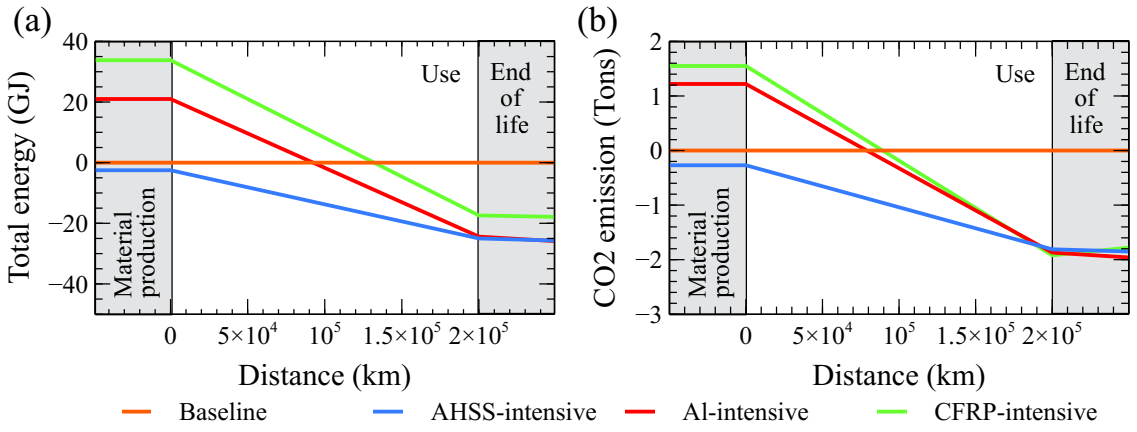

Figure 10: (a) Total energy and (b) CO_2 emissions relative to driving distances (up to 200,000 km) for three lightweight body-in-white Scenarios compared to baseline state, including production and end-of-life stages.

aluminium for BIW production alone, i.e. **1/3 of world production** compared to **1/55 for steel**. Moreover, at the current rate of development, bauxite resources are no longer unlimited and would be exhausted in about a century. This is why, **the development of new-generation steels seems promising** in view of the almost similar results from a life-cycle point of view and the much greater quantity available worldwide.

Cette thèse est accessible à l'adresse : http://theses.insa-lyon.fr/publication/2020LYSEI120/these.pdf
© [A. MATHEVON], [2020], INSA Lyon, tous droits réservés

Chapter 1

Materials and experimental techniques

The purpose of this section is to present the different steels studied during this thesis and their initial microstructure. The chemical compositions, microstructural characteristics and manufacturing processes will be detailed for the two types of studied steels: on the one side, a series of 4 Fe-C-Mn steels used for calibration of the various models developed and on the other side, two industrial Dual-Phase steels. Subsequently, the different methods and experimental conditions used in this PhD-work will be described.

Contents

Cette thèse est accessible à l'adresse : http://theses.insa-lyon.fr/publication/2020LYSEI120/these.pdf
© [A. MATHEVON], [2020], INSA Lyon, tous droits réservés

1.1 Experimental strategy

The objective of this paragraph is to present the experimental strategy used in this work to follow microstructural evolutions and mechanical properties during the different processing stages of Dual-Phase steels. Table 1.1 provides an overview of the different techniques used for the study of the metallurgical mechanisms involved during the manufacture of Dual-Phase steel and which will be developed later in this work. Afterwards, a description of the different experimental techniques used during this PhD-work is proposed. In the present work, the following points were considered:

- **The initial states** of the various steels presented in Section 1.2 were observed by optical microscopy to determine the grain size and the distribution of pearlitic rich zones including cementite, which varies according to the chemical composition and manufacturing process (laboratory or industrial). Carbon replicas have made it possible to determine the cementite carbide enrichment in terms of substitutional elements.
- **Intercritical annealing**: During intercritical heating, the phenomena of austenite formation and recrystallization can interact and modify their kinetics. This interaction depends on many parameters such as chemical composition and heating rate. In order to avoid this interaction, all recrystallisation kinetics were studied below the austenite transformation start temperature ($< Ac_1$). The austenite formation kinetics performed on the Gleeble took place at a heating rate allowing a complete recrystallization before reaching Ac_1 or on a prior recrystallized state. Different techniques have been used to monitor these phenomena:
  1. The recrystallization kinetics of the 6 grades available for this study were obtained from hardness measurements. The experiments on cold-rolled steels took place over a temperature range of 600 to 700 °C as well as for different reduction ratios between 25-75%.
  2. The austenite formation kinetics have mainly been followed by optical dilatometry on the Gleeble with heating ramps or complex cycles including intercritical stages on the different compositions. These results were validated by optical microscopy quantification using a *Bandoh* etching.
- **Quenching**: The austenite decomposition from the annealing temperature was monitored by optical dilatometry mainly at high cooling rates to ensure martensite formation. The initial phase fraction before cooling in the case of two-phase steels was measured by optical microscopy.
- **Tempering**: The evolution of hardness and Thermoelectric Power (TEP) has made it possible to study metallurgical phenomena occurring during tempering. In order to determine the cementite precipitation temperature, a monitoring by Differential Scanning Calorimetry (DSC) and observations by Focused Ion Beam (FIB) was realized. The volumic fraction of precipitated cementite was evaluated using FIB experiments.
- **Mechanical properties**: The mechanical properties of the various steels were determined using tensile and hardness tests on 100% martensitic states as well as on Dual-Phase materials with various martensite fractions after quench. Finally, these

Cette thèse est accessible à l'adresse : http://theses.insa-lyon.fr/publication/2020LYSEI120/these.pdf
© [A. MATHEVON], [2020], INSA Lyon, tous droits réservés

different samples were then treated in salt baths for times between 30s and 1h for temperatures in the range of 250 to 450°C to study the mechanical properties after tempering using tensile and hardness tests.

1.2 Material

This study was carried out on four ternary Fe-C-Mn steels prepared in laboratory and on two industrial Dual-Phase steels. Their chemical composition is given in Table 1.2. The chemical composition of the ternary steels was selected to be close to that industrial steels in terms of C and Mn contents. Moreover, the C and Mn contents of the ternary steels were chosen in order to be able to analyze clearly the effect of these two elements on the different phenomena (recrystallization, phase transformation, tempering and mechanical properties). Concerning the industrial steels, they are two low-carbon and low-alloy steels with the addition of alloying elements to improve their manufacturing processes and mechanical properties. They have almost the same Mn, Cr and Si content but they differ mainly by their C content and by the presence of microalloying elements (Ti, Nb) in the case of the DP1000 steel.

The Fe-C-Mn ingots were cast in 100x100 mm section before being cooled. They were then heated to 1250 °C and hot forged to obtain bars with a 50 mm diameter and with a ferritic-pearlitic structure. The samples were machined by wire-cut electroerosion to obtain samples of 1 or 2 mm thickness. To study the phenomenon of recrystallization, the samples were cold-rolled with a hand operated rolling mill. Three different reductions ratios (25%, 50% and 75%) were used to analyze the effect of this parameter on the recrystallization kinetics. For the other studies, they were used without cold-rolling.

Concerning the two industrial steels, they have been hot-rolled in the austenitic domain, coiled around 600 °C and slowly cooled to obtain a ferritic-pearlitic structure. The sheets were finally cold-rolled with a 55% reduction ratio to obtain the sheets used in this study.

Furthermore, in view of the experimental recrystallization kinetics obtained for the different steels in this study (see Chapter 2), it appears clearly that for a conventional industrial heating of 5 °C/s, only the DP1000 is likely to present a limited recrystallized fraction ($< 20\%$) due to niobium addition at austenite formation. This is why, in order to decorrelate the interaction between the recrystallization and phase transformation phenomena, some samples of the DP1000 were prior recrystallized by a heat treatment of 1200 s at 700 °C (below Ac_1). This is why two denominations will be used in this work for the DP1000 according to its initial state: (i) the industrial state corresponding to cold-rolling called "DP1000-CR" and (ii) the previously recrystallized steel called "DP1000-ReX".

The initial microstructures of the individual steels are shown in Figure 1.1. The industrial steels (DP600 and DP1000-CR) are composed of ferrite-pearlite bands deformed in the rolling direction. In contrast, the laboratory grades and DP1000-ReX have a more homogeneous microstructure comprising recrystallized ferrite grains and pearlitic zones (see Figure 1.2). Due to the additional treatment to recrystallize the DP1000-ReX, a cementite spheroidization is observed. A Nital etching was performed on the different steels in order to define their respective initial ferritic grain sizes summarized in Table 1.3. A grain size close to 6 μm is observed for the two industrial DP steels while the ternary steels show

Cette thèse est accessible à l'adresse : http://theses.insa-lyon.fr/publication/2020LYSEI120/these.pdf
© [A. MATHEVON], [2020], INSA Lyon, tous droits réservés

Experimental techniques	Initial states	Intercritical annealing		Quenching	Tempering	Mechanical properties
		Recrystallization	γ-formation			
In-situ techniques						
Dilatometry	-	-	✓	✓	-	-
DSC	-	-	-	-	✓	-
"Indirect" techniques						
TEP	-	-	-	-	✓	-
Hardness	✓	✓	-	-	✓	✓
Tensile test	-	-	-	-	-	✓
Microstructural observations						
Optical microscopy	✓	-	✓	✓	-	✓
TEM observations on carbon replicas	✓	-	-	-	-	-
TEM observations on thin foils	-	-	-	-	✓	-
FIB tomography	-	-	-	-	✓	-

Table 1.1: Experimental techniques used for each investigated thermal stage.

© 2020 – Alexandre MATHEVON – MATEIS laboratory

Cette thèse est accessible à l'adresse : http://theses.insa-lyon.fr/publication/2020LYSEI120/these.pdf
© [A. MATHEVON], [2020], INSA Lyon, tous droits réservés

Steel grades	Chemical composition C_i^0 (in wt.%)						
	C	Mn	Cr	Si	Nb	Ti	N
Ternary steels	0.17	0.5	0.02	0.007	0.002	0.000	0.004
	0.17	1.7	0.02	0.008	0.002	0.000	0.004
	0.17	2.5	0.02	0.016	0.002	0.000	0.004
	0.08	1.7	0.02	0.007	0.002	0.000	0.0029
DP600	0.09	1.5	0.5	0.3	0.002	0.000	0.005
DP1000	0.17	1.7	0.4	0.3	0.03	0.03	0.006

Table 1.2: Chemical composition C_i^0 of the ternary and industrial steels investigated in this study for each element i.

a much larger grain size between 20 and 50 μm which can be clearly seen in Figure 1.1. In addition, using *ImageJ* software, the average half-spacing between the main pearlitic zones was evaluated and reported in Table 1.3.

Furthermore, the chemical composition of the cementite particles in pearlitic zones was measured by Energy Dispersive Spectroscopy (EDS) analysis using carbon replicas following the protocol detailed in Section 1.3.2. A significant enrichment in substitutional elements such as manganese and chromium was observed in the case of industrial steels, as outlined in Table 1.3. This enrichment comes from the coiling step which is associated with a very slow cooling allowing the substitutional elements to diffuse over a long distance and with a thermodynamic equilibrium predicting high concentrations (20-30% for manganese). This enrichment is relevant since differences in final mechanical properties are observed industrially along the length and width of the coil (up to 80 MPa measured on industrial DP1000 coils, unpublished results) due to a difference in cooling speed between the core and the edges of the coil. Similarly, the additional recrystallization treatment undergone by the DP1000-ReX steel has led to an increase in the content of substitutional elements. On the contrary, laboratory grades have only a low alloying enrichment in cementite close to the nominal composition due to a relatively fast cooling rate. Only the cementite particles enrichment in substitutional elements for Fe-0.17C-1.7Mn steel was determined, which made it possible to extrapolate an enrichment for the three other ternary steels.

Steel grades	Initial ferritic grain size D_α^0 (μm)	Pearlitic zone half spacing (μm)	Cementite enrichment	
			Mn (wt.%)	Cr (wt.%)
0.17C-0.5Mn	45	25	1*	-
0.17C-1.7Mn	30	20	2	-
0.17C-2.5Mn	20	12	4*	-
0.08C-1.7Mn	50	30	2*	-
DP600-CR	6	15	12	6.5
DP1000-CR	6	5	10	4
DP1000-ReX	6	10	13	7

Table 1.3: Microstructural informations on the ternary and industrial steels investigated in this study. DP1000-ReX steel has been recrystallized with an additionnal heat treatment of 1200 s at 700 °C. (*) Manganese enrichment of cementite particles supposed for the three ternary steels.

Cette thèse est accessible à l'adresse : http://theses.insa-lyon.fr/publication/2020LYSEI120/these.pdf
© [A. MATHEVON], [2020], INSA Lyon, tous droits réservés

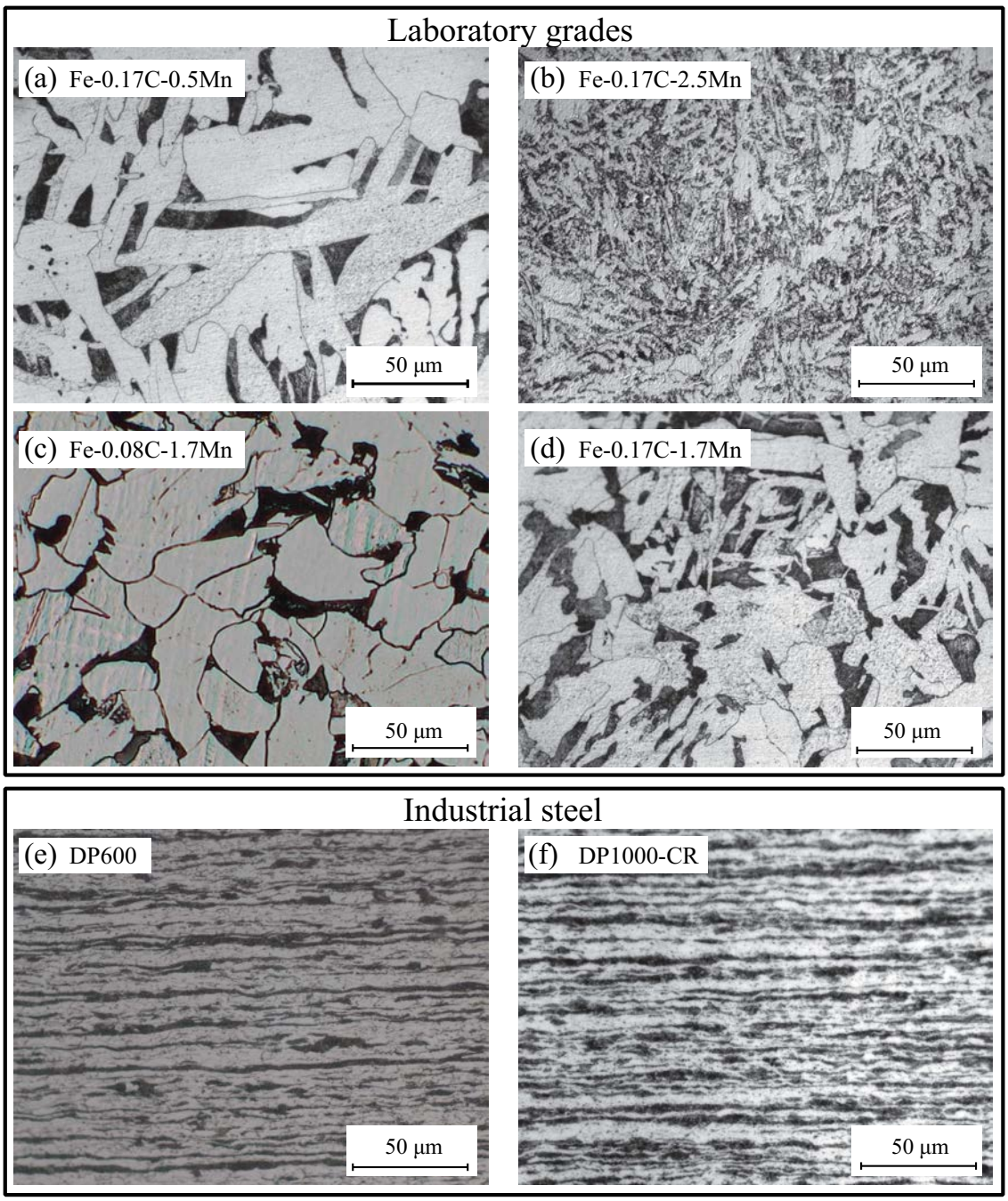

Figure 1.1: Initial microstructures of the different studied steels: (a) Fe-0.17C-0.5Mn, (b) Fe-0.17C-2.5Mn, (c) Fe-0.08C-1.7Mn, (d) Fe-0.17C-1.7Mn, (e) DP600, (f) DP1000-CR

Cette thèse est accessible à l'adresse : http://theses.insa-lyon.fr/publication/2020LYSEI120/these.pdf
© [A. MATHEVON], [2020], INSA Lyon, tous droits réservés

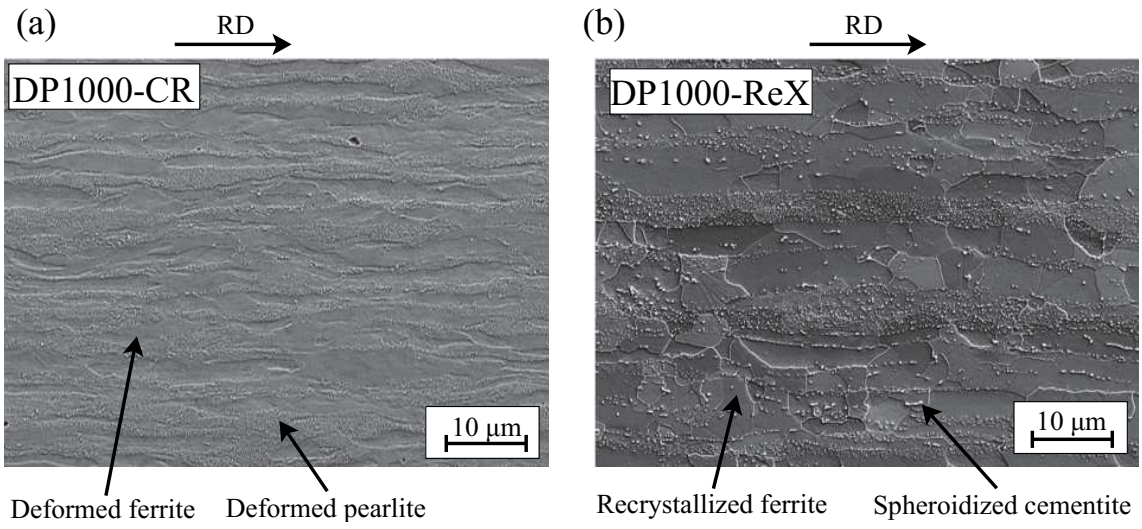

Figure 1.2: SEM micrographs of the (a) DP1000-CR steel and (b) DP1000-ReX steel. Cold-rolled steel is characterized by bands of deformed ferrite and pearlite while bands of spheroidized cementite islands and recrystallized ferrite grains are present in the prior recrystallized state.

1.3 Experimental techniques

This part aims at presenting the different experimental techniques used during this PhD, covering different heat treatment equipments, microstructural observation techniques, and also different characterization methods.

1.3.1 Thermal treatments

Two equipments were mainly used to perform the majority of the heat treatments of this PhD-work. Salt baths were used to determine the different recrystallisation kinetics (see Chapter 2) as well as the martensite tempering kinetics (see Chapter 6) during isothermal treatments. They also made it possible to achieve the various austenitizing treatments necessary for the different mechanical tests. On the other hand, the phase transformation kinetics during intercritical annealing were performed on a Gleeble 3500 thermodynamic simulator and determined by in-situ optical dilatometry and optical observation a posteriori.

1.3.1.1 Salt baths

Salt baths have three main advantages. First of all, they are characterized by a very high heating rate (~ 200 °C/s), which ensures good control of the temperature and processing time. They also allow interrupted tests to be carried out, particularly for the study of recrystallization and martensite tempering kinetics. Finally, salt baths guarantee a homogeneous thermal zone over the entire useful length of the sample without decarburization, unlike Gleeble.

Cette thèse est accessible à l'adresse : http://theses.insa-lyon.fr/publication/2020LYSEI120/these.pdf
© [A. MATHEVON], [2020], INSA Lyon, tous droits réservés

For the realization of low temperature range heat treatments ($150 - 550$ °C), sodium nitrite baths were used while for high temperature range ($600 - 900$ °C), a barium chloride salt bath was required.

1.3.1.2 Gleeble thermomechanical simulator

The Gleeble 3500 thermo-mechanical simulator was mainly used in this study for phase transformation kinetics (austenite and martensite formation). It ensures a perfect control of the heating/cooling rate, holding time and temperature, making it possible to reproduce thermal routes similar to those in the industry and to carry out non-isothermal tests for different controlled speeds.

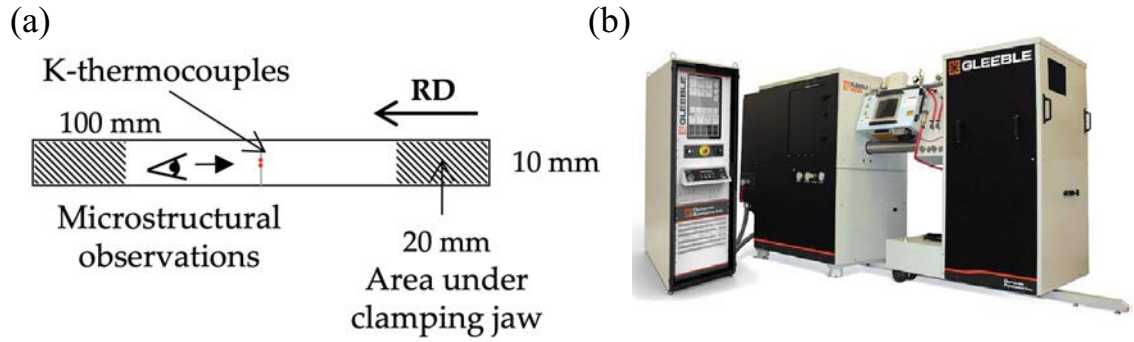

Figure 1.3: (a) Geometry of the samples used for the treatment in the *Gleeble* machine. (b) Picture of the *Gleeble* machine used.

Joule heating and water or air jet cooling are the basic principles of the Gleeble 3500 thermo-mechanical treatment simulator. The (100)×(10)×(1-2) mm samples are processed and fixed between the clamping jaws at 20 mm on each side. Type K thermocouples are welded to the sample center to provide accurate temperature control over the whole cycle in this zone. The cooling rates by air cooling cannot exceed 10 °C/s but it is possible to reach a cooling of 50 °C/s necessary for quenching on the Gleeble using a humid air spray. Water quenching is not possible in the case where the phase transformation kinetics has to be followed by optical dilatometry.

1.3.2 Microstructural observations

Coming from different steel sources, it was essential to study the initial states of the steels of this study and to monitor the microstructure evolution during heat treatment. The different methods of polishing, chemical etching and observation are described hereafter. It should be noted that microstructure observations have always been made at quarter thickness for reproducibility and in the plane of thermocouples for samples heat treated with Gleeble.

Cette thèse est accessible à l'adresse : http://theses.insa-lyon.fr/publication/2020LYSEI120/these.pdf
© [A. MATHEVON], [2020], INSA Lyon, tous droits réservés

Standard polishing process

For the preparation of the samples, SiC polishing papers (P-800, P-1200, P-2500, P-4000) were used before using polishing cloths with diamond solutions of 3 and 1 μm.

Optical microscopy (OM)

To observe the microstructures by optical microscopy, two chemical attacks were applied:

- Nital etching (4 mL nitric acid + 100 mL ethanol - 15s): this etching was used to reveal the initial state of our different steels by showing the grain boundaries (GB) of the ferrite as well as the carbides.
- Bandoh etching (2.3 mL Picral + 2.3 mL Metabisulfite + 1 mL Nital - 30 s): it was used to differentiate martensite from ferrite, which allows the proportion of each phase to be quantified. Usually, ferrite is coloured brown/blue and martensite white/yellow. A clear delimitation can be obtained between the phases as shown in Figure 1.4.(a) Nevertheless, as this attack is sensitive to oxidation, it is important to realize this etching just after finishing the polishing process.

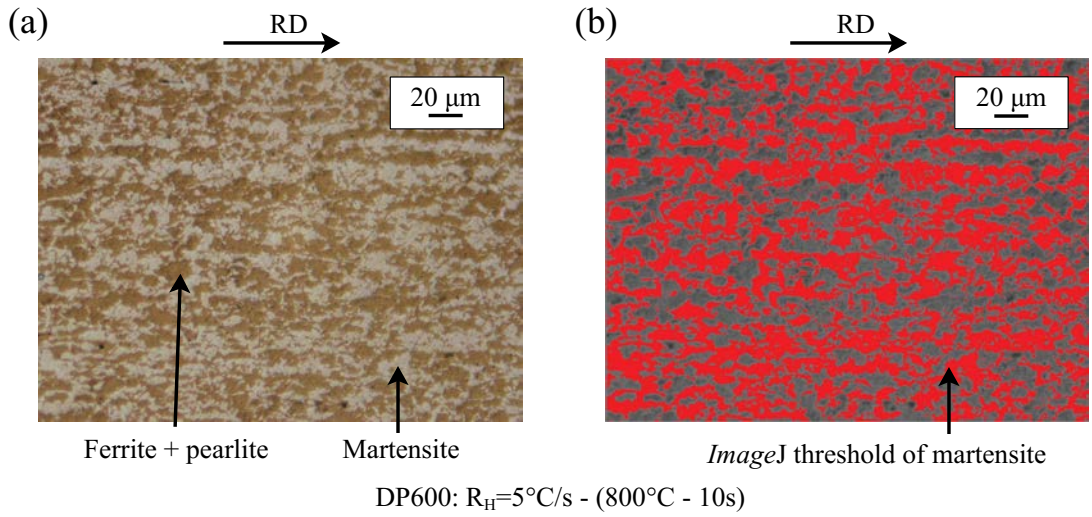

Figure 1.4: (a) Optical micrograph of DP600 after Bandoh etching: martensite appears white while (ferrite+pearlite) are brown. An example of martensite quantification using *ImageJ* software is given in (b).

The fractions of the respective phases can then be determined by image analysis using the *ImageJ* software. It is then possible to threshold the micrographs to separate one of the two phases with Otsu method [LIU 09, VAL 13]. Figure 1.4.(b) shows an example of thresholding performed on the microstructure with a red colored martensite. For each sample, about twenty micrographs were made for reproducibility. In addition, for each phase quantification measurement using optical micrography, a measurement error of $+-10\%$ was considered due to multiple sources of uncertainty (thresholding, reproducibility, chemical attack).

Cette thèse est accessible à l'adresse : http://theses.insa-lyon.fr/publication/2020LYSEI120/these.pdf
© [A. MATHEVON], [2020], INSA Lyon, tous droits réservés

Transmission Electron Microscopy (TEM)

Two main uses have emerged for the use of transmission electron microscopy observation. First, energy dispersive spectroscopy measurements were performed on a JEOL 2010 FEG microscope working at 200 kV. Then TEM observations on thin foils were performed on a JEOL 2010 microscope equipped with a CCD camera (Gatan Orius SC1000) working at 200 kV. The purpose of these two types of observations and the operational details are presented below:

- Energy dispersive spectroscopy (EDS) was used to characterize the initial precipitation state of cementite. It allows a measurement of the chemical composition of the different carbides in order to quantify their enrichment in substitutional elements (Mn,Cr) which can change according to the manufacturing process. In order to be able to carry out this measurement, it is essential to extract the different carbides from the matrix in order to avoid making quantification errors due to the presence of the matrix. To do this, carbon replicas were made by following the procedure detailed below:
  1. Nital etching 4% performed after a standard polishing process up to 1 μm.
  2. A *Baltech* evaporator was used to deposit a carbon film on the polished surface about 20-30 nm thick. To achieve this deposition, a voltage of 8 V, a current of 50-60 A and a secondary vacuum between $10^{-4} - 10^{-5}$ mbar are applied.
  3. The surface is then scraped with a cutter to obtain a 1 mm^2 square grid pattern.
  4. The grid sample is then immersed in a 4% Nital solution in which 2 drops of pure nitric acid are added every 30 minutes until it peels off.
  5. The carbon replicas are recovered with copper grids and then are cleaned successively 3 times in ethanol baths.

  To quantify the chemical composition of carbides, an average of 20 EDS measurements were performed. With regard to the study of the cementite's enrichment in alloying elements, only Fe, Mn and Cr are considered assuming a total equilibrium of C, which is the fastest element. The stoichiometry of precipitates is assumed to be the following $(Fe_xMn_yCr_z)_3C$ for which the coefficients x, y and z are determined from a mass balance $x + y + z = 1$ and the atomic ratios $\frac{Fe}{Mn}$ and $\frac{Fe}{Cr}$.
- Thin foils were prepared to perform TEM observations required to characterize the precipitation state of carbon within the tempered martensite. They were prepared according to a standard procedure (mechanical polishing down to 1 μm, punching and double jet-polishing). For electropolishing, a solution of 90% ethanol and 10% of perchloric acid was used at a temperature of -45 °C and with a voltage of 15 V.

Focused ion beam (FIB)

3-D FIB/SEM tomography analyses were performed on a Zeiss NVI-SION 40 microscope to quantify and characterize the volume fraction of precipitated carbide during tempering treatment. Once the area of interest is selected, two carbon and one tungsten layers are deposited to protect the study surface from early abrasion (see Figure 1.5.(a)). In addition, these marks will allow to control the depth of abrasion during the observation and allow a realignment of each image to reconstruct the final volume. Finally, a trapezoidal abrasion at the edge of the area of interest will allow the observation of this zone while limiting the

Cette thèse est accessible à l'adresse : http://theses.insa-lyon.fr/publication/2020LYSEI120/these.pdf
© [A. MATHEVON], [2020], INSA Lyon, tous droits réservés

shadowing effects (see Figure 1.5.(b)).

The ionic abrasion was realized with a voltage of 30 kV and a inoic current of 300 pA. Two kinds of electrons were collected: back-scattered electrons (electrons of high energy resulting from volume interaction) and in-lens electrons (secondary electrons collected with the column detector). Two complementary volumes of $10 \times 10 \times 10$ μm were analyzed for each FIB acquisition. A voxel size of 5 nm^3 was chosen.

Only the in-lens volumes were analyzed using *ImageJ* software. A 2-D Gabor filter with the VSNR2 plug-in was first used to reduce image noise. A 3-D thresholding using a WEKA learning machine plug-in was then performed on sub-volumes to extract the cementite precipitates after tempering.

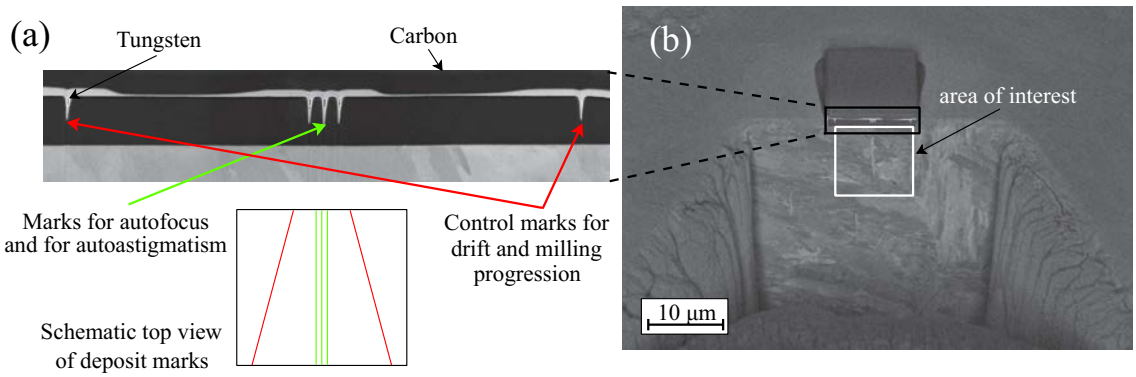

Figure 1.5: (a) Descriptive scheme concerning the carbon and tungsten deposits and (b) example of analyzed cross-section before the start of the FIB/SEM volume acquisition.

1.3.3 Characterization techniques

The microstructural evolutions of steels during their thermal cycles were monitored in-situ thanks to a follow-up by optical dilatometry on the Gleeble or by differential scanning calorimetry (DSC). At the same time, it is possible to monitor microstructural evolutions and mechanical properties after their heat treatment or during interrupted heat treatments using several techniques such as thermoelectric power (TEP), hardness and tensile tests.

1.3.3.1 Optical dilatometry

The austenite formation or decomposition kinetics were determined experimentally using optical dilatometry. The change in length of the sample by thermal expansion and phase transformation due to the heat treatment allows, thanks to its monitoring, to quantify the phase transformation kinetics. For the tests, a Scanning Non-Contact Optical Dilatometer and Extensometer with Green LED Technology was installed on the Gleeble in order to quantify precisely the sample length at the thermocouples without stress applied to the sample. With regard to the operating parameters, the austenite formation kinetics were performed under a secondary vacuum of $\sim 10^{-4}$ bar pressure to avoid sample oxidation

Cette thèse est accessible à l'adresse : http://theses.insa-lyon.fr/publication/2020LYSEI120/these.pdf
© [A. MATHEVON], [2020], INSA Lyon, tous droits réservés

and decarburization. On the other hand, for austenite decomposition kinetics, it was only possible to achieve a primary vacuum of $\sim 10^{-1}$ mbar of pressure due to the quenching system required to reach the cooling rates necessary for martensite formation.

It is possible to monitor the phase transformation by optical dilatometry since most phase transformations lead to a modification of the crystallographic structure which results in a volume change. Phase quantification can therefore be observed during slope breaks due to phase transformations compared to the linear evolution of the slope due to thermal expansion during sample heating. Figure 1.6.(b) shows the evolution of the sample dilatation during a heating simulating the intercritical annealing (see Figure 1.6.(a)) of a Dual-Phase steel with a 5 °C/s heating ramp followed by a 300s step at the temperature of the intercritical stage before a heating to 950 °C allowing the phase transformation to be completed. Two linear lines are observed in Figure 1.6.(b) corresponding respectively to the thermal expansion of ferrite (400 °C to 700 °C) and austenite (850 °C to 980 °C). The slope failure therefore corresponds to the phase transformation of ferrite into austenite occurring between 700 °C and 850 °C.

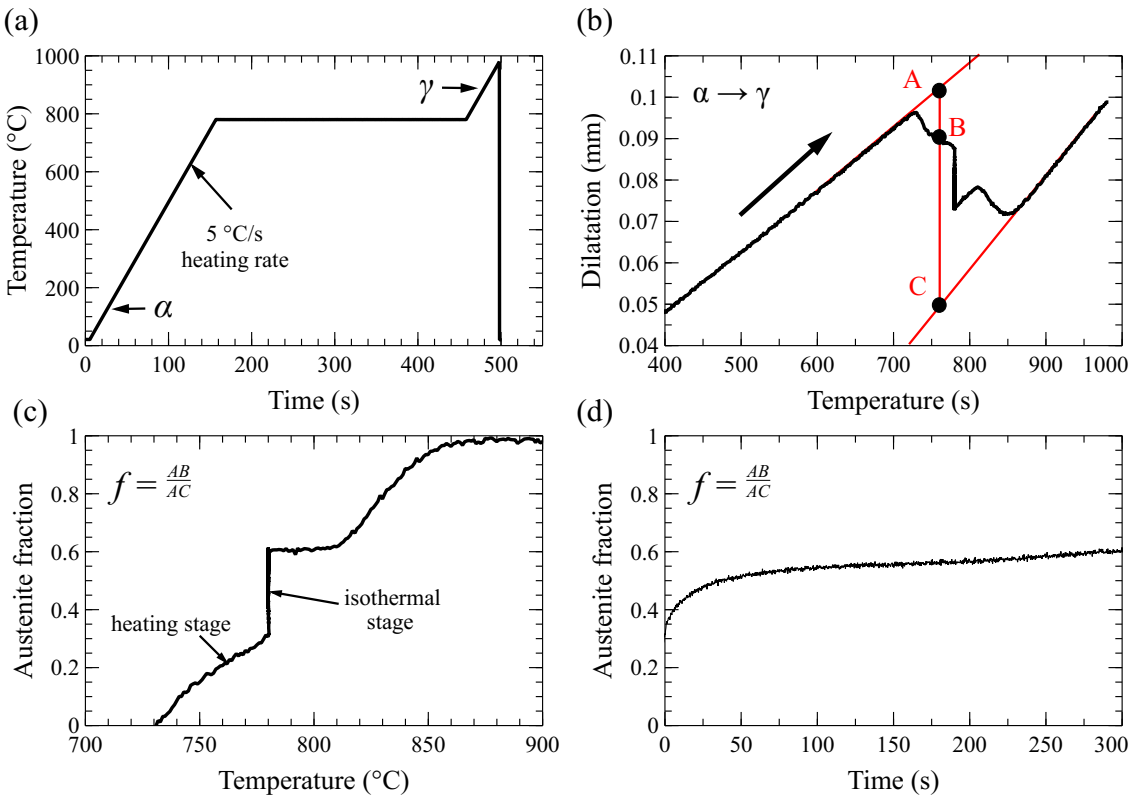

Figure 1.6: (a) Example of thermal cycle used to follow the austenite formation kinetics by reproducing industrial conditions. (b) Dilatometric curve obtained from the previous thermal cycle (c) Austenite formation kinetics determined from dilatometric experiments. (d) Austenite formation kinetics determined from dilatometric experiments on the intercritical stage.

Cette thèse est accessible à l'adresse : http://theses.insa-lyon.fr/publication/2020LYSEI120/these.pdf
© [A. MATHEVON], [2020], INSA Lyon, tous droits réservés

From an experimental point of view, optical dilatometry is conventionally used on heat treatments consisting of continuous heating. It is necessary to ensure that no force is applied on either side of the sample to avoid inducing a transverse deformation, if the longitudinal thermal expansion is blocked. On the other hand, divergence problems were observed on the Gleeble when holding the sample for 300s at the temperature of the intercritical annealing with a zero force condition. Since the regulators are not perfect, an oscillation of the piston rod is observed during the intercritical stage, which has the effect of bending the sample and inducing an error in the measured transverse dilatation value. To overcome this problem, a control change was used during the thermal cycles on the isothermal stage with the complete locking of the cylinder avoiding the drift of thermal expansion before applying a zero force on each side of the sample again during the final heating ramp.

The tangent method was then used to determine the phase transformation kinetics. For a given temperature, the austenite fraction can be calculated from the following formula: $f = \frac{AB}{AC}$. Points A and C are located on the tangent of the thermal expansion slopes of the two phases and point B is on the dilatation curve between the points A and C (see Figure 1.6.(b)). The austenite formation kinetics can therefore be followed during continuous heating or on the bearings of industrial thermal cycles as shown in Figure 1.6.(c-d).

1.3.3.2 TEP

The thermoelectric power (TEP) is based on a potential difference due to the Seebeck effect caused by the application of a thermal gradient at both ends of the studied sample in contact with two reference metal blocks (here, pure iron blocks) as shown in Figure 1.7.(a). The measurement of this potential difference is an indirect method that enables to follow the global microstructural evolutions of the sample since it is very sensitive to the presence of "defects" in the microstructure (*i.e.* dislocations, precipitates and solute atoms). In summary, it is possible to perform a relative TEP measurement ($S_{S/R}$) by defining a relative TEP corresponding to the difference between the TEP of the sample and that of the reference metal using the following formula:

$$S_{S/R} = S_{sample} - S_{reference\,metal} = \frac{\Delta V}{\Delta T} \tag{1.1}$$

The absolute TEP of a steel sample is the sum of various contributions and can be written as follows:

$$S_{steel\,sample} = S_{pure\,iron} + \Delta S_{ss} + \Delta S_{pre} + \Delta S_{\perp} \tag{1.2}$$

with $S_{pure\,iron}$ the TEP of pure iron. ΔS_{ss}, ΔS_{pre} and $\Delta S_{\perp}$ respectively correspond to the TEP variation due to solute atoms, precipitates and dislocations (see Figure 1.7.(b)). The effects of each contribution are detailed below:

- **Solute atoms** generate a contribution (ΔS_{ss}) which can be either positive or negative depending on the nature of each atom. Gorter-Nordheim's law [NOR 35] describes the effect of atoms in solid solution:

Cette thèse est accessible à l'adresse : http://theses.insa-lyon.fr/publication/2020LYSEI120/these.pdf
© [A. MATHEVON], [2020], INSA Lyon, tous droits réservés

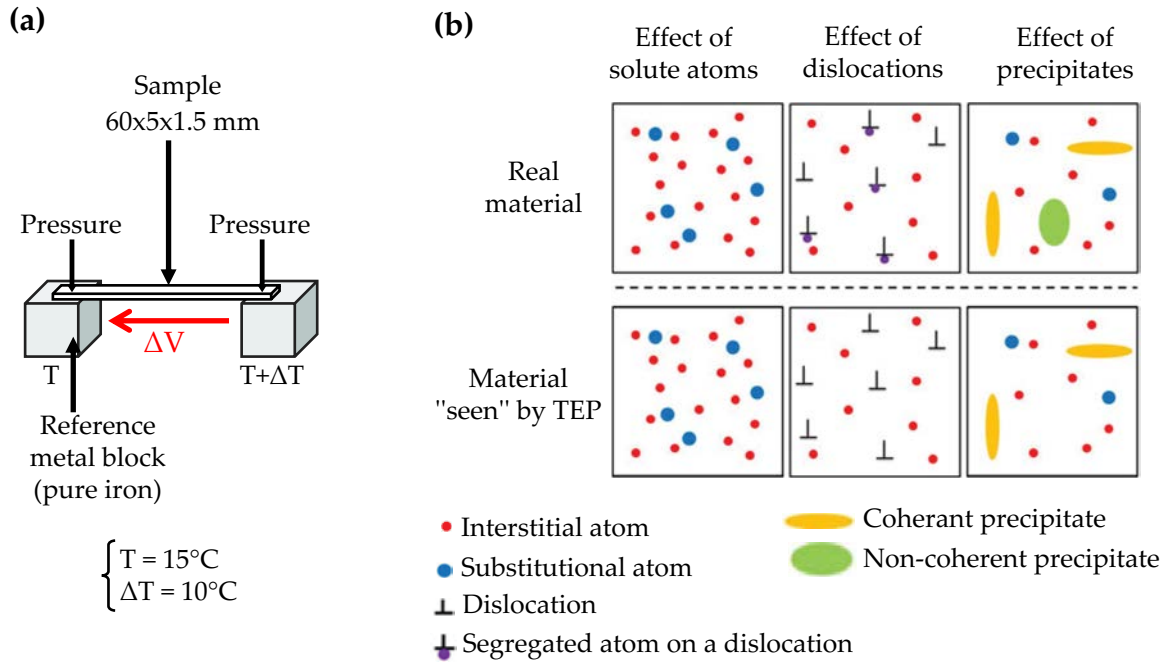

Figure 1.7: Schematic representation of (a) the TEP apparatus and (b) the effect of different defects (solute atoms, segregated atoms, dislocations and precipitates) on the TEP of iron [LAM 14].

$$\Delta S_{ss} \times \rho_s = \sum_i s_i \times \rho_s^i = \sum_i s_i \times c_i \times \alpha_s^i \tag{1.3}$$

where:

- ΔS_{ss} is the TEP variation due to the presence of alloying elements in solid solution in the steel;
- ρ_s is the steel resistivity equal to $\rho_{s0}^i + \sum_i \rho_s^i$ (Mathiessen law) with ρ_{s0}^i the resistivity of the pure metal of reference (*i.e.* pure iron) and ρ_s^i the resistivity variation due to the presence of element "i" in solid solution. Assuming that the resistivity (ρ_s^i) of the element i changes linearly with the concentration c_i of element i for low-alloyed steels, one can write:

$$\rho_s^i = \alpha_s^i \times c_i \tag{1.4}$$

  The proportionality coefficient α_s^i represents the specific resistivity of element i (expressed in $\mu\Omega$.cm/wt%)
- s_i is the specific TEP of element "i" (expressed in μV/°C).

It is thus possible to express ΔS_{ss} as a function of the concentration of solute atoms c_i by combining equations (1.3) and (1.4):

Cette thèse est accessible à l'adresse : http://theses.insa-lyon.fr/publication/2020LYSEI120/these.pdf
© [A. MATHEVON], [2020], INSA Lyon, tous droits réservés

$$\Delta S_{ss} = \sum_i \frac{\alpha_s^i \times s_i}{\rho_s} \times c_i \tag{1.5}$$

- **Precipitates** can have a contribution to TEP (ΔS_{pre}) in the case of coherent or semi-coherent precipitates. Indeed, during precipitation, two main contributions have to be considered: one due to the departure of atoms from the solid solution and one due to the precipitation themselves. The effect of the precipitates on TEP will depend on the nature, morphology, volume fraction and size of the precipitates. No laws have been established so far, but it is accepted that non-coherent precipitates have no effect if their volume fraction is less than 10%. In this study, the maximum volume fraction of cementite achievable is 2%, which allows us to take into account only the departure of the atoms of the solid solution during precipitation.
- **Dislocations** ($\Delta S_\perp$) are known to lower the TEP of pure iron. In the case of steels, it was observed that a correlation could be established between the increase in hardness due to cold-rolling and the corresponding drop in TEP, which makes it possible to admit that the TEP is sensitive to the amount of dislocations.

1.3.3.3 Hardness

Vickers hardness measurements were performed on a Buehler machine at quarter thickness with a load of 0.5 kg in the thermocouple plane for Gleeble treated samples. An average of 10 measurements was performed to ensure a standard deviation of less than 5 HV for recrystallization. On the other hand, for the tempering study, a standard deviation ~ 15 HV was obtained on fresh martensite or with low tempering time and temperature.

1.3.3.4 Tensile tests

Tensile tests were performed on an *Instron* machine using an optical extensometer. Tensile tests were realized with a velocity of 2 mm/min. Tensile specimens were machined by electro discharge machining to obtain the geometry given in Figure 1.8.(a). The working section measures 4xe mm^2 for a gauge length of 15 mm where e is the sample thickness. Tensile tests were tripled to confirm the mechanical behaviour of a given condition.

Usual mechanical properties were evaluated from tensile test as reported in Figure 1.8.(b): the Yield Stress (Ys, MPa) was defined as the stress at 0.2% of deformation. The Ultimate Tensile Strength (UTS, MPa) is the maximal applied stress before skrinkage and the uniform elongation (ε_u, %) is the deformation before shrinkage.

Cette thèse est accessible à l'adresse : http://theses.insa-lyon.fr/publication/2020LYSEI120/these.pdf
© [A. MATHEVON], [2020], INSA Lyon, tous droits réservés

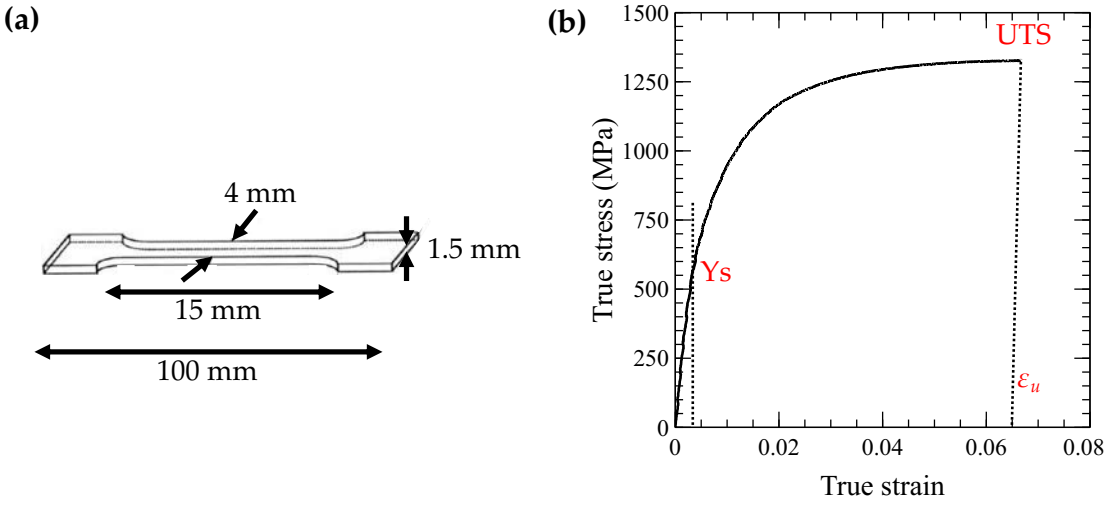

Figure 1.8: (a) Geometry of the tensile test specimens and (b) usual mechanical properties evaluated from tensile curve.

Cette thèse est accessible à l'adresse : http://theses.insa-lyon.fr/publication/2020LYSEI120/these.pdf
© [A. MATHEVON], [2020], INSA Lyon, tous droits réservés

Chapter 2

A microstructurally-based model for predicting the recrystallization kinetics in DP steels

This chapter is focused on the setting up of a microstructurally-based model for predicting the recrystallization kinetics of Dual-Phase steels that takes into account the effect of several physical parameters (chemical composition, temperature, cold-rolling reduction ratio and precipitation state). This model tends to generalize the extended recrystallization model formalism developed by Sinclair *et al.* [SIN 07]. Adjusting and predicting the ferrite recrystallization kinetics of cold-rolled Advanced High-Strength Steels during annealing is necessary to control their final microstructure and thus their mechanical properties as described in Section 2.1.2.2.

This Microstructurally-based model for Recrystallization (denoted MiReX) was first tested on the ternary ferritic-pearlitic Fe-C-Mn alloys of this study with various C and Mn contents and cold-rolled with three different reduction ratios, in order to adjust the parameters of the model relative to the Mn content and to the reduction ratio. The effect of other alloying elements (Si, Cr and Mo) was also analyzed using recrystallization kinetics from the literature. Lastly, the model was tested on the two industrial steels investigated in this PhD work: a DP600 steel and the micro-alloyed DP1000 steel also studied in the paper of Ollat *et al.* [OLL 17a]. In the latter case, the recrystallization model was coupled with a Precipitation Software (PreciSo) to take into account the effect of the micro-alloyed precipitates formed before or during recrystallization on the kinetics. Lastly, a discussion on the possible interaction between recrystallization and austenite formation during the annealing of cold-rolled DP steels was proposed.

Results of this chapter have been published in *Metallurgical and Materials Transactions A* [MAT 20] .

Cette thèse est accessible à l'adresse : http://theses.insa-lyon.fr/publication/2020LYSEI120/these.pdf
© [A. MATHEVON], [2020], INSA Lyon, tous droits réservés

Contents

Cette thèse est accessible à l'adresse : http://theses.insa-lyon.fr/publication/2020LYSEI120/these.pdf
© [A. MATHEVON], [2020], INSA Lyon, tous droits réservés

2.1 Literature review

The following section provides a short litterature review of the recrystallization phenomenon occurring during intercritical annealing. Then, a global view of the possible interaction consequences between recrystallization and phase transformation phenomena on the final microstructure is presented. Finally, the different approaches that may be used for the recrystallization modelling will be discussed.

2.1.1 Recovery and recrystallization

After cold-rolling, the microstructure's free energy is raised by the introduction of defects (dislocations, interfaces and vacancies), leading the material to a thermodynamically unstable state [HUM 12]. During intercritical annealing, the temperature is sufficient to activate the reorganization of the microstructure by means of two mechanisms: recovery and recrystallization [HUM 12, CHR 81b, OYA 08, DOH 97]. These thermally activated phenomena such as solid state diffusion can lead to a decrease in the system's free energy by an annihilation or rearrangement of defects. These two phenomena are in competition and lead to a softening of the steel mechanical properties.

- **Recovery** can occur when the temperature is above one-third of the fusion temperature allowing the dislocations to become mobile in order to rearrange and annihilate if their burger vectors are opposed. These microstructural changes are generally homogeneous and do not result in any Grain Boundary (GB) displacement. In general only partial recovery is achieved, since the dislocations will rearrange as a substructure within the grains without changing the interfaces between the deformed grains. These rearrangements reduce the total system free energy by restoring the dislocation stress fields [MCQ 77].
- **Recrystallization** process drastically reduces the free energy of the system by replacing deformed grains with equiaxed and dislocation-free grains. Recrystallization is a diffusive phenomenon that occurs through nucleation [HUM 12] and growth processes. Grain boundaries and dislocation substructures formed during recovery are preferential nucleation sites for the recrystallized grains growth. Recrystallization kinetics are driven by diffusion with an activation energy often associated with the self-diffusion of iron in ferrite (220-270 kJ/mol) [LÜ 11]. However in many alloys containing substitutional elements such as Mn, Mo, the solute drag hypothesis within the grain boundaries has been proposed to explain higher activation energies (350-380 kJ/mol). The driving pressure for recrystallization in ferrite, G_{Rex}, comes from the difference in dislocation density between a deformed grain (ρ^f) and a recrystallized grain (ρ_0^f) before and after displacement of a grain boundary.

$$G_{Rex} = \frac{1}{2}\mu b_{111}^2(\rho^f - \rho_0^f) \tag{2.1}$$

where μ is the shear modulus and b_{111} the burgers vector. Since ρ^f is usually several orders of magnitude greater than ρ_0^f, the following approximation can be applied: $\rho^f - \rho_0^f \cong \rho^f$.

Cette thèse est accessible à l'adresse : http://theses.insa-lyon.fr/publication/2020LYSEI120/these.pdf
© [A. MATHEVON], [2020], INSA Lyon, tous droits réservés

2.1.2 Interaction recrystallization/phase transformation

Many authors report an interaction between recrystallization and austenite formation during the annealing of Dual-Phase steels [YAN 85a, HUA 04, AZI 11, OGA 10, MOH 11, KUL 13, LI 13, CHB 14a, BAR 15, OLL 17a]. The objective of this part will be to present the conditions in which the interaction of these two phenomena is obtained. Finally the effects on the microstructures and the phenomena themselves are detailed.

2.1.2.1 Interaction map

Figure 2.1 simultaneously shows deformed ferrite grains (DF), recrystallized ferrite grains (F) as well as martensite (M, *i.e.* austenite before quenching) after intercritical annealing with a very high heating rate ($R_H = 300$ °C/s). This microstructure is typical of a partial recrystallization phenomenon resulting from an interaction with austenite formation during heating as pointed out by different authors [YAN 85a, KUL 13, BAR 15]. Moreover, Kulakov *et al.* proposed to establish an interaction map of the phenomena in order to highlight the conditions leading to their overlapping. Based on the individual kinetics of austenite formation and recrystallization phenomena, the interaction map can be plotted as a function of temperature and heating rate. Here, it has to be pointed out that this type of map is expected to depend on the addition of alloying elements (Ti, Nb, Mo, Mn, Cr) as these elements may shift the recrystallization domain to higher temperatures. In addition, one can note that increasing the heating rate on production lines (with induction heating) is more likely to lead to an interaction.

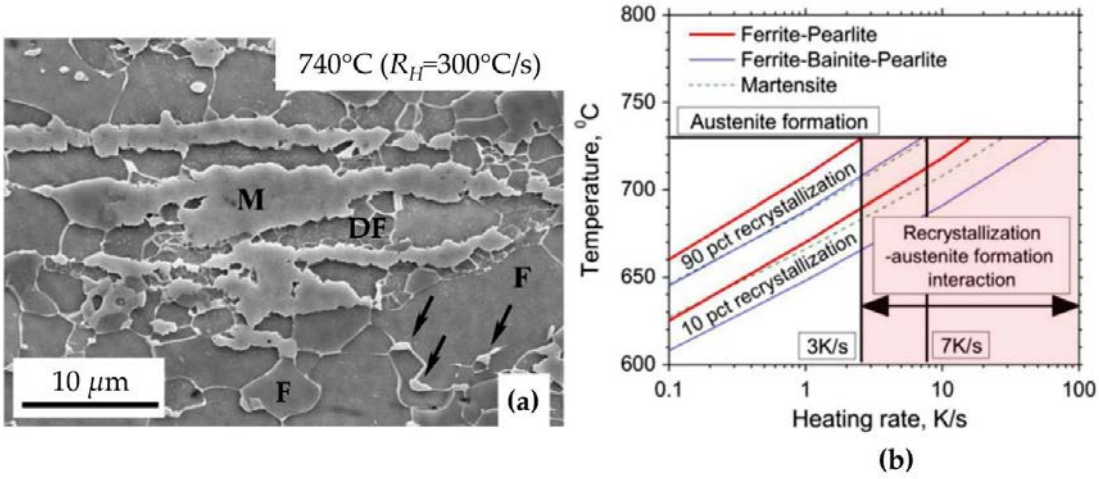

Figure 2.1: (a) SEM micrograph highlighting the phase transformation and recrystallization interaction by the presence of recrystallized ferrite (F), deformed ferrite (DF) and martensite grains (M, prior austenite grain) [AZI 11]. (b) Interaction map of intercritical phenomena proposed by Kulakov *et al.* [KUL 13].

Cette thèse est accessible à l'adresse : http://theses.insa-lyon.fr/publication/2020LYSEI120/these.pdf
© [A. MATHEVON], [2020], INSA Lyon, tous droits réservés

2.1.2.2 “Weak" or “Strong" interaction

An interaction between recrystallization and austenite formation is likely to occur during the annealing of Dual-Phase steels, notably during the intercritical annealing. This interaction has already been extensively studied in literature [OLL 17a, KUL 13, LI 13, HUA 04] and leads to two types of interactions called “weak” and “strong” by Chbihi *et al.* [CHB 14b]. The “weak” interaction corresponds to the case where the recrystallization is mostly completed at the austenite start temperature. By contrast, in the case of a “strong” interaction, recrystallization and austenite formation are assumed to occur simultaneously. This will affect (i) the recrystallization kinetics and (ii) the nucleation and growth of austenite. From an experimental point of view, this "strong" interaction can be observed: (i) at high heating rate as the recrystallization domain is shifted to higher temperatures [AZI 11, BAR 15] and/or (ii) with the presence of alloying elements (such as Mn, Cr, Mo, Ti, Nb) likely to segregate within the grain boundaries or to form precipitates [BLE 05].

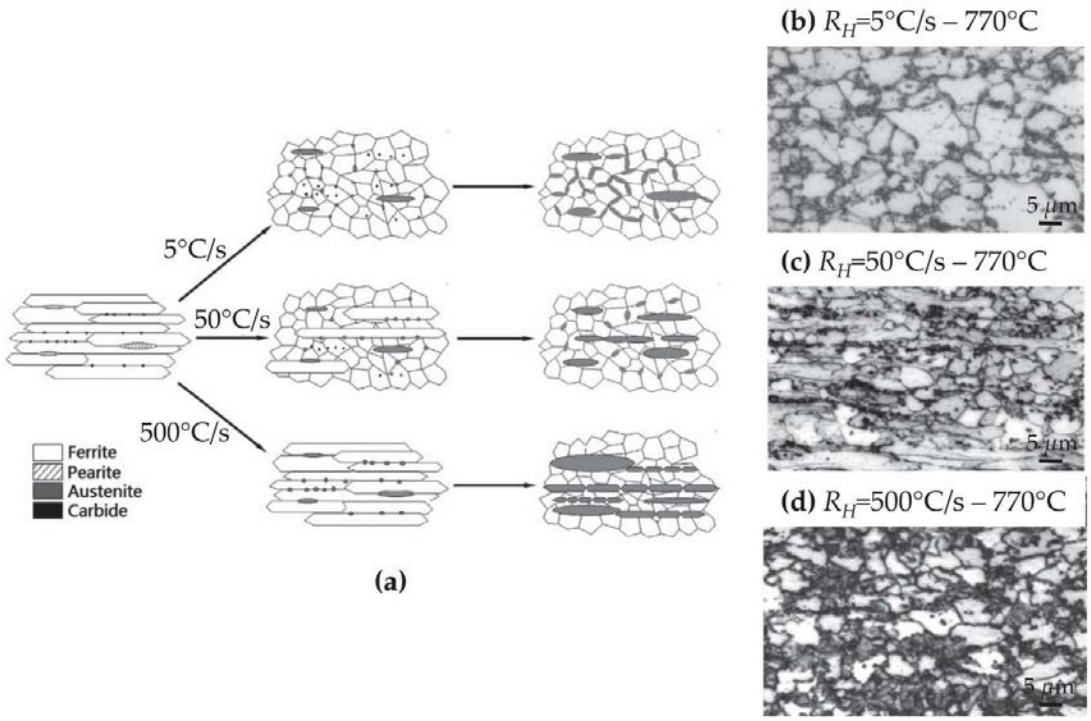

Figure 2.2: (a) Schematic representation of the heating rate influence [5-500°C/s] on the microstructure after annealing at 770 °C and (b-d) corresponding optical micrographs [LI 13].

A “strong” interaction results in a significant change in microstructure with a globally coarse and non homogeneous final microstructure of Dual-Phase steels [HUA 04, MOH 11, CHB 14a]. Li *et al.* [LI 13] described in detail the microstructures obtained for various heating rates (Figure 2.2). In the case of a “weak" interaction, austenite nucleation takes place at the ferrite-pearlite interfaces and at recrystallized grain boundaries, leading to

Cette thèse est accessible à l'adresse : http://theses.insa-lyon.fr/publication/2020LYSEI120/these.pdf
© [A. MATHEVON], [2020], INSA Lyon, tous droits réservés

a rather homogeneous microstructure. This case is equivalent to autenite formation on normalized or prior recrystallized steels. In contrast, in the case of a "strong" interaction due to the use of a high heating rate (>20 °C/s), a coarse, banded and heterogeneous microstructure is obtained. Different explanations are given in the literature : (i) moving recrystallizing ferrite boundaries are not favourable sites for austenite nucleation; (ii) deformed ferrite grains are high energy nucleation sites, so that the carbides near these grains are preferential nucleation sites; (iii) deformed ferrite grains may promote long-range carbon diffusion.

2.1.3 Modelling tools for recrystalization kinetics

The modelling of recrystallization kinetics depends on several parameters such as: (i) the amount of substitutional elements in solution, (ii) the precipitates formed before or during recrystallization, (iii) the reduction ratio and (iv) the type of thermal cycles (heating rate, annealing temperature and time). At present, the modelling of recrystallization in steels is not totally satisfying. Three types of approaches can be distinguished in the ongoing studies: (1) mean field, (2) full field and (3) phenomenological simulations.

2.1.3.1 Mean field

The first type of modelling is based on mean field methods (*i.e.* statistical, but usually physically based like cellular automaton [ZHE 13, SAL 12] and Monte-Carlo). They are associated with a 2-D or a 3-D geometric representation of the microstructure, discretized on a regular grid made of "cells", which are allocated to the grains. They still allow to reproduce the grain structure evolution of the microstructure during the recrystallization phenomenon, but also to reproduce the interaction between the phase transformation and recrystallization as shown in Figure 2.3 [ZHE 13]. Nevertheless, these methods scale well with parallelization as they rely on regular grids, but the lack of physical time in the Monte-Carlo method and the difficulty to approximate precisely the grain boundary curvature with cellular-automaton are still open issues. These approaches have some difficulties to treat the polycrystal deformation and the grain boundary motion in the same numerical framework.

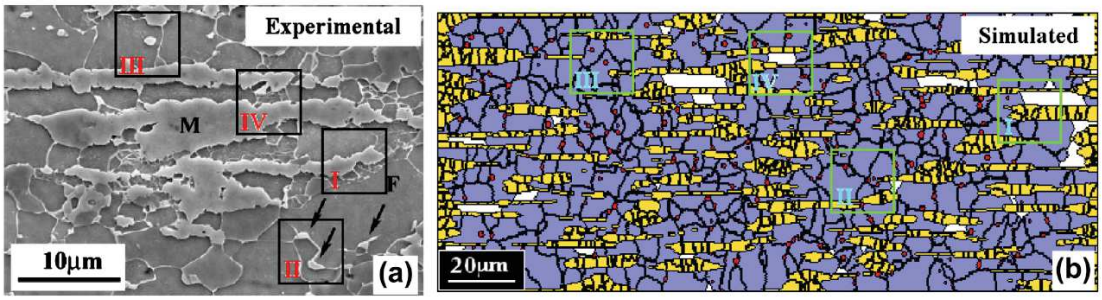

Figure 2.3: Comparison of the resultant microstructure between the micrographs (a) and the simulations (b) as a result of competitive ferrite recrystallization and austenitic transformation in carbon steels [ZHE 13].

Cette thèse est accessible à l'adresse : http://theses.insa-lyon.fr/publication/2020LYSEI120/these.pdf
© [A. MATHEVON], [2020], INSA Lyon, tous droits réservés

2.1.3.2 Full field

The second type of modelling is based on full field (*i.e.* mesh based like phase field [ZHU 12] and levelset [SCH 16, LOG 08, BER 09]). They currently allow the inclusion of complex 3-D simulations based on real or simulated microstructures. They avoid many numerical problems concerning the tracking of interfaces and allow a finer integration of nucleation phenomena, which makes it possible to reproduce most of the phenomena observed within the microstructure as well as their interaction with external phenomena (phase transformation, precipitation, mechanical stress). One interest of using a finite-element framework instead of uniform grids is the possibility to handle large polycrystal deformations with the well-known Crystal Plasticity Finite Element Method (CPFEM). However, they generate very long calculation times (from hours to days) and they cannot be easily extended over different ranges of steels due to the number of assumptions and input parameters.

2.1.3.3 Phenomenological approach

The third type of modelling is based on the Johnson-Mehl-Avrami-Kolmogorov (JMAK) equation which describes the evolution of the transformed fraction $f(T,t)$ (with $0 < f(T,t) < 1$) as a function of time (t) and temperature (T). Under a number of simplifying assumptions and considering isothermal conditions, this equation can be written as follows :

$$f(T,t) = 1 - \exp\left[-(bt)^n\right] \tag{2.2}$$

where :

$$b = b_0 \exp\left(-\frac{Q}{RT}\right) \tag{2.3}$$

This type of modelling is thus very simple and requires the determination of three parameters: n (the Avrami exponent), Q (the activation energy) and b_0 (a rate constant). These parameters can be easily obtained from the experimental recrystallyzation kinetics determined below the Ac_1 temperature (*i.e.* before any austenite formation). Then, once the parameters have been determined, the recrystallization kinetics can be predicted under isothermal or non-isothermal conditions. This type of approach has been widely used in the literature [OLL 17a, KUL 13, LI 13, YAN 85a, HUA 04] for different steel chemistries, as illustrated in Table 2.1 In particular, it was used to build interaction maps between recrystallization and austenite formation during the heating stage of Dual-Phase steels by coupling the JMAK model for recrystallization with a JMAK model for austenite formation (case of Kulakov *et al.* [KUL 13] on a DP600 steel) or with experimental austenite formation kinetics (case of the work of Ollat *et al.* [OLL 17a] on a DP1000 steel).

The main drawback of this type of approach is that it is unable to predict the influence of changes in chemical compositions and reduction ratios. As can be seen from the data of Table 2.1, such changes lead to different values of the three parameters of the model but the link between the values of n, Q and b_0 and the chemical composition or the reduction

Cette thèse est accessible à l'adresse : http://theses.insa-lyon.fr/publication/2020LYSEI120/these.pdf
© [A. MATHEVON], [2020], INSA Lyon, tous droits réservés

Authors	Grades	Reduction ratio %	n	b_0 (s^{-1})	Q (kJ/mol)
[KUL 13]	0.1C-1.8Mn-0.15Si-0.35Cr (DP)	50	1.7	1.1×10^{17}	342
Li [LI 13]	0.1C-1.6Mn-0.4Si (DP)	70	1.45	5.5×10^{19}	384
[YAN 85a]	0.08C-1.5Mn-0.2Si	25-50	-	-	226-272
[HUA 04]	0.18C-1.55Mn-1.7Si (TRIP)	55	1	1.6×10^{18}	350
[HUA 04]	0.06C-1.8Mn-0.15Mo (DP)	55	1	7.2×10^{16}	350
[OLL 17a]	DP1000 (see Table 2.2)	55	1	3×10^{15}	326

Table 2.1: Values of the JMAK parameters determined on different steels in the literature

ratio is not obvious. This is why, Sinclair *et al.* [SIN 07] came back to the original JMAK formalism and proposed an extended recrystallization model in which the different parameters of the microstructure are linked to physical parameters. In particular, these authors were able to explain the slower recrystallization kinetics induced by the presence of Niobium in pure iron by taking into account the segregation of this alloying element within the interface.

2.1.4 Conclusion: Objective of the present chapter

In view of the complexity of implementation of the mean field and full field models and their difficulty of extension for a wide range of chemical composition and microstructure properties, phenomenological models seem more appropriate for the constraints of this study. The objective of the present study was thus to generalize the extended recrystallization model formalism developed by [SIN 07] to the different types of alloying elements present in the chemical composition of Dual-Phase steels by linking the predicted kinetics to the cold-rolling reduction ratio, the chemical composition and to the diffusion coefficients of the elements. The Fe-C-Mn ternary steel grades have been used to calibrate the effect of manganese and carbon content as well as the cold-rolling reduction ratio. Subsequently, experimental kinetics of the literature allowed us to adjust the effect of additional alloying elements (Si, Cr, Mo) [KUL 13, LI 13, YAN 85a, HUA 04]. The model was then validated on the two industrial alloys (DP600 + DP1000) of this study. Moreover, the recrystallization model was coupled with a precipitation software (PreciSo) to take into account the effect of the micro-alloyed precipitates formed before or during recrystallization on the kinetics in the case of micro-alloyed DP1000. Lastly, a discussion on the possible interaction between recrystallization and austenite formation during the annealing of cold-rolled DP steels was proposed.

2.2 Materials and experimental procedures

2.2.1 Materials

This study was carried out on the four ternary Fe-C-Mn steels prepared in laboratory and on the two industrial Dual-Phase steels presented in Chapter 1. Their chemical

Cette thèse est accessible à l'adresse : http://theses.insa-lyon.fr/publication/2020LYSEI120/these.pdf
© [A. MATHEVON], [2020], INSA Lyon, tous droits réservés

composition is recalled in Table 2.2. The chemical composition of the ternary steels was selected to be close to that of the industrial steels in terms of C and Mn contents. Concerning the industrial steels, they have almost the same Mn, Cr and Si content but they differ mainly by their C content and by the presence of microalloying elements (Ti, Nb) in the case of the DP1000 steel. Additional initial microstructural information (pearlite fraction and initial ferrite grain size) was determined from optical observations of the microstucture after a Nital etching using *ImageJ* and is reported in Table 2.2.

Steel grades	Chemical composition C_i^0 (in wt.%)							Grain size (μm)	Pearlite fraction	Ac_1 (°C)
	C	Mn	Cr	Si	Nb	Ti	N			
Ternary steels	0.17	0.5	-	-	-	-	-	45	20	718
	0.17	1.7	-	-	-	-	-	30	28	705
	0.17	2.5	-	-	-	-	-	20	34	696
	0.08	1.7	-	-	-	-	-	50	15	705
DP600	0.09	1.5	0.5	0.3	-	-	-	6	26	724
DP1000	0.17	1.7	0.4	0.3	0.03	0.03	0.006	6	36	720

Table 2.2: Chemical composition and microstructural features of ternary and industrial steels investigated in this study. Ac_1 values were calculated using Andrew's formula *et al.* [AND 65].

2.2.2 Determination of the recrystallization kinetics

In order to determine the experimental recrystallization kinetics of the investigated steels in the ferritic domain, Vickers hardness measurements were performed on the steels annealed for different times at the chosen recrystallization temperature(s) within the range $600 - 700$ °C, below Ac_1. For each treatment, about 15 measurements were performed at quarter thickness and with a 0.5 kg load. This led us to determine the recrystallized fraction (f_α^{Rex}) which was calculated with the following relation :

$$f_\alpha^{Rex} = \frac{H_0 - H(t)}{H_0 - H_F} \tag{2.4}$$

in which H_0, $H(t)$ and H_F correspond respectively to the initial hardness (after cold-rolling), the hardness after a time t at temperature T and the hardness of the fully recrystallized steel.

The uncertainties associated with the use of Equation 2.4 were estimated at 10% and have been validated by comparing this method with optical observation.

With regard to the interaction between precipitation and recrystallization, only the DP1000 can exhibit precipitation of micro-alloying elements (Nb, Ti) (cementite does not influence the hardness of the steel). Furthermore, for the DP1000, the precipitates can at most increase the hardness of 25 Hv [SOT 99]. This value represents a maximum error of 20% compared to the hardness difference observed due to recrystallization.

Cette thèse est accessible à l'adresse : http://theses.insa-lyon.fr/publication/2020LYSEI120/these.pdf
© [A. MATHEVON], [2020], INSA Lyon, tous droits réservés

2.2.3 Determination of the austenite formation kinetics

The austenite formation kinetics of the DP600 and DP1000 steels were experimentally determined using an optical dilatometer set up on a Gleeble machine. The optical system avoids any dilatometer stress on the sample. The classical lever rule was used to monitor the austenite fraction during continuous heating from room temperature to 900 °C.

2.3 Description of the microstructurally-based model for recrystallization (MiReX model)

2.3.1 Fundamental equation

As explained in the introduction, the objective of the model developed in this study is to be able to predict the influence of each alloying element (either in solution or precipitated) as well as that of the reduction ratio on recrystallization kinetics. The model is based on the work done by Sinclair *et al.* [SIN 07] relying on the JMAK formalism. In this approach, for a transformation involving nucleation and growth and considering that the nuclei of the new phase are randomly distributed, the real transformed fraction can be expressed as follows :

$$f_{\alpha}^{Rex} = 1 - \exp\left(-F_{Ext}\right) \tag{2.5}$$

where F_{Ext} is the extended transformed (here, recrystallized) volume fraction. It represents the transformed fraction if the nuclei grow through each other and overlap without interfering.

Assuming saturation of the nucleation sites, during transformation, the extended recrystallized volume fraction F_{Ext} can be written as follows for a non-homogeneous growth in the three directions of space:

$$F_{Ext} = N_{Rex}\left[\int_0^t \dot{R}_{\alpha} dt\right]^n \tag{2.6}$$

where N_{Rex} corresponds to the density of nucleation sites available for recrystallization in the material, $\dot{R}_{\alpha}$ accounts for the evolution of the recrystallized grain radius with time and n is the Avrami exponent generally considered constant at different temperatures.

The growth rate of the nuclei, $\dot{R}_{\alpha}$, is supposed to be proportional to the mobility of the recrystallization front (M) in ferrite as well as to the energy available for the transformation of a deformed grain into a new recrystallized grain (G_{Rex}) and can be expressed by the following relation :

$$\dot{R}_{\alpha} = MG_{Rex} \tag{2.7}$$

This leads to define the extended recrystallized volume fraction as follows :

$$F_{Ext} = N_{Rex}\left[\int_0^t M\left(X^0_{\mathrm{C,Mn}}, .., T\right) G_{Rex} dt\right]^n \tag{2.8}$$

Cette thèse est accessible à l'adresse : http://theses.insa-lyon.fr/publication/2020LYSEI120/these.pdf
© [A. MATHEVON], [2020], INSA Lyon, tous droits réservés

where G_{Rex} is supposed to depend on the reduction ratio as well as on the presence of microalloying elements (which may precipitate before or during recrystallization), X_i^0 the initial molar fraction of element i and M is likely to vary with the temperature as well as with the content of each type of substitutional element.

Here, on can note that the model can be used both for isothermal and non-isothermal treatments as it may take into account the variations of input parameters during recrystallization.

2.3.2 Avrami exponent n

With regard to the Avrami exponent, it should be equal to 3 for isotropic growth of recrystallized ferrite grains. However, as the microstructures of the studied materials have been cold-rolled before annealing, this leads to an anisotropy during the growth of the grains. Consequently, this requires a reduction of the value of this parameter. Taking into account the experimental values determined in the literature for the Avrami coefficient by different authors [OLL 17a, KUL 13, LI 13, YAN 85a, HUA 04] and recalled in Table 2.1, the value of this parameter was fixed to 1.3 for all compositions and it was supposed to be independent of the chemical composition, reduction ratio and parameters of the thermal cycle.

2.3.3 Nucleation site density N_{Rex}

The nucleation site density, N_{Rex}, was evaluated by Sinclair *et al.* [SIN 07] from the measurement of recrystallized grain sizes in areas that have been freshly recrystallized. Their choice to study recrystallization with a temperature and niobium gradient within a unique sample allowed them to have all the steps of the recrystallization kinetics. So, they could observe the area for which recrystallization has just been completed. Then, they estimated to about 10 μm the average grain radius at the interface (R_{Int}). So, it makes possible to calculate the "density" of nuclei available for recrystallization in the case of an inhomogeneous growth of dimension n using the following formula:

$$N_{Rex} = \left(\frac{1}{R_{Int}}\right)^n \tag{2.9}$$

Several phenomena could play a role on this value but for the sake of simplicity and universality of the model, this parameter will be considered, in the present work, as independent of the chemical composition, reduction ratio and of the thermal cycle.

2.3.4 Driving pressure for recrystallization G_{Rex}

The driving energy available for recrystallization is related to the energy stored during cold-rolling, $G_{Rex,0}$, which can be expressed as follows :

$$G_{Rex,0} = \frac{1}{2}\mu\rho^f b_{111}^2 \tag{2.10}$$

Cette thèse est accessible à l'adresse : http://theses.insa-lyon.fr/publication/2020LYSEI120/these.pdf
© [A. MATHEVON], [2020], INSA Lyon, tous droits réservés

where ρ^f is the dislocation density in ferrite, μ the shear modulus of α-Fe and b_{111} the Burgers vector in α-Fe. $G_{Rex,0}$ is expected to evolve with time due to the decrease in the dislocation density occurring during recovery. However, this evolution will be neglected in the present study, assuming that above 600 °C the decrease in the quantity of dislocations is only due to recrystallization, which is the most energetically favorable phenomenon in this temperature range. In addition, the driving pressure due to the shape change (from elongated to spherical) between deformed and recrystallized grains is neglected.

In the case of micro-alloyed steels containing Nb and Ti, the driving pressure for recrystallization can be reduced by the Zener pinning effect due to the presence of complex carbides of (Ti, Nb)C type and can then be written in the following general form [RIO 10, SMI 48]:

$$G_{Rex}(t) = G_{Rex,0} - \frac{3}{2}\gamma_{Gb}\frac{f_v^{(Ti,Nb)C}}{R_{(Ti,Nb)C}} \tag{2.11}$$

where γ_{Gb} represents the interfacial energy of the grain boundaries, $f_v^{(Ti,Nb)C}$ the volume fraction of precipitates within the steel and $R_{(Ti,Nb)C}$ their radius.

As highlighted by Equation 2.10, the steel reduction ratio during cold-rolling is expected to be a key parameter on recrystallization kinetics, as it is likely to modify the dislocation density in the material. In previous studies of the literature [SIN 07], the dislocation density for cold-rolled steel sheets has been estimated from the hardness difference, ΔH, between the cold-rolled and recrystallized states of the material, assuming that the hardness difference is sensibly related to the difference in yield strength, $\Delta\sigma$, according to the following relation :

$$\Delta\sigma = \frac{\Delta H}{3} \tag{2.12}$$

and that :

$$\Delta\sigma = M_T \alpha_T \mu b_{111} \sqrt{\rho^f} \tag{2.13}$$

where M_T is the Taylor factor and α_T is a constant. Their values are given in Table 2.5.

Using this methodology on the ternary Fe-C-Mn steels investigated in this study after cold-rolling with three different reduction ratios, the dislocation density was evaluated for these reduction ratios. Table 2.3 gives the dislocation densities used in this work for three distinct reduction ratios.

The following relationship allows us to estimate the density of dislocations within the ferritic-pearlitic microstructure for deformation ratios between 25% and 75%:

$$\rho^f = (5.6 \times 10^{10}\tau^2 + 3.4 \times 10^{12}\tau - 7 \times 10^{13})\ \mathrm{m}^{-2} \tag{2.14}$$

where τ represents the cold-rolling reduction ratio.

Here, it has to be pointed out that the model could be extended to different initial microstructures (*e.g.* martensite, bainite) by adjusting some of the parameters (dislocation density, nucleation site density). For example, some authors decided to adjust the initial dislocation density successfully for a ferritic-martensitic microstructure [BEL 18].

Cette thèse est accessible à l'adresse : http://theses.insa-lyon.fr/publication/2020LYSEI120/these.pdf
© [A. MATHEVON], [2020], INSA Lyon, tous droits réservés

Reduction ratio $\tau(\%)$	Dislocation density ρ^f (m^{-2})	Vickers hardness difference $(\mathrm{kg.mm}^{-2})$
25	5×10^{13}	37
50	2.4×10^{14}	80
75	5×10^{14}	116

Table 2.3: Link between the cold-rolling reduction ratios and the dislocation densities within steels.

2.3.5 Determination of the interface mobility due to segregation

2.3.5.1 Equation governing mobility

The fundamental hypothesis driving the interface mobility is that it is slowed down by the segregation of substitutional elements to grain boundaries. This deceleration can be approximated with the slow part of Cahn's segregation model [WIC 15], in the case where the energy available for transformation is low and below a critical value that has been validated by Sinclair *et al.* [SIN 07]. This hypothesis enables, for low transformation energies, to suppose that the mobility is proportional to the interface mobility in pure iron (M_{pure}) and depends on the content of each type of alloying element according to Equation 2.15:

$$M\left(T, X^0_{\mathrm{Mn,Cr,Si,Mo,Nb,Ti}}\right) = \frac{M_{pure}}{1 + M_{pure} \sum_{i=1}^{n} \alpha_i X_i} \tag{2.15}$$

In Equation 2.15, α_i is a slowdown coefficient reflecting the influence of the segregation of substitutional element of type i within the interface on the interface mobility, X_i^0 is the initial molar fraction of element i and M_{pure} is the intrinsic grain boundary mobility in the case of pure iron. This mobility is assumed to evolve with the temperature T according to relation 2.16 :

$$M_{pure} = \beta_T \frac{V_m \delta_{Gb}}{b_{111}^2 RT} D^0_{Gb} \exp\left(-\frac{Q_{Gb}}{RT}\right) \tag{2.16}$$

where V_m is the ferrite molar volume, δ_{Gb} the width of the grain boundary and R the universal gas constant. D^0_{Gb} and Q_{Gb} are respectively the pre-exponential factor and the activation energy of the intrinsic diffusion coefficient of Fe along the grain boundaries. Table 2.5 summarizes the values used in this work for all the model parameters.

With regard to the slowdown coefficient, α_i, of each alloying element, it is given by the following relationship:

$$\alpha_i = \frac{(RT)^2 \delta_{Gb}}{V_m E_b^i D_i^{Int}} \left(\sinh\left(\frac{E_b^i}{RT}\right) - \frac{E_b^i}{RT}\right) \tag{2.17}$$

It depends on the binding energy (E_b^i) of the considered element to grain boundaries and on its diffusion coefficient in iron $\left(D_i^{Int} = \phi D_i^0 \exp\left(-\frac{Q_i}{RT}\right)\right)$ where $\phi = 15$ [SIN 07] is a coefficient describing the real transinterface diffusivity based on the diffusion coefficients of the elements within the bulk.

Cette thèse est accessible à l'adresse : http://theses.insa-lyon.fr/publication/2020LYSEI120/these.pdf
© [A. MATHEVON], [2020], INSA Lyon, tous droits réservés

Due to their major role on the recrystallization kinetics, the parameters (E_b^i and D_i^{Int}) involved in the calculation of the influence coefficient α_i of each element on the interface mobility have to be chosen very carefully. This is why, this particular point is discussed in the next section.

2.3.5.2 Choice of the values of the binding energy and of the diffusion coefficient for each element

The unknown parameters of the model are the diffusion coefficients of each element and their binding energy within the interface. These two parameters are difficult to measure and could be used as adjustable parameters. However, since our objective is to be able to provide a predictive model whatever the composition of the steels is, it has been chosen to use the values of these coefficients provided in the literature for each element when they are available.

As far as the values of D_i^0 and Q_i are concerned, they have been fixed for all simulations. Table 2.4 summarizes the data used to calculate the diffusion coefficients throughout the simulations for Mn [IRM 72], Cr [OON 03], Si [The 17a], Nb [OON 03] and Mo [OON 03].

For the binding energies, the values of the substitutional elements with a strong interaction such as niobium [SIN 07], molybdenum [ZUR 12] and manganese [DAN 16] (which is the fundamental element of Dual-Phase steels) have been determined in the literature. These values were applied in the model. In the case of Cr and Si for which no binding energy was reported in the literature, it was chosen to apply the same reported value as for manganese and to check, a posteriori, that the chosen value is consistent or not with the experimental results.

Here, it has to pointed out that titanium, which enters in the chemical composition of the DP1000 steel of this study, was not considered in Table 2.4 because its diffusion coefficient and its binding energy in steel are not accurately known. This is why, the influence of this element will be neglected for the study of the DP1000 steel. This analysis is supported by the results of Bellavoine *et al.* [BEL 18] on steels containing Ti and/or Nb. They clearly highlight that the influence of this element on recrystallization is weaker than that of Nb.

	Diffusion coefficients		
Elements	Pre-exponential factor ($m^2.s^{-1}$)	Q_i (kJ/mol)	E_b^i (kJ/mol)
Mn	1.48×10^{-4}	233	5 [DAN 16]
Cr	3.7×10^{-3}	267	5
Si	1.97×10^{-4}	218	5
Mo	1.48×10^{-2}	282	13.5 [ZUR 12]
Nb	1.5×10^{-1}	299	28.9 [SIN 07]

Table 2.4: Values of the diffusion coefficients and binding energies used in this work for each element.

At this stage, one can note that other combinations of diffusion coefficients and binding energies could be used. However, it is important to point out that this set of parameters

Cette thèse est accessible à l'adresse : http://theses.insa-lyon.fr/publication/2020LYSEI120/these.pdf
© [A. MATHEVON], [2020], INSA Lyon, tous droits réservés

Parameter	Symbol	Unit	Value used
Average recrystallized grain radius	R_{Int}	m	1×10^{-5}*
Avrami exponent	n	-	1.3
Shear modulus	μ	Pa	7.93×10^{10}
Burgers vector in α-Fe	b_{111}	m	2.48×10^{-10}*
Interfacial energy of GB in α-Fe	γ_{Gb}	$J.m^{-2}$	0.38
Taylor factor	M_T	-	3
Constant	α_T	-	0.25
Turnbull factor	β_T	-	0.7*
α-Fe molar volume	V_m	$m^3.mol^{-1}$	7.09×10^{-6}*
Grain boundary thickness	δ_{Gb}	m	10^{-9}*
Gas constant	R	$J.mol^{-1}.K^{-1}$	8.314
Transinterface diffusity coefficient	ϕ	–	15*
Fe diffusivity pre-exponential factor in GB	D^0_{Gb}	$m^2.s^{-1}$	1.5×10^{-4}*
Activation energy for Fe diffusity in GB	Q_{Gb}	$kJ.mol^{-1}$	148*

Table 2.5: Values of the key parameters used in the MiReX model. * Identical values to thos used by Sinclair *et al.* [SIN 07]

coming from data of the literature was fixed throughout the rest of the present study and it was no longer modified. Hence, the only input data to the model are the chemical composition and reduction ratio of the steel sheet and the parameters of the thermal cycle.

2.3.6 Case of the microalloyed steels - Description of the thermodynamic model for precipitation

The prediction of the recrystallization kinetics of microalloyed steels containing Ti and Nb is more complex since the kinetics can be delayed both by a pinning effect of the grain boundaries by the complex (Ti,Nb)C carbides that may form before or during the recrystallization and/or by the segregation within the interfaces of the Ti and Nb atoms remaining in solid solution. It is therefore essential to be able to predict the precipitation kinetics of these carbides throughout the whole thermal cycle of these steels. In particular, the volume fraction ($f_v^{(Ti,Nb)C}$) of the precipitates within the steel and their radius $R_{(Ti,Nb)C}$ are required as well as the solute fraction remaining in solid solution.

In this work, the Preciso software [PER 09, PER 08] was used to follow the evolution of the precipitation state of the (Ti,Nb)C carbides during heat treatments of the DP1000 steel of this study. It is based on the classical nucleation, growth and coarsening theories, fully described in [WAG 05].The precipitation state was characterized by the whole precipitate size distribution (Lagrange-like approach).

Thermodynamic calculations for a steel having the chemical composition of the DP1000 of the present study have shown that during hot rolling, precipitation is not able to reach the steady state predicted by Thermocalc [GRA 19]. However, during cooling, TiN precipitates can appear at high temperature in austenite, thus reducing slightly the Ti content in solid solution. Taking into account the slight decrease in the Ti content due to this precipitation, the TCFE8 database [The 17b] gave a relatively constant composition of

Cette thèse est accessible à l'adresse : http://theses.insa-lyon.fr/publication/2020LYSEI120/these.pdf
© [A. MATHEVON], [2020], INSA Lyon, tous droits réservés

the (Ti,Nb)C carbides that can form during subsequent cooling at lower temperature: $(Ti_{0.36\pm0.05},Nb_{0.64\pm0.05})C_{1\pm0.02}$ in austenite between 1200 °C and 700 °C and $(Ti_{0.6\pm0.05}, Nb_{0.4\pm0.05})C_{1\pm0.02}$ in ferrite between 700 °C and 300 °C. Thus, a simplified average composition was taken into account for each temperature domain. It was also assumed that the number of metallic (Ti and Nb) atoms was equal to the number of carbon atoms (no vacancy in precipitates), giving the following precipitate composition: $Ti_{0.36}Nb_{0.64}C$ in austenite and $Ti_{0.6}Nb_{0.4}C$ in ferrite. Then, using the evolution of austenite and ferrite composition with temperature at equilibrium, the solubility product was evaluated at each temperature with the following relations:

$$K_s^{\gamma} = (X_{Ti}^{eq,\gamma})^{0.36}(X_{Nb}^{eq,\gamma})^{0.64}(X_C^{eq,\gamma})^1 \tag{2.18}$$

$$K_s^{\alpha} = (X_{Ti}^{eq,\alpha})^{0.6}(X_{Nb}^{eq,\alpha})^{0.4}(X_C^{eq,\alpha})^1 \tag{2.19}$$

where $X_i^{eq,\alpha}$ and $X_i^{eq,\gamma}$ are the atomic fraction of element i in solution in ferrite and in austenite. Lastly, by linearly fitting the evolution of $log_{10}(K_s)$ with $\frac{1}{T}$, the following expression was taken for the solubility product of (Ti,Nb)C:

- in austenite :

$$\log_{10}(K_s^{\gamma}) = -\frac{9040\text{ K}}{T} + 0.15 \tag{2.20}$$

- in ferrite :

$$\log_{10}(K_s^{\alpha}) = -\frac{5531\text{ K}}{T} - 3.3 \tag{2.21}$$

Precipitate/matrix interface energy was taken equal to 0.35 $J.m^{-2}$, in order to be able to reproduce the experimental precipitation kinetics of the (Ti,Nb)C precipitates determined by Bellavoine *et al.* [BEL 18] under similar conditions and in accordance with Zurob's *et al.* values [ZUR 02].

2.4 Results

The aim of this section is to compare the predictions of the MiReX model for recrystallization with experimental recrystallization kinetics. This comparison is first performed on the Fe-C-Mn ternary alloys of this study in order to validate the effect of the reduction ratio and of the chemical composition (C and Mn content). Then, the effect of the presence of different alloying elements (Cr, Si, Mo) is presented and discussed using recrystallization kinetics extracted from the literature. Finally, the coupling of the recrystallization model with a software for predicting precipitation kinetics is performed to validate the model on an industrial micro-alloyed DP1000 steel.

Cette thèse est accessible à l'adresse : http://theses.insa-lyon.fr/publication/2020LYSEI120/these.pdf
© [A. MATHEVON], [2020], INSA Lyon, tous droits réservés

2.4.1 Modelling of the recrystallization in ternary Fe-C-X systems

2.4.1.1 Case of the Fe-C-Mn system - Influence of the C and Mn content and of the reduction ratio

The recrystallization model presented in Section 2.3 was first tested on the ternary steels of this study, in order to analyze separately the contribution of the : (i) carbon content, (ii) manganese content and (iii) reduction ratio on the recrystallization. For the validation of the model, the recrystallization kinetics of the cold-rolled ternary steels were modelled and experimentally determined for a recrystallization temperature of 625 °C.

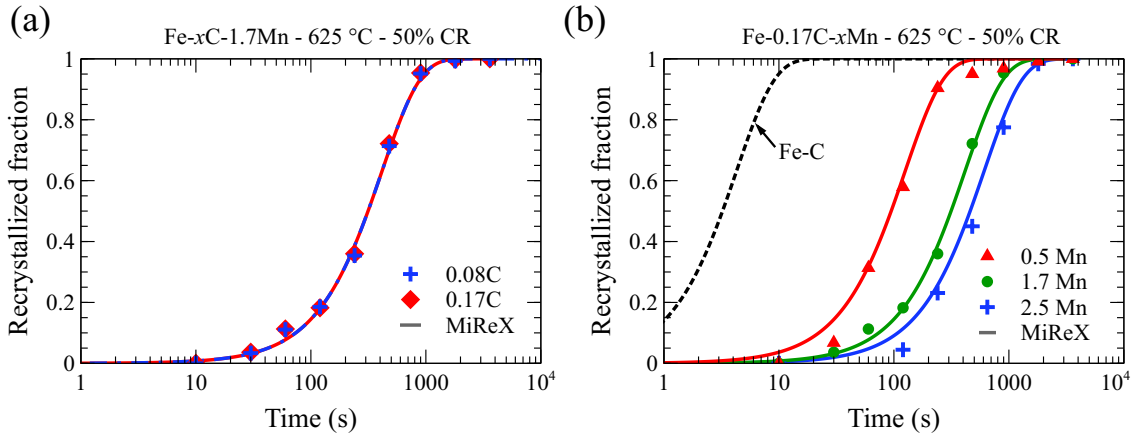

Figure 2.4: Effect on the recrystallisation kinetics at 625 °C of ternary Fe-C-Mn steels cold-rolled with a 50% reduction ratio : (a) of the C content; (b) of the Mn content

Figure 2.4.(a-b) show the effect of the carbon content and that of the manganese content on the recrystallization. As can be seen in Figure 2.4.(a), the change in the carbon content of the steel (from 0.08C to 0.17C) without modifying the manganese content (1.7 Mn) has no effect on the experimental recrystallization kinetics. This conclusion is consistent with the model which also predicts that the amount of carbon in the steel is not likely to influence the recrystallization kinetics. By contrast, as clearly highlighted in Figure 2.4.(b) for steels with 0.17C, manganese significantly retards recrystallization, since the kinetics is regularly shifted towards longer annealing times as the manganese content is increased. Figure 2.4.(b) shows that this effect is well taken into account by the model, which tends to indicate that the parameters of the model chosen for manganese and given in Table 2.4 are correct.

Figure 2.5 highlights the effect of the reduction ratio on the recrystallization of the ternary 0.08C-1.7Mn steel at 625 °C. In the case of Dual-Phase steels, this parameter is generally adjusted in order to control their microstructure during the intercritical annealing. The reduction ratio influences mainly the stored energy during the deformation: increasing the reduction ratio increases the available energy for recrystallization and thus accelerates this phenomenon. It is therefore essential for the model to be able to predict the influence of this parameter. As can be seen in Figure 2.5, with the data of Table 2.3 obtained from hardness experiments, the agreement between the experimental and modelled

Cette thèse est accessible à l'adresse : http://theses.insa-lyon.fr/publication/2020LYSEI120/these.pdf
© [A. MATHEVON], [2020], INSA Lyon, tous droits réservés

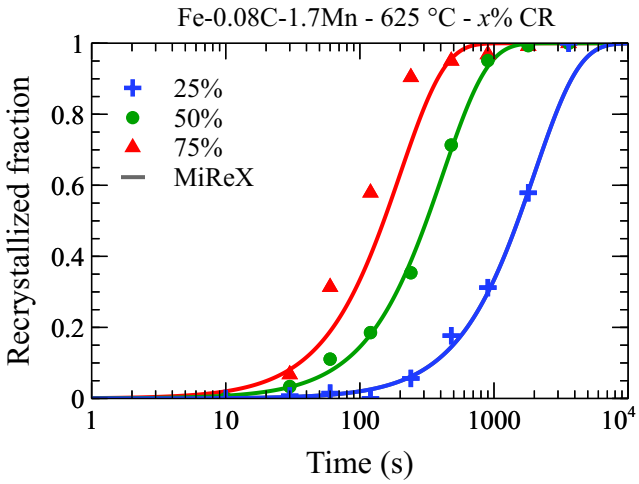

Figure 2.5: Effect of the reduction ratio on the recrystallization kinetics at 625 °C of the Fe-0.08C-1.7Mn steel

kinetics is quite satisfying. A slight discrepancy compared to the experimental kinetics is observed for 75% deformed steel which can be explained by the choice to ignore the effect of the reduction ratio and the dislocation density on the nuclei density.

2.4.1.2 Influence of the addition of Mn, Cr, Si, Mo and Nb

The preceding results showed that manganese is expected to play a major role on the recrystallization of DP steels. This is mainly due to its rather high concentration (between 1.5 and 2 wt.%) compared to that of the other substitutional elements (such as Cr, Si, Mo, Nb) commonly present in the chemical composition of industrial DP steels.

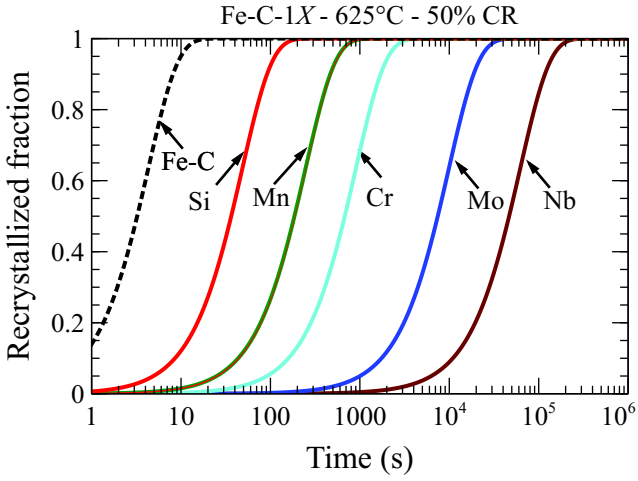

Figure 2.6: Modelling of the effect of the addition of 1 wt.% alloying element on the recrystallization kinetics of a Fe-C-1*X* system with the data of Table 2.4.

However, in spite of their lower concentration in DP steels, these elements may influence the recrystallization. This is why, before testing the MiReX model on more complex

Cette thèse est accessible à l'adresse : http://theses.insa-lyon.fr/publication/2020LYSEI120/these.pdf
© [A. MATHEVON], [2020], INSA Lyon, tous droits réservés

systems combining several types of substitutional elements, it seems interesting to use this model to determine the relative influence of the typical alloying elements of DP steels on recrystallization. To this end, it was chosen to compare the effect of adding 1 wt.% of alloying element in a Fe-C-X system.

Figure 2.6 shows that among the three most widely used elements in DP steels (Mn, Si, Cr), silicon is expected to have less effect on the retardation of recrystallization than manganese or chromium. Concerning niobium and molybdenum, these elements have a very important ability to slow down recrystallization kinetics. This explains why they will often drive the overall kinetics although they are added in very small quantities to steels.

2.4.2 Modelling of the recrystallization in more complex systems - Analysis of the influence of the addition of Cr, Si and Mo

After having analyzed the recrystallization kinetics of ternary systems and calibrated the model for manganese and reduction ratio, the recrystallization model was then tested on more complex systems studied in the literature and reported in Table 2.1, in order to determine notably the contribution of: (i) silicon (added to avoid carbides), (ii) chromium (added to improve quenchability) and (iii) molybdenum (added to improve mechanical impact properties).

For model validation, experimental data were extracted from studies of literature on three systems [KUL 13, HUA 04] : (i) a Fe-0.18C-1.5Mn-1.7Si steel to study the effect of a high Si addition, (ii) a Fe-0.06C-1.8Mn-0.15Mo steel to analyze the effect of molybdenum and (iii) a Fe-0.1C-1.8 Mn-0.35Cr-0.16Si steel to investigate the contribution of chromium. In each case, in order to highlight the contribution of each type of substitutional element of the chemical composition on the retardation of recrystallization, the recrystallization kinetics at 650 °C was modelled for : (i) the corresponding binary Fe-C system, (ii) the corresponding ternary Fe-C-Mn system and (iii) the whole system including all the alloying elements of the chemical composition.

Figure 2.7.(a) shows the effect of the silicon content on recrystallization. As can be seen in Figure 2.7.(a), the experimental kinetics obtained by Huang [HUA 04] on a Fe-0.18C-1.5Mn-1.7Si steel are well predicted by the model. However, it is interesting to compare the simulations carried out on a Fe-C-1.5 Mn steel with 1.7 Si and without Si : they highlight that this element has a negligible impact on recrystallization, when it is added in a steel containing already a high manganese content.

Figure 2.7.(b) shows the effect of the molybdenum content on the recrystallization kinetics of a Fe-0.17C-1.8Mn-0.15Mo steel [HUA 04] at two temperatures. The slowdown of the experimental kinetics due to molybdenum segregation is well predicted by the model. Furthermore, the simulations on a Fe-C-1.8Mn steel with or without molybdenum show that the addition of this element, even in small quantities, has a much greater impact on the retardation of the recrystallization than a high addition of silicon.

Lastly, Figure 2.7.(c-d) show the effect of the chromium content on the isothermal and non-isothermal recrystallization kinetics of a Fe-0.1C-1.8Mn-0.3Cr steel [KUL 13] assuming that no precipitation of chromium carbide occurs during the treatment. Unlike silicon, the chromium content has a non negligible impact on recrystallization despite its

Cette thèse est accessible à l'adresse : http://theses.insa-lyon.fr/publication/2020LYSEI120/these.pdf
© [A. MATHEVON], [2020], INSA Lyon, tous droits réservés

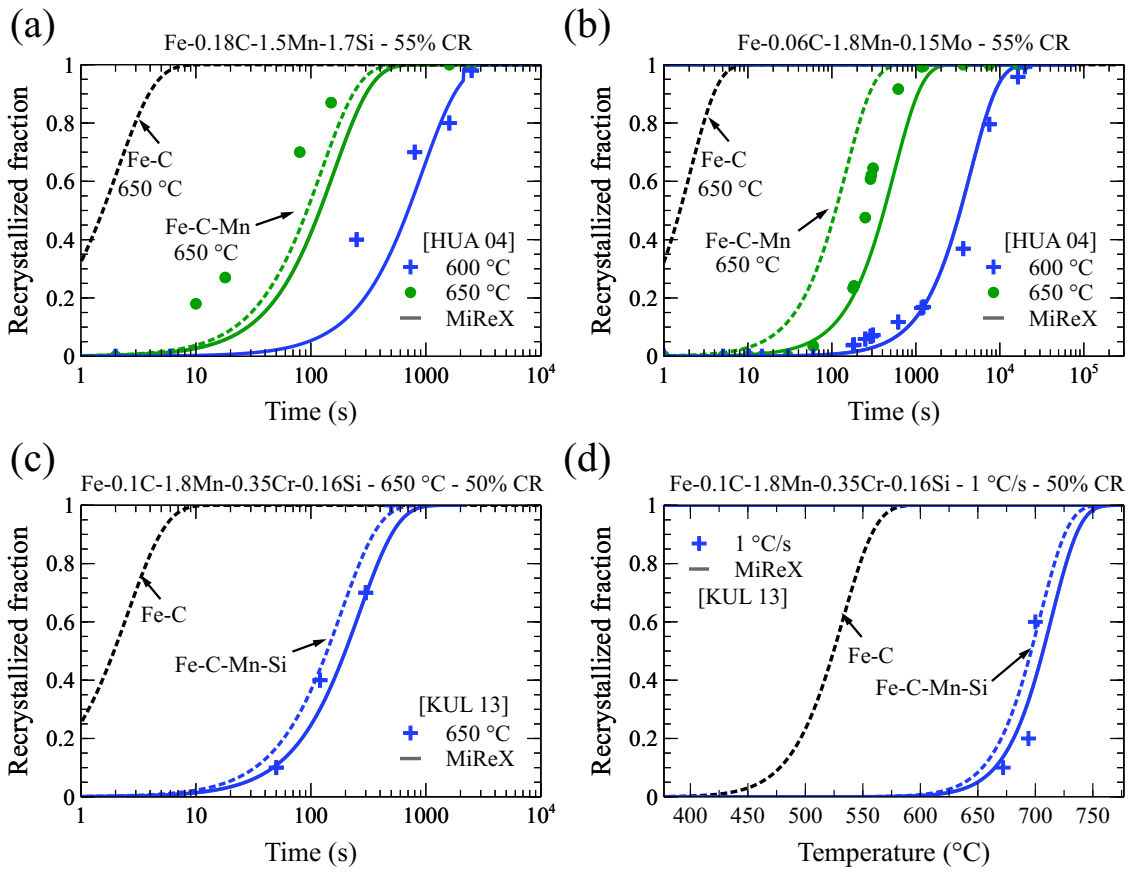

Figure 2.7: Effect of : (a) silicon, (b) molybdenum, (c) chromium on the isothermal recrystallization kinetics of cold-rolled Fe-C-Mn steels at 600 °C and/or 650 °C. (d) Non-isothermal recrystallization kinetics during continuous heating at 1 °C/s of a cold-rolled Fe-0.1C-1.8Mn-0.35Cr steel.

low content in the alloy. Furthermore, Figure 2.7.(d) shows that the model is likely to predict rather well recrystallization during continuous heating at 1 °C/s. At first sight, it seems that it can be applied a priori to complex thermal cycles including a heating stage followed by a holding at the considered annealing temperature.

2.4.3 Modelling of the recrystallization of industrial DP steels

2.4.3.1 Case of the DP600 steel

In order to test the validity of the model on an industrial steel without microyalloying element, the recrystallization kinetics of the DP600 steel of this study was obtained experimentally at three temperatures and modelled. The influence of each element of its composition having been studied before, it is clear that the two main elements responsible for the slowdown of the kinetics compared to pure iron are manganese and chromium. Figure 2.8 shows the very good experimental agreement obtained when the MiReX model is used on the DP600 steel of this study at the three investigated temperatures.

Cette thèse est accessible à l'adresse : http://theses.insa-lyon.fr/publication/2020LYSEI120/these.pdf
© [A. MATHEVON], [2020], INSA Lyon, tous droits réservés

Here, it has to be noted that the modelling of the recrystallization kinetics of the DP600 steel can also be performed with the JMAK model recalled in Section 2.1.3.3 (see Equation 6.19). Table 2.6 gives the three parameters (n, b_0 and Q) of the JMAK model of the DP600 steel determined from the experimental kinetics of Figure 2.8. The activation energy is equal to 355 kJ/mol. It is much higher than that for iron self-diffusion in ferrite (250 kJ/mol) as it is an apparent activation energy.

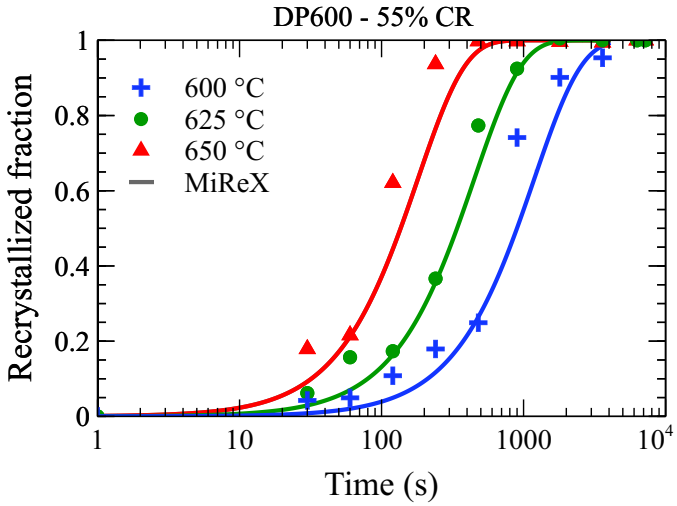

Figure 2.8: Effect of the temperature on the recrystallization kinetics of the DP600 steel cold-rolled with a 55% reduction ratio

Table 2.6: Definition of the JMAK parameters of the DP600 steel

Grade	n	Q (kJ/mol)	b_0 (s^{-1})
DP600	1.3	355	9×10^{17}

2.4.3.2 Case of the micro-alloyed DP1000 steel

For the study of the recrystallization of the DP1000 steel, it was first necessary to determine the degree of precipitation of Ti and Nb in the form of (Ti,Nb)C carbides at the end of the processing of the steel sheets (before the annealing step). This precipitation may occur either in austenite (during reheating of the slabs at 1250 °C and/or during hot-rolling) or in ferrite (during coiling at 600 °C followed by air cooling to ambient temperature). Using the Preciso software and the methodology presented in Section 2.3.6, the Time-Temperature-Transformation (TTT) diagrams of the DP1000 steel could be built. Figure 2.9.(a) concerns the precipitation of the $Ti_{0.36}Nb_{0.64}C$ carbide in austenite (above Ac_1), while Figure 2.9.(b) is relative to the formation of the $Ti_{0.6}Nb_{0.4}C$ carbide in ferrite (below Ac_3). As can be seen in Figure 2.9, precipitation is expected to be much more rapid in ferrite than in austenite (notably between 600 °C and Ac_3).

Cette thèse est accessible à l'adresse : http://theses.insa-lyon.fr/publication/2020LYSEI120/these.pdf
© [A. MATHEVON], [2020], INSA Lyon, tous droits réservés

In addition, the TTT diagrams present the limiting grain diameter (D_l) reachable when precipitation occurs within the steel. This diameter was calculated, for each state, using the modified Zener equation [GRA 19]:

$$D_l = \frac{2R_{(Ti,Nb)C}}{3f_v^{(Ti,Nb)C}} \tag{2.22}$$

where $R_{(Ti,Nb)C}$ and $f_v^{(Ti,Nb)C}$ are the radius and volume fraction of the (Ti, Nb)C precipitates.

Figure 2.9 shows that over short periods of time at a given temperature, no precipitation is expected. Then, when precipitation occurs, the limiting grain diameter decreases due to pinning pressure before increasing due to precipitate coarsening.

Taking into account the real industrial cycle of the studied steel and the TTT diagrams of Figure 2.9, it was possible to conclude that almost no precipitation occurred during the processing of the steel (hot-rolling, coiling and air cooling), suggesting that all the microalloying elements should be in solid solution before the annealing step.

In Figure 2.10.(a), the MiReX model was thus tested at three annealing temperatures under two different conditions : (i) assuming that all the niobium atoms remain in solid solution during recrystallization and (ii) considering the precipitation of (Ti, Nb)C particles during the annealing as predicted by PreciSo. As can be seen in Figure 2.10.(a), the MiReX model is likely to reproduce the experimental isothermal recrystallization kinetics of the DP1000 steel with the two considered conditions. This can be explained by the fact that precipitation starts at a relatively late stage of recrystallization in all cases, so that the kinetics are not notably affected by this phenomenon. Nevertheless, a stronger interaction could be observed for lower cold-rolling reduction ratios leading to slower recrystallization kinetics.

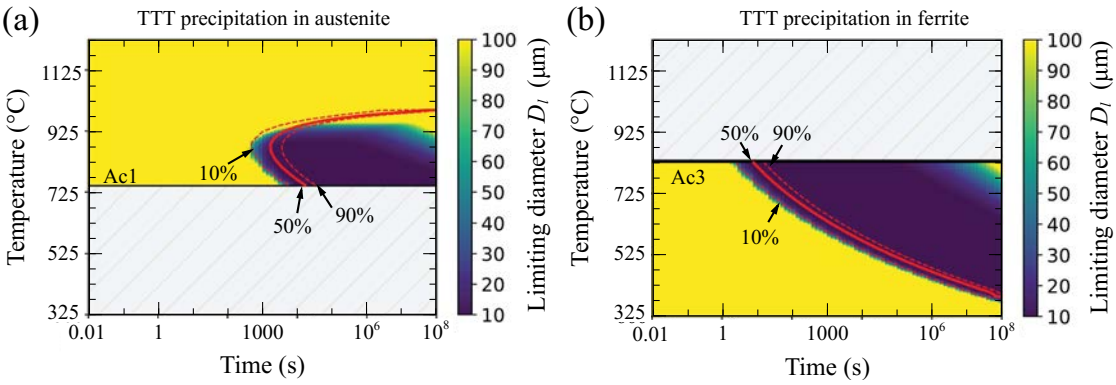

Figure 2.9: TTT diagram for the precipitation of the (Ti,Nb)C carbides and limit grain diameter obtained by the Zener equation: (a) in austenite and (b) in ferrite.

This is why, in order to compare the relative effect on the recrystallization kinetics of the pinning pressure exerted by the precipitates and of the solute Ti and Nb atoms, the DP1000 was pre-treated for 20 min at 700 °C so that all the Ti and Nb leave the solid

Cette thèse est accessible à l'adresse : http://theses.insa-lyon.fr/publication/2020LYSEI120/these.pdf
© [A. MATHEVON], [2020], INSA Lyon, tous droits réservés

solution (as predicted by the TTT diagram of Figure 2.9.(b)). It was then cold-rolled with a 55% reduction ratio before being annealed at 650 °C.

Figure 2.10.(b) clearly shows the acceleration of the recrystallization kinetics when precipitates have formed before annealing, suggesting that their effect on the slowdown of recrystallization is less pronounced than that due to the segregation of the micro-alloying elements within the interface. This observation is in good agreement with the conclusions of Bellavoine *et al.* [BEL 18] and is well taken into account by the recrystallization model of this study when the effect of the precipitates is considered. It was therefore possible, during this study, to simulate the precipitation kinetics of (Ti,Nb)C carbides and to combine it with the recrystallization model in order to be able to reproduce the recrystallization kinetics of the micro-alloyed DP1000 steel of this study. Here, one can note that the MiReX model could be extended to the study of the effect of other types of precipitates on the recrystallization.

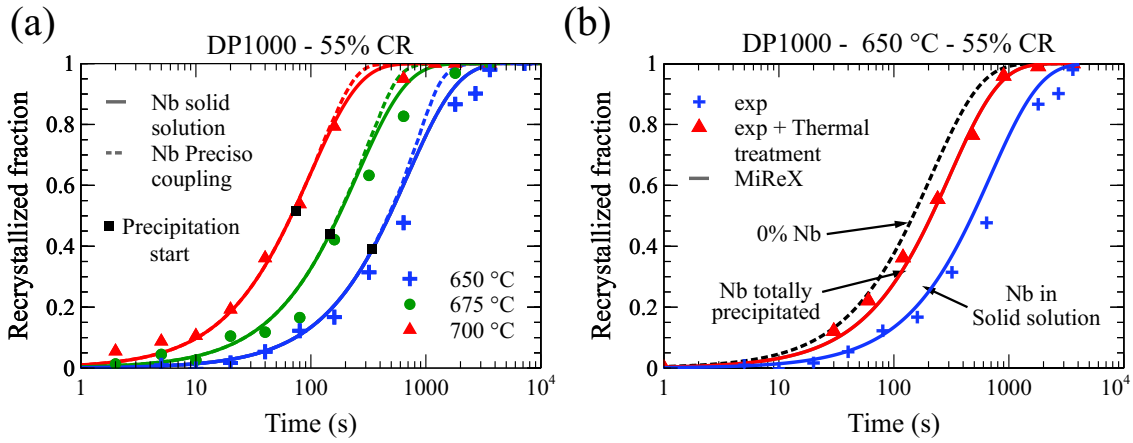

Figure 2.10: Effect of : (a) the temperature and (b) the precipitation state of Nb on the recrystallization kinetics of the DP1000 steel cold-rolled with a 55% reduction ratio.

2.5 Discussion: Interaction between recrystallization and austenite formation

2.5.1 Consequence of the interaction on the microstructure and on the austenite formation kinetics

As mentioned in the the literature review of this chapter (see Section 2.1.2), an interaction between recrystallization and austenite formation is likely to occur during the annealing of Dual-Phase steels, notably during the heating stage to the annealing temperature. This interaction leads to two types of interactions called “weak” and “strong” by Chbihi *et al.* [CHB 14b]. The “weak” interaction corresponds to the case where the recrystallization is mostly completed at the austenite start temperature leading to a rather homogeneous microstructure. By contrast, in the case of a “strong” interaction, recrystallization and

Cette thèse est accessible à l'adresse : http://theses.insa-lyon.fr/publication/2020LYSEI120/these.pdf
© [A. MATHEVON], [2020], INSA Lyon, tous droits réservés

austenite formation are assumed to occur simultaneously leading to a coarse, banded and heterogeneous microstructure.

As already mentioned, the degree of interaction between recrystallization and austenite formation may affect the final microstructure and thus, the final mechanical properties. However, it is also likely to modifiy notably the austenite formation kinetics during heating. This is illustrated in Figure 2.11 which shows the kinetics obtained by dilatometry for the two industrial DP steels investigated in this study for a heating of 30 °C/s starting from a cold-rolled state and from a recrystallized state (prior thermal treatment of 20 min at 700 °C and 30 min at 650 °C for respectively DP1000 and DP600). The austenite formation kinetics of the cold-rolled DP600 steel exhibits a slight acceleration at the beginning of the transformation compared to the recrystallized steel. This could be explained by the fact that the recrystallization phenomenon is not complete at Ac_1 for the considered heating rate. On the other hand, the austenite formation kinetics of the cold-rolled DP1000 steel presents a very strong acceleration throughout the transformation compared to the kinetics of the recrystallized steel, which could be due to a near-zero fraction of recrystallized ferrite at the start of the phase transformation.

The preceding considerations highlight the necessity to be able to model the recrystallization during continuous heating of the steel up to its annealing temperature in order to know the temperature domain for recrystallization and to predict whether an interaction with austenite formation will occur or not. The aim of the next section is thus to discuss about the modelling of recrystallization under non-isothermal treatments.

2.5.2 Modelling of recrystallization during continuous heating - Application to the industrial steels

The modelling of the recrystallization under non-isothermal conditions can be easily performed from the simple JMAK formalism recalled in Section 2.1.3.3 (see Equation 6.19). After having determined the three parameters (n, b_0 and Q) of this equation using isothermal experiments performed below Ac_1, the differential form of the JMAK law can be used to predict the recrystallization during continuous heating :

$$\frac{df(T,t)}{dt} = n.[1 - f(T,t)].b[-\ln(1 - f(T,t))]^{\frac{n-1}{n}} \tag{2.23}$$

This type of approach has already been used with success in literature by different authors [OLL 17a, KUL 13, LI 13, HUA 04] and it was partly validated thanks to a comparison of the modelled kinetics with experimental kinetics (determined as in the present study). However, one can note that the comparisons were always performed in the case where the heating rate did not exceed 10 °C/s. Namely, in these conditions, the recrystallization domain is at relatively low temperature (mostly, below Ac_1) and thus, relatively close to the domain of the isothermal experiments which were used to determine the parameters of the model.

The MiReX model developed in this study can also be used under non-isothermal conditions. This was already done in the case of Figure 2.7.(d) which corresponds to a continuous heating at 1 °C/s. In this case, the model describes well the recrystallization

Cette thèse est accessible à l'adresse : http://theses.insa-lyon.fr/publication/2020LYSEI120/these.pdf
© [A. MATHEVON], [2020], INSA Lyon, tous droits réservés

and it gives similar results to those of the JMAK model based on Equation 2.23 used by [KUL 13].

In this context, it seems interesting to compare the modelling of recrystallization during continuous heating using: (i) the JMAK approach based on Equation 2.23 and (ii) the MiReX model. This comparison was performed in the case of the DP600 steel of this study for which the parameters (n, b_0 and Q) of the JMAK model are given in Table 2.6.

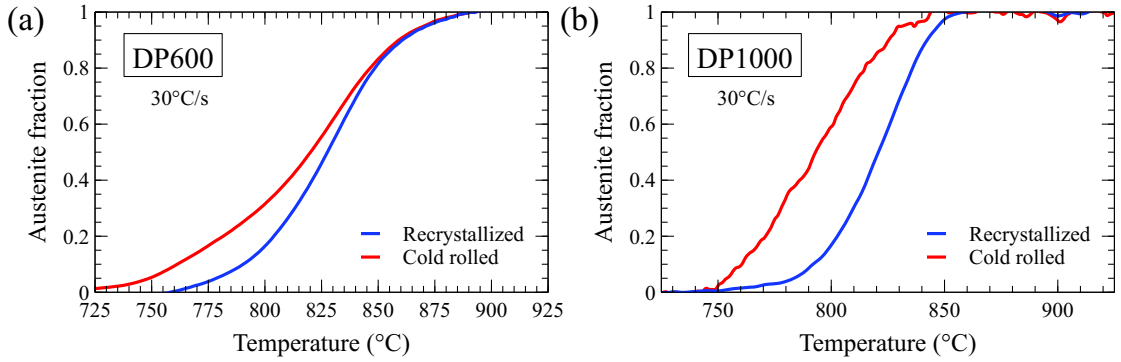

Figure 2.11: Experimental austenite formation kinetics during continuous heating at 30 °C/s starting from a recrystallized and cold-rolled steel : (a) DP600 steel: (b) DP1000 steel

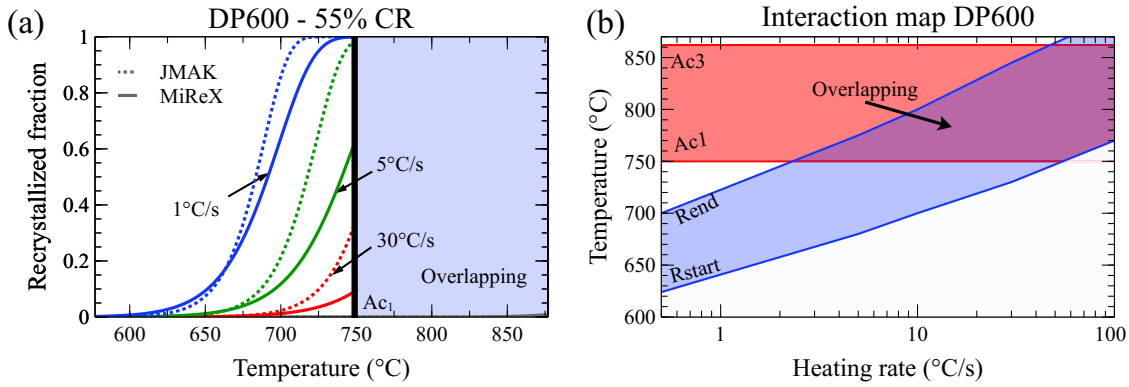

Figure 2.12: (a) Modelled recrystallized fractions of the DP600 steel during continuous heating with three different heating rates using the simple JMAK formalism and the MiReX model (No results are shown for temperatures above Ac_1 since phase transformation may strongly affect the ReX kinetics in the overlapping domain [BAR 15]); (b) Interaction map of the DP600 steel using the MiReX model to predict the recrystallization domain.

Figure 2.12.(a) shows the comparison of the two types of recrystallization modelling during continuous heating with different heating rates used industrially from 1 °C/s to 30 °C/s. Note that above Ac_1, autenite formation may modify the recrystallization kinetics as highlighted by some authors [YAN 85a, CHB 14b, BAR 15]. Therefore, no results are shown above Ac_1 in Figure 2.12. First of all, we can note a very good agreement between the two types of modelling for kinetics at 1 °C/s as already mentioned in the case of Figure 2.7.(d). For higher heating rates, the two types of modelling are in relatively good

Cette thèse est accessible à l'adresse : http://theses.insa-lyon.fr/publication/2020LYSEI120/these.pdf
© [A. MATHEVON], [2020], INSA Lyon, tous droits réservés

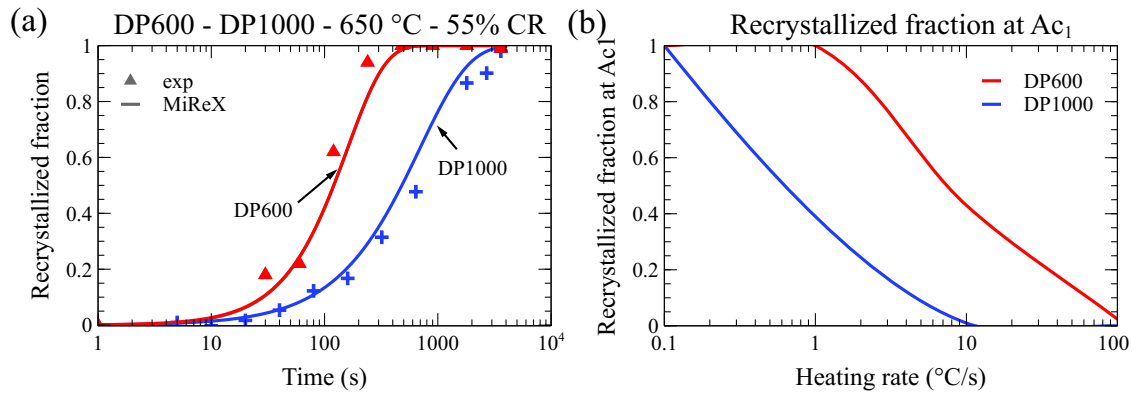

Figure 2.13: (a) Experimental and modelled recrystallized fractions of the DP600 and DP1000 steels as a function of time at 650 °C. (b) Predicted recrystallized fractions at Ac_1 for the two steels with the MiReX model.

agreement as long as the temperature is below the Ac_1 temperature (around 750 °C). This is consistent with the fact that the models were calibrated in this temperature range and gave similar results in this temperature domain under isothermal conditions.

From the kinetics of Figure 2.12.(a), the temperatures at which the recrystallisation kinetics starts and ends (calculated for a recrystallized fraction of 5% and 95%) could be determined with the MiReX model for different heating rates (Figure 2.12.(b)). The austenite start and austenite finish temperatures determined on previously recrystallized steel, by optical dilatometry, were also plotted leading to the interaction map of Figure 2.12.(b) for the DP600 steel of this study. Interaction can only be observed for heating rates higher than 3 °C/s. This is consistent with the results of Kulakov *et al.* [KUL 13] based on the simple JMAK formalism. Here, it is also important to point out the fact that the interaction domain of the micro-alloyed DP1000 steel determined by Ollat *et al.* [OLL 17a] starts at lower heating rates. This is due to the fact that the micro-alloying elements (Ti and Nb) of the DP1000 steel significantly delay the recystallization kinetics, compared to the case of the DP600 steel, due to the segregation of these elements within the interface and/or by the formation of (Ti,Nb)C precipitates (see Figure 2.13.(a)). The consequence is that the recrystallization domain of the DP1000 steel is obtained at higher temperatures, thus decreasing the value of the minimum heating rate for which interaction starts to be detected.

To complete this work, the recrystallized fractions at the austenite start temperature predicted with the MiReX model were plotted as a function of the heating rate in Figure 2.13.(b) for the DP600 and DP1000 steels of this study. At the lowest heating rates, no interaction is expected in the DP600 steel, while it can be important in the DP1000 steel. By contrast, above 10 °C/s, a strong interaction is possible in the two steels as illustrated in Figure 2.11.

As a conclusion, these results highlight the importance of paying attention to industrial trends that tend towards the increasingly important addition of substitutional elements for the development of new grades and to the use of furnaces with higher heating rates (until

Cette thèse est accessible à l'adresse : http://theses.insa-lyon.fr/publication/2020LYSEI120/these.pdf
© [A. MATHEVON], [2020], INSA Lyon, tous droits réservés

100 °C/s). It is therefore essential to have a tool for predicting recrystallization kinetics as a function of chemical composition, thermal cycle and reduction ratio to optimize chemical compositions and thermal paths.

2.6 Conclusions

1. The modelling of the recrystallization kinetics of cold-rolled ferritic-pearlitic DP steels was performed using a microstruturally-based recrystallization model (denoted MiReX model) likely to take into account the reduction ratio of the steel sheet, the pinning effect of the precipitates that may form before or during recrystallization and the solute drag of substitutional elements (Mn, Si, Cr, Mo, Nb) within the interfaces. In this model, the effect of each type of alloying element segregated within the interfaces on the retardation of the recrystallization kinetics was taken into account thanks to a slowdown coefficient depending on the diffusion coefficient of the element and its affinity to be segregated at grain boundaries. The data (diffusion coefficient, binding energy to grain boundaries) of each element were extracted from the literature. The kinetics predicted by the MiReX model were performed without any adjustable parameters and compared to a wide range of experimental kinetics.
2. A validation of the model was first conducted on ternary Fe-Mn-C alloys with various C and Mn contents and cold-rolled with different reduction ratios, in order to confirm the influence of the chemical composition (notably, of the Mn content) and reduction ratio on recrystallization kinetics. It was observed that Mn due to its rather high concentration in DP steels plays a major role on the recrystallization kinetics which is significantly delayed compared to that of binary Fe-C steels.
3. The model was then confronted with experimental results from the literature on more complex systems of Fe-C-Mn-X type, representative of the chemical composition of DP or TRIP steels, notably to validate the influence of the addition of Si, Mo and Cr. Contrary to silicon, molybdenum may have a strong influence on recrystallization due to its low diffusion coefficient and its high binding energy to grain boundaries. A rather good agreement between the MiReX model and experiment was noted in a wide domain of chemical composition of AHSS and UHSS as well as standard cold rolling reduction ratios without fitting parameters.
4. In the case of the micro-alloyed DP1000 steel, a coupling with a precipitation modelling sofware was used to include the effect of the (Ti,Nb)C precipitates. It was highlighted that Ti and Nb have a crucial role in kinetics both in solid solution and as precipitates due to their pinning effect on the grain boundaries. The integration of precipitates into the MiReX model made it possible to reproduce the interaction of precipitation and recrystallization for micro-alloyed steels.
5. Lastly, the MiReX model was used to predict recrystallization during continuous heating and to analyze the possibility of interaction of this phenomenon with austenite formation. For DP600 steels, this type of interaction is expected for heating rates higher than 3 °C/s and it leads to an acceleration of the austenite formation kinetics.

Cette thèse est accessible à l'adresse : http://theses.insa-lyon.fr/publication/2020LYSEI120/these.pdf
© [A. MATHEVON], [2020], INSA Lyon, tous droits réservés

Cette thèse est accessible à l'adresse : http://theses.insa-lyon.fr/publication/2020LYSEI120/these.pdf
© [A. MATHEVON], [2020], INSA Lyon, tous droits réservés

Chapter 3

Gibbs energy minimization model for the austenite-ferrite phase transformation in Fe-C-X-Y alloys

In Chapter 2, a microstructurally-based model for predicting the recrystallization phenomenon was developed. The present chapter aims at modelling the austenite $\leftrightarrow$ ferrite transformation kinetics in the case of quaternary systems during heating and holding thermal cycle. The model's objective stems from that, for each alloying element, the concentration profile is computed solving a *unique* diffusion equation (including the 3 phases and interfaces). The interface is described assuming linear variation of chemical potentials, saving thus computational time. Interface motion is driven by the minimization of Gibbs energy. Furthermore it is also possible to deal with systems containing several interfaces, necessary for the cementite dissolution for non-isothermal treatment in Fe-C-X-Y quaternary systems.

First, a study of the influence of the different numerical model parameters was carried out. Secondly, the effect of the cementite enrichment in alloying elements as well as its impact on cementite dissolution during the thermal treatment was discussed. The integration of cementite dissolution allows the GEM model to reproduce the experimental kinetics of austenite formation on a wide range of Fe-C-Mn steels and on two industrial Fe-C-Mn-Cr steels. The use of complex thermal cycle allowed us to validate the model's predictive capability on the different physical parameters influencing the phase transformation (chemical composition and temperature). Modifications are proposed in the case of DP1000 steel in order to capture the observed interaction between recrystallization and phase transformation for this steel. Finally, the ability of the model to move the interface without respecting the local equilibrium conditions at the interface and the integration of the diffusion of C and Mn in the bulk allowed us to reproduce the experimental kinetics of decarburization and cyclic transformation.

Cette thèse est accessible à l'adresse : http://theses.insa-lyon.fr/publication/2020LYSEI120/these.pdf
© [A. MATHEVON], [2020], INSA Lyon, tous droits réservés

Contents

Cette thèse est accessible à l'adresse : http://theses.insa-lyon.fr/publication/2020LYSEI120/these.pdf
© [A. MATHEVON], [2020], INSA Lyon, tous droits réservés

3.1 Literature review

The following section provides a short literature review relative to the ferrite to austenite phase transformation occurring during intercritical annealing. Finally, the different approaches that may be used for the phase transformation modelling will be discussed.

3.1.1 Phase transformation α+Fe_3C→ γ

From an initial microstructure composed of a ferrite-pearlite mixture, a solid-state transformation occurs leading to the austenite formation during the intercritical annealing process. This initial microstructure evolves to a ferrite-austenite mixture for thermal treatments in the intercritical domain ($Ac_1 < T < Ac_3$) and finally to a fully austenitic structure above Ac_3. The steel's chemical composition strongly affects start and end temperatures of the austenitic transformation [GRA 47, AND 65]. Additionally, it is interesting to point out that new initial microstructures (bainite and martensite) before annealing in the intercritical domain are emerging for the DP steel manufacture [BEL 18, MAR 20c].

The phase transformation complexity stems from the possibility for austenite to nucleate and grow from several sites in the initial two-phase microstructure. (*i.e.* cementite and ferrite).

3.1.1.1 Austenite nucleation

Austenite nucleates preferentially on non-equilibrium high-energy defects and high-carbon areas. Preferred nucleation sites can therefore be classified as follows:

(a) As the phase transformation is mainly driven by carbon diffusion, the Fe_3C carbides play a key role that may depend on their morphologies:
   - **Pearlite (Fe_3C and ferrite lamellae):** Austenite nucleation in pearlite is very rapid due to the short spacing between cementite lamellae [SAV 07]. In addition, pearlite grain boundaries are generally favorable nucleation sites. Namely, they are more highly disordered sites compared to the cementite/ferrite interfaces due to their high orientation energy, leading to faster nucleation.
   - **Spheroidized Fe_3C islands:** Intergranular carbides are preferential nucleation sites compared to intragranular sites due to their highly disoriented crystallography, making them high-energy nucleation sites as shown in Figure 3.1 [LAI 16, YAN 85b].

(b) Triple grain boundaries are second order nucleation sites with respect to carbide interfaces [OFF 12] [SAV 07] [SAV 10].

3.1.1.2 Austenite growth

Two major phenomena occur during the growth of the austenitic phase for non deformed steels: (i) the pearlite dissolution and then (ii) the ferrite-to-austenite transformation

Cette thèse est accessible à l'adresse : http://theses.insa-lyon.fr/publication/2020LYSEI120/these.pdf
© [A. MATHEVON], [2020], INSA Lyon, tous droits réservés

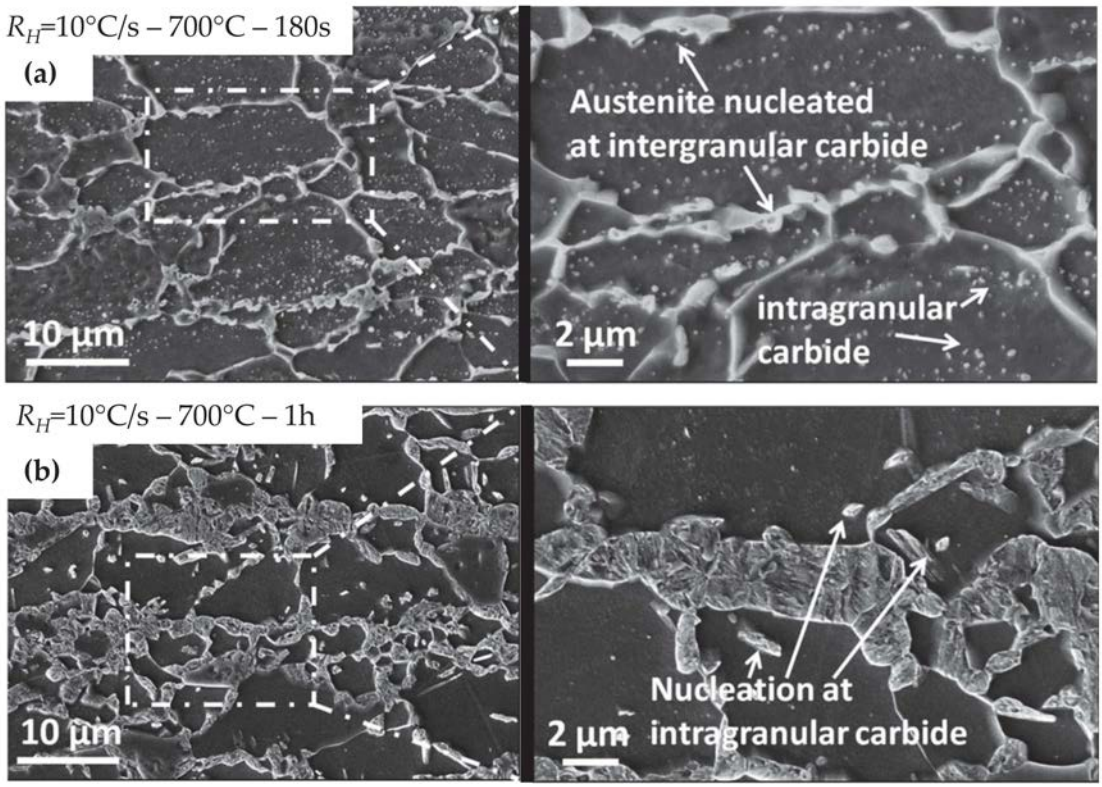

Figure 3.1: SEM micrographs highlighting austenite nucleation sites during intercritical annealing treatments at 700°C for (a) 180 s and (b) 1 h [LAI 16].

[OLI 07]. Speich *et al.* [SPE 81] divided the kinetics of austenitic formation into three phases as illustrated in Figure 3.2.(a):

- **Stage 1** : fast nucleation and growth driven by carbide (or pearlite) dissolution;
- **Stage 2** : austenite growth controlled by C diffusion in austenite (2.a) and slow Mn diffusion in ferrite (2.b);
- **Stage 3** : very slow equilibration of phases limited by Mn diffusion in austenite.

Figure 3.2.(b) reports the different steps observed within a Time Temperature Transformation (TTT) graph. The different domains evolve according to the temperature. Short times are mainly governed by pearlite dissolution or by the carbon diffusion within austenite. Between 10 and 10^7 s, the transformation is controlled by the manganese diffusion to only reach a final equilibrium above 10^7 s.

Furthermore, it has to be pointed out that the pearlite dissolution can be considerably delayed by adding alloying elements such as manganese and chromium which lead to a cementite stabilization. As cementite dissolution drives the first stage of austenite formation, Gouné *et al.* [GOU 12] proposed a criterion enabling the definition of two dissolution regimes. Figure 3.3.(a) shows that a fast dissolution regime is obtained at high temperatures for which an almost instantaneous dissolution in austenite can be considered contrary to the second regime for which the diffusion of manganese is necessary. Lai *et al.*

Cette thèse est accessible à l'adresse : http://theses.insa-lyon.fr/publication/2020LYSEI120/these.pdf
© [A. MATHEVON], [2020], INSA Lyon, tous droits réservés

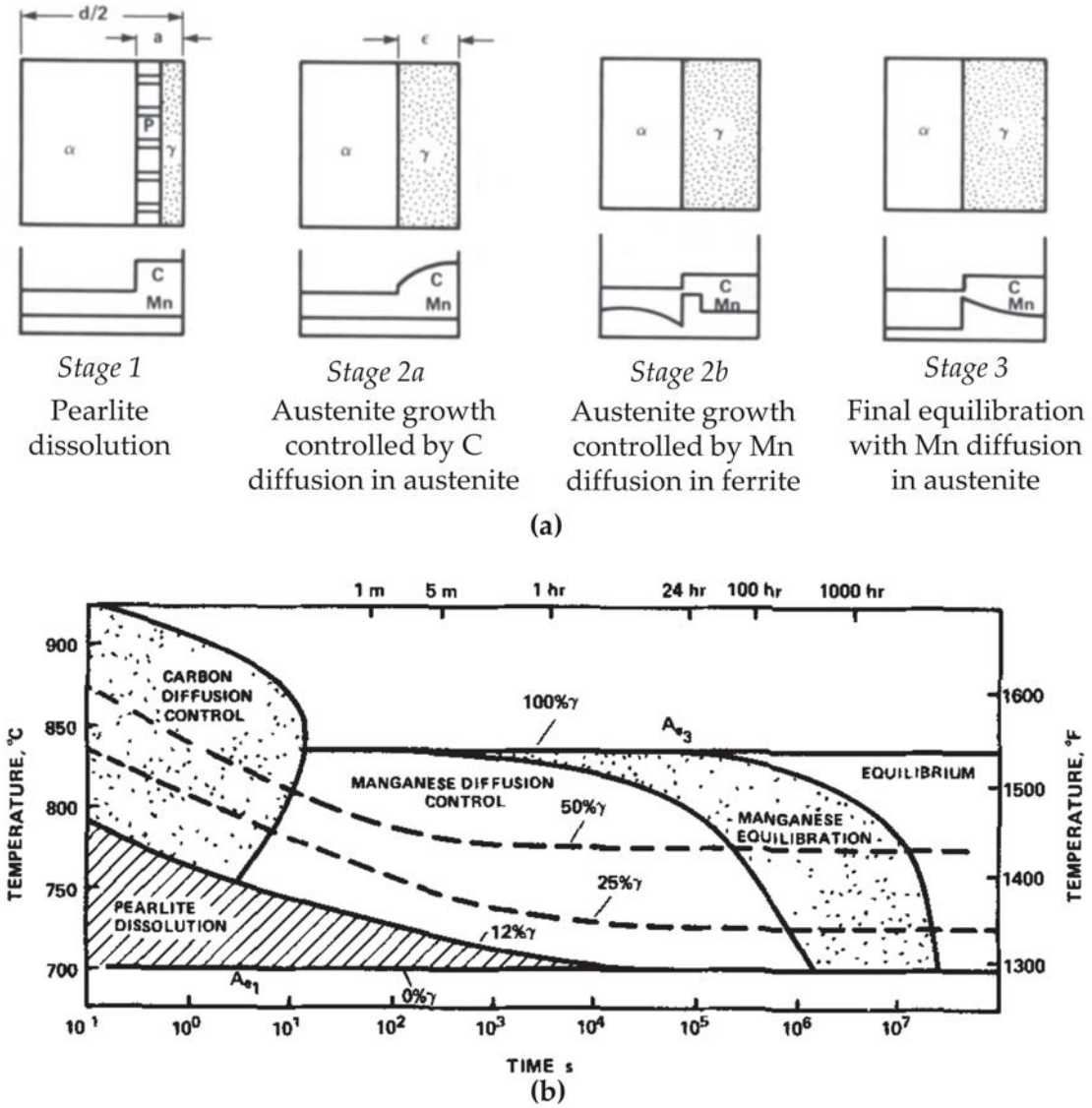

Figure 3.2: (a) Various transformation steps and (b) associated TTT diagram of the austenite formation according to Speich *et al.* [SPE 81].

[LAI 14] presents two kinetics of austenitic formation calculated with DICTRA software at 740 °C for two manganese enrichments. The steel containing the lowest cementite enrichment (7 wt.%Mn) has a faster kinetics than the one with a higher manganese content (25 wt.%Mn) in agreement with the criterion proposed by Gouné.

From a kinetic point of view, several authors [HUA 04, CHB 14b] have highlighted a strong influence of the heating rate (R_H) and of the initial state (hot-rolled or cold-rolled) on the kinetics of austenitic formation as shown in Figure 3.4. The treatment time used of the order of 600 s does not allow to reach the final thermodynamic equilibrium. From the diffusion point of view, a faster heating rate should lead to a lower austenite fraction, which

Cette thèse est accessible à l'adresse : http://theses.insa-lyon.fr/publication/2020LYSEI120/these.pdf
© [A. MATHEVON], [2020], INSA Lyon, tous droits réservés

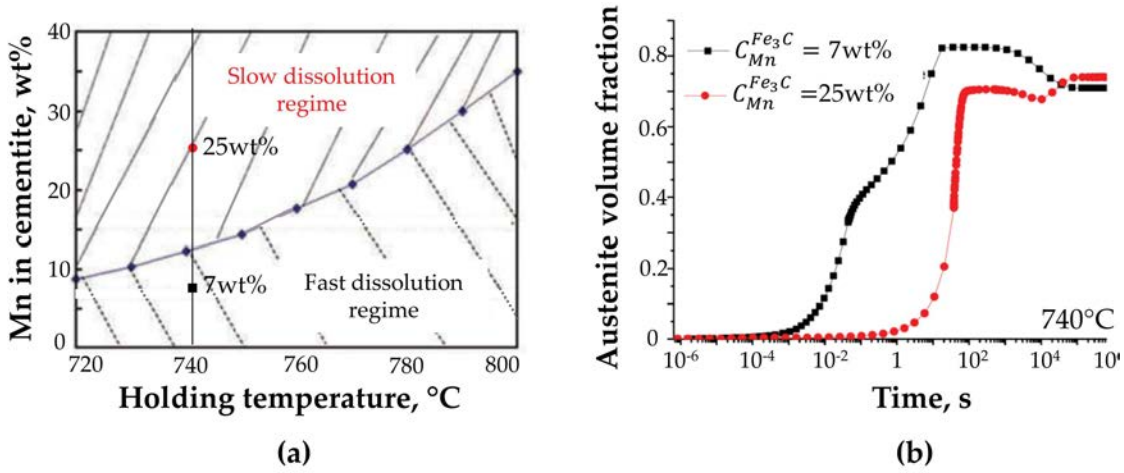

Figure 3.3: (a) Cementite dissolution regime as a function of Mn content in cementite and temperature defined by Gouné *et al.* [GOU 12] (b) Calculated kinetics of austenite growth at 740°C for 7 and 25 wt%Mn in cementite with DICTRA [LAI 14].

is not observed and thus suggests the intervention of additional phenomena. Furthermore, the use of a cold-rolled state leads for each heating rate to a faster kinetics in the beginning of transformation. This could be attributed to the increase in the nucleation site density for austenite caused by the deformation process.

To explain the lower austenite fraction for low heating rates, one can imagine an interaction with phenomena such as recrystallization, recovery as well as spheroidization [YAN 85a, KUL 13, AZI 11] and cementite enrichment. These different phenomena will stabilize the cementite particles and reduce the number of nucleation sites.

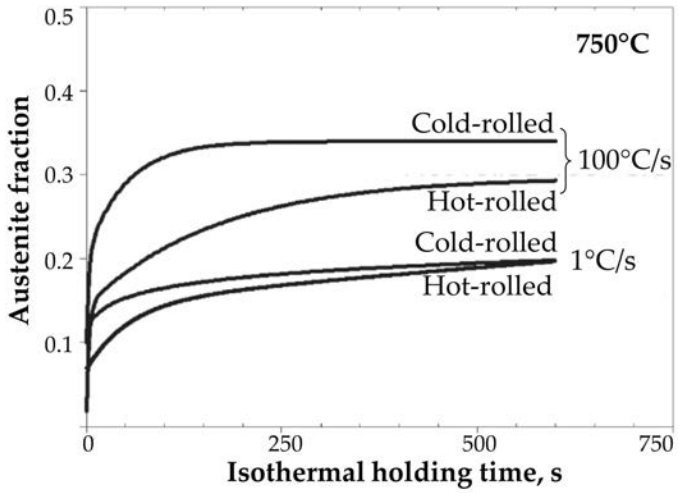

Figure 3.4: Effect of the heating rate (1 or 100 °C/s) on the isothermal austenite formation kinetics for hot-rolled and cold-rolled Fe-0.06C-1.86Mn-0.11Mo (wt.%) steels at 750 °C [HUA 04].

Cette thèse est accessible à l'adresse : http://theses.insa-lyon.fr/publication/2020LYSEI120/these.pdf
© [A. MATHEVON], [2020], INSA Lyon, tous droits réservés

3.1.2 Modelling tools for the prediction of phase transformation

Since diffusion-controlled phase transformations are one of the key parameters controlling the microstructures and mechanical properties of AHSS [TSU 16], it seems necessary to predict them. For many years, diffusion-controlled phase transformations in Fe-C-X alloys, in which the partitioning of substitutional and interstitial elements at the interface is essential, have been particularly studied [PUR 11, GOU 15, NAK 14, WEI 13b, DAN 16]. However, the difference in diffusivity between the substitutional and interstitial elements often leads to numerical issues [HIL 07, HIL 99, AND 92].

This section starts with an overview on thermodynamic aspects considering phase transformations [HIL 98] [AGR 06] [POR 09] [GOU 15], in which the different equilibrium conditions, named as orthoequilibrium, local equilibrium (LE, LEP and LENP) and paraequilibrium, cited in the literature will be detailed. Thereafter, a description of physically based approaches for the phase transformations simulation will be provided.

3.1.2.1 Thermodynamics of allotropic phase transformation

During the phase transformation study, the effect of temperature as well as the role of alloying elements (C, Mn, Cr,...) allowed the knowledge of thermodynamic equilibria to be improved. Following this, several hypotheses for equilibria were developed on ternary systems in order to characterize the kinetics of systems that are not at equilibrium.

Orthoequilibrium, OE

Whatever the complexity of the studied system, for a constant temperature and pressure, the thermodynamic equilibrium condition is characterized by the minimum of the total Gibbs free energy (G) of the system. In the two-phase ($\alpha+\gamma$) domain, it is demonstrated that Gibbs energy in each phase is affected not only by temperature, but also by all involved chemical elements. For a binary system Fe-C, it is commonly accepted that the equilibrium corresponds to the common tangent of the Gibbs energy of each phase. This definition is extended in the case of complex systems containing N number of species by determining the tangent hyperplane in a space of N-dimensions. This thermodynamic equilibrium is also defined by the chemical potential equality between ferrite and austenite for all chemical elements. (*i.e.* Fe,C,X....):

$$\begin{cases} \mu_{Fe}^{\alpha} = \mu_{Fe}^{\gamma} \\ \mu_{C}^{\alpha} = \mu_{C}^{\gamma} \\ \mu_{X}^{\alpha} = \mu_{X}^{\gamma} \\ ... \end{cases} \tag{3.1}$$

The common tangent method can therefore be applied to the case of a ternary Fe-C-X system for which a plane ensuring an equality of the chemical potentials of Fe, C and X between ferrite and austenite is illustrated in Figure 3.5.(a). For the sake of simplicity, the ternary diagram is usually represented in an isothermal form as shown in Figure 3.5.(b)

Cette thèse est accessible à l'adresse : http://theses.insa-lyon.fr/publication/2020LYSEI120/these.pdf
© [A. MATHEVON], [2020], INSA Lyon, tous droits réservés

for a Fe-C-Mn system at 760 °C. Each green line corresponds to equilibrium conditions between the different phases. However, using the nominal composition of the steel (C_C^0, C_{Mn}^0) (identified by a star), a single operating tie-line is crossing the initial chemical composition which determines the equilibrium state reached after long heat treatments [SPE 81] (also called orthoequilibrium).

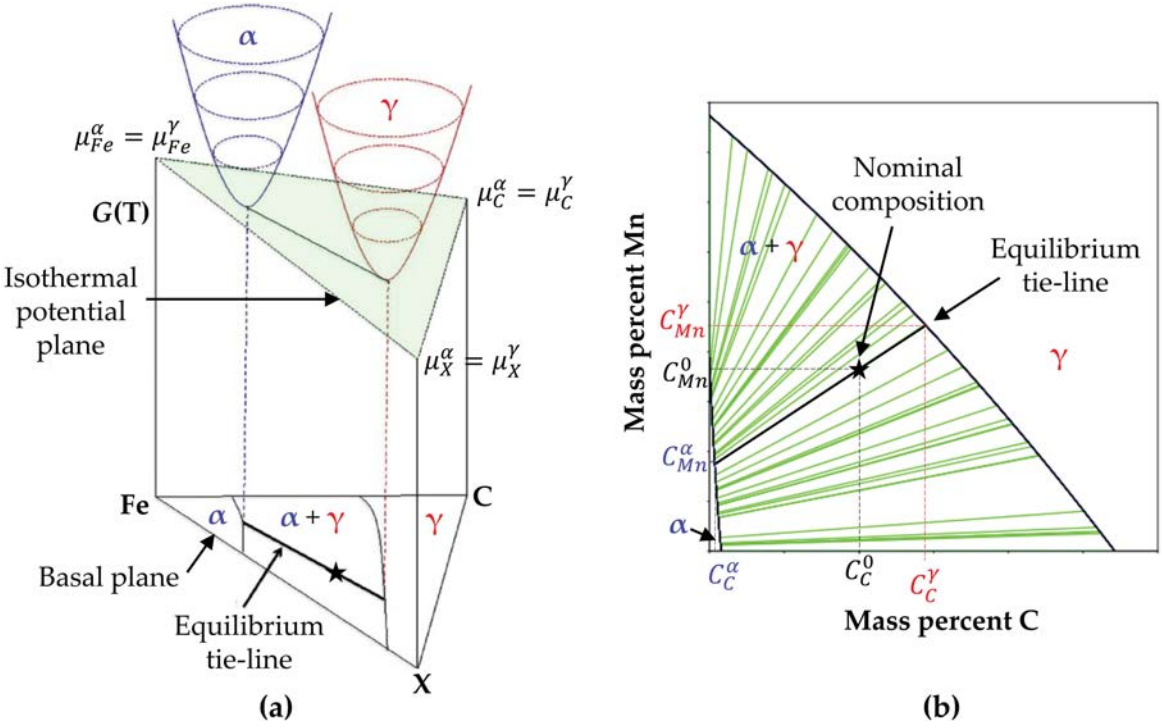

Figure 3.5: (a) 3D-schematic representation of Gibbs free energy diagram highlighting the iso-chemical potential plane [GOU 15]. (b) Isothermal section of Fe-C-Mn system at 760 °C. C $(C_C^{\alpha}, C_C^{\gamma})$ and Mn $(C_{Mn}^{\alpha}, C_{Mn}^{\gamma})$ equilibrium concentrations are emphasised for the nominal composition (C_C^0, C_{Mn}^0).

Intermediate equilibria

The orthoequilibrium defined earlier is only relevant when the entire system reaches equilibrium. However, practical applications usually involve or require the achievement of a transient equilibrium. In order to be able to reproduce the observed global kinetics, several examples of transient equilibrium were proposed in the literature.

Local equilibrium, LE

The local equilibrium is based on the respect of the equilibrium condition at the α/γ interface. It evolves during the phase transformation advancement and is only valid in ternary systems. The large difference of diffusivities $\left(\frac{D_C{}^{\gamma}}{D_X{}^{\gamma}}\right)$ between C and X elements induces a deviation from the orthoequilibrium tie-line to satisfy both (i) the respect of local equilibrium at the α/γ interface; and (ii) the same interface velocity of C and X.

Cette thèse est accessible à l'adresse : http://theses.insa-lyon.fr/publication/2020LYSEI120/these.pdf
© [A. MATHEVON], [2020], INSA Lyon, tous droits réservés

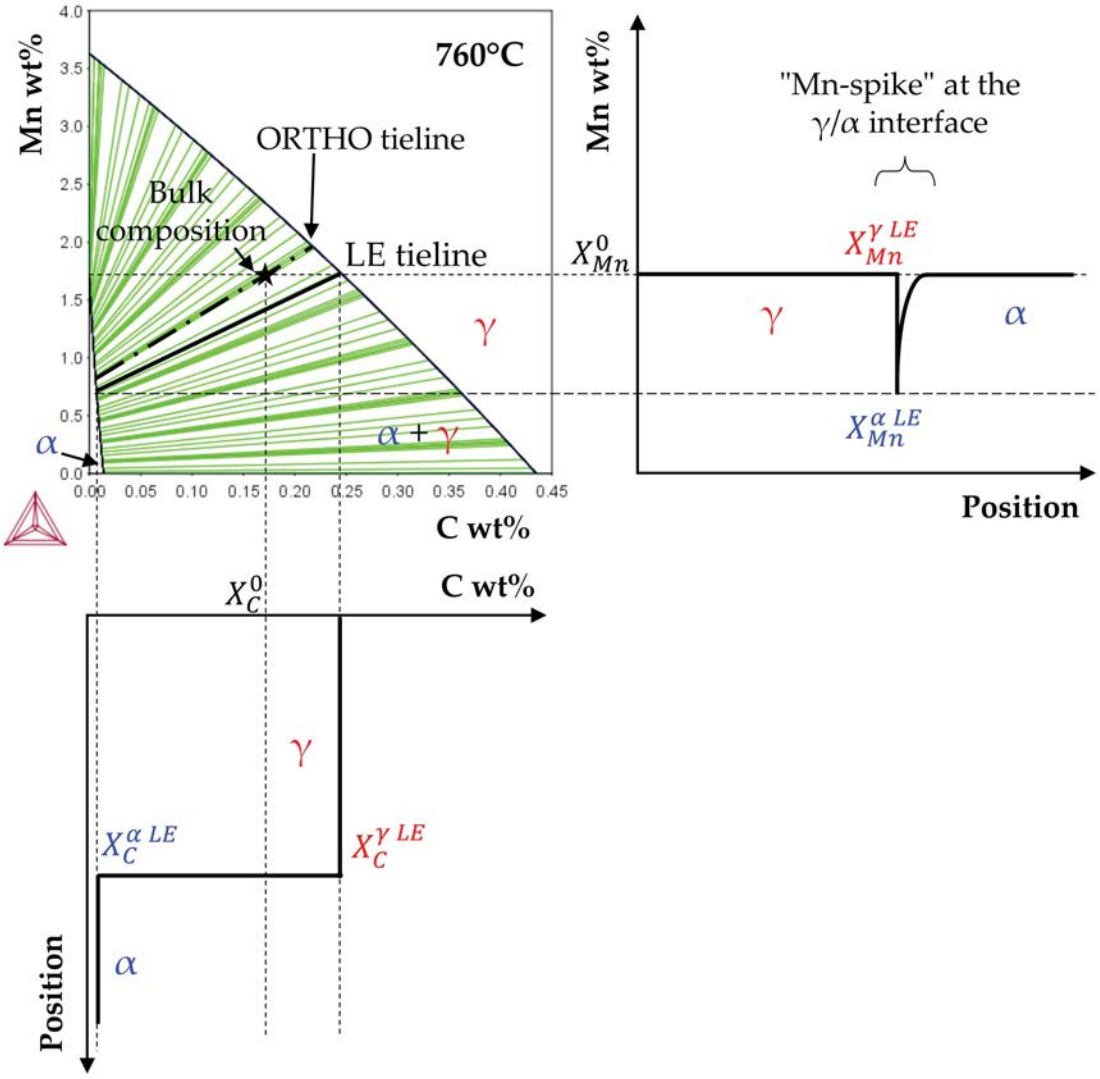

Figure 3.6: Isothermal section of the Fe-C-Mn system at 760 °C. C and Mn concentration profiles are reported for the $\alpha \rightarrow \gamma$ phase transformation according to the LENP condition. A characteristic Mn narrow "spike" is present at the γ/α interface.

Coates *et al.* [COA 72, COA 73] have even suggested to divide the local equilibrium into two parts, *i. e.*, LE with negligible partitioning (LENP) below the zero-partition line imposing for the growing phase a concentration of substitutional element X identical to the initial phase and LE with partitioning (LEP) above zero-partition line for $\gamma \rightarrow \alpha$ phase transformation. The LE condition was then applied to the $\alpha \rightarrow \gamma$ phase transformation and the tie-line corresponding to a local equilibrium assuming a low redistribution of manganese (*i.e.* industrial conditions with t<1h is represented in Figure 3.6 [WEI 13a, CHE 14b]. Since austenite is formed without manganese redistribution within the austenite, a manganese concentration spike is imposed to respect local equilibrium conditions at the α/γ interface. This condition will thus evolve throughout the transformation as a function of the global manganese diffusion within the different phases until

Cette thèse est accessible à l'adresse : http://theses.insa-lyon.fr/publication/2020LYSEI120/these.pdf
© [A. MATHEVON], [2020], INSA Lyon, tous droits réservés

the orthoequilibrium is reached.

Paraequilibrium, PE

Paraequilibrium is based on the assumption that the phase transformation is only driven by carbon diffusion while all other elements are supposed to be fixed [AGR 06]. Since only carbon can diffuse within the system, this means that only carbon is equalizing its chemical potential within ferrite and austenite:

$$\begin{cases} \mu_C^\alpha = \mu_C^\gamma \\ \mu_X^\gamma - \mu_X^\alpha = \frac{X_{Fe}}{X_X}\left(\mu_{Fe}^\gamma - \mu_{Fe}^\alpha\right) \end{cases} \tag{3.2}$$

with X_{Fe} and X_X respectively the iron and X mole fractions.

Figure 3.7 shows the Gibbs energy diagram for PE conditions and the corresponding isothermal diagram which differs from the local equilibrium with only horizontally tie-lines due to the assumption of substitutional element immobility. This is why, paraequilibrium can only be applied for short treatment times or fast kinetics in which manganese is not allowed to diffuse. Furthermore, a transition of interface equilibrium is necessary to reach the final orthoequilibrium in the case of austenite formation in the intercritical domain.

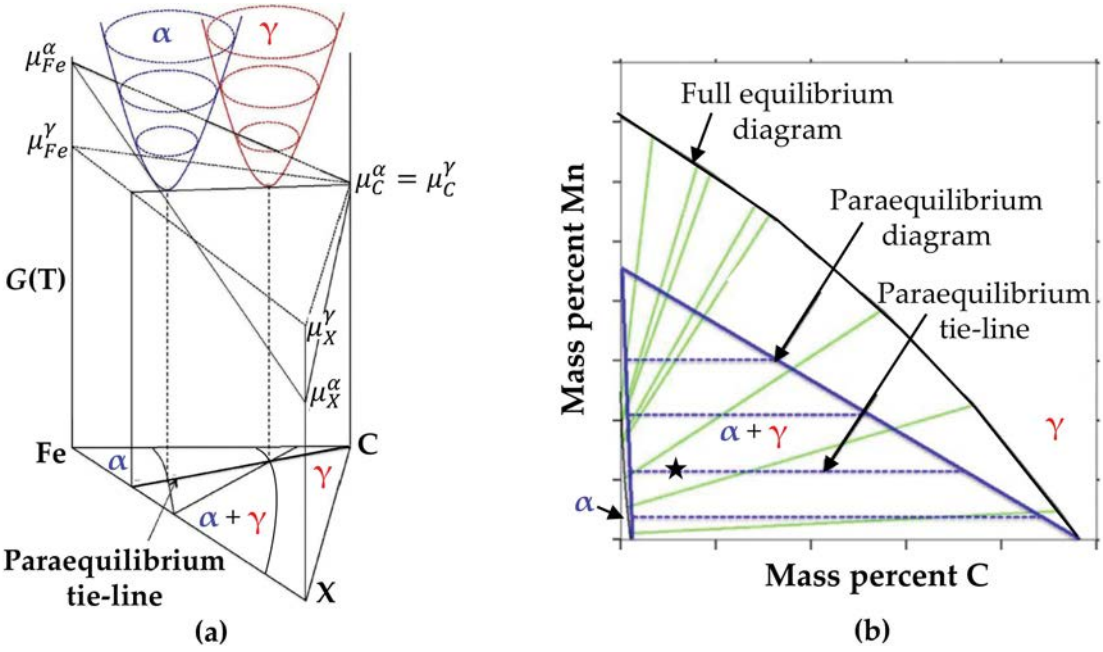

Figure 3.7: Schematical representation of (a) the Gibbs free energy diagram and (b) the phase diagram in the case of the $\gamma \rightarrow \alpha$ transformation supposing PE condition.

Cette thèse est accessible à l'adresse : http://theses.insa-lyon.fr/publication/2020LYSEI120/these.pdf
© [A. MATHEVON], [2020], INSA Lyon, tous droits réservés

3.1.2.2 Physically based modelling

Although empirical models and different types of transient equilibria are useful, their generalizations for different temperature or chemical composition ranges are difficult because of their lack of physical assumptions. The objective of this section is to list the different approaches developed in the literature for phase transformation prediction.

Diffusion-controlled model

The phase transformation can be modelled by taking into account only the diffusivity of the transformation [AKB 94]. The interface is thus defined as a sharp interface respecting the local equilibrium conditions on both sides of the interface. The allotropic transformation kinetics is thus driven by the respect of local equilibrium conditions at the interface and an interface velocity equality for the different elements. From a practical point of view, the model is therefore based on the resolution of the Fick equation in each phase with the following relationship:

$$\frac{\partial C_i}{\partial t} = D_{i,j} \frac{\partial^2 C_i}{\partial z^2} \tag{3.3}$$

with $D_{i,j}$ and C_i respectively the diffusion coefficient and concentration of i element in the phase j.

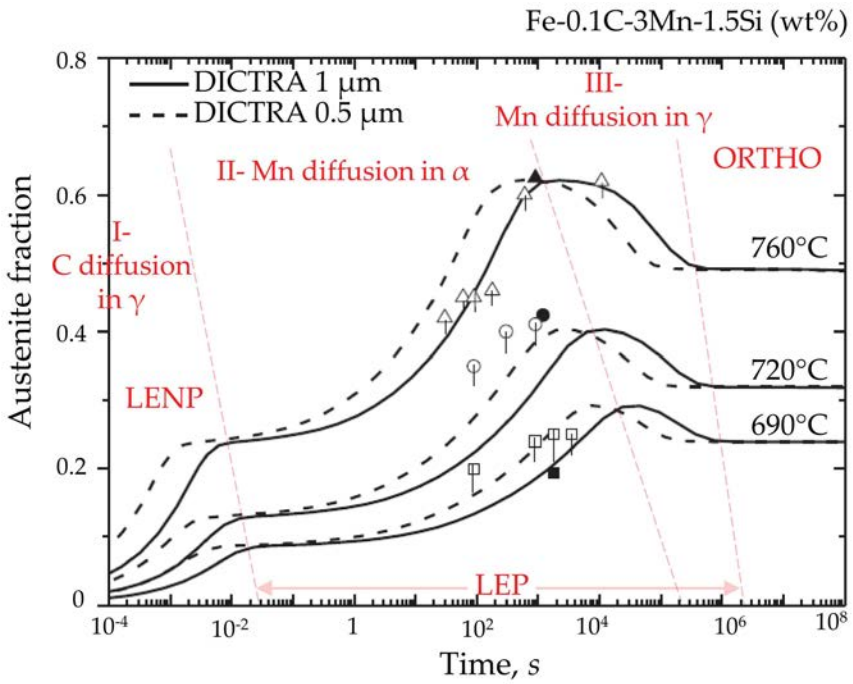

Figure 3.8: Model and experimental kinetics of austenite formation during isothermal holding of a quaternary Fe-0.1C-3Mn-1.5Si (wt%) alloy [WEI 13a]. The ORTHO equilibrium is achieved after 10^6 s. Intermediate equilibriums are reported (*i.e.* LENP and LEP).

Cette thèse est accessible à l'adresse : http://theses.insa-lyon.fr/publication/2020LYSEI120/these.pdf
© [A. MATHEVON], [2020], INSA Lyon, tous droits réservés

The interface velocity v is therefore expressed from a mass balance for each elements as follows:

$$v = \frac{dz}{dt} = \frac{J_{i,\gamma} - J_{i,\alpha}}{C^{eq}_{i,\gamma} - C^{eq}_{i,\alpha}} \tag{3.4}$$

where $J_{i,\alpha}$ and $J_{i\gamma}$ are fluxes of i at ferrite and austenite side of the interface. $C^{eq}_{i\gamma}$ and $C^{eq}_{i,\alpha}$ correspond to the solubility limits of i element which are determined thanks to thermodynamics.

Thermocalc diffusion module (DICTRA) is based on LE assumptions [AND 02] and the equilibrium conditions are obtained using CALPHAD methods. DICTRA allow the different steps of austenite formation kinetics to be reproduced. As can be seen in Figure 3.8: first stage, below 10^{-2} s, driven by carbon diffusion with negligible Mn partitioning (*i.e.* LENP); (ii) second stage ($10^{-2} - 10^{3}$ s) controlled by Mn diffusion in ferrite; (iii) third stage ($10^{3} - 10^{5}$ s) controlled by Mn diffusion in austenite (*i.e.* LEP); and finally (iv) the orthoequilibrium.

Although the LE model can reproduce a large number of experiments ranging from austenite formation during intercritical heating, ferrite precipitation to decarburization [ZUR 12, QIU 13, LIU 13, CHE 14c, CHA 19, LAI 16, WEI 13a], several authors have observed deviations of the local equilibrium mainly on Fe-C-Ni alloys that LE model cannot reproduce [OI 00, HUT 04]. Moreover, its extension to more complex systems and the integration of cementite dissolution generally leads to numerical problems, although recently Marceaux *et al.* have succeeded in modelling the austenite formation on a quaternary Fe-C-Mn-Cr alloy during heating treatment at 1 °C/s (see Figure 3.9)[MAR 20c].

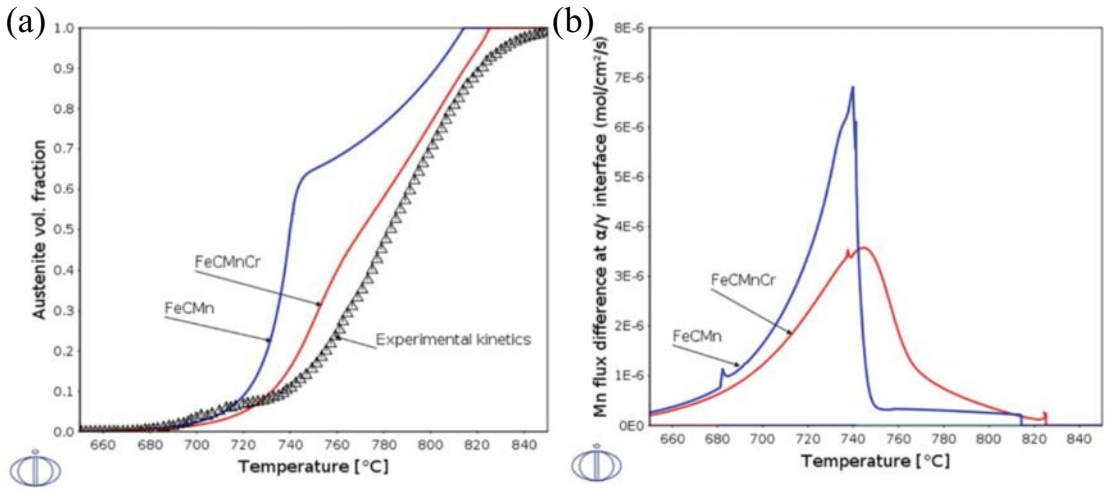

Figure 3.9: a) Comparison of simulated (Fe–C–Mn and Fe–C–Mn–Cr system) and experimental austenite formation kinetics with 1°C/s heating rate (by dilatometry) b) Evolution of Mn flux difference ΔJ_{Mn} at α/γ interface during heat treatment [MAR 20c].

Cette thèse est accessible à l'adresse : http://theses.insa-lyon.fr/publication/2020LYSEI120/these.pdf
© [A. MATHEVON], [2020], INSA Lyon, tous droits réservés

Mixed mode model

Mixed-mode models overcome the problem of solving complex multiple element diffusion profiles by introducing the concept of interface mobility [CHR 81a], with its own kinetics. The transformation kinetics is hence managed by the interface velocity which depends on the deviation of the interface conditions from equilibrium as expressed below:

$$v = M \times \chi(T) \times \left(C_{C,\gamma}^{Int} - C_{C,\gamma}^{Eq} \right) \tag{3.5}$$

with $C_{C,\gamma}^{Int}$ and $C_{C,\gamma}^{Eq}$ corresponding respectively to the interfacial and equilibrium carbon content in austenite. $\chi(T)$ is a temperature dependent parameter. The interface mobility M is usually assumed to follow an Arrhenius law:

$$M = M_0 \exp\left(-\frac{Q}{RT}\right) \tag{3.6}$$

with Q the activation energy and M_0 a mobility constant. Figure 3.10 presents an illustration of the carbon profile evolution in the mixed-mode model for different transformation times [MEC 15]. This approach makes it possible to reproduce experimental kinetics [KRI 97, SIE 04, BOS 07, BOS 09, OLL 18], but the mobility applied to take into account the interaction of other elements has no physical meaning, limiting thus predictive capacities of such models.

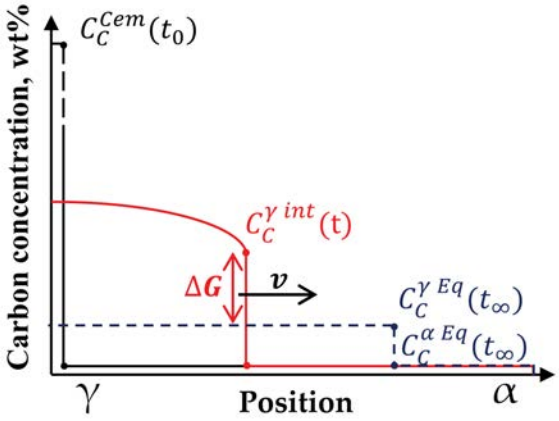

Figure 3.10: Schematic representation of the mixed-mode model system [OLL 17b]. Carbon concentration profiles are plotted at different times: at t_0, at an intermediate time t and at the infinite time t_∞(for which the γ/α equilibrium is reached). The interface velocity is evaluated as the deviation to the equilibrium by the relation $v = M \times \Delta G$ with $\Delta G = \chi(T) \times \left(C_{C,\gamma}^{Int} - C_{C,\gamma}^{Eq} \right)$.

Solute drag model

Another family of models assumes a quasi-permanent regime at the interface, where the transformation kinetics is driven by the balance between energy dissipation and driving force [ZUR 12, CHE 14c] allowing to reproduce the non-equilibrium interface condition in diffusion-controlled phase transformations. Zurob *et al.* [ZUR 12] were thus able to

Cette thèse est accessible à l'adresse : http://theses.insa-lyon.fr/publication/2020LYSEI120/these.pdf
© [A. MATHEVON], [2020], INSA Lyon, tous droits réservés

model the non-partitioning planar ferrite growth from alloyed austenite for different types of Fe-C-X ternary systems (X = Mn, Ni, Mo) and thus provide a physical explanation of the transition between the PE model and the LENP model observed during experimental decarburization kinetics (see Figure 3.11.(a). In parallel, [CHE 14a] have successfully captured the phenomenon of "stasis transformation" during the isothermal formation of bainitic ferrite for a wide range of Fe-C-X ternary alloys (X = Mo, Ni, Si) by taking into account the energy dissipation by element diffusion *trans*-interface. Figure 3.11.(b) shows both the energy dissipation curve within the interface and the chemical energy available for the transformation decreasing as the transformation progresses to a fraction of 90% bainite from which the kinetic transition is observed.

In spite of their various applications [QIU 13, LÜC 57, CAH 62, HIL 76, SVO 02, ODQ 03], the diffusion of X within the bulk is generally neglected which can be necessary in some case (e.g. cyclic transformation) [CHE 11, CHE 13a, CHE 13b, CHE 13c, CHE 16]. In addition, the need to define and calibrate interface properties and their difficulty in extrapolating them in the case of multi-component alloys limits the model's prediction capabilities [QIU 15].

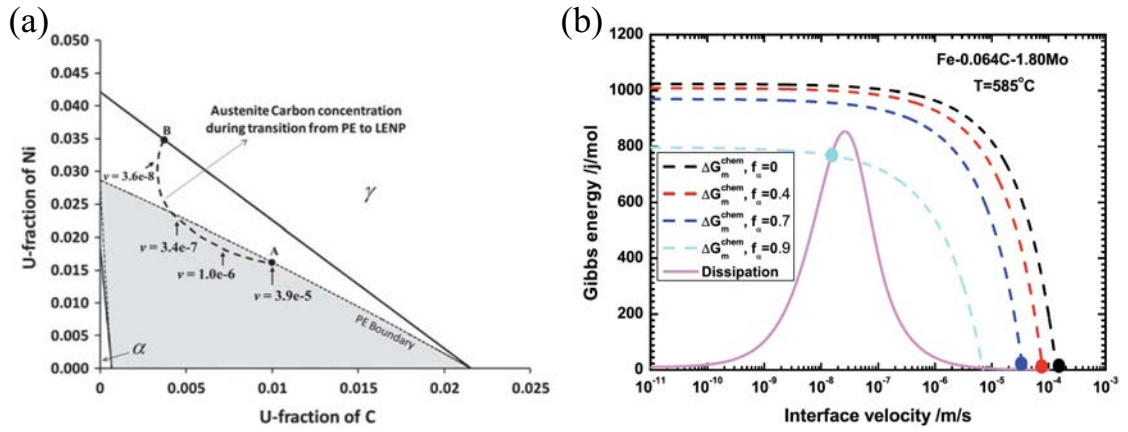

Figure 3.11: a) Isothermal sections for Fe-Ni-C at 775 °C. Path taken by the system is shown along with arrows indicating interface velocity (m/s) [ZUR 12]. b) The total dissipation and the available chemical driving force for the isothermal bainite transformation in the Fe-0.064C-1.80Mo alloy at 585 °C [CHE 14a].

Phase-Field model

Phase Field (PF) model [MIL 11] are used to model austenite formation during a heating within a ferrite-pearlite matrix [PER 14, RUD 11, RUD 12, ZHU 15], cyclic phase transformations in Fe-C-Mn alloys [CHE 16] and banding in steels due to manganese microsegregation [MAA 16]. The PF approach is nevertheless based on a mathematical approach that aims to smooth interface and interpolate the properties of each phase within the interface, posing the problem of the real *vs* modelled interface characteristic size. Benefits of phase-field method consist in the possibility to be easily extended to 2-D or 3-D systems, although model assumptions often need to be simplified, as they generally neglect the diffusion of chemical elements across the interface or in the bulk.

Cette thèse est accessible à l'adresse : http://theses.insa-lyon.fr/publication/2020LYSEI120/these.pdf
© [A. MATHEVON], [2020], INSA Lyon, tous droits réservés

Thermodynamic extremal principle

Recently, the thermodynamic extremal principle was developed to solve the complex additional constraints and derive the evolution equations in multi-component alloys [SVO 04, GAM 07, FIS 14, KUA 16]. Kuang *et al.* used thermodynamic extremal principle model [KUA 18], in which trans-interface diffusion, interface migration and bulk diffusion of C and X are integrated. Figure 3.12.(a) shows the ability of this model to reproduce different transition trajectories at the interface during ferrite formation for isothermal treatment at 670 °C in Fe-0.217C-2.17Mn. Its validation has been extended for cyclic phase transformation in the Fe-0.023C-0.17Mn. Figure 3.12.(b) highlights its capability to reproduce stagnant phases during the cycle due to manganese partitioning at the interface as well as the inverse phase transformation stage. However, thermodynamic extremal principle model to our knowledge was never coupled to the cementite dissolution during annealing treatment and to the phase transformation prediction with 2 interfaces.

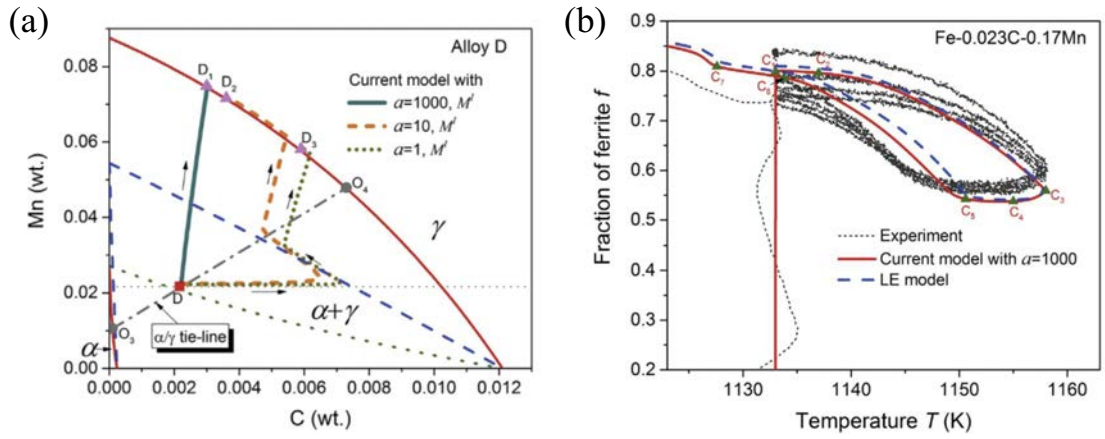

Figure 3.12: a) Transition trajectories of compositions of γ at the interface on the isothermal section of the Fe-C-Mn phase diagram at 943 K for phase transformations in Fe-0.217C-2.17Mn b) Evolution of the ferrite volume fraction for the cyclic phase transformation in the Fe-0.023C-0.17Mn alloy. Thermodynamic extremal principle model with a=1000, where $C_1 \rightarrow C_2$ and $C_4 \rightarrow C_5$are the stagnant stages, $C2 \rightarrow C_3$ and $C_5 \rightarrow C_6$ are the regular phase transformation stages, $C_3 \rightarrow C_4$ is the inverse phase transformation stage. [KUA 18]

3.1.3 Conclusion: Objective of the present chapter

Thermodynamic equilibria or mixed mode models are interesting to reproduce some experimental kinetics but the lack of physics ingredients limits their extensions for a wide range of chemical compositions. The other types of models allow to reproduce a large number of applications, but an adjustment of different parameters or a difficulty in the prediction of the $\alpha \leftrightarrow \gamma$ transformation is generally observed. In addition, the assumptions of the different models, imposing often a diffusion system for each phase and linking equations, can be problematic when extending the models for complex systems, non-isothermal heating or the additional cementite introduction.

From this assessment, the objective of this study was to create a physical-based model likely to reproduce the $\alpha \leftrightarrow \gamma$ transformation for a wide range of chemical compositions

Cette thèse est accessible à l'adresse : http://theses.insa-lyon.fr/publication/2020LYSEI120/these.pdf
© [A. MATHEVON], [2020], INSA Lyon, tous droits réservés

and microstructural parameters. After an investigation of the different numerical parameters effect on the resolution, the GEM model was compared to DICTRA for austenite formation during isothermal heating. The interest of introducing the cementite dissolution for austenite formation during isothermal or non-isothermal heating was then discussed in relation to the work done by Gouné *et al.*. [GOU 12]. An experimental comparison carried out on ternary Fe-C-Mn steels during a complex cycle (heating with a 5 °C/s heating rate followed by isothermal holding) has allowed us to validate the model's ability to capture the effect of temperature and of chemical composition. The interest of modelling a quaternary system and introducing an interaction with the recrystallization phenomenon was respectively discussed with DP600 and DP1000 steels. Finally, the ability of the model to reproduce the reverse $\gamma \rightarrow \alpha$ transformation by avoiding nucleation problems was performed on experimental kinetics of decarburization [ZUR 12, SUN 17, QIU 15, PAN 15] and cyclic transformation [CHE 16] of the literature.

3.2 Materials and procedures

This study was carried out on the four ternary Fe–C–Mn steels prepared in laboratory and on the two industrial Dual-Phase steels presented in Section 1.2. Their chemical composition is recalled in Table 3.1. The initial microstructures (obtained either after forging or cold-rolling) of the studied steels were presented in Figure 1.1 (see Chapter 1).

Steel grades	Chemical composition C_i^0 (in wt.%)						Pearlitic zone half-spacing L (μm)	Cementite enrichment (wt.%)	
	C	Mn	Cr	Si	Nb	Ti		Mn	Cr
Ternary steels	0.17	0.5	-	-	-	-	25	1*	-
	0.17	1.7	-	-	-	-	20	2	-
	0.17	2.5	-	-	-	-	12	4*	-
	0.08	1.7	-	-	-	-	30	2*	-
DP600	0.09	1.5	0.5	0.3	-	-	15	12	6.5
DP1000-CR	0.17	1.7	0.4	0.3	0.03	0.03	5	10	4
DP1000-ReX	0.17	1.7	0.4	0.3	0.03	0.03	10	13	7

Table 3.1: Chemical composition and microstructural informations of the ternary and industrial steels investigated in this study.

For the ternary steels, the increase in carbon and manganese content leads to a refinement of the initial microstructure. In comparison, the initial ferritic grain size of the industrial steels is much smaller due to hot rolling process and elongated in cold-rolled direction. The average distance between pearlitic zones was determined by image analysis using the *ImageJ* software from the various micrographs and is summarized in Table 3.1. In addition, the chemical composition of the cementite islands was measured by EDS analysis using carbon replicas and it is summarized in Table 3.1. A significant enrichment in substitutional elements such as manganese and chromium was observed in the case of industrial steels, as outlined in Table 3.1 whereas a chemical composition of the cementite close to the nominal content is observed for ternary Fe-C-Mn steels. This

Cette thèse est accessible à l'adresse : http://theses.insa-lyon.fr/publication/2020LYSEI120/these.pdf
© [A. MATHEVON], [2020], INSA Lyon, tous droits réservés

enrichment comes from the coiling step which is associated with a very slow cooling (10-20 °C/h) allowing the substitutional elements to diffuse over a long distance and with a thermodynamic equilibrium predicting high concentrations (15-25% for manganese) for industrial steels. Additional enrichment is noticed in the case of the DP1000-ReX due to the additional heat treatment of 20 min at 700 °C required for prior recrystallization.

In order to reproduce the heat treatments used industrially, complex cycles including a 5 °C/s heating ramp followed by a 300s step at the temperature of the intercritical stage were performed before a heating to 950 °C used to complete the phase transformation. The phase transformation kinetics during intercritical annealing and complex cycle were performed on a Gleeble 3500 thermodynamic simulator and determined by in-situ optical dilatometry under a secondary vacuum of $\sim 10^{-4}$ bar pressure to avoid sample oxidation and decarburization. The tangent method was then used to determine the phase transformation kinetics assuming that each phase has a unique dilatation coefficient (see Section 1.3.3.1).

3.3 Gibbs Energy Minimization model

The model described in this work is based on the prediction of (i) concentration profiles for all elements in ferrite, cementite and austenite, and (ii) interface migration, thanks to the minimization of the total Gibbs energy in the entire system (*i.e.* phase field approach). The GEM model aims at solving a unique diffusion profile within 3 phases (*i.e.* cementite, ferrite and austenite). In this study, it has been applied to model the $\alpha + (\mathrm{Fe, Mn, Cr})_3\mathrm{C} \rightarrow \gamma$ phase transformation over complex thermal cycles for Fe-C-Mn and Fe-C-Mn-Cr systems with cementite dissolution and $\alpha \leftrightarrow \gamma$ phase transformation. A full description of the model will be given in this section.

3.3.1 Definition of a representative system

In order to model the kinetics of austenite formation with the best accuracy, a discussion was dedicated to the choice of a representative simulation state.

3.3.1.1 Geometry and characteristic lengths

Based on the knowledge of austenite formation kinetics, several systems vave been suggested to model austenite formation kinetics (see Figure 3.13):

(i) **Austenite growth within ferrite bands** can occur with a characteristic size system equal to the half-length between pearlite rich zones. This microstructure can be modelled with a linear geometry representing the cementite dissolution and austenite growth between the pearlite bands.

(ii) **Dissolution of cementite lamellae** can be modelled as a sub-system for austenite formation. A linear geometry can be considered with a characteristic size equal to half the length of the cementite lamellae spacing assuming nucleation at the cementite/ferrite interfaces. Due to the small system size, this modelling choice generally leads to a very fast austenite formation.

Cette thèse est accessible à l'adresse : http://theses.insa-lyon.fr/publication/2020LYSEI120/these.pdf
© [A. MATHEVON], [2020], INSA Lyon, tous droits réservés

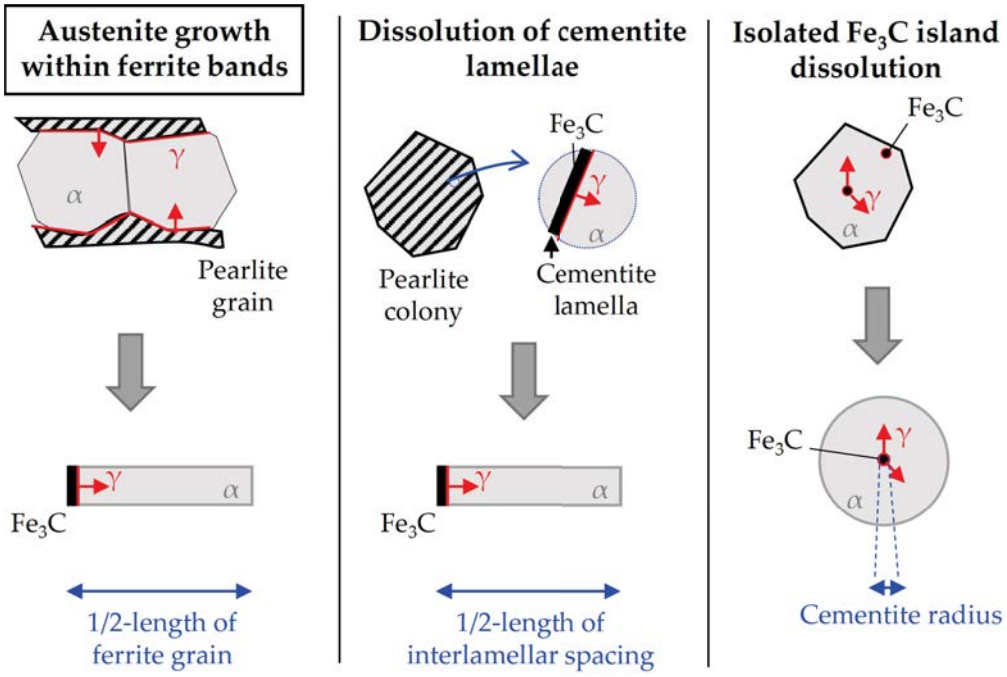

Figure 3.13: Schematic representation of three different modelling configurations: (i) austenite growth within ferrite bands; (ii) cementite lamellae dissolution and (iii) isolated carbide dissolution [OLL 17b]

(iii) **Isolated cementite dissolution** can also be considered as a system for austenite formation. This choice leads to a 1-D system with a spherical geometry starting from a fixed cementite radius. Nevertheless a homogeneous distribution of the cementite islands within the microstructure is necessary to validate the choice of this system.

In fact, a competition between these different representations takes place and each suggested system is likely to be involved in austenite formation.

In this work, it was chosen to work in the system describing the austenite growth within ferrite bands. This system is valid for industrial steels due to cold-rolling and segregation bands of alloying elements during cooling. However, for ternary alloys, the modelling choice is more questionable since the initial states contain mostly heterogeneously distributed pearlite zones. The formation of austenite within the pearlite bands was nevertheless applied to all steels by defining an average distance between the different pearlitic zones by image analysis leading to the results of Table 3.1.

3.3.1.2 Description of the different simulation configurations

The present work aims at modelling the austenite formation kinetics with or without cementite dissolution starting from a ferritic-pearlitic structure during complex-cycle.

The real ferritic-pearlitic microstructure is assimilated to a linear 1-D system, composed of cementite and ferrite (see Figure 3.14.(a)). The total size of the system L corresponds to the half-length between the pearlitic zones measured experimentally and summarized in Table 3.1. This system is modelled using a nodal method composed of nn nodes with a

Cette thèse est accessible à l'adresse : http://theses.insa-lyon.fr/publication/2020LYSEI120/these.pdf
© [A. MATHEVON], [2020], INSA Lyon, tous droits réservés

dx space step. The fraction of cementite in the initial state $f^0_{M_3C}$ is calculated by applying a mass balance with the system equilibrium carbon concentrations in cementite and ferrite (respectively $C^0_{C,M_3C} = 6.7$ wt% and $C^0_{C,\alpha} = 6.683 \times 10^{-3}$ wt%). The concentration of alloying elements in cementite is imposed according to the EDS analysis performed on the different carbides. The initial concentration of alloying elements within ferrite is then finally determined for each steel with a mass balance based on the cementite fraction and its content of alloying elements.

From a numerical point of view, 2 types of configurations for initial states have been considered for the simulation (see Figure 3.14.(b-c)):

- (**Configuration 1 interface: Without cementite dissolution**): The first configuration without cementite dissolution was used to calibrate the model simulation parameters and to benchmark it against other types of models. The common hypothesis used for austenite formation modelling in isothermal treatment is to assume an instantaneous cementite dissolution, valid from a critical temperature dependent on the cementite enrichment according to Gouné *et al.* [GOU 12] (see Figure 3.3.(a)). This choice makes it possible to simplify the system by conserving only austenite and ferrite with an interface of width δ whose influence will be studied later. The initial austenite fraction as well as its chemical composition in alloying elements is identical to that of cementite in the initial configuration. Finally, the concentrations of initial alloying elements within the γ/α interface and ferrite are identical to that of ferrite in the initial configuration. .
- (**Configuration 2 interfaces: With cementite dissolution**): The second configuration involves the presence of cementite in the initial states and leads to 3 phases and 2 interfaces in the system. The cementite fraction calculated in the initial configuration includes the cementite and the M_3C/γ interface with a chemical composition equal to that of the cementite in the initial configuration. For the numerical resolution, an initial austenite node is required for the growth of the austenitic phase. Finally, the initial concentration of alloying elements within the austenite node, the γ/α interface and the ferrite are identical to that of the ferrite in the initial configuration.

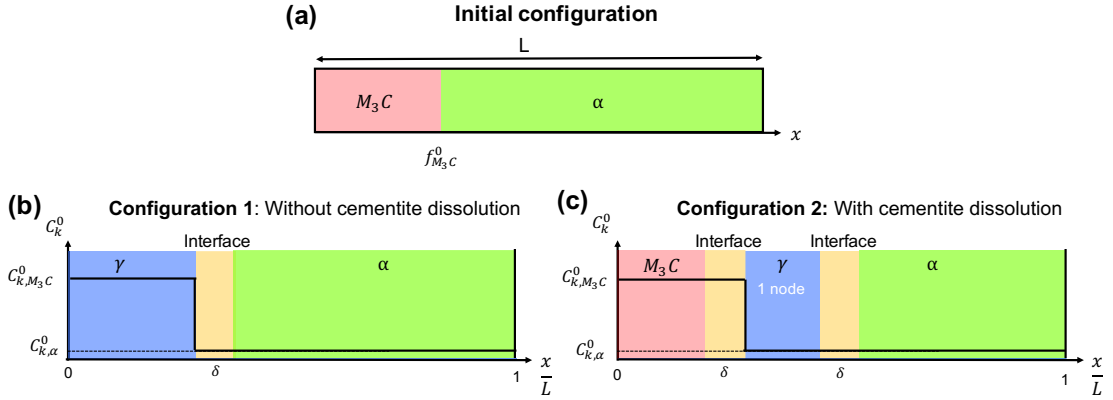

Figure 3.14: (a) Description of the schematization for the real microstructure. Description of the 2 initial configurations used during this study (b) without cementite dissolution and (c) with cementite dissolution.

Cette thèse est accessible à l'adresse : http://theses.insa-lyon.fr/publication/2020LYSEI120/these.pdf
© [A. MATHEVON], [2020], INSA Lyon, tous droits réservés

3.3.2 Diffusion equation

The $\alpha \leftrightarrow \gamma$ phase transformation is driven by the diffusion of alloying elements (carbon, manganese, chromium, *etc.*) between the different phases, according to their respective chemical potential. The alloying element concentration evolution within the system can be defined in 1-D for each element k, in phase j by the following equation:

$$\frac{\partial}{\partial x}\left(\frac{D_{k,j}C_k}{RT}\frac{\partial \mu_{k,j}}{\partial x}\right) = \frac{\partial C_k}{\partial t} \tag{3.7}$$

where C_k is the mass concentration of element k, T is the temperature, x is the position, R is the ideal gas constant, $D_{k,j}$ is the diffusion coefficient and $\mu_{k,j}$ is the chemical potential of element k in phase j. In addition, assuming an ideal solution, each chemical potential depends exclusively on the standard chemical potential for pure iron in phase j ($\mu^0_{k,j}$) and the concentration of this element k according to the following relation:

$$\mu_{k,j} = \mu^0_{k,j} + RT\ln(C_k) \tag{3.8}$$

The diffusion equation providing the concentration profiles of each chemical element k in 1-D is extended to the whole system in a fixed reference frame (Eulerian scheme). Combining Equation 3.7 and Equation 3.8 leads to:

$$\frac{\partial}{\partial x}\left(D_{k,j}\frac{\partial C_k}{\partial x} + \frac{C_k D_{k,j}}{RT}\frac{\partial \mu^0_{k,j}}{\partial x}\right) = \frac{\partial C_k}{\partial t} \tag{3.9}$$

In their Gibbs Energy Balance model, Chen *et al.* [CHE 14c] used a modified Fick's equation to model diffusion profiles within a mobile interface with chemical potential gradients. Here, velocity does not appear explicitly in Equation (3.9) because we use a Eulerian specification (fixed integration grid), whereas Chen *et al.* used a Lagrangian specification (following the interface).

The studied system is closed and boundary conditions are:

$$\left.\frac{\partial C_k}{\partial x}\right|_{x=0^-,L^+} = 0 \text{ (closed)} \tag{3.10}$$

Within the interfaces of size δ, the chemical potential is supposed to vary linearly between the chemical potential of ferrite ($\mu^0_{k,\alpha}$), austenite ($\mu^0_{k,\gamma}$) and cementite (μ^0_{k,M_3C}). (see Figure 3.15.(a)).

Equation (3.9) is equivalent to the classical Fick's law outside the interface ($\partial\mu^0_{k,j}/\partial x = 0$), where chemical element fluxes occur to remove the concentration gradients in each phase.

The standard potential difference between each phase leads to a flux of alloying elements and thus drives the phase transformation. Contrary to local equilibrium models, no chemical composition is imposed at each phase boundary. The concentration profile of each chemical element is established independently of other elements.

Diffusion coefficients of element k inside the M_3C/γ interface are fixed and equal to their values in austenite.

Cette thèse est accessible à l'adresse : http://theses.insa-lyon.fr/publication/2020LYSEI120/these.pdf
© [A. MATHEVON], [2020], INSA Lyon, tous droits réservés

The diffusion coefficient of element k inside the α/γ interface $D^{Int}_{k,\alpha/\gamma}$ is not easy to measure due to the dependence on the interface properties and is generally fitted in the literature. Nevertheless, many studies have shown a diffusion coefficient increase within the interface [Fri 69, SMI 78], which led us to define the diffusion coefficient within the interface as follows:

$$D^{Int}_{k,\alpha/\gamma} = aD_{k,\alpha} \tag{3.11}$$

where a is a constant modifying the diffusion coefficient within the interface compared to bulk diffusion coefficient in ferrite $D_{k,\alpha}$. A value of parameter $a = 1$ will allow a fast diffusion within the interface equal to that of bulk ferrite (approaching sharp interface conditions), whereas $a = \frac{1}{100}$ will rather approach para-equilibrium conditions with a diffusion coefficient in the interface close to that of bulk austenite. Effect of this parameter on the transformation kinetics will be detailed in Section 3.4.1.1.

3.3.3 Gibbs energy calculation

The local Gibbs energy of a given phase is the weighted sum of the partial molar Gibbs energies (chemical potentials $\mu_{k,j}$) of each element, given by Gibbs-Duhem relation. For the sake of computational time, it is assumed here that the energy of a multi-component system (*e.g.* FeXY) is the linear combination of the energy of binary systems (FeX+FeY) composing the multi-component system. This hypothesis leads to a modified expression for the Gibbs energy:

$$G|_i = \mu^0_{\mathrm{Fe},j} + \sum_k \left[\mu^B_{\mathrm{Fe},j}(X_k) \cdot (1 - X_k) + \mu^B_{k,j}(X_k) \cdot X_k - \mu^0_{\mathrm{Fe},j}\right] \tag{3.12}$$

where $\mu^0_{\mathrm{Fe},j}$ is the chemical potential of pure iron in phase j, $\mu^B_{\mathrm{Fe},j}(X_k)$ and $\mu^B_{k,j}(X_k)$ are the chemical potentials of iron and element k in a binary Fe/k system of composition X_k in phase j (α or γ).

With such an approach, the energy of a multi-component system containing n elements only requires the knowledge of n binary databases, that can be calculated from TCFE8 Thermocalc database *a priori*. In other words, cross interaction terms between substitutional alloying elements are neglected with such a linear assumption.

A validation test was carried out to compare the use of Gibbs-Duhem equation (using TQ interface and TCFE8 database) instead of Equation (3.12). It led to less than 3% error on the phase fractions at the final equilibrium for a 0.17C − 1.7Mn steel at 780 °C. Despite providing exact fractions predicted by TCFE8 database, the complete coupling (Gibbs-Duhem equation and TQ interface) suffers from intractable computational times. This is why we use Equation (3.12) to previously generate a database from TCFE8.

These conditions are valid in all applications presented hereafter because they are limited to rather low-alloy compositions. For more concentrated alloys, an additional term or new Gibbs energy interpolation method should be considered.

In the same time, the local Gibbs energy of cementite was extracted from the TCFE8 Thermocalc database according to its chromium and manganese enrichment.

Cette thèse est accessible à l'adresse : http://theses.insa-lyon.fr/publication/2020LYSEI120/these.pdf
© [A. MATHEVON], [2020], INSA Lyon, tous droits réservés

The weighted sum of the Gibbs energies over all nodes gives the total energy of the system as follows:

$$G^{tot} = \sum_i G|_i \tag{3.13}$$

The total gibbs energy of the system will be the potential function, that will be minimized when considering interface motion.

3.3.4 Interface motion calculation

The interface displacement is based on total Gibbs Energy Minimization (GEM) with respect to the interface position according to the chosen configuration:

$$\textbf{Configuration 1, interface}: \frac{\partial G^{tot}}{\partial x_{\gamma/\alpha}} = 0 \tag{3.14}$$

$$\textbf{Configuration 2, interfaces}: \frac{\partial G^{tot}}{\partial x_{M_3C/\gamma}} = \frac{\partial G^{tot}}{\partial x_{\gamma/\alpha}} = 0 \tag{3.15}$$

where $x_{M_3C/\gamma}$ and $x_{\gamma/\alpha}$ are the positions of the two interfaces within the system. Depending on the configuration chosen, the system consists of one or two independent interfaces (*i.e.* M_3C/γ and γ/α) which have the freedom to move in such a way to minimize the system's total energy for a given time step.

3.3.5 Numerical implementation

This section aims at describing the numerical resolution used for the phase transformation $\alpha \leftrightarrow \gamma$ with a nodal 1-D method. The diffusion equation (see Equation 3.9) is solved using 1-D implicit scheme for each element k. The numerical schemes choice for the different derivatives leads to the following discretized equation for each node i

$$\begin{aligned}
&\frac{C_k|_i^{t+\Delta t} - C_k|_i^t}{\Delta t} \\
&= \frac{D_{k,j}|_i \left(C_k|_{i+1}^{t+\Delta t} - C_k|_i^{t+\Delta t}\right) + D_{k,j}|_{i-1} \left(C_k|_{i-1}^{t+\Delta t} - C_k|_i^{t+\Delta t}\right)}{\Delta x^2} \\
&+ \frac{D_{k,j}|_{i+1}\, C_k|_{i+1}^{t+\Delta t} \left(\mu_{k,j}^0\Big|_{i+1} - \mu_{k,j}^0\Big|_i\right) - D_{k,j}|_i\, C_k|_i^{t+\Delta t} \left(\mu_{k,j}^0\Big|_i - \mu_{k,j}^0\Big|_{i-1}\right)}{RT\Delta x^2}
\end{aligned} \tag{3.16}$$

This discretization coupled with the boundary conditions makes it necessary to solve for each chemical element k the following system:

Cette thèse est accessible à l'adresse : http://theses.insa-lyon.fr/publication/2020LYSEI120/these.pdf
© [A. MATHEVON], [2020], INSA Lyon, tous droits réservés

$$\begin{bmatrix} C_1^{t+\Delta t} \\ C_2^{t+\Delta t} \\ C_3^{t+\Delta t} \\ \vdots \\ \vdots \\ C_{nn-1}^{t+\Delta t} \\ C_{nn}^{t+\Delta t} \end{bmatrix} = \begin{bmatrix} b_1 & c_1 & 0 & \cdots & \cdots & \cdots & 0 \\ a_2 & b_2 & c_2 & \ddots & & & \vdots \\ 0 & a_3 & b_3 & \ddots & \ddots & & \vdots \\ \vdots & \ddots & \ddots & \ddots & \ddots & \ddots & \vdots \\ \vdots & & \ddots & \ddots & b_{nn-2} & c_{nn-2} & 0 \\ \vdots & & & \ddots & a_{nn-1} & b_{nn-1} & c_{nn-1} \\ 0 & \cdots & \cdots & \cdots & 0 & a_{nn} & b_{\ nn} \end{bmatrix}^{-1} \begin{bmatrix} C_1^t \\ C_2^t \\ C_3^t \\ \vdots \\ \vdots \\ C_{nn-1}^t \\ C_{nn}^t \end{bmatrix} \tag{3.17}$$

with the generic expression of each term a_i, b_i, c_i and the 4 boundary conditions terms.

$$b_1 = 1 + \frac{2\ D_{k,j}|_1\ \Delta t}{\Delta x^2} \tag{3.18}$$

$$c_1 = -\frac{2\Delta t}{\Delta x^2}\left(D_{k,j}|_1 + \frac{D_{k,j}|_2}{RT}\left(\mu_{k,j}^0\Big|_2 - \mu_{k,j}^0\Big|_1\right)\right) \tag{3.19}$$

$$a_i = -\frac{D_{k,j}|_{i-1}\ \Delta t}{\Delta x^2} \tag{3.20}$$

$$b_i = 1 + \frac{\Delta t}{\Delta x^2}\left(D_{k,j}|_{i-1} + D_{k,j}|_i \left(1 + \frac{\left(\mu_{k,j}^0\Big|_i - \mu_{k,j}^0\Big|_{i-1}\right)}{RT}\right)\right) \tag{3.21}$$

$$c_i = -\frac{\Delta t}{\Delta x^2}\left(D_{k,j}|_i + \frac{D_{k,j}|_{i+1}}{RT}\left(\mu_{k,j}^0\Big|_{i+1} - \mu_{k,j}^0\Big|_i\right)\right) \tag{3.22}$$

$$a_{nn} = -\frac{2\ D_{k,j}|_{n-1}\ \Delta t}{\Delta x^2} \tag{3.23}$$

$$b_{nn} = 1 + \frac{2\Delta t}{\Delta x^2}\left(D_{k,j}|_{n-1} + D_{k,j}|_n \left(1 + \frac{\left(\mu_{k,j}^0\Big|_n - \mu_{k,j}^0\Big|_{n-1}\right)}{RT}\right)\right) \tag{3.24}$$

Once the general discretization is presented, it is important to understand the specifications of the different configurations (see Figure 3.15.(a)):

- **Configuration 1 interface:** System boundary conditions for all chemical elements are applied to the system boundaries of size L. A linear variation of the standard chemical potential in the interface $\mu_{k,\alpha/\gamma}^0$ is used.
- **Configuration 2 interfaces:** For cementite dissolution, the numerical resolution is more complex, with a particular processing for carbon. The system boundary conditions for all chemical elements other than carbon are applied at the system boundaries of size L. The cementite and its interface must be excluded from the system for the resolution of the carbon concentration fields, since cementite is a stoichiometric phase $(Fe,Mn,Cr)_3C$ with no possibility of modifying its carbon concentration. As the M_3C/γ interface is moved back, the system size for carbon

Cette thèse est accessible à l'adresse : http://theses.insa-lyon.fr/publication/2020LYSEI120/these.pdf
© [A. MATHEVON], [2020], INSA Lyon, tous droits réservés

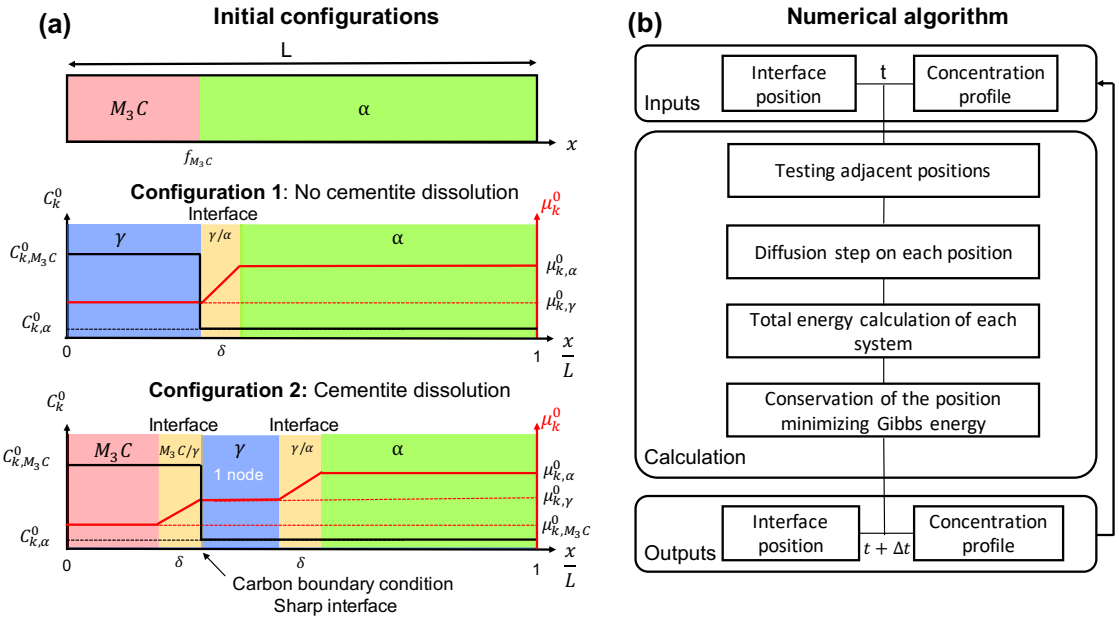

Figure 3.15: (a) Description of the 2 initial configurations used during this study to account or not for the cementite dissolution. The shape of the standard concentration and chemical potential profiles used in this work are presented (b) Numerical GEM model scheme of the different resolution steps.

resolution increases by one node. The added node has the same concentration of cementite (6.67 wt.%). This dissolution makes it possible to enrich the austenitic phase in carbon as the cementite dissolution becomes interesting to minimize the total Gibbs energy of the system. This addition will notably enable the preservation of cementite during non-isothermal treatments as long as it remains stable.

The general algorithm used in this approach is shown in Figure 3.15.(b). At each time step, the concentration fields are calculated for the possible position combinations. For configuration 1, only the α/γ interface is present within the system and can remain fixed, move forward or backward by one space step. For configuration 2, the interfaces α/γ and M_3C/γ are included in the system. The α/γ interface can thus remain fixed, move forward or backward by one space step, whereas the M_3C/γ interface can only remain fixed or move backward. Then a concentration field relative to each combination of interface positions is calculated (respectively 3 for configuration 1 and 6 for configuration 2). Once the concentration fields have been calculated for the different interface position combinations, the total Gibbs energy of the system is calculated. The retained interface positions are those that minimize the total Gibbs energy of the system. Time and space steps are identical for all elements and have been optimized in order to obtain an accurate solution (small enough to be independent of time and space steps). The effects of different parameters such as time step, system size, space step and austenite ferrite interface size will be detailed later.

Cette thèse est accessible à l'adresse : http://theses.insa-lyon.fr/publication/2020LYSEI120/these.pdf
© [A. MATHEVON], [2020], INSA Lyon, tous droits réservés

3.4 Results and discussion

The aim of this section is first to understand and measure the effect of model numerical parameters as well as the addition of cementite dissolution on austenite formation during isothermal annealing treatments. Then, an experimental validation of the GEM model to reproduce the non-isothermal experimental kinetics of complex cycle on ternary Fe-C-Mn alloys and industrial alloys has been performed. Finally, a cyclic heat treatment test on an Fe-0.023C-0.17Mn alloy was simulated in order to highlight the model's ability to handle the alternative $\alpha \leftrightarrow \gamma$ transformations during non-isothermal treatment.

3.4.1 Austenite formation during isothermal cycle

3.4.1.1 Austenite formation without cementite dissolution

With the aim of highlighting the effect of the simulation parameters (time and space steps, interface width, system size and diffusion coefficient within the interface), the GEM model was tested to predict the austenite formation kinetics of a fictive low-alloy Fe-0.17C-1.7Mn steel during isothermal treatment and compared to DICTRA.

Usually during the manufacturing of Dual-Phase steels, the initial microstructure formed before intercritical annealing is a mixture of pearlite and deformed ferrite in the cold-rolling direction (see Figure 1.1). First, for testing simulation parameters and compare the kinetics of the GEM model to DICTRA, an initial fictive microstructure was modelled considering a 5 μm 1-D simulation cell (10000 nodes and δ=2.5 nm) with closed boundary conditions for each element, corresponding to half-spacing between the pearlitic zones. Diffusion coefficients and chemical potential have been extracted from the MOBFE3 mobility and TCFE8 database. The simulation starts with an austenitic region of 2.4% volume fraction (containing 6.67 wt.%C and 10 wt.%Mn), resulting from the fast transformation of cementite into austenite (see ref. [CHA 19, OLL 18]) as shown in Figure 3.16. A mass balance is performed to determine the flat profile concentrations within the ferrite (containing 0.0066 wt.%C and 1.55 wt.%Mn).

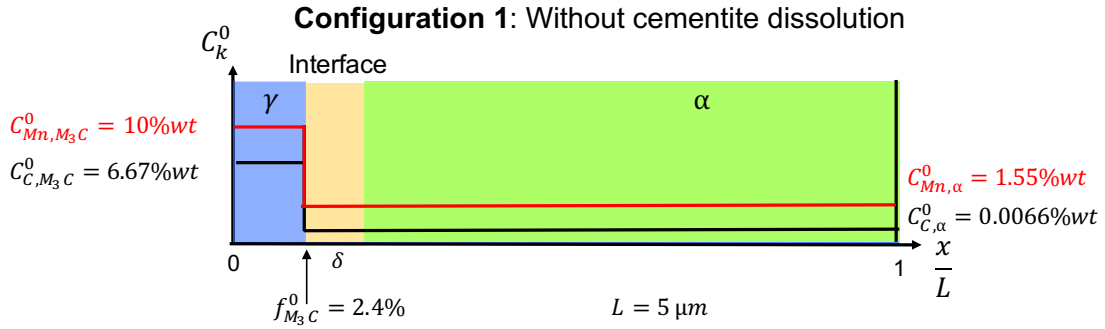

Figure 3.16: Diagram of the fictive system used to evaluate the effect of internal system parameters and to compare kinetics with DICTRA. Results are obtained using configuration 1 without cementite dissolution.

Cette thèse est accessible à l'adresse : http://theses.insa-lyon.fr/publication/2020LYSEI120/these.pdf
© [A. MATHEVON], [2020], INSA Lyon, tous droits réservés

Effect of internal parameters

It is essential to validate, just as for finite elements, that the improvement of the calculation resolution (time and space steps) leads to a unique result. Figure 3.17.(a) presents the austenitic transformation kinetics for different evolutions of the time step. It clearly appears that since the interface motion is limited to 1 node per time step, it is necessary to choose a time step small enough not to underestimate the real kinetics of the interface. Moreover, the choice to adjust the time step according to the interface kinetics allows to optimize the calculation time while keeping the accuracy on the transformation kinetics. At the simulation start, a small time step (Δt=10^{-10} s) is used before being adjusted using a logarithmic increment when the γ/α interface is considered immobile during at least 5 time steps (Δt = $1.03\Delta t$). However, if the interface moves before remaining 3 times at the same position, the time step is divided by a factor two. This time step control allows to optimize the computing time by adjusting it to the different interface velocities encountered during the different thermal cycles. It also allows to be sure not to underestimate the real kinetics of the interface in the case of larger fixed time steps as observed in Figure 3.17.(a).

The evolution of the space step within the system has only a limited influence on the final result (see Figure 3.17.(b)) and it is necessary to keep a minimum node number in the system in order to ensure that the α/γ interface with 5 nodes remains negligible in front of the whole system. Thereafter all simulations will be performed with a system containing 10000 nodes and with a time step adjusted during the simulation as described earlier.

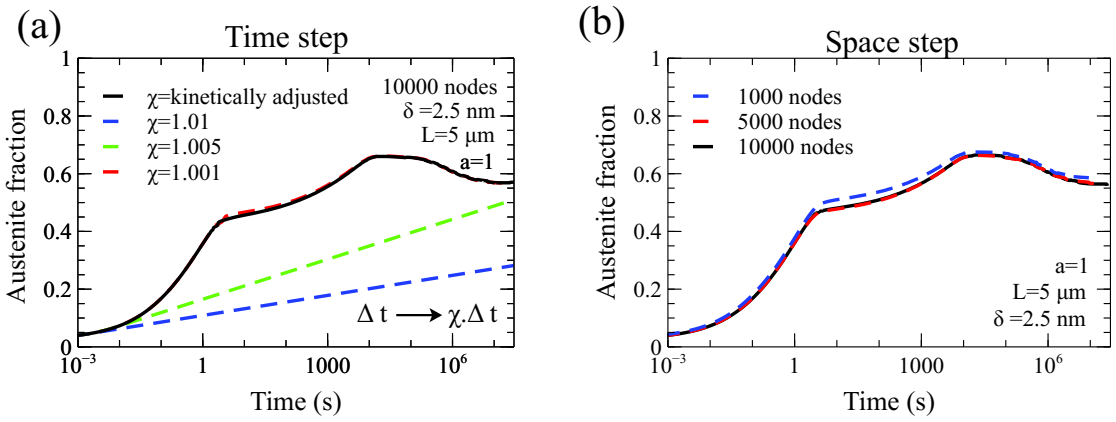

Figure 3.17: Comparison of the numerical effects associated with the variation of the: (a) time step, (b) space step.

Furthermore, Figure 3.18 presents the primordial role of the global system size on transformation kinetics driven mainly by carbon diffusion. As expected, a decrease in the system size tends to accelerate the kinetics It is nevertheless interesting to note that the austenite fraction formed at each stage of the kinetics is identical since they are driven by the system thermodynamics (temperature and chemical composition).

Cette thèse est accessible à l'adresse : http://theses.insa-lyon.fr/publication/2020LYSEI120/these.pdf
© [A. MATHEVON], [2020], INSA Lyon, tous droits réservés

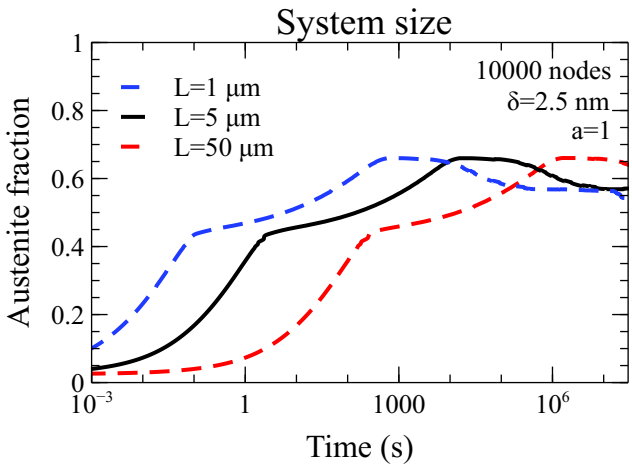

Figure 3.18: Comparison of the system size effect

Comparison between DICTRA and the GEM model

After calibration of the model numerical parameters, a comparison of the austenite formation kinetics obtained with a LE model (DICTRA) and the GEM model on the system described in Figure 3.16 is performed.

Figure 3.19.(a) shows the ferrite to austenite transformation kinetics during isothermal treatments performed at 760 °C and 780 °C according to the GEM model and LE model (DICTRA). The austenite formation from a pearlitic microstructure is composed of 4 steps as shown in Figure 3.19.(a). This stage succession during the austenite formation on Fe-C-Mn steels has already been observed by Wei *et al* [WEI 13a] in Figure 3.8 and Chantrenne *et al* [CHA 19].

The transformation is first controlled by the carbon diffusion within austenite (I. stage) up to the point H1 in Figure 3.19.(a). For the GEM model this first step leads to a close para-equilibrium state with the same manganese concentration on either side of the interface (see Figure 3.19.(d)). However, for the same stage, the LE model (DICTRA) presents a LENP equilibrium at the interface with a spike of manganese in the ferrite necessary to respect the equilibrium at the interface.

Then, the second stage of the kinetics up to the H2 point is controlled by the diffusion of Mn within ferrite (II. stage). During this stage, the GEM model evolves towards a state close to LENP equilibrium leading to a manganese spike in ferrite (see Figure 3.19.(e)) corresponding to the equilibrium observed in the LE model (DICTRA). As Mn diffuses into ferrite, the equilibrium boundary conditions at the interface evolve until the H2 point has been reached.

Finally the kinetics is controlled by Mn diffusion in austenite (III. stage) to remove the previous initial Mn enrichement in cementite (see Figure 3.19.(f)) to finally reach (IV. stage) the final equilibrium (*i.e.* ortho-equilibrium). The back and forth interface motion observed in Figure 3.19.(a) is due to the high initial Mn concentration of cementite, that needs to redistribute along the whole sample before reaching full equilibrium (see diffusion

Cette thèse est accessible à l'adresse : http://theses.insa-lyon.fr/publication/2020LYSEI120/these.pdf
© [A. MATHEVON], [2020], INSA Lyon, tous droits réservés

profiles in Figure 3.19.(b-c)).

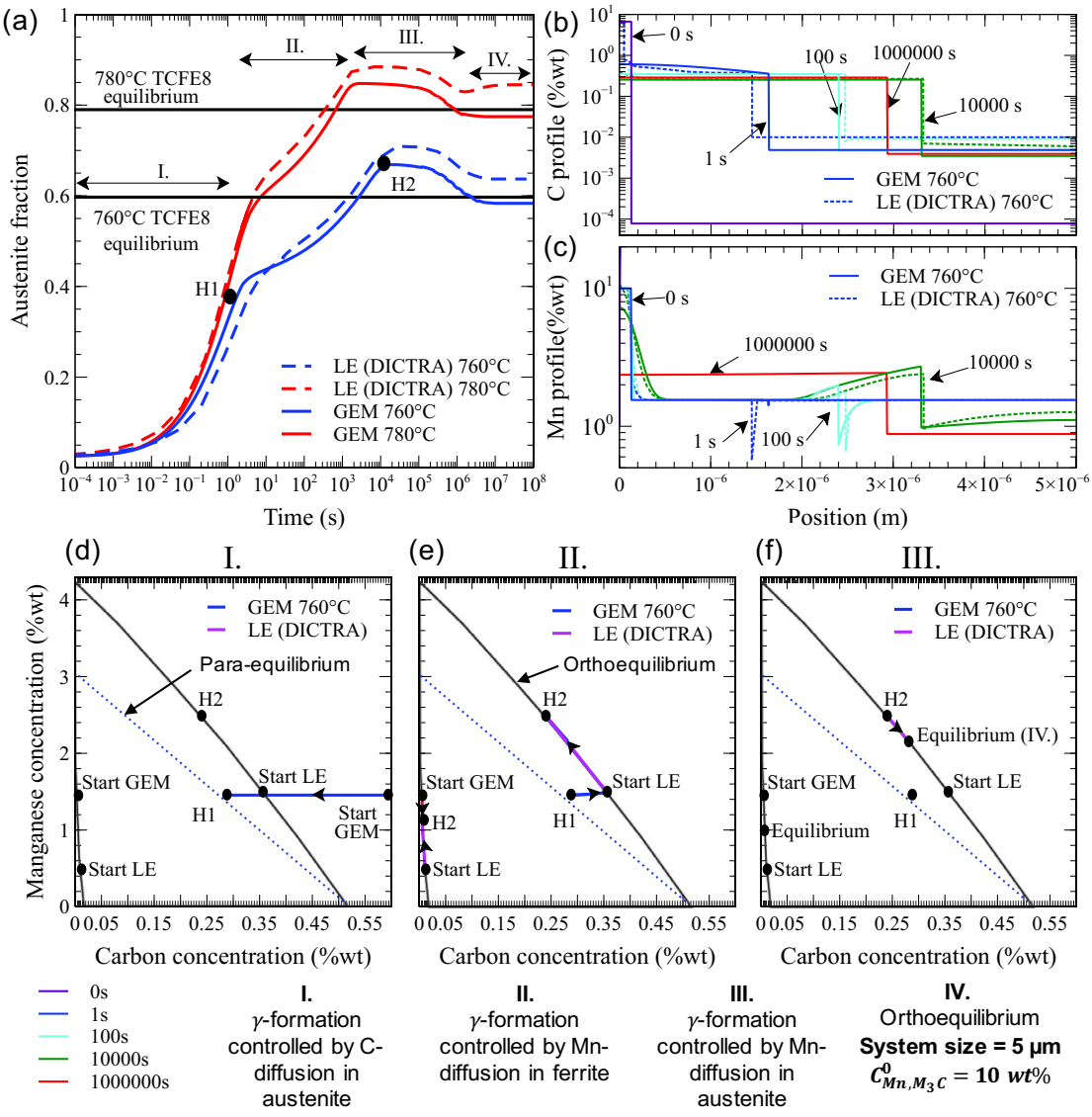

Figure 3.19: (a) Comparison of the austenitic formation kinetics predicted with the LE model (DICTRA) and GEM model (a=1, $\delta = 2.5$ nm and 10000 nodes). Thermocalc TCFE8 equilibrium for this composition is added for both temperatures. (b) Carbon concentration profile snapshots at 760 °C. (c) Manganese concentration profile snapshots at 760 °C. Path taken by the interface is shown on the isothermal section of the Fe-C-Mn phase diagram at 760 °C for phase transformations in stage: (d) I. ,(e) II. and (f) III.

This example illustrates the capability of the GEM model to move the interface from one way to the other without any modification of the code. The GEM model also shows good agreement with the LE (DICTRA) model for austenite formation kinetics without imposing equilibrium conditions at the interface. This avoids the development of a manganese spike for short heating times. The GEM model solving algorithm is based on the choice to check only the adjacent motion positions of the different interfaces instead of

Cette thèse est accessible à l'adresse : http://theses.insa-lyon.fr/publication/2020LYSEI120/these.pdf
© [A. MATHEVON], [2020], INSA Lyon, tous droits réservés

finding its position for a given time step (minimization loop that finds the interface velocity satisfying local equilibrium and mass balance), thus reducing numerical problems and improving computing time. For the same simulation system, the GEM model enables to divide the calculation time by 60 compared to DICTRA and a factor 50 compared to another implementation of LE model [CHA 19], while respecting the conservation laws of material (mass balance). This improvement is becoming even more important as the number of substitutional elements in the system increases or when performing non-isothermal thermal cycle simulation.

Effect of interface properties

The mechanisms and intrinsic physical properties of phase transformation interfaces are still not fully known. New methods, such as the atomic probe, enable the observation of alloying element concentration within interface (from 0.5 nm to 20 nm depending on the authors [CHE 14c, DAN 16, MAR 20a]). An increase in diffusion coefficients for substitutional elements within the interface has been observed, although precise quantification is difficult.

Figure 3.20 enables to discuss the effect of the interface diffusion coefficient (obtained by varying the values of a defined in Equation 3.27) which mainly controls the interface transition from a regime close to para-equilibrium to a regime close to local-equilibrium already observed by Kuang *et al.* [KUA 18]. GEM model leads to a natural transition between the different types of equilibria without imposing a specific concentration at the interface. A global kinetics close to that obtained using DICTRA with a sharp interface imposing the local equilibrium is obtained with an interface diffusion coefficient equal to that of ferrite ($a = 1$) as highlighted in Figure 3.20.(a).

Diffusion coefficient variation within the interface only affects the kinetics of the transition region between the paraequilibrium and the local equilibrium with partioning (between the $H1$ and $H2$ points). Whatever the diffusion coefficient in the interface, the kinetics start is driven by the carbon diffusion in austenite allowing to switch from the initial carbon concentration of prior cementite to a nominal carbon concentration in austenite close to the one predicted by the para-equilibrium without manganese diffusion.

Subsequently, a high interface diffusion coefficient ($a = 1$) enables to reach an equilibrium state with manganese diffusion on the ferritic side. This state is close to local equilibrium without partitioning and is followed by a local equilibrium at the interface before reaching finally the ortho-equilibrium. On the other hand, with an interface diffusion coefficient close to that of austenite ($a = \frac{1}{100}$), a more direct transition between para-equilibrium and local equilibrium with partitioning is obtained as shown in Figure 3.20.(c).

In the following, the choice of an interface diffusion coefficient equal to that of bulk ferrite ($a = 1$) was made to minimize the differences in properties between the different nodes of the system while being in the order of magnitude of those used and measured in literature [Fri 69].

Cette thèse est accessible à l'adresse : http://theses.insa-lyon.fr/publication/2020LYSEI120/these.pdf
© [A. MATHEVON], [2020], INSA Lyon, tous droits réservés

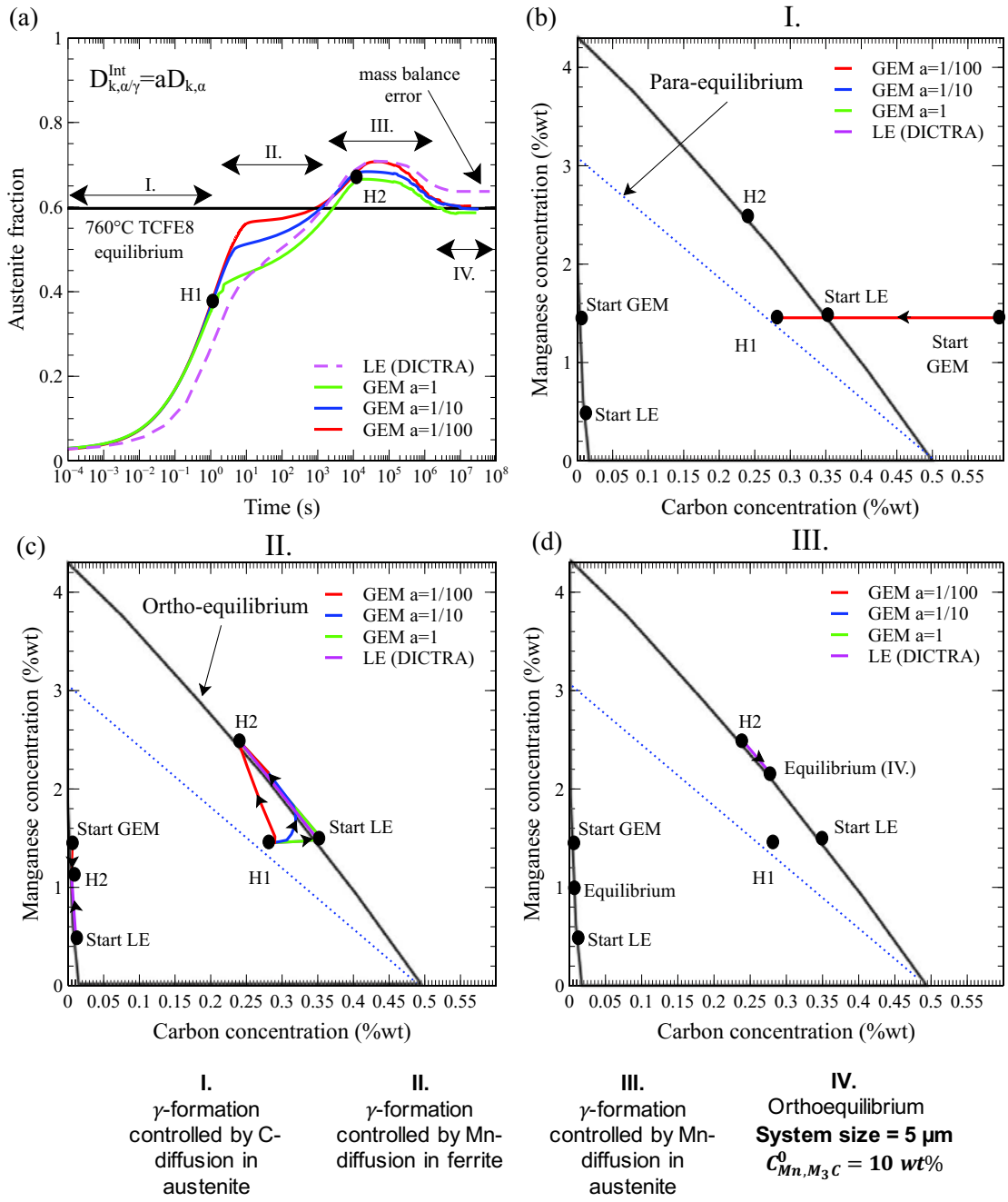

Figure 3.20: (a) Comparison of the austenitic formation kinetics predicted by the GEM model using different values of interface diffusion coefficients ($a = 1$, $a = \frac{1}{10}$ and $a = \frac{1}{100}$ see Figure3.27). Path taken by the interface is shown on the isothermal section of the Fe-C-Mn phase diagram 760 °C for phase transformations in stage: (b) I. ,(c) II. and (d) III.

Cette thèse est accessible à l'adresse : http://theses.insa-lyon.fr/publication/2020LYSEI120/these.pdf
© [A. MATHEVON], [2020], INSA Lyon, tous droits réservés

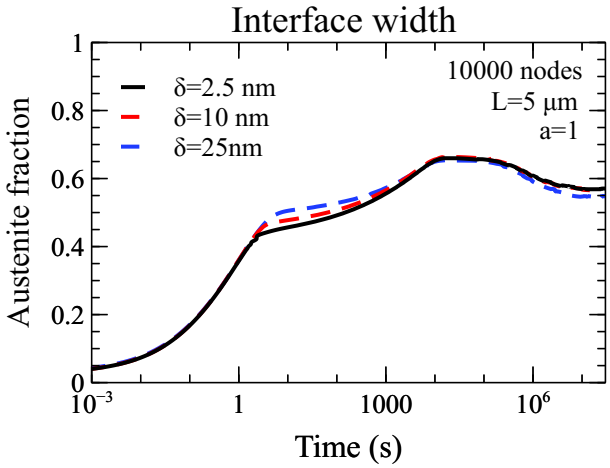

Figure 3.21: Comparison of the interface width effect on austenite formation kinetics

Furthermore, it has to be noted that the increase in the interface width is equivalent to artificially decrease the interface diffusion coefficient although its effect is weaker (see Figure 3.21). A constant general interface size of 2.5 nm was thus applied throughout this study.

3.4.1.2 Austenite formation with cementite dissolution

Although the study of austenite formation during high-temperature isothermal cycles justifies the instantaneous transformation of prior cementite to austenite as shown by Gouné *et al.* [GOU 12], it is essential to integrate cementite for annealing treatments at lower temperatures or during non-isothermal cycles to be able to model its dissolution. Moreover, the high cementite enrichment in manganese and chromium, during coiling and subsequent cooling for industrial alloys, delays cementite dissolution. This is why, the same initial system was model using a 6 μm 1-D simulation cell (10000 nodes and δ=2.5 nm) for cementite dissolution. Configuration 2 of Figure 3.15.(a) was used for the modelling with a cementite region of 2.4% volume fraction (containing 6.67 wt.%C and 10-30 wt.%Mn).

Figure 3.22.(a) shows the modelled kinetics of austenite formation for different cementite manganese enrichment content at 760 °C. The kinetics obtained with the GEM and DICTRA models with cementite dissolution are in good agreement and exhibit a significant transition with a cementite enrichment of 20 wt.% in manganese. At this temperature, up to an enrichment of the order of 20 wt.% in manganese, the carbon diffusion is sufficient to dissolve cementite, thus enabling an almost instantaneous dissolution of the whole cementite. On the other hand, beyond this value it is necessary to partition the manganese in order to dissolve the cementite. This requires much longer heat treatment times and a potential over-estimation of the real austenite fraction if the cementite dissolution during the simulation is not taken into account. The evolution of this critical fraction as a function of temperature was notably studied by Gouné *et al.* [GOU 12] (see Figure 3.3). Figure 3.22.(b) confirms the important effect of cementite dissolution on austenite for-

Cette thèse est accessible à l'adresse : http://theses.insa-lyon.fr/publication/2020LYSEI120/these.pdf
© [A. MATHEVON], [2020], INSA Lyon, tous droits réservés

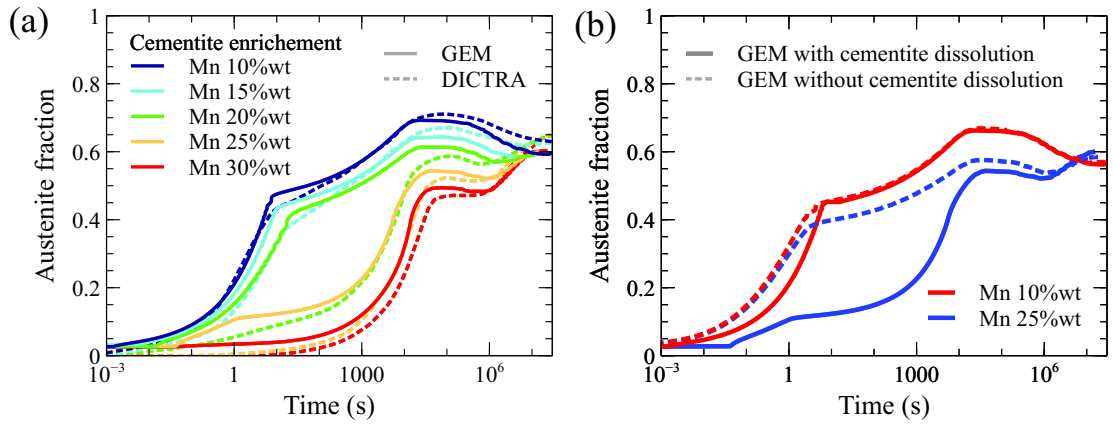

Figure 3.22: (a) Effect of manganese enrichment in cementite on austenite formation kinetics during isothermal annealing treatment at 760 °C and (b) Comparison of austenite formation kinetics modelled without and with consideration of cementite dissolution (respectively with configurations 1 and 2) for 2 cementite manganese enrichments (10 wt.% and 25 wt.%).

mation kinetics. For a manganese enrichment lower than the critical enrichment at 760 °C (around 20 wt.% Mn), an almost identical kinetics is obtained for the two configurations: this validates the hypothesis of instantaneous cementite dissolution to reproduce the industrial kinetics. However, for enrichments higher than the critical enrichment, a significant change is observed in the kinetics. In this case, the kinetics is driven by the cementite dissolution up to long intercritical annealing times.

In view of the preceding results, the cementite dissolution is not negligible for low transformation temperatures or for high manganese enrichments of cementite. This result led us to further investigate this effect in the case of a non-isothermal heat treatment. In this case, the two configurations presented previously were compared to the experimental austenite formation kinetics of the ternary Fe-0.17C-0.5Mn steel with a heating rate of 5 °C/s. The initial system was modelled using a 25 μm 1-D simulation cell (10000 nodes and δ=2.5 nm) with a cementite region of 2.4% volume fraction (containing 6.67 wt.%C and 1 wt.%Mn). Figure 3.23 presents the kinetics obtained for both types of simulation. A good experimental agreement is obtained in the case of configuration 2 with the cementite dissolution occurring around 750 °C. However, in the case of configuration 1 without cementite dissolution, a too fast austenite formation at low temperature is observed due to the carbon diffusion in the austenite. This overestimation is due to the absence of cementite in configuration 1 and the thermodynamic interest for austenite to decrease its initial imposed carbon concentration of 6.67 wt.%.

3.4.2 Austenite formation during complex cycle

The aim of this section is to compare the predictions of the GEM model for austenite formation with cementite dissolution with experimental austenite formation kinetics during complex cycles involving a heating stage followed by an isothermal holding at a given annealing temperature. This comparison was first performed on the four Fe-C-Mn ternary alloys of this thesis to validate the effect of the temperature and of the chemical composi-

Cette thèse est accessible à l'adresse : http://theses.insa-lyon.fr/publication/2020LYSEI120/these.pdf
© [A. MATHEVON], [2020], INSA Lyon, tous droits réservés

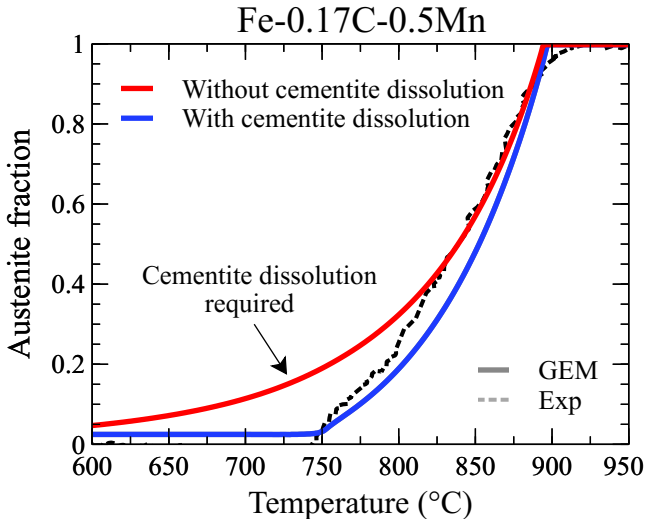

Figure 3.23: Comparison of the experimental and modelled austenite formation kinetics during continuous heating at 5 °C/s with and without accounting for cementite dissolution for a Fe-0.17C-0.5Mn steel ($L = 25\mu$m and $C_{(Fe,Mn)_3C} = 1wt.\%$). Overestimation of the real austenite fraction when the cementite dissolution is not taken into account at low temperature.

tion (C and Mn content). Finally, the GEM model was tested on the DP600 and DP1000 steels to underline the effect of chromium and the interaction with recrystallization phenomenon.

3.4.2.1 Definition of the modelled systems

To faithfully reproduce the thermal cycles used industrially during the simulation, complex thermal cycles comprising a heating rate of 5 °C/s followed by an isothermal holding at different temperatures for 3 min and by a heating ramp of 5 °C/s up to 1000 °C were used. A monitoring by optical dilatatometry (see Figure 3.25.(a)) allowed us to obtain the austenite fraction throughout the thermal cycle using the tangent method.

The experimental kinetics for the four ternary steels and the industrial steels (DP600 and DP1000) were modelled using configuration 2 in a 1-D system of size L corresponding to the half-spacing between the carbon-rich zones given in Table 3.1 according to chemical compositions (see Figure 3.24 and Table 3.2). The system (10000 nodes and δ=2.5 nm) consists, at the initial time, in a mixture of cementite, austenite and ferrite allowing a progressive dissolution of the cementite during the complex thermal cycle (see Figure 3.24). The cementite fraction is defined using a global mass balance (see Table 3.2) with respect to the carbon content of cementite (6.67 wt.%) and the two other phases (0.0066 wt.%). The manganese and chromium concentration within cementite was measured by EDS analysis using carbon replicas, the manganese and chromium enrichment content of each grade are summarized in Table 3.2. Subsequently from a mass balance on the manganese remaining in the ferrite, linear initial manganese concentration profiles were applied for each steel according to Table 3.2. This hypothesis enables to reproduce both the heterogeneities of chemical composition within ferrite in the different steels as well as the experimental

Cette thèse est accessible à l'adresse : http://theses.insa-lyon.fr/publication/2020LYSEI120/these.pdf
© [A. MATHEVON], [2020], INSA Lyon, tous droits réservés

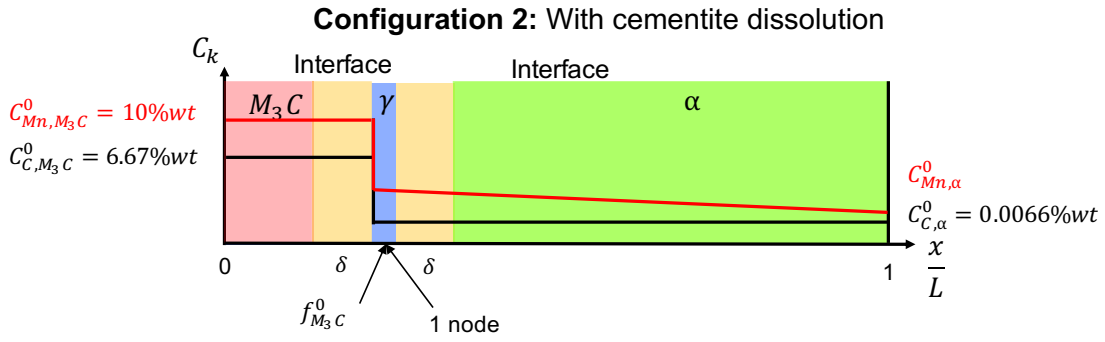

Figure 3.24: Diagram of the system used to reproduce experimental austenite formation kinetics during complex cycles. Results are obtained using configuration 2 with cementite dissolution and with a linear variation of the Mn content in ferrite.

spacing distribution of the pearlitic zones. Modelling may include the chromium content evolution in the case of industrial steels by assuming an initial concentration within ferrite determined from a mass balance of the system.

Steel grades	Cementite fraction (%)	Cementite enrichment (in wt.%)		Concentration profile in ferrite (in wt.%)	
	$f^0_{M_3C}$	C^0_{Mn,M_3C}	C^0_{Cr,M_3C}	$C^0_{Mn,\alpha}$	$C^0_{Cr,\alpha}$
Fe-0.17C-0.5Mn	2.45	1*	-	$0.8 \rightarrow 0.1$	-
Fe-0.17C-1.7Mn	2.45	2	-	$2.1 \rightarrow 1.2$	-
Fe-0.17C-2.5Mn	2.45	4*	-	$2.6 \rightarrow 2.3$	-
Fe-0.08C-1.7Mn	1.1	2*	-	$2.1 \rightarrow 1.2$	-
DP600	1.25	12	6.5	$1.7 \rightarrow 1$	$0.33 \rightarrow 0.33$
DP1000-CR	2.54	10	4	$1.75 \rightarrow 1.35$	$0.32 \rightarrow 0.32$
DP1000-Rex	2.54	13	7	$1.7 \rightarrow 1.3$	$0.27 \rightarrow 0.27$

Table 3.2: Cementite fraction and its enrichment in manganese and chromium used in the model. Initial linear profile of manganese and chromium chemical contents applied for the simulation of complex cycles within ferrite

3.4.2.2 Ternary Fe-C-Mn steels

In this part, the ability of the model to reproduce the annealing temperature effect for the Fe-0.17C-0.5Mn steel as well as the effect of the chemical composition of different ternary Fe-C-Mn steels is studied. A low cementite enrichment in manganese was observed in the initial states of these steels (see Table 3.2).

Temperature influence on the austenite formation kinetics (Fe-0.17C-0.5Mn)

Figure 3.25.(b-c) show the effect of the annealing temperature on austenite formation for the Fe-0.17C-0.5Mn steel. As can be seen in Figure 3.25.(b), the change in annealing temperature (from 760 °C to 800 °C) without modifying the chemical composition has a strong effect on austenite formation kinetics which is accelerated with an increase in

Cette thèse est accessible à l'adresse : http://theses.insa-lyon.fr/publication/2020LYSEI120/these.pdf
© [A. MATHEVON], [2020], INSA Lyon, tous droits réservés

the annealing temperature. This is consistent with the austenite stabilization at higher temperature.

Figure 3.25.(b-c) shows the excellent agreement obtained in the prediction of the austenite amount both during continuous heating and during isothermal annealing with GEM model presented in Section 3.3. Cementite dissolution starts at 745 °C, which is in good agreement with the observed experimental temperature only due to carbon diffusion as shown in Figure 3.25.(d-e). After the isothermal holding, the curves associated with the different annealing temperatures end up converging towards the same Ac_3 temperature (around 890 °C). GEM model predictions are in good agreement with the experimental kinetics while retaining the ability to reproduce both the cementite dissolution temperature and austenite formation during a complex cycle.

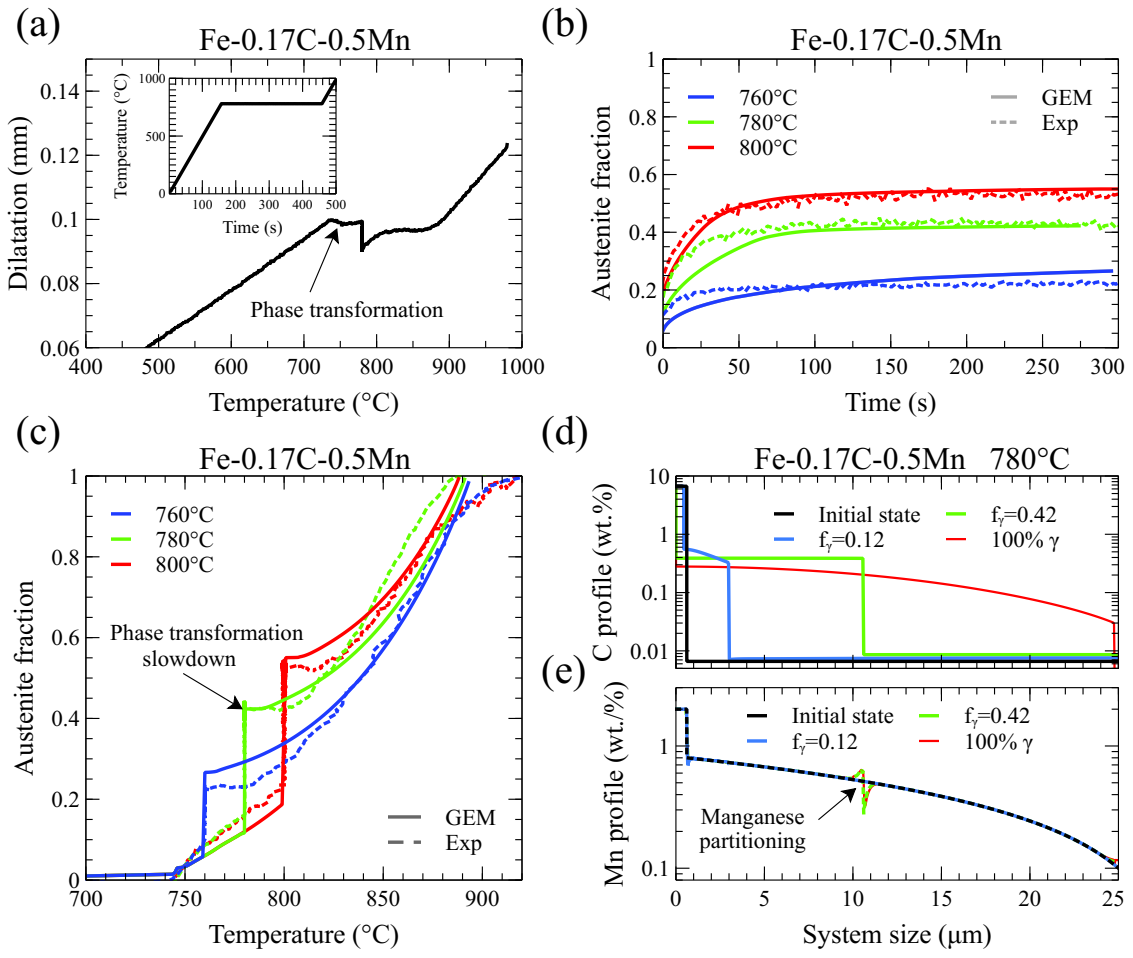

Figure 3.25: (a) Dilatation curve obtained with Led dilatometry over a complex cycle including a heating stage of 5 °C/s and a holding stage of 300s at 780 °C. Austenite formation kinetics for the Fe-0.17C-0.5Mn steel during (b) the 300s isothermal stage at different temperatures and (c) as a function of temperature over the entire cycle. Concentration profiles at different interface positions in the simulation with a holding at 780 °C for (d) carbon and (e) manganese.

It is interesting to note that during continuous heating, only carbon diffusion controls austenite formation as manganese has not enough time to partition. On the other hand,

Cette thèse est accessible à l'adresse : http://theses.insa-lyon.fr/publication/2020LYSEI120/these.pdf
© [A. MATHEVON], [2020], INSA Lyon, tous droits réservés

during isothermal annealing, carbon equilibrium within the sample is quickly reached, leading to the beginning of the manganese partitioning at the interface, as can be seen in Figure 3.25.(e).

Manganese content decrease within the ferrite leads to a phase transformation slowdown above the annealing temperature until a sufficiently high temperature is reached to ensure sufficient driving force for carbon to overcome the manganese partitioning. This phase transformation slowdown phenomenon has been observed especially during cyclic tests [KUA 18, CHE 16]. In addition, since the system can evolve with out-of-equilibrium interface concentrations, it is not necessary to achieve manganese concentrations in the order of 20-30 wt.% at cementite interface as observed in non-isothermal simulation with cementite dissolution in a Fe-C-Mn-Cr system with DICTRA [MAR 20c].

Influence of the manganese content on the austenite formation kinetics (Fe-0.17C-XMn)

Figure 3.26.(a-b) illustrates the effect of the manganese content on austenite formation. The increase in the manganese content of the steel (from 0.5Mn to 2.5Mn) without modifying the carbon content (0.17C) leads to a decrease in the Ac_1 and Ac_3 temperatures as Mn extends the stability range of austenite. This results in a acceleration of the austenite formation kinetics with an increase in the Mn content. It has to be noted that the GEM model perfectly reproduces this acceleration.

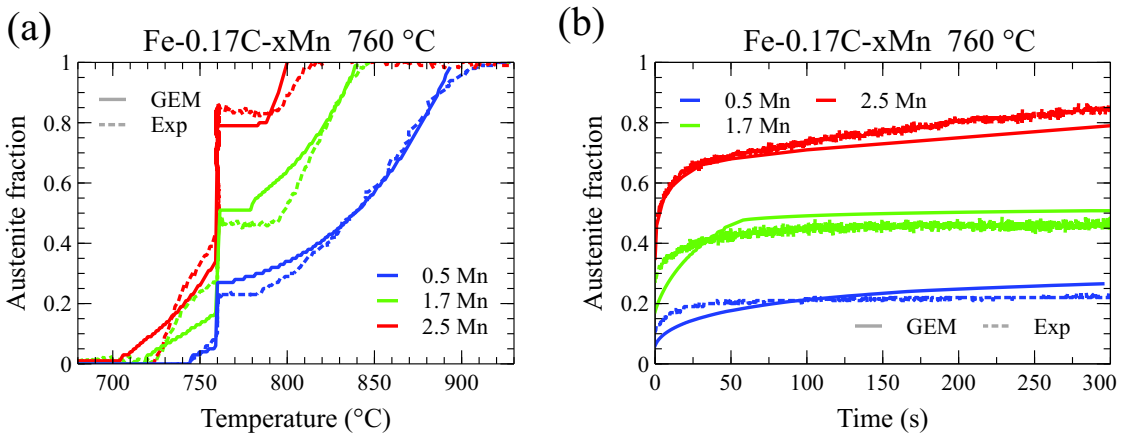

Figure 3.26: Comparison of the manganese content effect on the austenite formation kinetics modelled with the GEM model and determined experimentally by LED dilatometry: (a) as a function of temperature and (b) during isothermal holding.

Influence of the carbon content on the austenite formation kinetics (Fe-XC-1.7Mn)

As clearly highlighted in Figure 3.27.(a-b) for steels with 1.7Mn, carbon significantly accelerates the austenite formation, since the kinetics is regularly shifted towards lower temperatures as the carbon content is increased. The acceleration can be explained by a

Cette thèse est accessible à l'adresse : http://theses.insa-lyon.fr/publication/2020LYSEI120/these.pdf
© [A. MATHEVON], [2020], INSA Lyon, tous droits réservés

decrease in the half-spacing between the pearlitic zones when the carbon content increases as observed in Figure 1.1. During isothermal holding, the austenite fraction formed is higher with a high carbon content since it also stabilizes the austenitic phase.

Nevertheless, it should be pointed out that for the investigated manganese content (1.7Mn), the temperature range for which phase transformation slowdown is observed on the modelled kinetics after intercritical annealing is lower than that observed experimentally. This case is very close to the results obtained in the literature for the simulation of cyclic treatment, which generally involves a phase transformation slowdown over a lower temperature range than that observed experimentally [CHE 16, KUA 18].

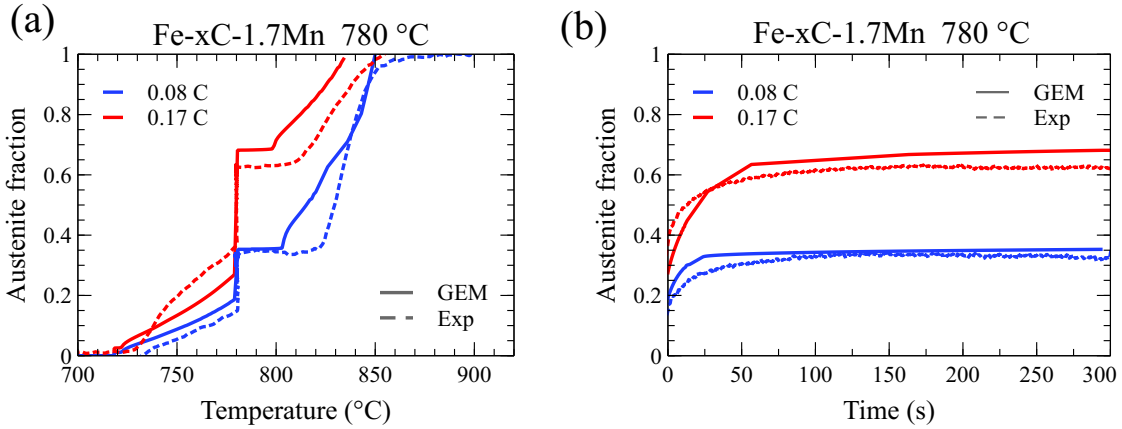

Figure 3.27: Comparison of the carbon content effect on the austenite formation kinetics modelled with the GEM model and determined experimentally by LED dilatometry: (a) as a function of temperature and (b) during isothermal holding.

3.4.2.3 Industrial DP600 steel: Almost totally recrystallized before Ac_1

In order to test the validity of the model on an industrial steel almost totally recrystallized before Ac_1, the austenite formation kinetics of the DP600 steels was obtained and modelled for two annealing temperatures with the same complex thermal cycle (see Figure 3.25.(a)). With a heating rate of 5 °C/s, the recrystallization prediction model and the experiments ensure that recrystallization is almost completed at the beginning of austenite formation as shown in Figure 3.28.

To reproduce the experimental austenite formation results, the same simulation parameters as those used for the ternary steels were used, although the manganese content of cementite is much higher (12 wt.%) due to the hot-rolling and coiling step during the manufacture.

Figure 3.29.(a) highlights the model's inability to reproduce the experimental kinetics by modelling it only as a ternary Fe-C-Mn system. Indeed, the cementite dissolves too rapidly at a temperature closer to that observed in the case of the ternary Fe-0.08C-1.7Mn alloy. However, by modelling the system as a quaternary Fe-C-Mn-Cr alloy with a chromium enrichment of cementite of 6 wt.%, a marked stabilisation of the cementite is observed. The chromium addition significantly retards the cementite dissolution, since the

Cette thèse est accessible à l'adresse : http://theses.insa-lyon.fr/publication/2020LYSEI120/these.pdf
© [A. MATHEVON], [2020], INSA Lyon, tous droits réservés

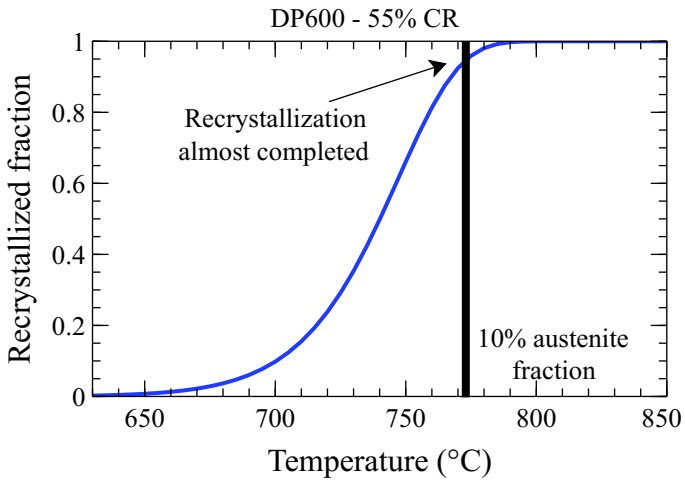

Figure 3.28: Recrystallization kinetics during continuous heating at 5 °C/s of the DP600 steel using the MiReX model. Recrystallization is almost completed when 10% austenite has formed allowing the interaction between the two phenomena to be neglected.

kinetics are shifted towards higher temperatures. The modelling of the industrial alloy by a quaternary Fe-C-Mn-Cr system thus enables to reproduce both the experimental austenite formation kinetics and the cementite dissolution temperature.

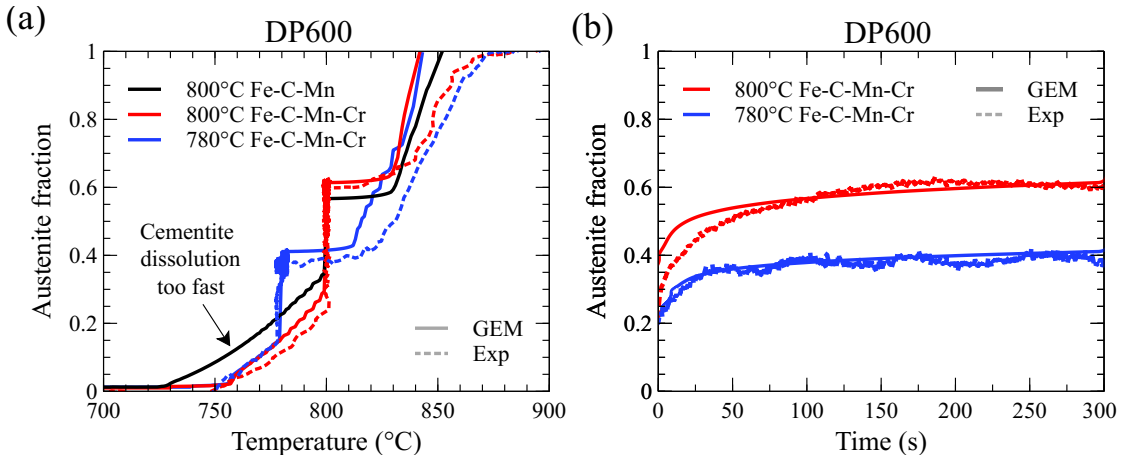

Figure 3.29: Comparison of the experimental and modelled austenite formation kinetics for the DP600 steel: (a) as a function of the temperature for ternary and quaternary simulation and (b) during isothermal holding for quaternary simulation. The chromium addition is necessary to delay the cementite dissolution in the case of the DP600 steel.

3.4.2.4 Industrial DP1000 steel

In the case of the DP1000-CR industrial steel, phase transformation modelling is more complex since an interaction between recrystallization and phase transformation is possible as was explained in Chapter 2 (see Section 2.5.2).

The interaction of all these phenomena and their extensions to different microstructures

Cette thèse est accessible à l'adresse : http://theses.insa-lyon.fr/publication/2020LYSEI120/these.pdf
© [A. MATHEVON], [2020], INSA Lyon, tous droits réservés

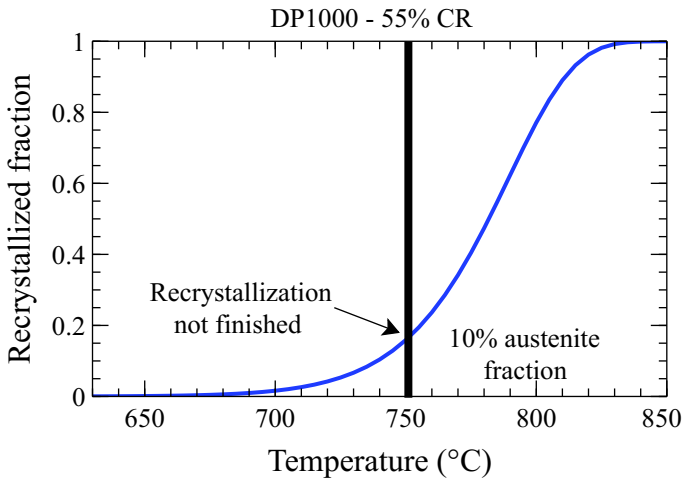

Figure 3.30: Recrystallization kinetics during continuous heating at 5°C/s of the DP1000 steel using the MiReX model. Recrystallization is not finished when 10% austenite has been formed requiring the interaction between the two phenomena to be added.

seems complex in view of the choice made to model austenite formation in a 1-D system. Nevertheless, thanks to the two initial states available in the case of the DP1000 (*i.e.* DP1000-CR and DP1000-Rex), the half-spacing between pearlitic zones as well as its enrichment have been determined.

A coupling with the Mirex recrystallization model is performed to define the fraction of recrystallized ferrite in the system. Using the recrystallization prediction model, only 20% of the microstructure could recrystallize before reaching the 10% austenite fraction threshold [OLL 17b] with 5 °C/s heating ramp (see Figure 3.30). Assuming a competition between the recrystallization phenomenon and austenite formation at the nucleation sites, it was chosen to grow the recrystallized ferrite zone at the opposite side of the cementite. Four parameters were thus adapted within the model to reproduce the interaction between these two phenomena:

- The Gibbs energy of the deformed ferrite was modified by adding a term corresponding to the energy stored during cold-rolling as follows:

$$G_{\alpha-deformed} = G_{\alpha} + \frac{1}{2}\mu\rho^{f}b_{111}^{2} \tag{3.25}$$

- The diffusion coefficient within the deformed ferrite for the subsitutional elements (Mn, Cr) was increased due to the high density of dislocations:

$$D_{k,\alpha-deformed} = 3aD_{k,\alpha} \tag{3.26}$$

- The half-spacing between pearlitic zones can vary depending on the initial state and therefore the recrystallisation degree of the steel at the phase transformation start. A linear relationship with respect to the size of the system before L_{CR} and after complete recrystallization L_{Rex} is applied as a function of the recrystallized ferrite fraction f_{α}^{ReX} when 10% austenite has been formed:

Cette thèse est accessible à l'adresse : http://theses.insa-lyon.fr/publication/2020LYSEI120/these.pdf
© [A. MATHEVON], [2020], INSA Lyon, tous droits réservés

$$L = L_{CR} + f_{\alpha}^{ReX}(L_{ReX} - L_{CR}) \tag{3.27}$$

- The cementite enrichment during heating is neglected compared to the treatment applied to ensure complete recrystallization on the DP1000-Rex and only the average concentrations measured using EDS analysis on TEM replicas was used for the two types of initial states.

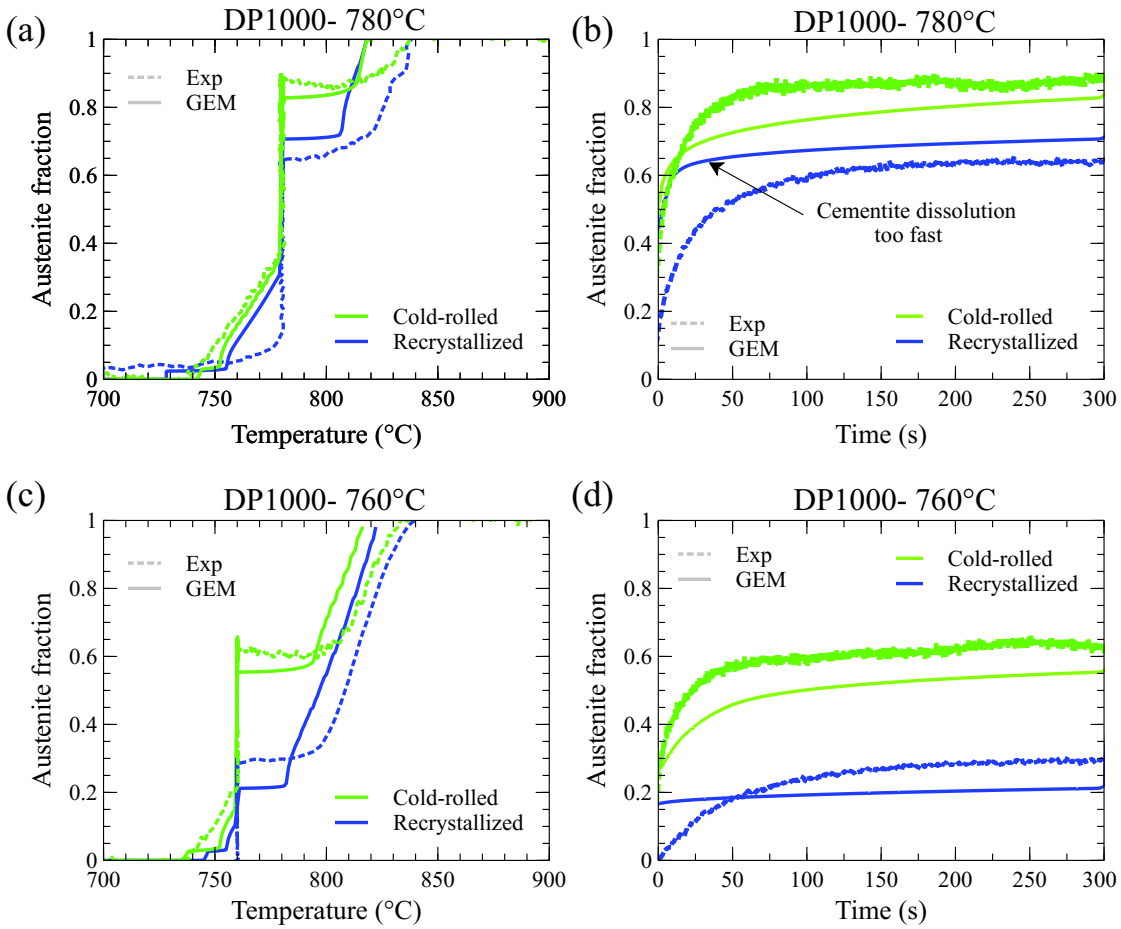

Figure 3.31: Comparison of the experimental and modelled austenite formation kinetics for the two DP1000 initial states: as a function of the temperature with holding at (a) 780 °C and (c) 760 °C and (b) during isothermal holding at (b) 780 °C and (d) 760 °C.

The adjustments introduced within the GEM model to take into account the interaction between the recrystallization phenomenon and the phase transformation are first applied in the case of a complex cycle with a heating ramp of 5 °C/s before a holding at 760 or 780 °C. Figure 3.31 shows a significant increase in the austenite fraction formed in the case of DP1000-CR steel. Indeed, the austenite fraction formed after holding for 300s is higher than the various thermodynamic equilibria predictions (PE, LENP, ORTHO), which seems to indicate the requirement to introduce the energy stored during the deformation, which also allows to increase the austenite fraction for an equivalent heat treatment. In fact, the

Cette thèse est accessible à l'adresse : http://theses.insa-lyon.fr/publication/2020LYSEI120/these.pdf
© [A. MATHEVON], [2020], INSA Lyon, tous droits réservés

austenite formation kinetics in the case of DP1000-CR steel is in good agreement with the model both for the austenite fraction during holding and for the dissolution kinetics of the cementite. However, in the case of DP1000-Rex steel, the cementite stabilization with its enrichment in manganese and chromium as well as the increase of the system size does not seem to be sufficient to reproduce the cementite dissolution kinetics. Indeed, both on the heating ramp and on the isothermal holding, the cementite dissolution kinetics seems to be faster than the one observed experimentally. This faster dissolution in modelling could be explained by different phenomena: (i) the spheroidization of the cementite, (ii) the experimental dispersion of manganese enrichment within the microstructure and (iii) the incubation time and the energy barrier necessary for the creation of austenite nuclei.

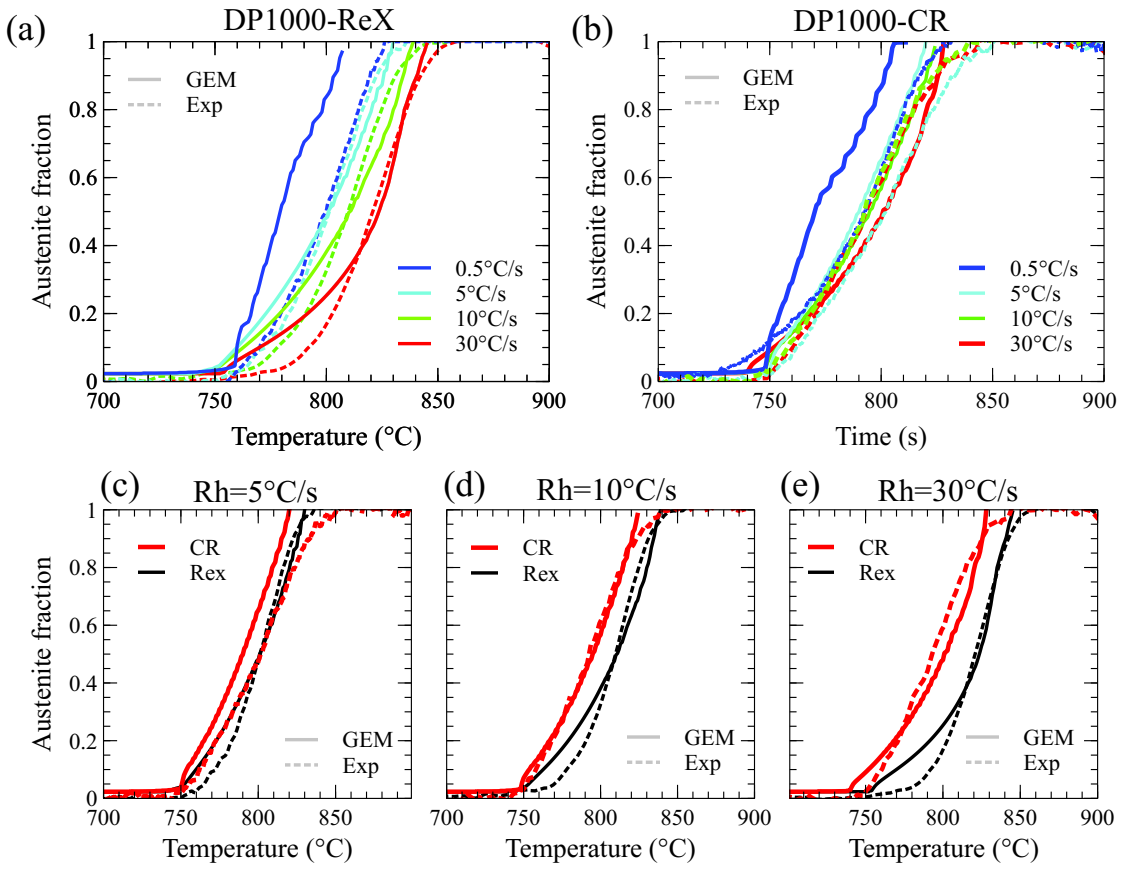

Figure 3.32: Comparison of the experimental and modelled austenite formation kinetics of the DP1000 steel during continuous heating at different heating rates: (a) DP1000-Rex and (b) DP1000-CR. Comparison of the initial state effect and the degree of interaction with recrystallization on austenite formation during continuous heating with a heating ramp of (c) 5°C/s, (d) 10 °C/s and (e) 30 °C/s.

Finally, the heating rate effect (0.5-30 °C/s) on the two types of initial states is studied to validate the assumptions selected for the interaction between recrystallization and phase transformation. In the case of the DP1000-Rex, a slowing down of the experimental austenite formation kinetics is observed in Figure 3.32 with the increase of the heating rate. This delay seems logical as the heating rate increases, the time available for phase transformation at each temperature decreases. However, this slowdown is not observed

Cette thèse est accessible à l'adresse : http://theses.insa-lyon.fr/publication/2020LYSEI120/these.pdf
© [A. MATHEVON], [2020], INSA Lyon, tous droits réservés

in the case of the DP1000-CR which presents more or less similar kinetics whatever the heating rate. However, as the heating rate increases, the ferrite fraction recrystallized at the time of austenite formation decreases, which has the additional effect of accelerating austenite formation.

First of all, we observe a good agreement between the experimental kinetics and the predictions of the GEM model for all heating rates except 0.5 °C/s. Indeed, for both initial states, the formation kinetics are too fast with a too early dissolution of the cementite which can come from neglecting the incubation time of the different austenitic interfaces more critical during slow heating. Nevertheless, Figure 3.32.(c-e) clearly shows the ability of the two models coupling to reproduce the interaction between these two phenomena. Indeed with a slow heating rate and a complete recrystallization, the kinetics of formation predicted for the two states are very close. When the heating rate increases and the recrystallized ferrite fraction decreases, a marked increase is observed in the austenite formation kinetics of the GEM model.

3.4.3 Ferrite formation

Although the model is able to predict the phase transformation $\alpha + M_3C \rightarrow \gamma$, it seems necessary to validate the accuracy of the model to predict the phase transformation $\gamma \rightarrow \alpha$. First of all, the GEM model will be used on isothermal decarburization kinetics on different ternary and quaternary systems. Finally, the simulation of an Fe-0.023C-0.17Mn alloy during cyclic heat treatment was studied.

3.4.3.1 Decarburization modelling

Decarburization experiments are a smart way of studying austenite to ferrite transformation because they overpass many difficulties encountered in more "classical", so called precipitation transformations (*e.g.* nucleation, overlap of carbon diffusion fields). In addition, the literature includes numerous accurate results on Fe-C-X and Fe-C-X-Y systems: *i.e.* the displacement of the interface is measured with a precision of approximately 5 μm over distances of about 300 μm [ZUR 12, SUN 17, QIU 15, PAN 15]. Note that these decarburization experiments involve temperatures close to Ac_1 and transformation kinetics ten times slower than precipitation transformations.

Initial simulation boxes for decarburization are semi-infinite 1D (500 µm, 100000 nodes and δ=50 nm) with homogeneous nominal composition of the steel. Simulation starts with one node of ferrite, for which the C concentration is forced to be 0, at one extremity of the simulation cell. The other extremity has a zero flux condition. The carbon diffusion coefficient in austenite and ferrite was obtained from [ÅGR 82, ÅGR 86].

Figure 3.33 compares GEM model with experiments for 2 ternary and 2 quaternary alloys. Without any fitting parameter, the agreement is remarkable for all systems. For the sake of comparison, interface position under local equilibrium with negligible partitionning and paraequilibrium are represented in Figure 3.33. These equilibrium conditions are rarely satisfied in real systems. The self consistent model of Zurob *et al* [ZUR 12] based on Gibbs Energy balance between interface friction and driving force is also compared to experiments and GEM model. It can be observed on Figure 3.33 that GEM and Zurob's

Cette thèse est accessible à l'adresse : http://theses.insa-lyon.fr/publication/2020LYSEI120/these.pdf
© [A. MATHEVON], [2020], INSA Lyon, tous droits réservés

models are superimposed for all cases, except for the the quaternary Fe-C-Mn-Si system, where Zurob's model fails to describe experimental results with the same parameters as those adjusted on ternary systems.

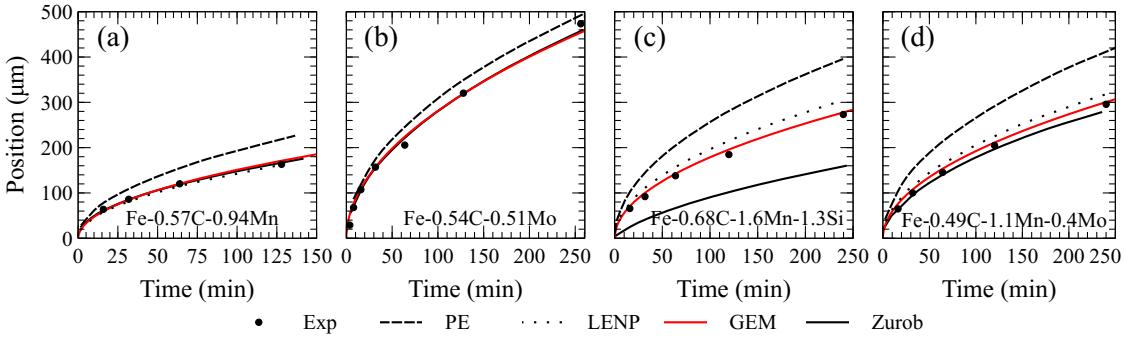

Figure 3.33: Decarburization kinetics for (a) Fe-0.57C-0.94Mn (806 °C) (b) Fe-0.54C-0.51Mo (806 °C) (c) Fe-0.68C-1.58Mn-1.33Si (806 °C) (d) Fe-0.49C-1.09Mn-0.42Mo (806 °C). The results of the Zurob model were extracted from [ZUR 12, QIU 15, SUN 17]

Note that solute drag, which is the basis of the GEM model and the self consistent model of Zurob (as well as the GEB model of Chen *et al* [CHE 14c]), is responsible for monitoring phase-transformation kinetics. We have also tested the GEM model with the same potential well as Zurob and GEB models, without any significant effect on both transformation kinetics which establishes that potential well is not a necessary ingredient of GEM model to reproduce decarburization kinetics.

3.4.3.2 Cyclic phase transformation

For testing the GEM model's ability to describe both an $\alpha \rightarrow \gamma$ and an $\gamma \rightarrow \alpha$ transformation, the phase transformation kinetics for cyclic heating and cooling between 860 °C and 885 °C at a rate of 10 °C min^{-1} for an Fe-0.023C-0.17Mn alloy obtained by Chen *et al.* [CHE 16] was modelled. This method avoids all problems of nucleation and germination of the different interfaces and allows to follow the kinetics of the interface with only 2 phases in presence (austenite and ferrite). During the simulation an initial 1D system (L =25 μm, 10000 nodes and δ =2.5 nm) without cementite dissolution was simulated with a single ferrite node with a homogeneous chemical element content identical to the nominal composition throughout the sample.

Figure 3.34.(a) presents the experimental kinetics resulting from the cyclic heat treatment [CHE 16] , which is composed of six steps. A preliminary step $C_0 \rightarrow C_1$ corresponds to the 20 min stage at 860 °C which allows the ferrite to nucleate and growth close to the equilibrium fraction. Indeed, Figure 3.34.(b-c) illustrates that carbon is able to homogenize within the different phases while manganese starts to partition with the creation of a concentration spike in austenite towards the interface that will remain throughout the cyclic treatment. The stages $C_1 \rightarrow C_2$ ($C_4 \rightarrow C_5$) correspond to the phenomenon of stagnant phase observed during complex cycles where the interface stays fixed while the temperature increases (decreases) promoting the phase transformation. The transforma-

Cette thèse est accessible à l'adresse : http://theses.insa-lyon.fr/publication/2020LYSEI120/these.pdf
© [A. MATHEVON], [2020], INSA Lyon, tous droits réservés

tion stages $C_2 \rightarrow C_3$ ($C_5 \rightarrow C_6$) propose an advance of the transformation logically related to the increase (decrease) of the temperature and their thermodynamic effects. The phase $C_3 \rightarrow C_4$ refers to the area in which the transformation $\alpha \rightarrow \gamma$ takes place despite a temperature inversion that should, from the thermodynamic point of view, have caused a change in the transformation's direction. Figure 3.34.(b-c) are used to follow during the transformation the concentration profiles accounting for the different stages obtained during the kinetics. First, the two phases for which the interface is locked correspond to 2 stages with a partitioning of the manganese on each side of the interface, thus stabilizing this state over a temperature range for which the carbon diffusion becomes more energetically interesting allowing the interface to be unlocked. By contrast, as the transformation evolves in phases $C_2 \rightarrow C_3$ ($C_5 \rightarrow C_6$), a slight gradient within the carbon profile is observed indicating that even the carbon equilibrium is not reached. This transformation retardation relative to thermodynamic equilibrium explains the $C_3 \rightarrow C_4$ zone where the transformation still occurs to recover its retardation even though the temperature is reversed. Chen *et al.* [CHE 16] study in detail the origins of these stages in various thermal cycles.

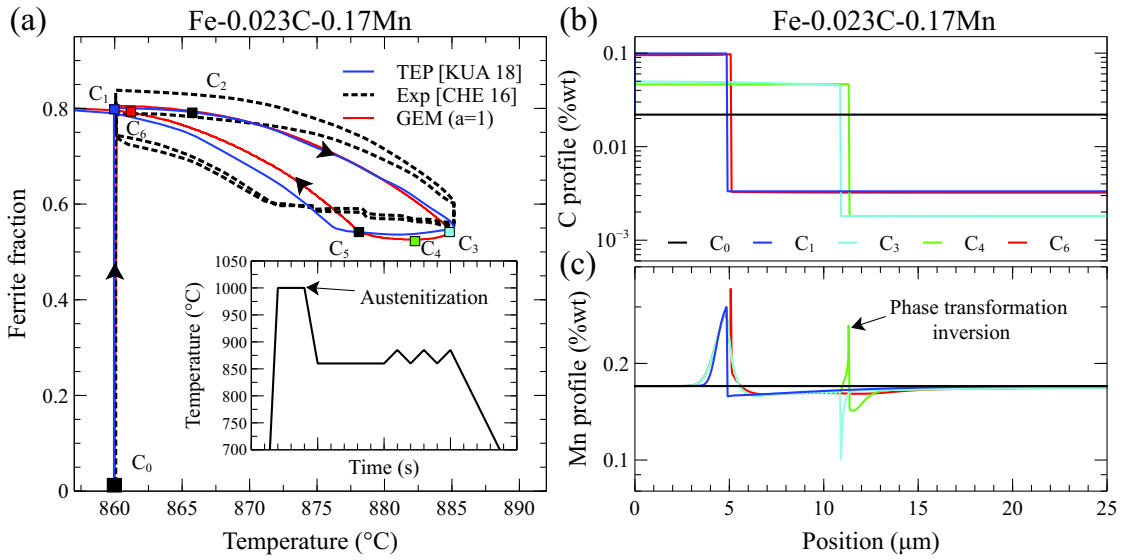

Figure 3.34: (a) Evolution of the volume fraction of ferrite for the cyclic phase transformation in the Fe-0.023C-0.17Mn alloy. $C_1 \rightarrow C_2$ and $C_4 \rightarrow C_5$ are the stagnant stages, $C_2 \rightarrow C_3$ and $C_5 \rightarrow C_6$ are the regular phase transformation stages, $C_3 \rightarrow C_4$ is the inverse phase transformation stage [CHE 16, KUA 18] (b) Carbon concentration profile snapshots. (c) Manganese concentration profile snapshots.

The GEM model provides interesting results in comparison with experimental kinetics close to those obtained with the TEP model. In both cases, the predicted stagnant stage is lower than the one obtained experimentally and the $\gamma \rightarrow \alpha$ transformation kinetics are also lower. Nevertheless, as shown with the TEP model [KUA 18], one of the key parameters controlling the length of the stagnant stage is the diffusion coefficient within the interface. The choice was made during this study to keep $a = 1$ to be consistent with the transformation simulations during complex cycles. Nevertheless, the diffusion coefficient increase in the interface leads to a higher manganese partitioning which induces

Cette thèse est accessible à l'adresse : http://theses.insa-lyon.fr/publication/2020LYSEI120/these.pdf
© [A. MATHEVON], [2020], INSA Lyon, tous droits réservés

an extension of the stagnant stage. This model can therefore be applied in the case of complex systems on cyclic heat treatments since it allows to take into account both the mobility of the interface and the diffusion inside the interface as well as in the bulk for the different chemical elements of the system.

3.5 Conclusions

A Gibbs Energy Minimization model was developed in this thesis and it was tested on ternary and quaternary systems with complex thermal cycles including cementite dissolution. This model provides the kinetics of $\alpha \rightarrow \gamma$ and $\gamma \rightarrow \alpha$ transformations without imposing any type of equilibrium conditions at the interface while including diffusion within the interface. This numerical approach respect mass balance and leads to drastic reduction of the computation times compared to existing models.

First, the effects of the numerical parameters of the system as well as the physical parameters (interface diffusion coefficient, length size) were analyzed. The effect of the cementite dissolution and cementite enrichment was then studied in the case of ternary Fe-C-Mn alloy. Subsequently, complex cycles reproducing industrial cycles were used to validate the accuracy of the model on a wide range of Fe-C-Mn steels. It was thus possible to use the half distance between the pearlite rich zones and the cementite enrichment in alloying elements to highlight the model's sensitivity to the annealing temperature and to the alloy's chemical composition.

The requirement to introduce chromium into the simulation in order to stabilize the cementite for the prediction of transformation kinetics in the case of an industrial grade was highlighted. The interaction between the recrystallization and the phase transformation model allowed to reproduce the sensitivity of the different initial states of the DP1000 to the heating rate during the annealing treatment.

Finally, the model was tested on a cyclic thermal cycle and on decarburization tests which allowed to prove the model's reversibility for $\gamma \rightarrow \alpha$ transformations.

Cette thèse est accessible à l'adresse : http://theses.insa-lyon.fr/publication/2020LYSEI120/these.pdf
© [A. MATHEVON], [2020], INSA Lyon, tous droits réservés

Cette thèse est accessible à l'adresse : http://theses.insa-lyon.fr/publication/2020LYSEI120/these.pdf
© [A. MATHEVON], [2020], INSA Lyon, tous droits réservés

Chapter 4

Thermodynamic based model coupled with phase transformation simulation to predict the Ms temperature in the case of two-phase steel

Once the austenite fraction has been obtained during the intercritical annealing, the ferrite-martensite microstructure is produced during the cooling stage which influences the final microstructure. This chapter proposes to study the different mechanisms driving the austenite → martensite phase transformation, as well as to suggest solutions to predict it from existing models in the literature. From a Continuous Cooling Transformation (CCT) diagram established for two initial states (*i.e.* partially or fully austenitic) in the PhD-work of Melanie Ollat [OLL 17b], the objective is to understand austenite stabilization and the martensitic transformation delay observed in the case of partially austenitic steels compared to fully austenitic steels. Several hypotheses will be added to the Bohemen prediction model [BOH 17] such as carbon enrichment of austenite, grain size refinement and partitioning of subsitutional elements. Two thermal cycles leading to the same austenite volume fraction but with different levels of manganese partitioning will allow us to observe the effect of subsitutional element partitioning. Then, the coupling with the GEM phase transformation model will enable to model the martensite start temperature (M_S) as well as the kinetics of the martensitic transformation.

Cette thèse est accessible à l'adresse : http://theses.insa-lyon.fr/publication/2020LYSEI120/these.pdf
© [A. MATHEVON], [2020], INSA Lyon, tous droits réservés

Contents

Cette thèse est accessible à l'adresse : http://theses.insa-lyon.fr/publication/2020LYSEI120/these.pdf
© [A. MATHEVON], [2020], INSA Lyon, tous droits réservés

4.1 Literature review

Several types of cooling can be applied after austenite formation during annealing. The steel can be industrially cooled down to room temperature or to an intermediate temperature in the case of direct coating using a liquid zinc bath. Since martensitic transformation generally occurs at low temperatures, it is important from the final product quality point of view to be able to predict the temperature associated with the beginning of the martensitic transformation and the transformation kinetics.

4.1.1 Austenite decomposition

Depending on the cooling rate, R_C, applied from the intercritical annealing temperature, the austenite can decompose into different phases [THO 90]. Figure 4.1 [BOH 10] shows the 3 types of decomposition products which can be formed as a function of the cooling rate for different temperature stages: (i) the ferritic/pearlitic domain above 600 °C, (ii) the bainitic domain between 300-600 °C, and (iii) the martensitic domain below 300 °C. Although each decomposition product has its own temperature range for its formation, the fraction of formed products will depend on many parameters such as: (i) the cooling rate, (ii) the austenitic phase which is more or less stabilised by the steel chemical composition, (iii) the intercritical annealing conditions which may change the austenite grain size and chemical composition and (iv) the other decomposition products [ZHU 13]. As the final microstructure of DP steels is a mixture of ferrite and martensite, it is interesting to understand precisely the mechanisms involved in the martensitic transformation.

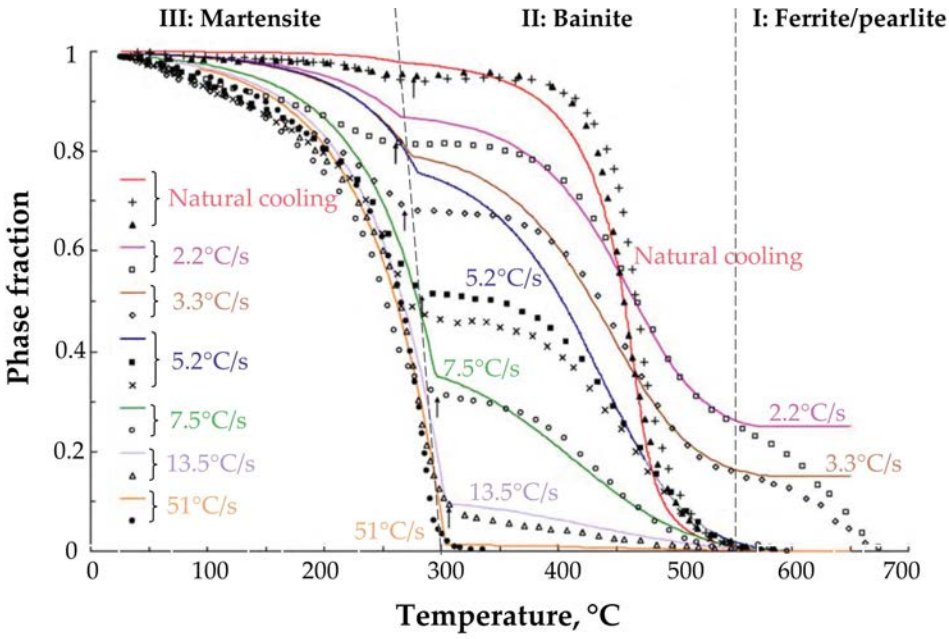

Figure 4.1: Examples of austenite decomposition paths as a function of the cooling rate for a 0.41C-1.04Cr-0.71Mn-0.22Si-0.26Ni wt.% steel (Lines correspond to a modified Koistinen-Marburger law and points correspond to experimental points) [BOH 10].

Cette thèse est accessible à l'adresse : http://theses.insa-lyon.fr/publication/2020LYSEI120/these.pdf
© [A. MATHEVON], [2020], INSA Lyon, tous droits réservés

4.1.2 $\gamma \rightarrow \alpha'$ phase transformation

The martensite formation is due to a crystallographic change from a body-centered cubic phase (austenite, fcc) to a face-centered tretragonal phase (martensite, bct) as schematically shown in Figure 4.2.(a) [OLS 76a, OLS 76b, OLS 76c, KRA 99]. This phase appears at high cooling rates and is obtained by a displacive transformation since the atoms reorganize themselves over a very short distance (about the inter-atomic spacing). Not allowing the chemical species diffusion during the transformation, martensite has the same chemical composition as the prior austenite. Generally inheriting a carbon supersaturation of the austenitic phase, martensite is a metastable phase. The volume change between martensite and austenite during the transformation generates a strong deformation within the steel. This phenomenon is responsible for a complex microstructure on several scales (it is made of packets, blocks, laths) [MOR 15] and the appearance of a dislocation cell network (see Figure 4.2.(b)).

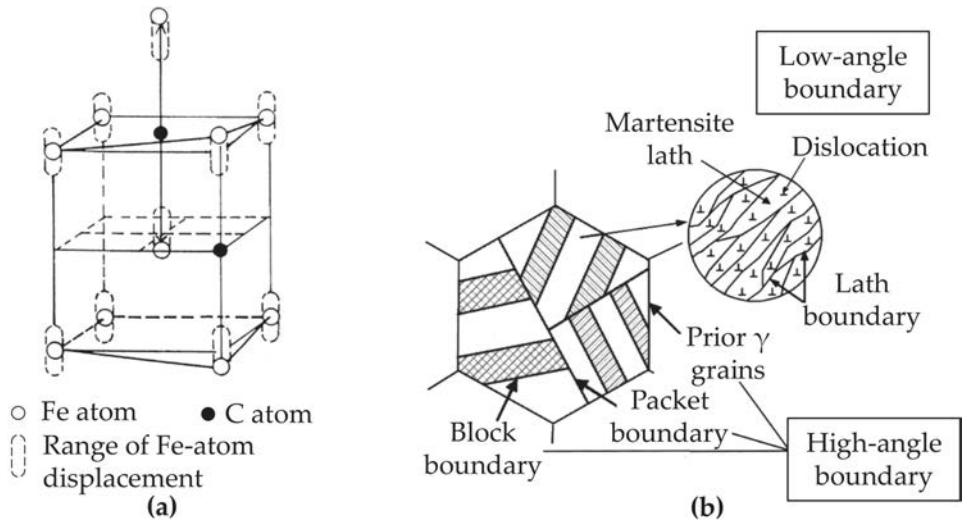

Figure 4.2: Schematic representation of (a) the displacement required for the atoms to enable the crystallographic transformation from fcc to bct structure [KRA 99] and (b) the complex arrangement of the martensite microstructure [FUR 04].

Many parameters influence the martensitic transformation which is naturally very heterogeneous from a chemical point of view due to segregation during cooling and the inheritance of the previous thermal cycle [KHA 90]. First of all the austenite carbon enrichment will delay the martensite formation towards lower temperatures since it decreases the driving energy. More recently authors have shown that the decrease in the prior austenitic grain size (D_γ) could also delay the martensitic transformation [SAS 65, YAN 09, LEE 05, GAR 08]. This could be explained by a Hall-Petch effect: fine austenite grains could have a better resistance to deformation. Moreover, the decrease in grain size forces the martensite laths to deform the austenitic grains during their formation leading to an increase in the energy required for transformation [MOR 05].

On the one hand, the kinetics of martensitic transformation is athermal [BOH 14] since it does not depend on the cooling speed once the critical cooling speed has been reached.

Cette thèse est accessible à l'adresse : http://theses.insa-lyon.fr/publication/2020LYSEI120/these.pdf
© [A. MATHEVON], [2020], INSA Lyon, tous droits réservés

The dislocations generated during phase transformation generate numerous nucleation sites for the martensite leading to a self-catalytic nucleation [BHA 01]. On the other hand the plastic deformation generated by the volume change close to the transformation zone leads to austenite stabilization which requires a higher driving force to progress.

Although many studies detail and propose mechanisms to understand martensitic transformation in fully austenitic steels, very few focus on the two-phase states (partially austenitic steels). It has been shown [GHO 94, BOH 17] that the transformation is delayed mainly due to a grain size refinement and due to the austenite enrichment in substitutional elements resulting from the partitioning of these elements. Zhu *et al.* [ZHU 13] showed the presence of numerous ferrite/austenite interfaces that do not seem to play an important role although increasing the number of possible nucleation sites.

4.1.3 Modelling tools for the M_S prediction of fully austenitic steels

This part describes the different models available in the literature to predict the martensite start temperature M_S and the kinetics of the martensitic transformation in the case of fully austenitic steels. The hypotheses to consider the effect of the two-phase states will also be discussed in Section 4.3.2.

4.1.3.1 Empirical models

Many models [AND 65, ELD 77, RAN 46, KUN 82, NEH 46, PAY 44b, STE 56, EIC 53, SVE 97, CAR 44, WAN 99, BOH 12, BAR 14] were developed to evaluate the M_S temperature of steels quenched from the fully austenitic domain. Table 4.1 lists most of those proposed in the literature. These models are based on an empirical approach and generally account for the effect of alloying elements on the M_S temperature value. Among all these elements, carbon plays a major role, as it is known to decrease strongly the M_S temperature. However, it has to be noted that the abovementioned models often neglect the effect of the prior austenite grain size on the transformation and are usually calibrated for a given range of chemical composition.

In order to improve preceding models, neural networks models have been developed. They use artificial intelligence and numerous input variables to refine the result [CAP 02, CAP 03, PEE 15]. These models can predict the martensite start temperature, M_S, more accurately than classical empirical models by calibrating the neural network with a large input database. More recently, Peet *et al.* have proposed to use the results of a thermodynamic-based prediction model as input data for the neural network to improve it. The main drawback of the neural network approach is its lack of physical basis which does not enable to include additional effects (grain sizes, enrichment of chemical composition) easily. In addition, the calibration is performed using a large number of experimental results over a defined data range which does not allow to extrapolate results without error risk outside this range.

Cette thèse est accessible à l'adresse : http://theses.insa-lyon.fr/publication/2020LYSEI120/these.pdf
© [A. MATHEVON], [2020], INSA Lyon, tous droits réservés

Authors	Equations (All values are dimensionless, compositions are in weight percent, M_S is in °C)
Payson & Savage [PAY 44a]	M_S=499-308C-32.4Mn-10.8Si-27Cr-16.2Ni-10.8Mo -10.8W
Nehrenberg [BAR 14]	M_S=499-292C-32.4Mn-10.8Si-22Cr-16.2Ni-10.8Mo
Grange & Steward [BAR 14]	M_S=538-350C-37.7Mn-18.9Ni-27Mo
Eichman & Hull [BAR 14]	M_S=41.7(14.6-Cr)+61.1(8.9-Ni)+33.3(1.33-Mn)+27.8(0.47-Si)+1666.7(0.068-(C+N))-17.8
Steven & Haynes [BAR 14]	M_S=561-474C-33Mn-17Cr-17Ni-21Mo
Kung & Rayment [BAR 14]	M_S=539-423C-30.4Mn-7.5Si-12.1Cr-17.7Ni-7.5Mo+10Co
Sverdlin & Ness [BAR 14]	M_S=520-320C-50Mn-30Cr-20(Ni+Mo)-5(Cu+Si)
Andrews (1) (1965)	M_S=462-273C-26Mn-13Cr-16Ni-30Mo
Andrews (2) (1965)[BAR 14]	M_S=539-423C-30.4Mn-11Si-12.1Cr-17.1Ni-7Mo
Andrews (3) (1965)[BAR 14]	M_S=512-453C-71.5Mn+15Cr-16.9Ni-9.5Mo-67.7C*Cr
Eldis (1977)[BAR 14]	M_S=531-391.2C-43.3Mn-16.2Cr-21.8Ni
Wang (1) (2000) [WAN 00]	M_S=545-470.7C-37.7Mn-21.5Cr-3.96Si+38.9Mo (0.2<C<0.5, 0.2<Si,Mn,Cr<2, 0.1<Mo<0.7)
Wang (2) (2000) [WAN 00]	M_S=540-584.9C-117.7Mn-23.1Si-42.5Cr+49.9Mo-62.5C.Si+178.3C.Mn - 10C.Cr+52.5C.Mo+117.2Si.Mn+50.9Si.Cr-142.2Si.Mo-29.2Mn.Cr-9.7Mn.Mo+69.9Cr.Mo
Capdevilla (2002)[CAP 02]	M_S(K)=764.2-302.6C-30.6Mn-14.5Si-8.9Cr-16.6Ni+2.4Mo-11.3Cu+8.58Ci+7.4W
Carapella (2012)[BAR 14]	M_S=496(1-0.62C)(1-0.092Mn)(1-0.033Si)(1-0.045Ni)(1-0.07Cr)(1-0.03Mo)(1-0.018W)(1-0.01Co)
Barbier (2014)[BAR 14]	M_S=545-601(1-exp(-0.87C))-34.4Mn-13.7Si-9Cr-17.3Ni-15.4Mo+11V+5Co-1.4Al-16Cu-361Nb-2.4Ti (1.9<C, 10<Mn, 2<Si, 18<Cr, 30<Ni, 5<Mo, 1<V, 16<Co, 3<Al, 2<Cu, 0.1<Nb, 1.6<Ti)
Bohemen (2012) [BOH 12]	M_S (K)=565-600(1-exp(-0.96C))-31Mn-13Si-10Cr-18Ni-12Mo 0.1<C<1.9, 3<Mn, 2<Si, 4<Cr, 5<Ni, 0.8<Mo

Table 4.1: Martensite start (M_S) temperature as a function of steel chemistry (composition in wt.%).

© 2020 – Alexandre MATHEVON – MATEIS laboratory

Cette thèse est accessible à l'adresse : http://theses.insa-lyon.fr/publication/2020LYSEI120/these.pdf
© [A. MATHEVON], [2020], INSA Lyon, tous droits réservés

4.1.3.2 Thermodynamically-based model

Several authors [GHO 94, BOH 17] have developed models based on thermodynamics, for which new contributions can be added. This is the case of the model developed by Bohemen *et al.* [BOH 17] who improved the basic model of Gosh and Olson [GHO 94] by integrating the grain size effect on the M_S prediction. They added two contributions enabling to take into account the M_S temperature decrease resulting from a grain size refinement and the change in the martensite lath aspect ratio.

General equation for M_S prediction

The phase transformation of austenite into martensite is assumed to occur when the change in free energy (ΔG_c) accompanying the transformation is greater than the energy required to achieve it. This energy is generally related to the energy required to overcome expansion resistance, deformation energy and the creation of new interfaces.

As already mentioned, the model used in the present study was developed by Bohemen *et al.* [BOH 17]. It enables to take into account the effect of the chemical composition and that of the austenitic grain size on the M_S temperature using the following formula:

$$M_S = T_1 - \left(\frac{\Delta G_c}{S}\right) \tag{4.1}$$

where : (i) T_1 is the temperature for which α and γ have the same Gibbs energy, (ii) ΔG_c is the driving force necessary to achieve austenite $\rightarrow$ martensite transformation at $T = M_s$ (see Figure 4.3) and (iii) S is the assumed constant entropy of the steel.

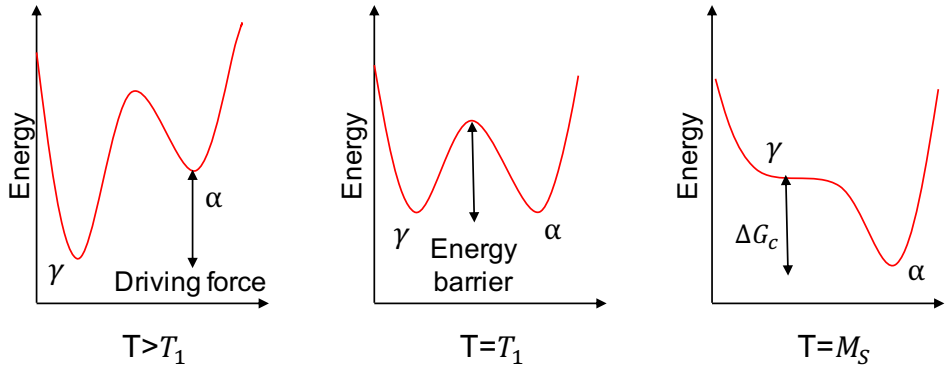

Figure 4.3: Schema illustrating the energy evolution between austenite and ferrite for several temperatures: (i) T>T1 austenite is the stable phase, (ii) T=T_1 the energy of the two phases is equivalent but an energy barrier prevents the phase transformation and (iii) T=M_S the driving force is equal to the energy barrier required to achieve the phase transformation.

Thermodynamic model for the prediction of T_1

In order to determine the chemical energy gain when transforming austenite into martensite, it is possible to use a thermodynamic simulation software (such as Thermocalc or

Cette thèse est accessible à l'adresse : http://theses.insa-lyon.fr/publication/2020LYSEI120/these.pdf
© [A. MATHEVON], [2020], INSA Lyon, tous droits réservés

FactStage) or to assume a linear variation of the free energy as a function of temperature for different compositions over a certain range of values. This simplification makes it possible to determine the value of T_1 as a function of the alloy composition using the following formula:

$$T_1 = T_0 + \sum_i K_0^i C_i^0 \tag{4.2}$$

for steels with $C_C^0 < 1\,\text{wt\%},\ C_{Mn}^0 < 5\,\text{wt\%},\ C_{Si}^0 < 3\,\text{wt\%},\ C_{Cr}^0 < 3\,\text{wt\%}, \text{C}_{Ni}^0 < 6\,\text{wt\%},$ $C_{Mo}^0 < 4\,\text{wt\%}$. C_i^0 is the mass element content of the element i in steel.

The value of T_0 and the various K_0^i coefficients were determined using a linear extrapolation of FactStage thermodynamic data [BOH 17].

Units	T_0	K_0^C	K_0^{Mn}	K_0^{Si}	K_0^{Cr}	K_0^{Ni}	K_0^{Mo}
(K)	718.3	-291	-24	-1.8	-5.6	-18.4	3.5

Table 4.2: Summary of the constants used in Equation 4.2

Model for the prediction of ΔG_c (Chemical composition and grain size effect)

Bohemen's model novelty is based on the addition of two terms (ΔG_{HP} and ΔG_{SH}) in the critical driving force ΔG_c expression originally proposed by Ghosh and Olson [GHO 94] in order to take into account the grain size effect. This leads to the following equation for ΔG_c :

$$\Delta G_c = \Delta G_0 + \Delta G_\mu(K_\mu^i, C_i^0) + \Delta G_{HP}(K_{HP}, D_\gamma) + \Delta G_{SH}(K_{SH}, D_\gamma^c, D_\gamma) \tag{4.3}$$

with ΔG_0 a constant, ΔG_μ the additionnal free chemical energy due to the friction forces coming from the alloying elements [GHO 94], ΔG_{HP} the free energy due to grain refinement (Hall and Petch mechanism), ΔG_{SH} the free energy due to the martensite unit shape factor [BOH 17] .

The term ΔG_μ is given by the following equation :

$$\Delta G_\mu = K_\mu^C \sqrt{C_C^0} + \sqrt{\sum_i \left(K_\mu^i \sqrt{C_i^0} \right)^2} \tag{4.4}$$

The different values of the K_μ^i coefficients have been adjusted from a database of 120 steels [BOH 17] and C_i^0 concentrations are expressed in wt.%.

Units	K_μ^C	K_μ^{Mn}	K_μ^{Si}	K_μ^{Cr}	K_μ^{Ni}	K_μ^{Mo}
(J.mol^{-1})	670	195	140	170	-18.4	3.5

Table 4.3: Summary of the constants used in Equation 4.4

In Equation 4.3, two mechanisms are supposed to contribute to the M_S temperature variation when the grain size varies.

Cette thèse est accessible à l'adresse : http://theses.insa-lyon.fr/publication/2020LYSEI120/these.pdf
© [A. MATHEVON], [2020], INSA Lyon, tous droits réservés

The first mechanism corresponds to a hardening of Hall and Petch type as proposed by Ansell *et al.* [BRO 83, BRE 70, NIC 77]. It results from the fact that the increase in the autenite grain leads to a local reduction of plastic deformations in austenite. Brofman and Ansell [BRO 83] have shown that the M_S reduction is proportional to the square root of the austenitic grain size. This dependence leads to the following expression of ΔG_{HP}:

$$\Delta G_{HP} = \frac{K_{HP}}{\sqrt{D_\gamma}} \tag{4.5}$$

The second mechanism is due to an increase in the martensite unit aspect ratio (c/a) [NIC 77] with a grain size decrease. This shape change can only occur with a higher driving force and therefore with a lower M_S temperature. The free chemical energy associated with this shape change is described by the following formula:

$$\Delta G_{SH} = K_{SH} \exp\left(-\frac{6D_\gamma}{D_\gamma^C}\right) \tag{4.6}$$

where D_γ^C is the austenitic critical grain diameter before the formation of a martensitic sub-unit single package.

The coefficients present in the various contributions defined above are summarized in Table 4.4.

ΔG_0 ($\mathrm{J.mol^{-1}}$)	K_{HP} ($\mathrm{J.mol^{-1}}$)	K_{SH} ($\mathrm{J.m^{0.5}.mol^{-1}}$)	D_γ^C (μm)	S ($\mathrm{J.mol^{-1}.K^{-1}}$)
1015	370	350×10^{-3}	11	7.22

Table 4.4: Summary of the constants used in the model

4.1.4 Martensite formation kinetics

Several empirical laws are generally used to describe the martensitic transformation kinetics [KOI 59, BOH 09a, BOH 09b, BOH 12, SKR 91]. We can cite:

- **The Koistinen-Marburger** law expressed as follows:

$$f_{\alpha'} = 1 - \exp\left(-\alpha_m \left(M_S - T\right)\right) \tag{4.7}$$

with M_S the martensite start temperature and α_m a parameter governing the slope of the curve. Several expressions of α_m have been proposed according to the chemical composition by different authors in addition to the expression of the M_S temperature summarized in Table 4.5.

Cette thèse est accessible à l'adresse : http://theses.insa-lyon.fr/publication/2020LYSEI120/these.pdf
© [A. MATHEVON], [2020], INSA Lyon, tous droits réservés

Authors	Equations (Values are dimensionless, compositions are in wt%, M_S is in °C)
Andrew [BOH 09a]	α_m=0.0224-0.0107C_C^0-0.0007C_{Mn}^0-0.00005C_{Ni}^0-0.00012C_{Cr}^0-0.0001C_{Mo}^0 (C_C^0<1.9, C_{Ni}^0<14.9, C_{Cr}^0<8)
Bohemen [BOH 12]	α_m=(27.2-19.8(1-exp(-1.56C_C^0))-0.14C_{Mn}^0-0.21C_{Si}^0-0.11C_{Cr}^0-0.05C_{Mo}^0)×10^{-3} (C_C^0<1.9, C_{Mn}^0<3, C_{Si}^0<2, C_{Cr}^0<4, C_{Mo}^0<0.8)

Table 4.5: Expression of M_S and α_m parameters for the Koistinen-Marburger equation (compositions in wt.%).

- **The skrotzki** equation which is defined from 3 parameters (M_S, M_F, p):

$$f_{\alpha'} = 1 - \left(\frac{T - M_S}{M_S - M_F}\right)^p \tag{4.8}$$

where M_F is the martensite end temperature.

These empirical formulas allow to reproduce the experimental kinetics observed for fully austenitic states. It is driven by the mechanical stabilization of austenite during transformation. Nevertheless, these formulas cannot be extended to two-phase states [OLL 17b] since they are based on the M_S definition defined for entirely austenitic states.

4.1.5 Conclusion: Objective of the present chapter

In the above mentioned context, the objective of the works presented in this chapter is to generalize the new M_S temperature predictive model developped by Bohemen *et al.* [BOH 17] for fully austenitic steels to the case of two-phase steels since the majority of the models have been designed only for fully martensitic steels. This model makes it possible to include grain size refinement during the phase transformation. Moreover a coupling with the GEM phase transformation prediction model developed in Chapter 3 will allow us to include the possible enrichment of the different chemical elements at the interface. The martensitic kinetics prediction models will then be applied using the new M_S temperature prediction model for two-phase steels.

4.2 Material and procedure

The works of this chapter were carried out on the industrial DP1000 steel of this study (see Table 1.2). In order to investigate the influence of the microstructural state before cooling on the M_S temperature, three different states (fully or partially austenitic) were produced in the Gleeble thermo-mechanical simulator using heating by Joule effect and cooling through direct air projection on the specimens. For this purpose, samples (10 mm wide by 100 mm long) were heated to the chosen temperature with a heating rate of 5 °C/s and then, isothermally treated with a precise temperature control (± 3 °C) thanks to the use of type-K thermocouples welded on the surface of the specimens.

The thermal cycles used for each state are summarised in Figure 4.4. A fully austenitic state (denoted 100%γ-state herafter) was obtained after 120 s of holding at 850 °C as shown in Figure 4.5.(a). In addition, two partially austenitic states, for which the target

Cette thèse est accessible à l'adresse : http://theses.insa-lyon.fr/publication/2020LYSEI120/these.pdf
© [A. MATHEVON], [2020], INSA Lyon, tous droits réservés

austenite fraction was 60 %, were produced thanks to (i) an annealing treatment at 760 °C for 300 s, thus allowing a manganese spike at the interface to be created ($60\%\gamma - 1$ state) (see Figure 4.5.(b)) and (ii) a continuous heating up to 805 °C followed by a subsequent rapid cooling ($60\%\gamma - 2$ state).

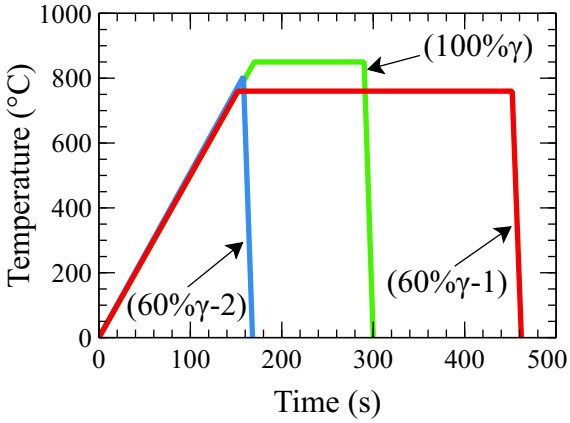

Figure 4.4: Thermal cycle applied for the different states ($100\%\gamma, 60\%\gamma - 1, 60\%\gamma - 2$)

An optical Led dilatometer was used to monitor the samples length changes during martensite transformation and to determine the M_S temperature from the three initial states. The tangent method was applied to determine the kinetics of transformation as described in Ollat thesis [OLL 17b].

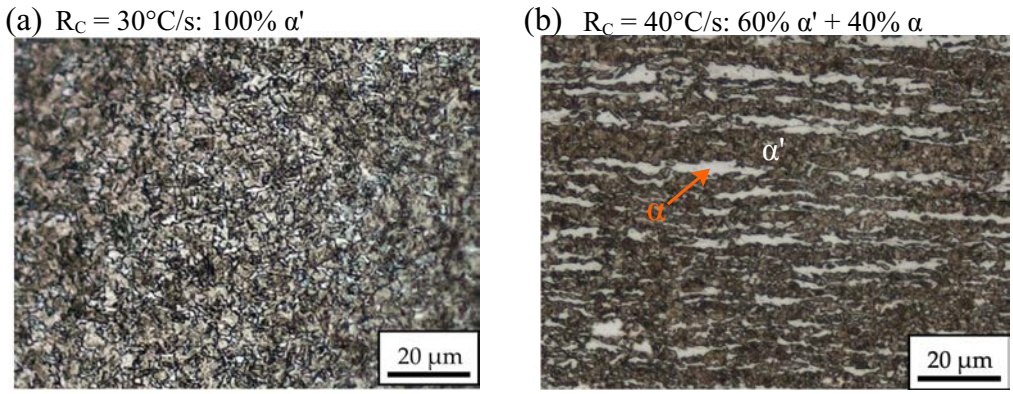

Figure 4.5: Optical micrographs of (a) the ($100\%\gamma$) state cooled at R_C=30 °C/s and (b) the ($60\%\gamma$-1) state cooled at R_C=40 °C/s. Quantified phase fractions evaluated by optical analysis are reported in the caption of each micrograph after nital etching.

4.3 Results and discussion

As already explained, the aim of the studies presented in this chapter is to propose a new approach to predict the M_S temperature in the case of two-phase steels (such as Dual-Phase steels). The approach originality consists in coupling the thermodynamic

Cette thèse est accessible à l'adresse : http://theses.insa-lyon.fr/publication/2020LYSEI120/these.pdf
© [A. MATHEVON], [2020], INSA Lyon, tous droits réservés

model developed by Bohemen *et al.* [BOH 17] for the M_S prediction with the GEM phase transformation model likely to determine the composition in the alloying element at α/γ interfaces before quenching.

4.3.1 Preliminary work - CCT diagrams from a fully or partially austenitic state

Figure 4.6.(b) shows the Continuous Cooling Transformation (CCT) diagrams of the insvestigated steel built by Ollat [OLL 17b], using LED dilatometry, starting from the $(100\%\gamma)$ and $(60\%\gamma - 1)$ states for cooling rates between 1 °C/s and 40 °C/s. Dilatation curves were analyzed using the tangent method in order to get the austenite decomposition kinetics (see Figure 4.6.(a)) and to determine the start and finish temperatures for ferrite and pearlite $((F+P)_S, (F+P)_F)$, bainite (B_S, B_F), and martensite (M_S, M_F).

The main conclusions which can be drawn from Figure 4.6.(b) are the following :

1) The domain associated with ferrite and pearlite remains globally unchanged regardless of the initial austenite fraction but it is slightly shifted towards lower temperatures with decreasing the austenite fraction (*i.e.* with increasing the austenite carbon content).

2) The bainitic domain is extended for the $(60\%\gamma - 1)$ state. Bainite is obtained for a larger range of cooling rate (10-30 °C/s) compared to only 20 °C/s for the $(100\%\gamma)$ state.

3) The martensitic domain is shifted towards lower temperatures when the austenite fraction of the initial state decreases.This is in agreement with the austenite carbon enrichment in the partially austenitic steel. Table 4.6 summarizes the M_S temperatures obtained for the three different initial states considered in this study as well as their prior austenite grain sizes.

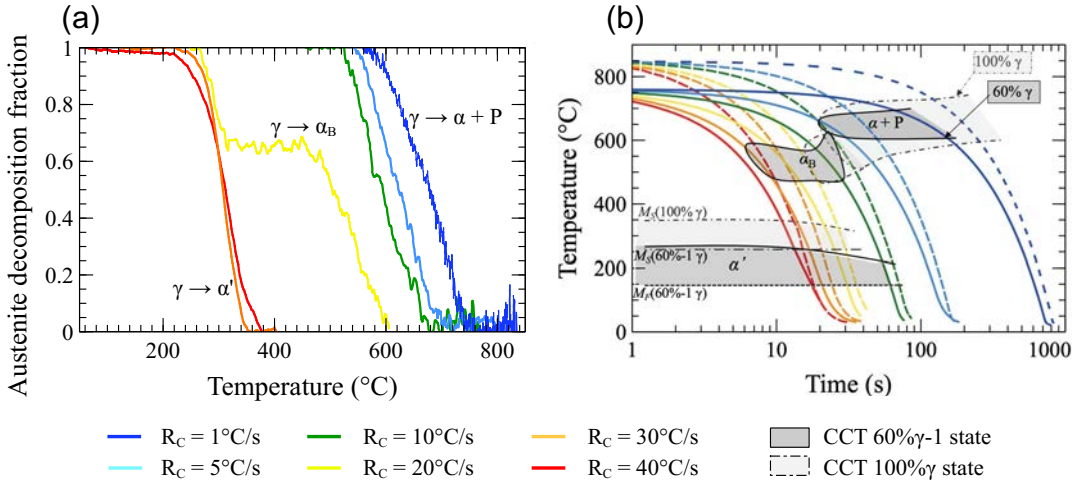

Figure 4.6: a- Austenite decomposition fractions of the $100\%\gamma$-state during continuous cooling from 850 °C to room temperature at 1, 5, 10, 20, 30 and 40 °C/s and b- Comparison of the CCT diagrams obtained during continuous cooling of the $(100\%\gamma)$ state (dashed lines) and of the $(60\%\gamma - 1)$ state (full lines) [OLL 17b].

Cette thèse est accessible à l'adresse : http://theses.insa-lyon.fr/publication/2020LYSEI120/these.pdf
© [A. MATHEVON], [2020], INSA Lyon, tous droits réservés

State	$(100\%\gamma)$	$(60\%\gamma - 1)$	$(60\%\gamma - 2)$
M_S (°C)	360	265	295
D_γ (μm)	3.8	1.8	1.7

Table 4.6: Summary of the experimental values for the M_s temperature and for the prior austenite grain size obtained for all initial states

4.3.2 Prediction of the M_S temperature in two-phase steel

Figure 4.7 presents the results of the different prediction models for the M_S temperature when they are applied to the DP1000 steel in the $(100\%\gamma)$. These models can be divided in two categories: (i) the empirical models based only on the steel chemistry (presented in Table 4.1) and (ii) the thermodynamic model of Bohemen *et al.* [BOH 17] presented in Section 4.1.3.2 which also enables to take into account the grain size.

For the application of the models to the case of the $(100\%\gamma)$ state, its M_S temperature was calculated using the bulk composition of the DP1000 steel and a mean austenitic grain size of 3.6 μm in the direction perpendicular to the cold-rolling direction. As can be seen in Figure 4.7, most models are able to reproduce the $(100\%\gamma)$ experimental data. This is consistent with the fact that the models were developed for fully austenitic steels In the following, the objective is to discuss the application of these models to the case of the $(60\%\gamma)$ states by considering, in a first approach, that the only change to take into account is due to the austenite carbon enrichment. Then, due to the inability of this assumption to account for the experimental results, the effect of other factors (grain size, substitutional enrichment of austenite) will be discussed in the case of the thermodynamic model of Bohemen.

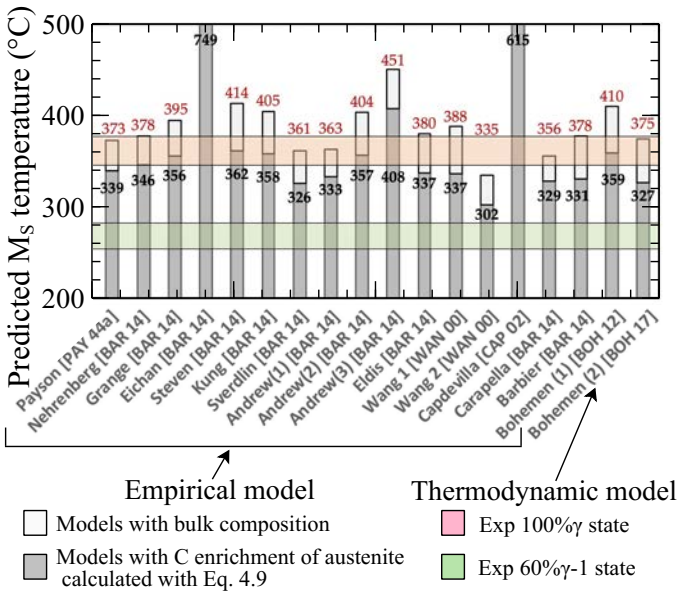

Figure 4.7: Comparison of the different M_s prediction models of the literature on the $(100\%\gamma)$ and $(60\%\gamma - 1)$ states. The empirical formulas used for calculating M_S temperatures are listed in Table 4.1 and the thermodynamic model retained in this work proposed by Bohemen [BOH 17] is detailed in Section 4.1.3.2.

Cette thèse est accessible à l'adresse : http://theses.insa-lyon.fr/publication/2020LYSEI120/these.pdf
© [A. MATHEVON], [2020], INSA Lyon, tous droits réservés

4.3.2.1 Austenite carbon enrichment

In order to apply the preceding models to the case of the (60%γ) states, it was first considered that the only change to bring is to modify the austenite carbon content in the chemical composition of the steel. The carbon enrichment of austenite can be calculated from the mass balance of carbon in the steel expressed by the following formula:

$$\left(C_C^{\gamma} = \frac{C_C^0 - (1 - f_{\gamma})\, C_C^f}{f_{\gamma}} \right) \tag{4.9}$$

where C_C^{γ}, C_C^f, C_C^0 are respectively the austenite before quenching, ferrite ($0.015 wt\%$) and bulk carbon composition.

Including the hypothesis of austenite carbon enrichment for the two-phase ($60\%\gamma - 1$) state, no model presented in Figure 4.7 faithfully reproduces the observed experimental drop of about 100 °C between the 100%γ and $60\%\gamma - 1$ since the predicted M_S values are overestimated of approximatively 50-100 °C.

The present results thus disagree with the works of Bohemen and Sietsma [BOH 09b] who showed that the carbon content is the only parameter to modify in the chemical composition to predict the M_S temperature of partially austenitized steels. These discrepancies could be due to that fact that their expriments were performed on steels with a much higher carbon content (0.46-0.8 wt%) and with a much lower content of alloying elements (Mn 0.7 wt%).

Taking into account the results obtained in this work on the two-phase states, it seems necessary to consider that other factors are likely to play a role on the M_s temperature value in the case of multiphase steels (austenite grain size refinement and presence of alloying elements such as Mn, Cr, Si....). Only the thermodynamic model developed by Bohemen *et al.* [BOH 17] allows to include all these potential contributions and was therefore the only one retained in the following study.

4.3.3 Austenite grain size refinement

To take into account the grain refinement in the thermodynamical model [BOH 17] , it is necessary to evaluate the average distance between grain boundaries perpendicular to the direction of cold-rolling, which may be different from the average grain size depending on the cold-rolling reduction ratio. Using microscopic observations and the Fiji software, a local thickness algorithm [HIL 96, SAI 94] was applied to each investigated state of this study leading to the grain size values given in Table 4.6. In this study, only the values measured by microscopic observation were used in the simulations. Nevertheless for the sake of simplicity, in order to estimate the γ grain size in two-phase steel, we propose the following formula:

$$D_{\gamma}^{f_{\gamma}} = f_{\gamma} D_{\gamma}^{100\%\gamma} \tag{4.10}$$

where $D_{\gamma}^{f_{\gamma}}$ and $D_{\gamma}^{100\%\gamma}$ are respectively the austenitic grain size of two-phase and single-phase steel. This relationship assumes a constant grain number between $f_{\gamma} = 60\%\gamma$ and

Cette thèse est accessible à l'adresse : http://theses.insa-lyon.fr/publication/2020LYSEI120/these.pdf
© [A. MATHEVON], [2020], INSA Lyon, tous droits réservés

$f_\gamma = 100\%\gamma$. It slightly overestimates the observed experimental values but enables an efficient estimation.

Although the addition of the grain size refinement hypothesis reduces the M_S temperature in the case of the two-phase steel $(60\%\gamma - 1)$, Figure 4.8.(a) shows that it is not yet sufficient to fully explain the drop observed experimentally. However, in the case of the two-phase steel $(60\%\gamma - 2)$, the addition of the grain size refinement hypothesis is sufficient to explain the observed experimental drop, leading to a correct prediction of the M_S temperature (see Figure 4.8.(b)).

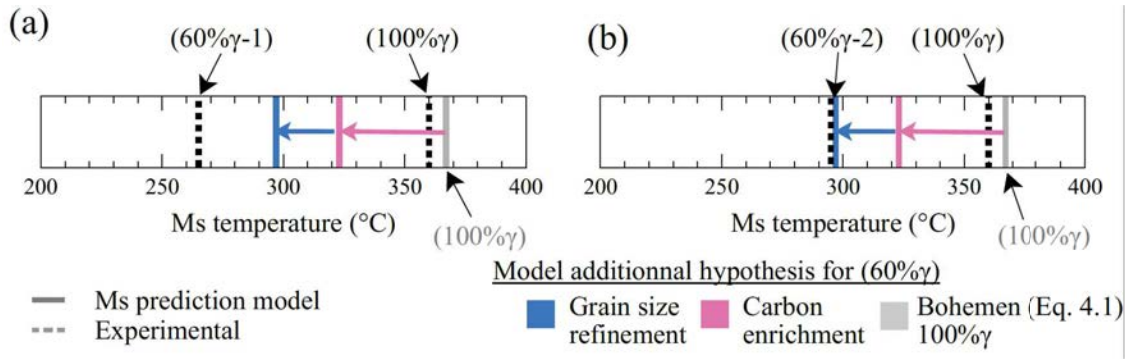

Figure 4.8: Comparison of the model predictions for M_S with the experimental data for : (a) the $(60\%\gamma - 1)$ state and (b) the $(60\%\gamma - 2)$ state.

4.3.4 Alloying element enrichment at the interface

The heat treatment necessary for austenite formation in the case of two-phase steels can, depending on the annealing conditions, lead to a partitioning of the substitutional elements at the interface which can delay the austenite-martensite transition. In order to predict and model the substitutional element enrichment at the interface, the GEM model was used. It allows to predict the austenite fraction formed during heating from the initial state at room temperature as well as the different diffusion profiles. According to this model, the phase transformation occurring in the DP1000 steel to reach the $(60\%\gamma - 2)$ state is not characterized by a manganese enrichment in austenite at the interface as can be seen in Figure 4.9.(d). In this case, the M_S modelling, shown in Figure 4.9.(b), can be performed by taking into account only the carbon enrichment in austenite and the grain refinement compared to that of the $(100\%\gamma)$ state. By contrast, for the $(60\%\gamma - 1)$ state, a manganese enrichment at the interface of 2.4 (wt.%) is clearly shown in Figure 4.9.(c). In this case, the M_S prediction requires to consider this enrichment (see Figure 4.9.(a)). By combining all factors involved in the model (C and Mn enrichment in austenite and grain refinement in Equation 4.4 and Equation 4.2), it is possible to obtain a M_S drop of about 85°C, which is consistent with experimental observation and measurements. As a conclusion, both two-phase steel states highlight the effect of the interface enrichment in manganese which may occur during a conventional industrial thermal cycle and lead to a drop of the M_S temperature of the order of 30 °C. As a conclusion, the M_S prediction models can be extended under the condition of knowing precisely the microstructural changes

Cette thèse est accessible à l'adresse : http://theses.insa-lyon.fr/publication/2020LYSEI120/these.pdf
© [A. MATHEVON], [2020], INSA Lyon, tous droits réservés

occurring during the thermal cycle. A coupling with a phase transformation model seems an essential point to efficiently predict the M_S temperature in the case of two-phase steels containing alloying elements. This model can be easily extended to industrial conditions for a DP600 steel containing 20% austenite, for example, although it is then difficult to verify it from an experimental point of view.

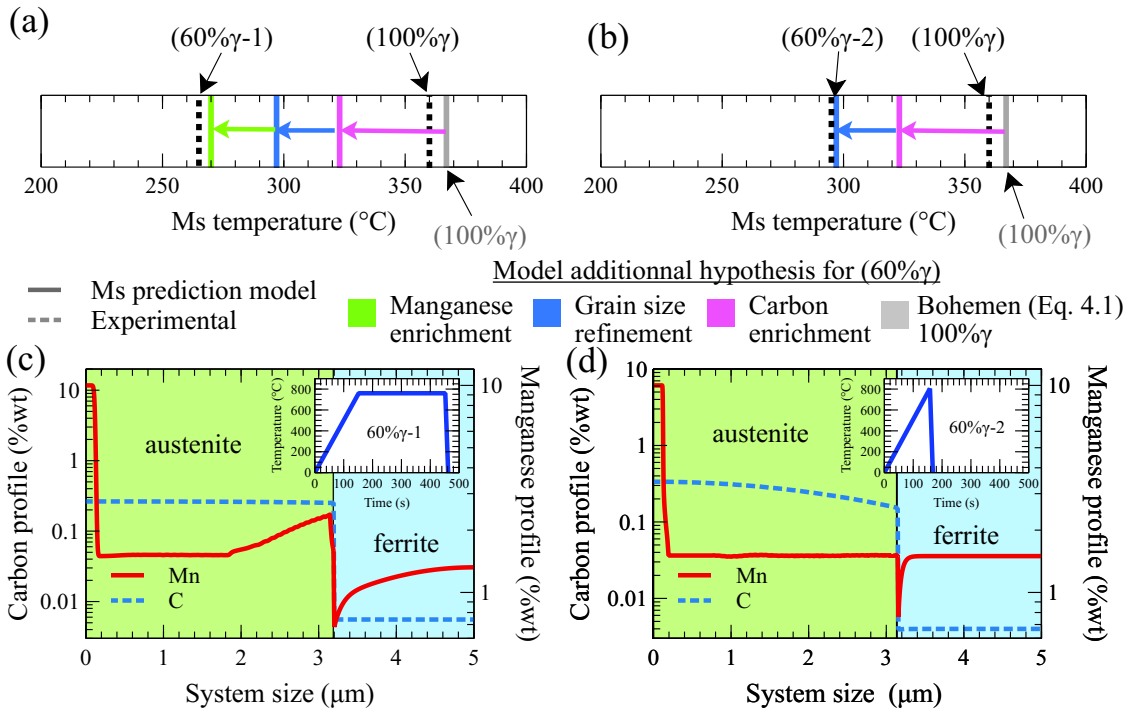

Figure 4.9: Comparison of the model predictions for Ms with the experimental data for : (a) the $(60\%\gamma - 1)$ state and (b) the $(60\%\gamma - 2)$ state. Concentration profiles within the sample for : (c) the $60\%\gamma - 1$ state and (d) the $60\%\gamma - 2$ state.

4.3.5 Prediction of the austenite-to-martensite transformation kinetics

Once the M_S temperature has been modelled, the martensitic transformation kinetics can be calculated. Using the Koistinen-Marburger law (see Equation 4.7) with the parameter α_m given in Table 4.5 and the predicted M_S values of this study, the austenite-to-martensite kinetics were modelled starting from the $(100\%\gamma)$ and $(60\%\gamma - 1)$ states. Figure 4.10.(b) shows that the experimental kinetics prediction gives good results in the case of the $(100\%\gamma)$ state. On the other hand, for the $(60\%\gamma - 1)$ state, the only carbon mass balance assumption is not sufficient to reproduce the experimental kinetics due to an M_S overestimation. The additional assumptions (grain size refinement and substitutional element segregation at the interface) provided in this chapter allow the experimental kinetics to be correctly modelled as presented in Figure 4.10.(a). In view of the results of this chapter, it seems that the key parameter needed to model the martensitic transformation kinetics is based on an accurate description of the M_S temperature. The consideration of all the elements that can delay the phase transformation, such as grain size refinement

Cette thèse est accessible à l'adresse : http://theses.insa-lyon.fr/publication/2020LYSEI120/these.pdf
© [A. MATHEVON], [2020], INSA Lyon, tous droits réservés

and the addition of alloying elements that can be partitioned at interfaces, is thus required for an accurate prediction of martensitic transformation kinetics in high strength steels. These modifications make it possible to consider an extension of the martensitic transformation kinetics prediction in the case of two-phase steels.

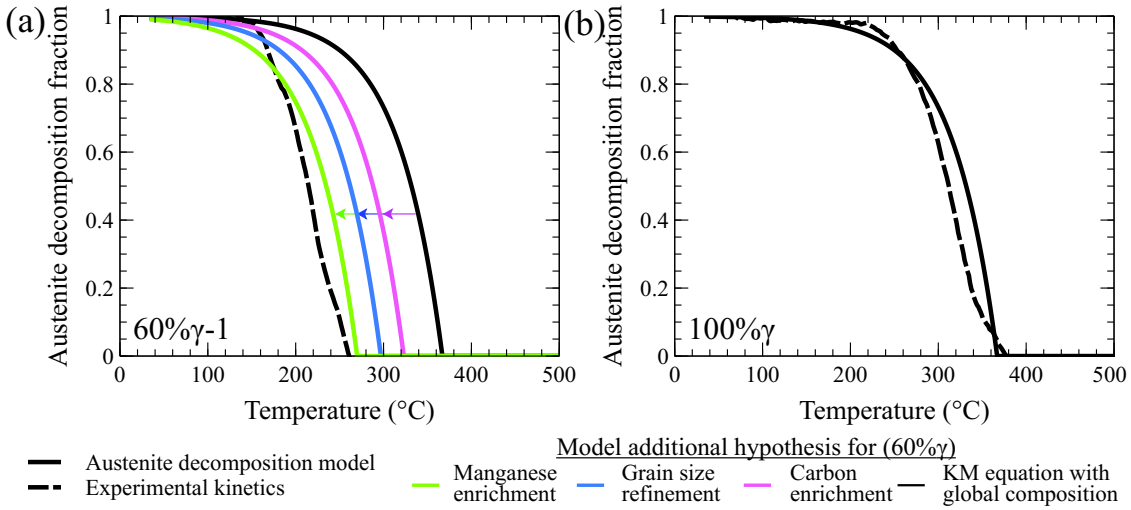

Figure 4.10: Comparison of the martensitic transformation kinetics for: a. the $60\%\gamma - 1$ state and b. for the $100\%\gamma$ state.

4.4 Conclusions

Following the development of predictive models for M_S in recent years based on thermodynamic models and taking into account the grain size effect, it is now possible to predict the M_S temperature and the austenite-to-ferrite kinetics with accuracy for fully austenitic steels. However, very few studies had examined the case of the two-phase steels on the martensitic transformation, even though most new-generation high-strength steels include several phases and high content of alloying elements. The purpose of this study was to model the considerable drop in experimental M_S temperatures observed in the two-phase states that no model in the literature was able to capture. As this drop cannot be totally explained in some cases by the carbon austenite enrichment and by the grain austenite refinement, it was assumed that the substitutional enrichment at the austenite/ferrite interface level can be partly responsible for the M_S fall. The GEM model was thus used to predict this enrichment and then, to predict successfully the M_S temperature of Dual-Phase steels. These hypotheses make it possible to support the model thermodynamic foundations applied to the $(100\%\gamma)$ states when the exact chemical elements profile is known within the material, allowing thus its extension for two-phase states and other applications than Dual-Phase steels.

Cette thèse est accessible à l'adresse : http://theses.insa-lyon.fr/publication/2020LYSEI120/these.pdf
© [A. MATHEVON], [2020], INSA Lyon, tous droits réservés

Cette thèse est accessible à l'adresse : http://theses.insa-lyon.fr/publication/2020LYSEI120/these.pdf
© [A. MATHEVON], [2020], INSA Lyon, tous droits réservés

Chapter 5

Investigation and mean-field modelling of the microstructural mechanisms driving the DP steel mechanical properties

Previously, physically based models have been used to describe the phase transformation phenomena in the intercritical domain as well as the martensitic transformation temperature. This chapter aims at developing a model likely to describe accurately the mechanical behaviour of DP steels based on the physical microstructure parameters (martensite fraction, initial ferritic grain size) for a wide range of chemical composition. It should be applicable to a wide range of steels from fully ferritic Interstitial free (IF) steels to fully martensitic steels as well as to the whole range of Dual-Phase steels. This is why, this study is based on the "composite" mean field model originally developed by Allain *et al.* [ALL 15] based on an iso-work interaction law and the addition of a geometrically necessary dislocation density in ferrite. This model enables a fine description of the interactions between the different phases and was completed, in this thesis, by the development of a new interaction law for the homogenization of the mechanical behaviours.

In order to calibrate and improve the fully ferritic and martentitic model, a wide range of chemical composition and microstructure size was used to include the Hall-Petch effect within the properties of martensite.

Finally, an ex-situ tensile test followed by EBSD in the SEM allowed us to observe and understand the different mechanisms required for the mechanical property simulation of DP steels. These observations allowed us to observe early fractures in the ferrite grains surrounded by martensite islands resulting in the modification of the interaction law for DP steels. This modified law is based on a linear transition from an iso-strain law for small deformations to an iso-work law for the failure deformation of fully martensite steel enabling to reproduce the percolation effect of the two phases and the progressive fracture observed in the microstructure of DP steels.

Cette thèse est accessible à l'adresse : http://theses.insa-lyon.fr/publication/2020LYSEI120/these.pdf
© [A. MATHEVON], [2020], INSA Lyon, tous droits réservés

Contents

Cette thèse est accessible à l'adresse : http://theses.insa-lyon.fr/publication/2020LYSEI120/these.pdf
© [A. MATHEVON], [2020], INSA Lyon, tous droits réservés

5.1 Literature review

DP steels are characterized by a low Yield Strength (YS) compared to their high Ultimate Tensile Strength (UTS). In addition, the lack of yield point and Yield Point Elongation (YPE) and the presence of a high Work-Hardening (WH) can also be noted, which is the basis of their forming and energy absorption ability. The high strain-hardening rate of DP steels is due to the presence of a hard phase in a soft matrix which can be associated with a matrix composite effect.

5.1.1 Link between microstructure and mechanical property

The particular macroscopic behaviour of Dual-Phase steels is due mainly to the intrinsic properties of the different phases (ferrite and martensite) but also to their interactions which are strongly related to the microstructure. The intrinsic properties of each phase are strongly dependent on their chemical composition and grain size. Many authors have also shown that the martensite fraction is a key parameter controlling the ultimate tensile strength and the yield stress, as shown in Figure 5.1 [MAR 82, LIE 02].

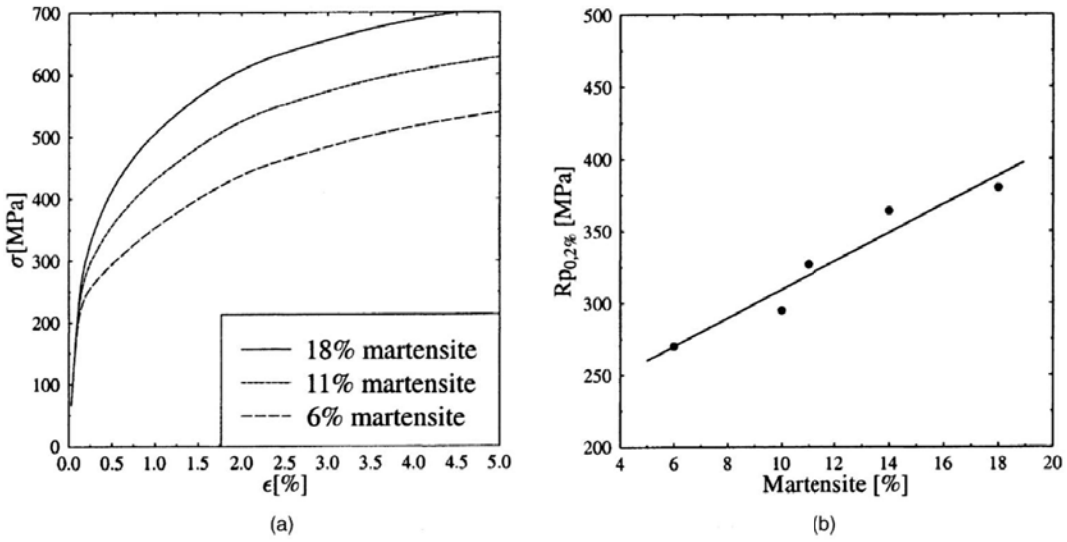

Figure 5.1: Experimental results of tensile tested Dual-Phase steel grades: (a) stress-strain diagrams for different martensite volume fractions and (b) 0.2% yield strength (Rp0.2%) as a fonction of the martensite volume fraction [LIE 02].

One specific feature of Dual-Phase steels is their low yield strength, which can be explained in particular by the low flow stress of the ferritic matrix but also by the low yield strength of the martensitic phase. A recent study conducted by Hutchinson *et al.* [HUT 18] explained the early appearance of plasticity within martensite due to the presence of residual internal stresses remaining after the martensitic transformation. The orientation of these internal stresses with respect to the direction of tensile test leads to a progressive martensite yielding. Furthermore, the high martensite strain-hardening rate as well as the presence of a high density of mobile dislocations at the ferrite/martensite

Cette thèse est accessible à l'adresse : http://theses.insa-lyon.fr/publication/2020LYSEI120/these.pdf
© [A. MATHEVON], [2020], INSA Lyon, tous droits réservés

interfaces [TIM 07, GAR 05] explains the lack of Lüders plateau in these steels.

The high strain-hardening rate of Dual-Phase steels is very often compared to that of metal matrix composites due to the presence of a hard phase (martensite) within the ferrite. Indeed, it has been shown that the elasto-plastic transition behaviour of martensite plays a major role in the overall behaviour of DP steels and cannot be simplified to a perfectly elasto-plastic behaviour [ALL 15]. Indeed, the stress difference between the two phases [SUG 97, ASA 75, JIA 95] generates a kinematic contribution to strain-hardening which explains the marked Bauschinger effect of these steels. Moreover, the difference in mechanical properties between the two phases leads to strain incompatibility at the microstructure level [JIA 95, KAD 11, KIM 12]. Numerous studies [LAN 07, TIM 07, GAR 05, TSI 11, KOR 84, CAL 10] have thus observed the formation of strain gradients and the presence of a high density of Geometrically Necessary Dislocations (GND) within the ferrite around the martensite islands as illustrated in Figure 5.2.

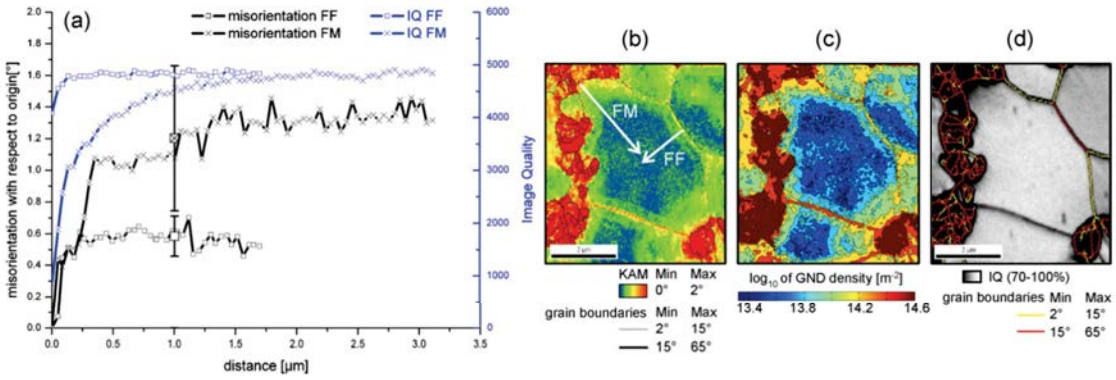

Figure 5.2: (a) Misorientation and Image Quality (IQ) evolution from grain boundary to grain center obtained from 2D profile vectors starting from ferrite-martensite (FM) interfaces and ferrite-ferrite interfaces (FF) indicated in (b). Error bars show the statistical result obtained from a range of misorientation profiles. (b) Kernel Average Misorientation (KAM) map and grain boundaries. (c) GND density calculated from kernel data. (d) IQ map showing the gradual decrease in the dislocation density from the ferrite-martensite boundaries to the center [CAL 10].

DP steels have a high sensitivity to ferritic and martensitic grain size [RAM 12], which is explained by the importance of the strain gradients encountered at the ferrite/martensite interfaces. Nevertheless, it is extremely delicate to decorrelate the different microstructural parameters (martensite fraction, martensite carbon content, phase morphology, ferritic and martensitic grain sizes), which explains the difficulty to calibrate and develop models from literature data. For example, Pierman *et al.* [PIE 14] showed a strong effect of local morphology while varying the size of the microstructure (which does not allow to isolate only the morphology effect). More surprisingly, many authors have shown a weak effect of phase morphology (spatial distribution and shape of the martensitic structure) on the global properties of DP steels [KRE 09, LEI 84], which allows the use of mean-field models to reproduce the mechanical properties of DP steels.

Cette thèse est accessible à l'adresse : http://theses.insa-lyon.fr/publication/2020LYSEI120/these.pdf
© [A. MATHEVON], [2020], INSA Lyon, tous droits réservés

5.1.2 Modelling tools for the mechanical property of DP steels

The modelling of mechanical properties in DP steels is not yet fully satisfying. Four types of approaches can be distinguished in the ongoing studies: (1) empirical approaches, (2) "Monophase" mean field approaches, (3) "Composite" mean field approaches, and (4) Local field approaches.

5.1.2.1 Empirical approach

The empirical approach consists in extrapolating the experimental data results in order to be able to predict the three key markers of the Dual-Phase steel mechanical properties (yield strength, ultimate yield strength and uniform elongation). Several studies have proposed a relationship depending solely on the martensite fraction of Dual-Phase steels to predict yield strength [DAV 78], ultimate yield strength [DAV 78, MAR 82] and uniform elongation [MAR 82]. Other studies proposed a combination of the martensite fraction and the carbon chemistry of martensite to predict the mechanical properties [SPE 79, CHE 89, PIE 13]. Although easy to use, these different equations are generally limited to a martensite fraction lower than 60%. Moreover, they are not sensitive to variations in grain size and chemical composition of alloying elements since they are generally applicable on limited range around the studied values.

5.1.2.2 The ”Monophase” approach

The ”Monophase” approach [SUG 97, JIA 95, PER 03, BOU 01, MA 89] consists in simplifying the composite microstructure of DP steels to the ferritic phase considering that it is hardened by the martensitic phase. Generally, two contributions are added: (i) a kinematic contribution coming from the strain gradient which depends on the martensite fraction and (ii) an isotropic contribution of structural hardening in accordance with the forest equation due to the GND distribution within the ferrite. These hypotheses, while interesting, assume an elastic martensite behaviour and are restricted to non-percolating microstructures with low martensite contents.

5.1.2.3 The ”Composite” approach

The "composite" mean-field approach [LIA 91, BER 04, LAN 07, DEL 07, PIE 14, JAC 07, TOM 92, ALL 15] considers the mechanical DP steel behaviour as a function of the behaviour of the two components (ferrite, martensite) weighted by their mean fraction. Subsequently, several homogenization methods have been used in the literature to reproduce the mechanical properties of DP steels. However, these methods generally suffer from a simplification of the constituent mechanical behaviour, particularly of the martensite which is often assumed to be purely elastic. Moreover, models are often not able to be sensitive to grain size and to account for strain incompatibility effects at the interfaces. Nevertheless, it is important to underline that Delince *et al.* [DEL 07] and Allain *et al.* [ALL 15] have proposed more sophisticated models likely to reproduce the sensitivity to the initial ferrite grain size (see Figure 5.3), but they still present limits when used on

Cette thèse est accessible à l'adresse : http://theses.insa-lyon.fr/publication/2020LYSEI120/these.pdf
© [A. MATHEVON], [2020], INSA Lyon, tous droits réservés

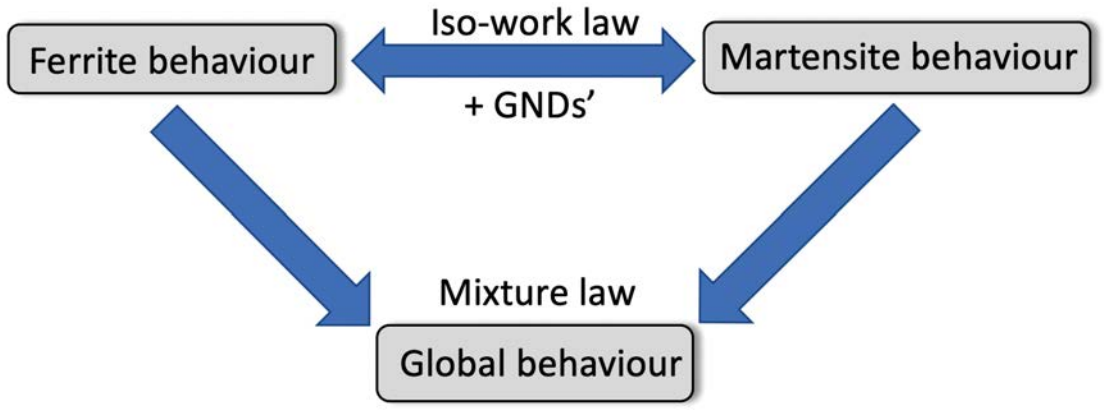

Figure 5.3: Schema of the sophisticated model developed by Allain [ALL 15] for the prediction of DP steel mechanical properties.

industrial steels for high martensite fractions and neglect the Hall-Petch effect observed in martensite as a function of the prior austenitic grain size.

5.1.2.4 Local approach

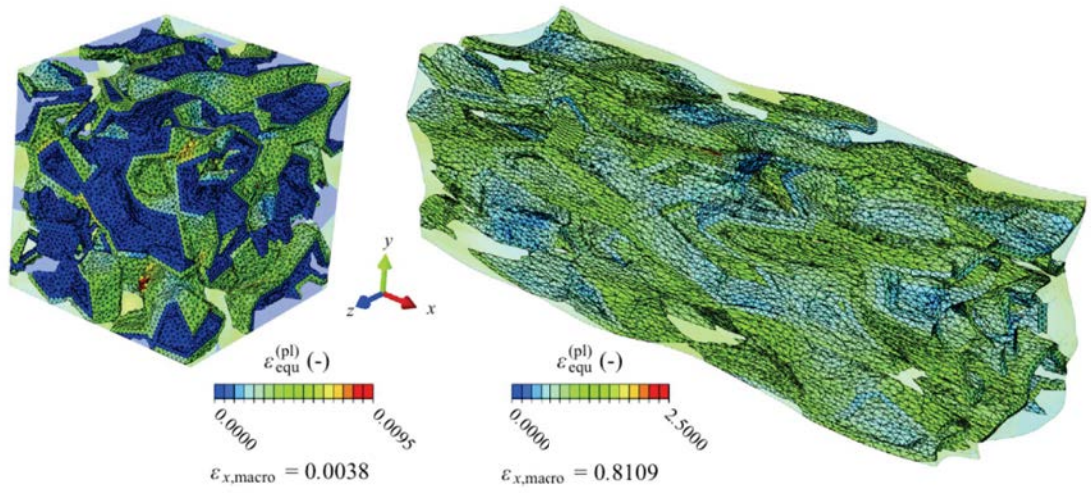

Figure 5.4: A finite element mesh in which the martensite elements are plotted solid, while the other ferrite elements (absent from the failure criteria) are plotted semi-transparent. The field plot shows the plastic equivalent strain due to uniaxial stress in tensile direction. Left: Close to the macroscopic yield point; right: at 81% log. macro strain. [FIL 14]

Local approaches aim at calculating the mechanical field on a Representative Volume Element (RVE) of the microstructure which can be created numerically as illustrated in Figure 5.4 [PRA 07, LIE 02, KAD 11, HÜP 99, ALA 07, FIL 14] or based on real microstructures in Figure 5.5 [RAM 12, KRE 09, LI 90b, LI 90a, PAU 12, PAU 13, CHO 09, PAR 12]. Simulations could thus be conducted using either Finite Element (FE) or Fast

Cette thèse est accessible à l'adresse : http://theses.insa-lyon.fr/publication/2020LYSEI120/these.pdf
© [A. MATHEVON], [2020], INSA Lyon, tous droits réservés

Fourier Transform (FFT) solving methods. These approaches can be used to study the effects of martensite fraction and morphology but also to study more local phenomena such as fracture or decohesion. Nevertheless, this family of models has an important drawback which is the long time needed to set up and solve a very particular case of microstructure. It is therefore difficult to consider being able to generalise these methods for all steels in an automatic way for the design and monitoring of the mechanical properties of DP steels.

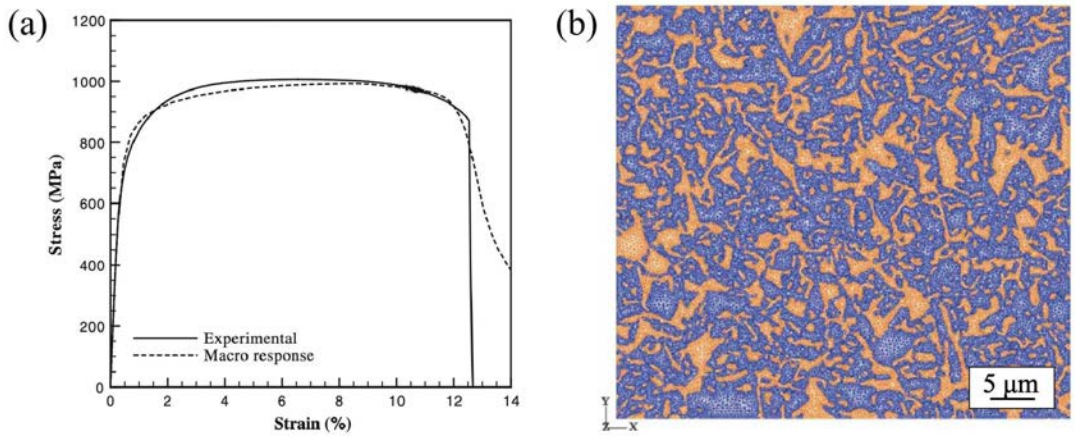

Figure 5.5: (a) Macroscopic stress-strain curve response of representative volume element (RVE) with 38% martensite fraction under tensile loading based on calibrated input stress-strain curves for ferrite and martensite phases. (b) The finite element model associated with the computation of the stress-strain curve [CHO 09].

5.1.3 Conclusion: Objective of the present chapter

In this context, the aim of the present study is to develop a model enabling to describe accurately the mechanical behaviour of DP steels based on the physical microstructure parameters (martensite fraction, microstructure size) for a wide range of chemical composition. The model has to be able to capture the complexity of the real microstructure and thus its has to be sensitive to different physical parameters. The model is intended to be used in production as well as in alloy design requiring low computational time. It should be applicable to a wide range of steels from fully ferritic IF steels to fully martensitic steels as well as the whole range of Dual-Phase steels. This is why this study is based on the "composite" mean field model developed by Allain *et al.* [ALL 15].

Nevertheless, the existing model has revealed these limitations on the prediction of the mechanical properties of fully martensitic steels. The addition of a Hall-Petch dependency capturing the effect of prior-austenitic grain size on martensite properties is added within the model.

The ex-situ EBSD observation of a DP600 steel during a tensile test allowed to characterize and validate the fine description of the interactions between the different phases proposed initially by Allain. The integration of a GND density in the ferrite due to the martensite dilatation during quenching and the accommodation of the difference in mechanical properties between the two phases is confirmed. However, early fractures of the ferritic grains in contact with martensite islands in a bi-percolant microstructure lead to

Cette thèse est accessible à l'adresse : http://theses.insa-lyon.fr/publication/2020LYSEI120/these.pdf
© [A. MATHEVON], [2020], INSA Lyon, tous droits réservés

the definition of a new interaction law. This study proposes a linear transition from an iso-strain law for small deformations to an iso-work law for the failure deformation of fully martensite steel to reproduce the hardening of DP steels with a percolating martensitic microstructure.

5.2 Materials and procedures

This study was carried out on the four ternary Fe-C-Mn steels of this PhD-work and on the two industrial DP steels presented in Chapter 1. Their chemical composition is given in Table 1.2. The initial microstructures (obtained either after forging or cold-rolling) of the studied steels are presented in Figure 1.1. The microstructure is very sensitive to hot-rolling parameters. For laboratory grades, the addition of carbon and manganese leads to a refinement of the initial microstructure. Moreover, it is clear that the grain size of the industrial steels is much smaller, as evidenced in Table 1.2.

Austenitization treatments on the industrial steels and on the ternary steels were performed in salt baths. Samples (10 mm wide by 100 mm long) were treated at varying temperatures to obtain various martensite fractions (see Table 1.2) before being water-quenched in order to follow the mechanical properties using tensile tests. An optical quantification of the martensite fraction was performed using a Bandoh etching (2.3 mL picral + 2.3 mL Metabisulfite + 1 mL Nital - 30S). A thresholding performed by Otsu's method [VAL 13, LIU 09] using *ImageJ* led to the different fractions presented in Table 5.1 (see Figure 5.6). The 100% martensitic states were obtained after a 3 min treatment at 850 °C followed by water quench.

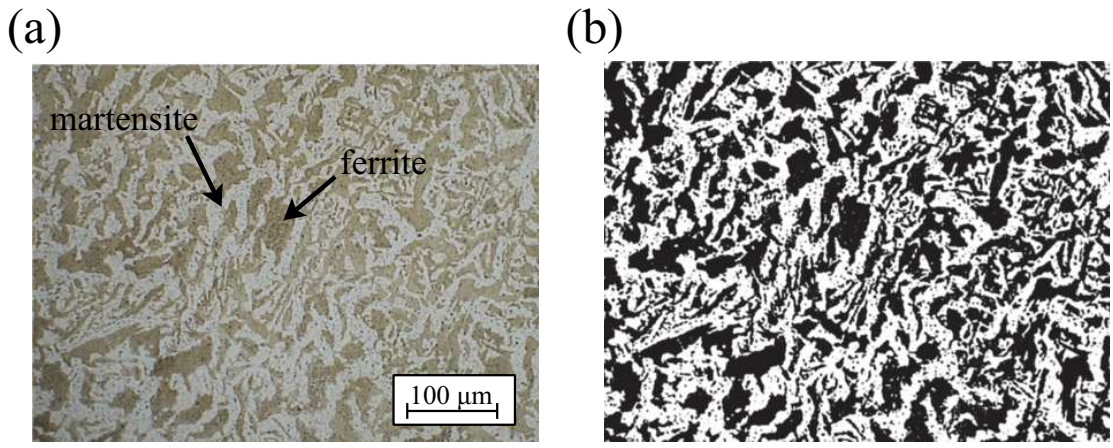

Figure 5.6: (a) Optical micrograph of Fe-0.17C-1.7Mn after Bandoh etching with a martensite fraction of 45%. and (b) an example of threshold performed by the *ImageJ* software to calculate the martensite fraction.

An ex-situ tensile test followed by Electron Backscattered Diffraction (EBSD) in a Scanning Electron Microscope (SEM) allowed us to observe and understand the different mechanisms which will serve as mandatory ingredients for the mechanical property simulation of DP steels. The tensile test was performed on a Gatan Deben 2000E tensile

Cette thèse est accessible à l'adresse : http://theses.insa-lyon.fr/publication/2020LYSEI120/these.pdf
© [A. MATHEVON], [2020], INSA Lyon, tous droits réservés

Steel grades	Martensite fraction	Austenitization treatment		Initial ferrite grain size (μm)
		Temperature	Time	
0.07C-1.7Mn	29%	780°C	3min	50
	45%	800°C	3 min	
	100%	850°C	3 min	
0.17C-0.5Mn	100%	850°C	3 min	45
0.17C-1.7Mn	45%	760°C	3 min	30
	70%	780°C	3 min	
	100%	850°C	3 min	
0.17C-2.5Mn	100%	850°C	3 min	20
DP600	30%	780°C	3 min	6
	45%	800°C	3 min	
	100%	850°C	3 min	
DP1000	28%	735°C	3 min	6
	62%	760°C	5 min	
	100%	850°C	3 min	

Table 5.1: Thermal cycle, martensite fraction and grain size observed for different steel grades.

machine, with a 70°pretilt devoted for in-situ EBSD tensile tests and with a maximum load of 2000N. The specimen had an effective length of 8 mm and an area of 1 mm^2. EBSD maps were performed using an Oxford Instrument Symmetry detector, with an accelerating voltage of 20 kV in a ZEISS Supra 55VP field emission gun (FEG) scanning electron microscope (SEM). 3 states have been observed for a DP600 steel containing 40% martensite with global strain of 0%, 4.5% and 7%.

Results from the literature have been used for the calibration of the fully ferritic model over a wide range of grain sizes as well as for the calibration of the carbon content effect on the mechanical properties of fully martensitic steels.

5.3 Hybrid Mean-Field Composite (Hy-MFC) model

The aim of the hybrid mean-field composite (Hy-MFC) model developed in this study is to predict of the tensile properties of DP steels under linear monotonic loading taking into account the fraction, chemical composition, and grain size of all the phases. The model is intended to be applicable on-the-fly to a wide range of steels from fully ferritic to fully martensitic steels. It should be able to be coupled to the different models of microstructural evolution prediction developed in the previous chapters.

The mechanical model developed in this chapter is based on the work of Allain *et al.* [ALL 15] and aims at: (1) integrating the martensite sensitivity to the prior austenitic grain size and (2) adding a new interaction law between phases likely to describe the tensile behaviour of DP steels with a high martensite fraction. Once the properties of each of the single phases (ferrite and martensite) have been modelled, an interaction law was applied between the two phases with a plasticity model that reproduces the mechanisms involved during the phase transformations and composite loading. Finally, a homogenization law

Cette thèse est accessible à l'adresse : http://theses.insa-lyon.fr/publication/2020LYSEI120/these.pdf
© [A. MATHEVON], [2020], INSA Lyon, tous droits réservés

was applied according to the phase fractions to recover the macroscopic properties of the steel.

5.3.1 Ferrite behaviour (Model for fully ferritic steels)

Grain size and dislocation densities are the main parameters governing the mechanical properties of ferrite. Since the pioneering work of Hall and Petch [HAL 51, PET 53], many researchers have proposed physical approaches to reproduce the different hardening mechanisms of polycrystals [DEL 07, SIN 06]. The ferrite constitutive law used in this work is based on the work of Bouaziz *et al.* [BOU 08].

The flow stress in ferrite σ^f is considered to be a function of the plastic deformation and can be decomposed as follows:

$$\sigma^f(\epsilon_p^f) = \sigma_0^f + \sigma_R^f + \sigma_X^f \tag{5.1}$$

where:

- σ_0^f is the sum of the Peierls force contribution and of the friction stress resulting from the alloying elements in solid solution. It is directly related to the chemical composition of the steel according to the following law :

$$\sigma_0^f = 52 + 33C_{Mn}^0 + 80C_{Si}^0 + 60C_{Cr}^0 + 80C_{Mo}^0 \tag{5.2}$$

  with σ_0^f in MPa and the chemical content in C_{Mn}^0, C_{Si}^0, C_{Cr}^0 and C_{Mo}^0 expressed in wt%. Only the effects of the main elements present in the composition of DP steels are considered in Equation 6.16, namely Mn, Si, Mo, and Cr. The others could be further added in the future.
- σ_R^f is the forest dislocation hardening (*i.e.* isotropic hardening) governed by ρ^f, the density of Statistically Stored Dislocations (SSDs) in ferrite expressed as follows:

$$\sigma_R^f = \alpha_T M_T \mu b_{111} \sqrt{\rho^f} \tag{5.3}$$

  where α_T is the forest hardening coefficient, M_T is the Taylor factor, μ is the elastic shear modulus, and b_{111} is the Burgers vector, indicating the direction of lattice distortion due to dislocations, with the other lattice distortion directions being neglected.
- σ_X^f is the back-stress (*i.e.* kinematic hardening). Unlike the previous contribution of SSDs, GNDs created during elastic energy storage pile up at Grain Boundaries (GBs). They thus generate a non-relaxed internal back-stress contribution that contributes to the overall macroscopic stress as kinematic hardening. It can be expressed as follows:

$$\sigma_X^f = \frac{M_T \mu b_{111}}{D_\alpha^0} n^f \tag{5.4}$$

  where D_α^0 is the initial ferrite grain size and n^f is the average number of dislocations accumulated at GBs required to accommodate the strain gradients.

Cette thèse est accessible à l'adresse : http://theses.insa-lyon.fr/publication/2020LYSEI120/these.pdf
© [A. MATHEVON], [2020], INSA Lyon, tous droits réservés

The total deformation of ferrite ϵ^f_{tot} is the sum of elastic (ϵ^f_{el}) and plastic(ϵ^f_p) deformations:

$$\epsilon^f_{tot} = \epsilon^f_{el} + \epsilon^f_p \tag{5.5}$$

According to the Kocks-Mecking-Estrin law [EST 84], the evolution of dislocation density as a function of deformation depends on a dislocation-dislocation pinning term as well as a dislocation-annihilation term due to dynamic recovery, which is dependent on the deformation ratio and temperature. An additional term is added to account for the effect of grain size on the increase in dislocation density by assuming an accumulation of GNDs at GBs [SIN 06, BOU 08]:

$$\frac{d\rho^f}{d\epsilon^f_p} = M_T \left[\frac{\left(1 - \frac{n^f}{n^f_0}\right)}{b_{111} D^0_\alpha} + k^f \sqrt{\rho^f} - f^f \rho^f \right] \tag{5.6}$$

where k^f and f^f are the two classical parameters controlling the Kocks-Mecking-Estrin law. n^f_0 represents the maximum number of dislocations piled up at GBs required to accommodate the strain gradients.

In addition, to reproduce the back-stress saturation with plastic deformation, the evolution of the number of dislocations accumulated at the GBs (n^f) can be described as follows:

$$\frac{dn^f}{d\epsilon^f_p} = \frac{\lambda^f}{b_{111}} \left(1 - \frac{n^f}{n^f_0}\right) \tag{5.7}$$

where λ^f is the average spacing between slip bands at GBs. The corrective term $\left(1 - n^f/n^f_0\right)$ reproduces site saturation, and the term λ^f/b_{111} represents the number of GNDs per slip band to accomodate the deformation.

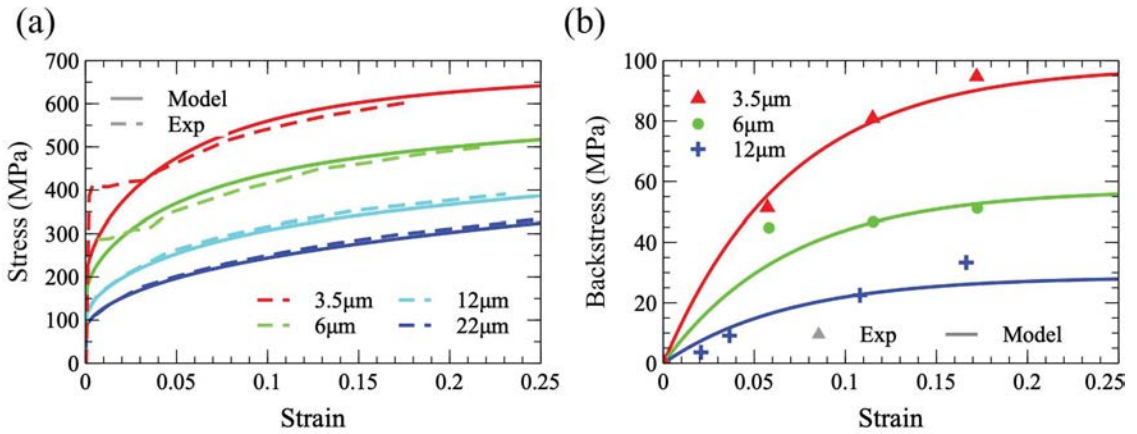

Figure 5.7: Model calibration for ferritic steels with grain sizes ranging between 3.5 and 22 μm: (a) stress and (b) backstress evolution during tensile test. The experimental data and model were extracted from [BOU 08], and the Luders' plateau was excluded from the model calibration.

Cette thèse est accessible à l'adresse : http://theses.insa-lyon.fr/publication/2020LYSEI120/these.pdf
© [A. MATHEVON], [2020], INSA Lyon, tous droits réservés

Using the formalism presented in this section for modelling the ferrite behaviour, the model was calibrated to be able to reproduce the effect of ferritic grain size on stress-strain evolution as well as back-stress evolution for a wide range of interstitial-free steels with grain sizes between 3.5 to 22 μm, as shown in Figure 5.7. The different parameters used in this model are listed in Table 5.2 and are identical to those used by Allain *et al.* [ALL 15]. The experimental curves were extracted from the work of Bouaziz *et al.* [BOU 08].

5.3.2 Martensite behaviour (Model for fully martensitic steels)

To reproduce the mechanical properties of martensitic steels, it is essential to be able to model the plastic behaviour and strain hardening up to failure. Conventional dislocation storage strain-hardening mechanisms cannot explain the strain-hardening behaviour of fully martensitic steel observed between the yield strength and its ultimate tensile strength. Moreover, regardless of the carbon content of martensite, it has a practically unique microplastic yield strength of approximately 400 MPa.

Martensite must be considered as a "continuous heterogeneous" composite. Indeed, studies have shown that the internal stresses and carbon content within martensitic islands can be highly variable, leading to important modifications of local mechanical properties in DP steels as well as in fully martensitic steels [PUS 13, HE 14, HUT 18].

To model the elasto-plastic transition of martensite, a Continuous Composite Approach (CCA) was used in agreement with Allain *et al.* [ALL 12]. The soft phase controls the deformation while the hard phase, assumed to be elastic, leads to significant strain hardening of the composite. The behaviour of the composite is controlled by the interaction of elastic and perfectly plastic domains. The Young's modulus Y (identical for each phase) and the respective elasticity limit allow the mechanical behaviour of each domain to be precisely described. The composite can thus be described by a continuous distribution of density of probability $f(\sigma_l)$ to find a domain having a local yield stress σ_l.

To describe the interaction between the different phases of the composite, a constant parameter β is fixed as

$$\beta = \frac{\sigma^m - \sigma_l}{\epsilon^m - \epsilon_l} \tag{5.8}$$

where σ_l and ϵ_l are the local stress and strain of each composite part, respectively, and σ_m and ϵ_m are the macroscopic stress and strain of martensite, respectively. Note that β ranges between 0 (iso-stress) and ∞ (iso-strain). Hereafter, β was set at 50 GPa (as in reference [ALL 15]).

It is then possible to express σ_l as follows [ALL 12]:

$$\sigma_l\left(\epsilon^m\right) = \frac{\sigma^m + \beta\epsilon^m}{1 + \frac{\beta}{Y}} \tag{5.9}$$

Assuming that the macroscopic stress is given by $\sigma^m = \int_0^\infty f(\sigma)\sigma d\sigma$ and assuming a elasto perfectly plastic behaviour of each domain leads to:

Cette thèse est accessible à l'adresse : http://theses.insa-lyon.fr/publication/2020LYSEI120/these.pdf
© [A. MATHEVON], [2020], INSA Lyon, tous droits réservés

$$\frac{d\sigma^m}{d\epsilon^m} = \frac{1}{\frac{1}{Y} + \frac{F(\sigma_l)}{\beta}} \left(1 - F\left(\sigma_l\right)\right) \tag{5.10}$$

where $F(\sigma_l) = \int_0^{\sigma_l} f(\sigma) d\sigma$ is the cumulative probability density.

To capture the Bauschinger effect on different martensitic steels, the stress spectrum is defined using an Avrami-like law with three adjustable parameters (Δ, m, $\sigma_{min} + \sigma_0^m$):

$$\begin{aligned} &\text{if } \sigma_l < \sigma_0^m + \sigma_{min} \text{ then } F\left(\sigma_l\right) = 0 \\ &\text{else } F\left(\sigma_l\right) = 1 - \exp\left[-\left(\frac{\sigma_l - \left(\sigma_{min} + \sigma_0^m\right)}{\Delta}\right)^m\right] \end{aligned} \tag{5.11}$$

where

- σ_0^m is the sum of the Peierls force and of the friction stress due to solid-solution hardening and depends on the chemical composition in wt% of the steel as follows:

$$\sigma_0^m = 52 + 33C_{Mn}^0 + 80C_{Si}^0 + 60C_{Cr}^0 + 80C_{Mo}^0 \tag{5.12}$$

- $\sigma_{min} = 320$ MPa and $m = 1.8$ are the two constants of Avrami's law controlling the yield strength and the rate of strain hardening of the composite, respectively, enabling the strain hardening of the martensitic steels to be reproduced after calibration.
- Δ is the width of the local yield-strength distribution that controls the magnitude of the strain hardening between the yield strength and ultimate tensile strength. Allain *et al.* [ALL 12] proposed a description of this parameter depending only on the nominal carbon composition in martensite. Figure 5.8 illustrates the inability of this description to reproduce the mechanical properties of the industrial and ternary grades (with the same C and Mn contents). As suggested by the optical micrographs of the ternary and industrial steels, this poor reproducibility could stem from a marked difference in the microstructure characteristic sizes. This explanation is also supported by the important effect of the prior austenitic grain size before quenching on the martensite mechanical properties highlighted in several studies [PRA 12, OHM 01]. The difference in former austenitic grain size (5-6 μm for the industrial steels and 30-60 μm for the ternary alloys) explains the difference observed in the mechanical properties. The Hall-Petch effect must thus be included in the description of Δ in addition to the effect of the carbon content in martensite equivalent to the nominal composition for fully martensitic steels C_C^0 (in wt%), leading to the following original expression:

$$\Delta = K_0 + \frac{K_1}{\sqrt{D_\gamma}} + K_2 (C_C^0)^{1.34} \tag{5.13}$$

where D_γ is the diameter of the austenitic grains before quenching.

Considering the limited number of phenomena (chemical composition and prior austenitic grain size) affecting the mechanical properties, the model was calibrated for predicting the martensite mechanical properties over the wide range of carbon content encountered in DP

Cette thèse est accessible à l'adresse : http://theses.insa-lyon.fr/publication/2020LYSEI120/these.pdf
© [A. MATHEVON], [2020], INSA Lyon, tous droits réservés

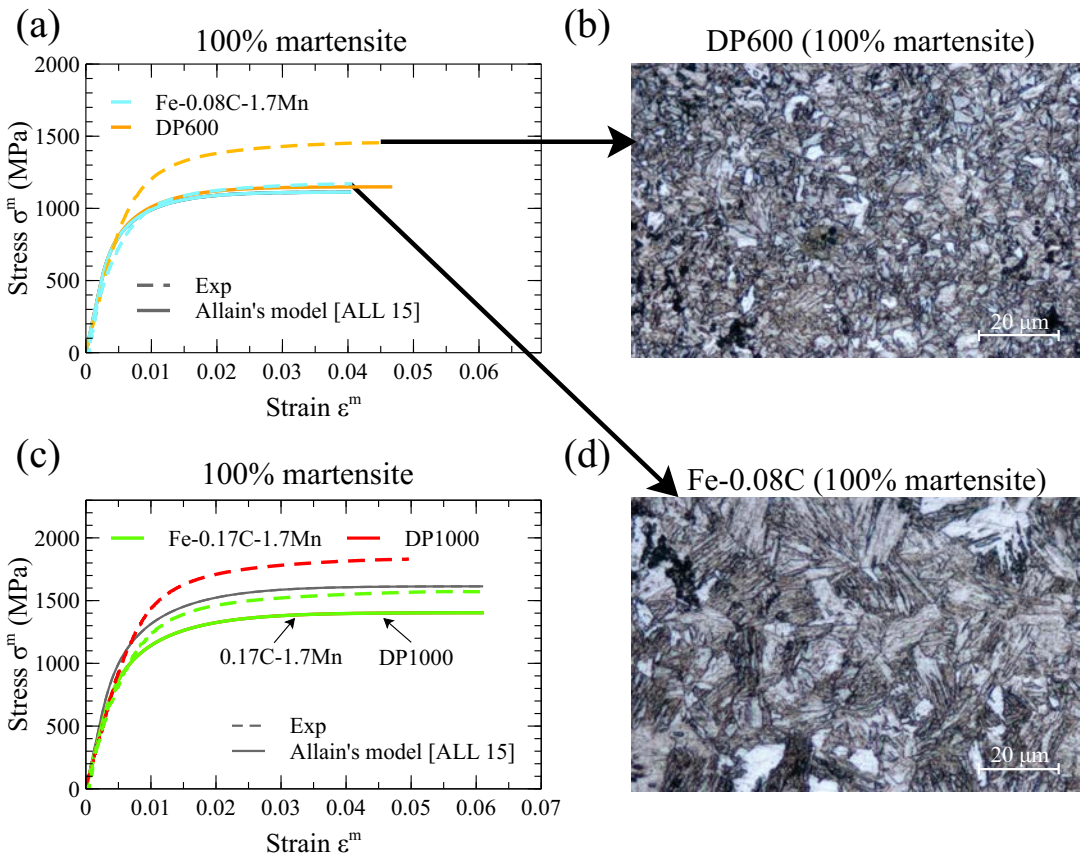

Figure 5.8: Comparison of the results of Allain's model [ALL 15] ($K_1 = 645$, $K_2 = 0$ and $K_3 = 5053$) with the experimental true stress-true strain tensile curves of (a) the DP600 steel and ternary Fe-0.08C-1.7Mn and of (c) the DP1000 and ternary Fe-0.17C-1.7Mn. Optical micrograph of (b) DP600 and (d) Fe-0.08C-1.7Mn steels. Allain's model fails to reproduce the different properties of the industrial and ternary grades as it does not take into account the prior autenitic grain size.

steels due to austenite carbon enrichment in two-phase states and for different manganese contents. All these effects are described hereafter.

- **Carbon content effect:** Figure 5.9 shows the effect of carbon content from 0.08 wt% C to 0.36 wt% C on the tensile properties and the strain-hardening rate. As can be seen in Figure 5.9.(a), the change in the carbon content (from 0.08C to 0.36C) with globally the same manganese content and grain size significantly increases the tensile properties of the steel. Figure 5.9 shows that the model captures the effect of carbon content on not only the tensile properties but also the strain-hardening rate.
- **Manganese content effect:** As all the ternary grades were produced using the same manufacturing process (leading to approximately the same grain size), the change in the manganese content of the steel (from 0.5Mn to 2.5Mn) has only a small effect on the experimental tensile properties, related to the solid solution effect of manganese. Figure 5.10.(a) shows that the model captures the manganese content effect of the different steels in solid solution through the parameter σ_0^m.
- **Grain size effect:** The refinement of the microstructure in the austenitic phase

Cette thèse est accessible à l'adresse : http://theses.insa-lyon.fr/publication/2020LYSEI120/these.pdf
© [A. MATHEVON], [2020], INSA Lyon, tous droits réservés

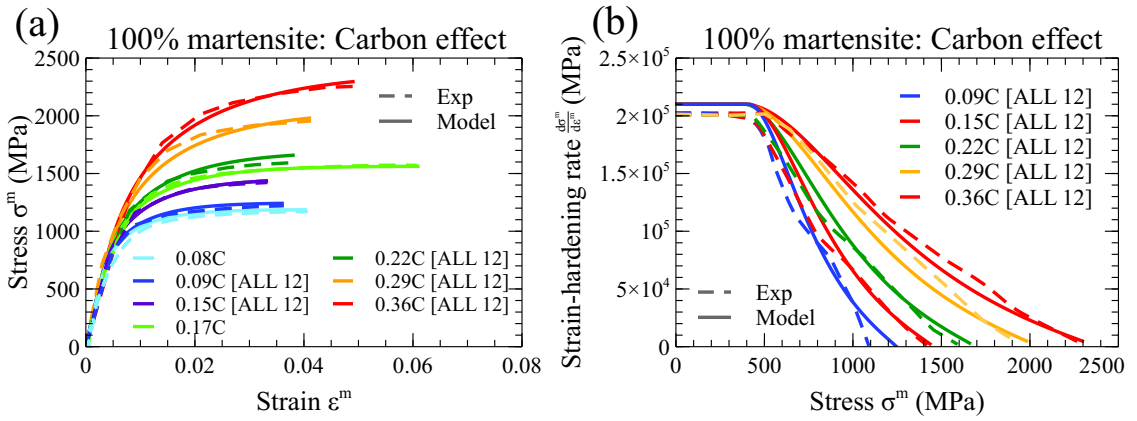

Figure 5.9: Comparison between experimental data and modelling. Effect of the carbon content (in wt%) on the (a) tensile curves and (b) strain-hardening rates of the ternary steels of this study and on other steels studied in the literature [ALL 12].

appears to be a key parameter controlling the mechanical properties of martensite as well as M_S temperature [BOH 17]. Figure 5.10.(b) highlights the non-negligible effect of grain size on the tensile properties of ternary steels ($\simeq 30\,\mu$m) and industrial steels ($\simeq 6\,\mu$m) for an identical chemical composition. It also shows the ability of the model, through the incorporation of the Hall-Petch effect in the Δ parameter, to reproduce the mechanical properties of both industrial and ternary grades. This term will thus play a decisive role in the development of new medium manganese grades with refined microstructure.

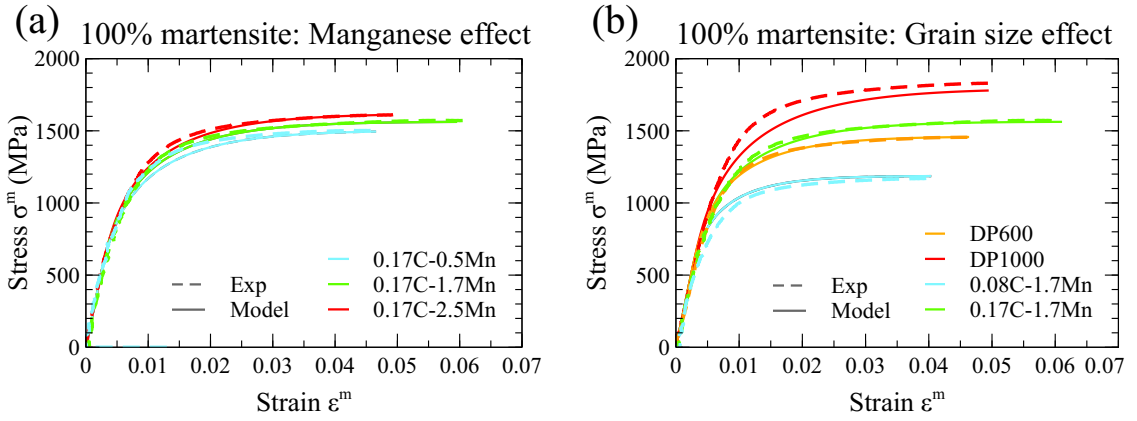

Figure 5.10: Comparison between experimental data and modelling. Effect on the tensile properties of the (a) manganese content and (b) prior austenitic grain size.

5.3.3 Composite model design definition for DP steels

Using the fully ferritic (section 5.3.1) and martensitic (section 5.3.2) constitutive laws, the aim of the present section is to propose a composite mechanical model accounting for their interactions. Preliminary tensile tests followed by EBSD observations were used to

Cette thèse est accessible à l'adresse : http://theses.insa-lyon.fr/publication/2020LYSEI120/these.pdf
© [A. MATHEVON], [2020], INSA Lyon, tous droits réservés

better understand these fine interactions at the level of the microstructure. The interaction formalism between the phases and homogenization method is based on Allain *et al.*'s [ALL 15] approach. Our observations validate their assumptions to introduce additional GNDs in ferrite. However, the scale transition law has been modified to reproduce the hardening of DP steels containing a martensitic percolant microstructure.

5.3.3.1 Preliminary microstructural observations

With the aim of understanding the mechanical interactions between the two phases, an ex-situ tensile test was performed on the DP600 steel. It was interrupted after three global deformation (0%, 4.5%, and 7%) and EBSD maps were performed after each deformation. Several grains were selected and followed during deformation to better describe the effect of their size and neighbourhood on their deformation behaviour. Ferrite and martensite, having similar crystallographic structures, were both indexed as a ferritic phase. Martensite islands can be distinguished by their specific lath morphology and by the slightly lower band contrast index. Using this last criterion, it was possible to measure the martensite fraction (41%, close to the value of 45% observed by metallographic analysis).

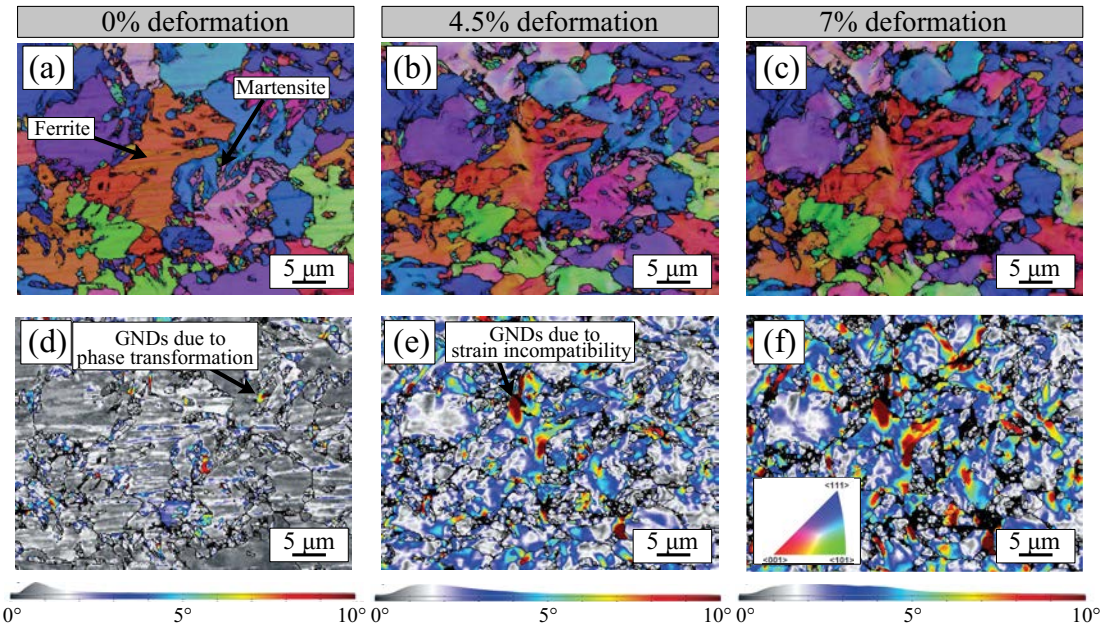

Figure 5.11: (a-c) Inverse Pole Figure in direction Z (IPFZ) colour maps and (d-f) kernel average misorientation (KAM) maps of EBSD observation of DP600 steel containing 41% martensite for three deformation states (0%, 4.5%, 7%).

Figure 5.11.(a-c) shows the IPFZ maps of the steel after the three considered deformations (0%, 4.5% and 7%). Upon deformation, many dark spots were observed between the ferrite and martensite grains. They correspond to martensitic grains that were too deformed to be indexed.

From the crystal orientations of Figure 5.11.(a-c), Kernel Average Misorientation maps were built. They give the average local misorientation of each pixel compared to the

Cette thèse est accessible à l'adresse : http://theses.insa-lyon.fr/publication/2020LYSEI120/these.pdf
© [A. MATHEVON], [2020], INSA Lyon, tous droits réservés

average orientation measured in the grain concerned. For a low KAM index, the local misorientation is very low and the corresponding colour is grey. By contrast, when the KAM index increases, the local misorientation is also increased and the colour evolves from blue to red. Moreover, the crystal misorientation can be directly related to the GND content [MUR 19, WIL 91]. Here, it has to be pointed out that the evolution of GNDs inside the ferritic grains can be qualitatively followed. However, because of the small size of martensitic laths, and thus the small number of pixels for each lath, the evolution of GNDs within the laths is not accurate. From the KAM maps of Figure 5.11.(d-f), it clearly appears that the deformation is clearly not homogeneous, with a globally higher GND density at ferrite/martensite phase boundaries. Additionally, the deformation of ferritic grains is not homogeneous and the two following trends can be identified :

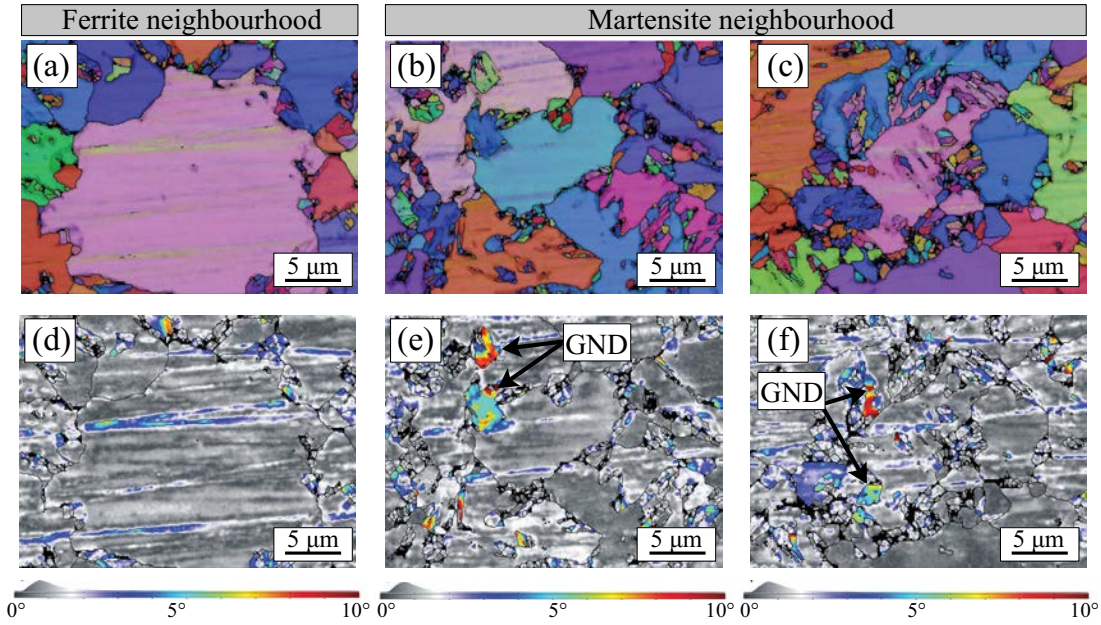

Figure 5.12: (a-c) IPFZ colour maps and (d-f) KAM maps of EBSD observation of initial state of DP600 steel containing 41% martensite.

- The martensitic transformation induces a volume change. To accommodate the induced deformation, GNDs appear in ferrite grains surrounding martensite islands. EBSD observations of the initial state of the DP600 steel in Figure 5.12.(a) and 5.12.(d) clearly reveal the absence of misorientation for ferrite grains not surrounded by martensite islands. In contrast, Figure 5.12.(b-c) and Figure 5.12.(e-f) show areas of misorientation for ferritic grains in contact with martensitic islands. These observations confirm previous findings for DP steels (see for example [TSI 11]) and underline the need to introduce GNDs in ferrite grains neighbouring martensite islands.
- The hardness difference between ferritic and martensitic phases induces the creation of GNDs required to accommodate deformation incompatibilities. This deformation incompatibility affects a given length noted L_f (see Figure 5.14.(a)) around the ferrite/martensite interface. EBSD observations after an overall deformation of

Cette thèse est accessible à l'adresse : http://theses.insa-lyon.fr/publication/2020LYSEI120/these.pdf
© [A. MATHEVON], [2020], INSA Lyon, tous droits réservés

7% (just before necking) reveal the importance of the surroundings of a given ferritic grain. Figure 5.13 presents the misorientation map of two ferrite grains with approximately the same crystallographic orientation. If the grain neighbourhood is mostly ferritic, it deforms rather homogeneously (see Figure 5.13.(a)), whereas when it is surrounded by martensitic islands, heterogeneous elongation of the grain is observed (see Figure 5.13.(b)). Experimentally a length of about 3-4μm is affected by the deformation incompatibility between the two phases, which is consistent with the result of other studies showing a higher dislocation density in ferrite close to martensite islands [TIM 07, GAR 05, TSI 11, KOR 84].

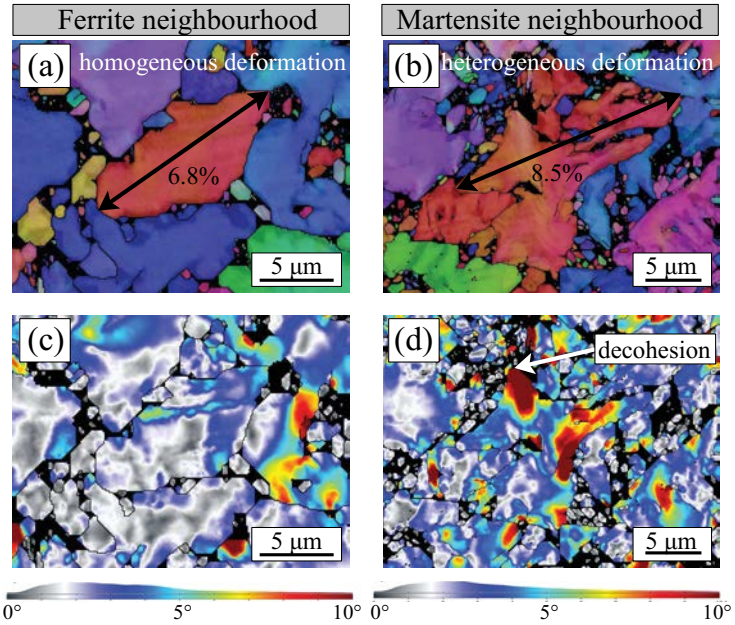

Figure 5.13: (a-b) IPFZ colour maps and (c-d) KAM maps of EBSD observation of DP600 steel containing 41% martensite at 7% global strain.

5.3.3.2 Accounting for extra hardening of ferrite

The equations developed to define the properties of the ferritic phase in Section 5.3.1 are only valid for a single-phase material. It is therefore essential to introduce the two mechanisms leading to the creation of GNDs discussed in Section 5.3.3.1. This hardening is introduced by means of GNDs distributed within the ferrite matrix.

First, these GNDs can be inherited from the expansion of the martensitic phase during its formation [TSI 11]:

$$\rho^f(\epsilon_p^f = 0) = f_{\alpha'} \frac{M_T}{b_{111} D_\alpha^0} \epsilon_0 \tag{5.14}$$

where $f_{\alpha'}$ is the martensite fraction and ϵ_0 is an average deformation term in the initial state allowing the experimental curves to be reproduced. It also allows the dislocation density to be integrated within the ferrite.

Cette thèse est accessible à l'adresse : http://theses.insa-lyon.fr/publication/2020LYSEI120/these.pdf
© [A. MATHEVON], [2020], INSA Lyon, tous droits réservés

Secondly, material deformation can also create GNDs to accommodate deformation incompatibilities between the two phases resulting from their different mechanical properties.

Figure 5.14.(a) schematically illustrates the microstructure simplification to introduce these two phenomena into the model, which consists in assuming that only a characteristic distance L_f in the ferritic grain interacts with the martensite islands. Allain *et al.* [ALL 15] proposed the following relationship based on Ashby's work [JIA 95, BOU 01]:

$$\rho^{GND} = \frac{f_{\alpha'}}{b_{111} L_f} \frac{\left[1 - \exp\left(-\beta_{GND}(\epsilon^f_{tot} - \epsilon^m + \epsilon_0)\right)\right]}{\beta_{GND}} \tag{5.15}$$

where L_f is the characteristic dispersion length of Ashby's GNDs in the ferrite from the ferrite/martensite interfaces and β_{GND} is a parameter controlling the saturation effect of the GNDs.

Once the amount of GNDs within the ferrite grains has been defined, it is necessary to update equations (5.3) and (5.6) as follows:

$$\sigma^f_R(\epsilon^f_p) = \alpha_T M_T \mu b_{111} \sqrt{\rho^f + \rho^{GND}} \tag{5.16}$$

$$\frac{d\rho^f}{d\epsilon^f_p} = M_T \left(\frac{\left(1 - \frac{n_f}{n^0_f}\right)}{b_{111} D^0_\alpha} + k^f \sqrt{\rho^f + \rho^{GND}} - f^f \rho^f \right) \tag{5.17}$$

5.3.3.3 Scale transition law

The mechanical behaviour of heterogeneous DP steel is modelled using a mixture law. The stress and macroscopic deformation of the composite are thus expressed as a function of the properties of the respective constituents weighted by their relative phase fractions using the following formulas [BOU 02]:

$$\sigma^{DP}(\epsilon^{DP}) = f_{\alpha'} \sigma^m(\epsilon^m) + (1 - f_{\alpha'}) \sigma^f(\epsilon^f_{tot}) \tag{5.18}$$

$$\epsilon^{DP} = f_{\alpha'} \epsilon^m + (1 - f_{\alpha'}) \epsilon^f_{tot} \tag{5.19}$$

To fully solve the problem, it is necessary to add a scale transition law between the two phases. There are several possible options, with the two most classic being the iso-strain and iso-stress laws. A more physical law, which supposes the equality of the mechanical work dissipated in each phase, called the iso-work law[BOU 02], has been used particularly for this type of system for small martensite fractions. However, for higher fractions (approximately 15%-20%), this model underestimates the composite strain hardening for small deformations. Therefore, the approach developed here assumes an iso-deformation law at the beginning of the deformation that will then tend linearly towards an iso-work law. The martensitic structure will thus block the ferrite deformation at the beginning

Cette thèse est accessible à l'adresse : http://theses.insa-lyon.fr/publication/2020LYSEI120/these.pdf
© [A. MATHEVON], [2020], INSA Lyon, tous droits réservés

before rearranging (fracture of ferritic or martensitic grains) and leading to a more homogeneous distribution of the stress within the material. The following hybrid interaction law allows us to account for the martensite percolation effect:

if $\epsilon_c^m < 0.04$ and $f_{\alpha'} > 20\%$ then [**hybrid law**]

$$d\epsilon^f = d\epsilon^m \left(1 + \left(\left(\frac{\sigma^m}{\sigma^f}\right) - 1\right)\left(\frac{\epsilon^m}{\epsilon_c^m}\right)\right) \tag{5.20}$$

else [**iso-work law**]:

$$d\epsilon^f \sigma^f = d\epsilon^m \sigma^m : \tag{5.21}$$

where ϵ_c^m is the critical deformation for which we assume martensite fracture and above which the iso-work law is assumed.

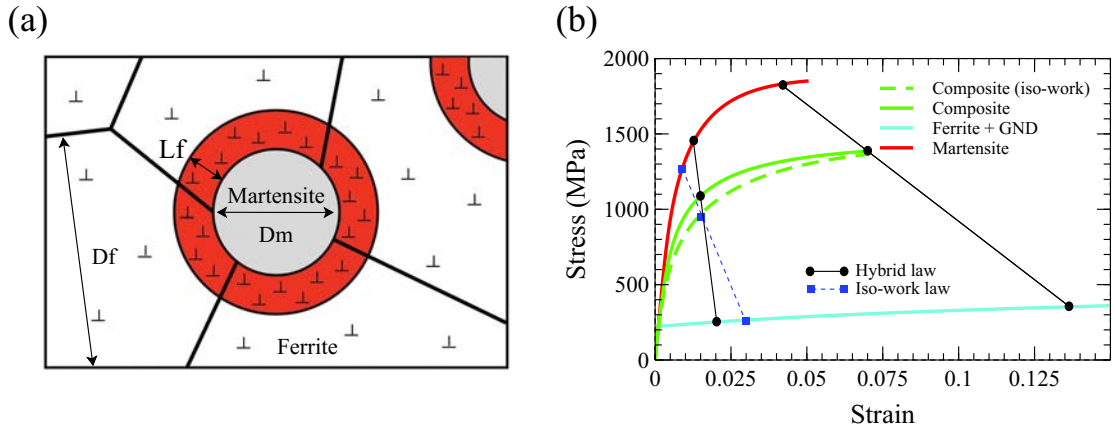

Figure 5.14: (a) Scheme describing the characteristic length L_f of the martensitic island interaction zone within a ferritic grain of diameter D_α^0. (b) Comparison of two mixing laws (iso-work and new hybrid law proposed in this study) to determine the macroscopic behaviour of DP steel from the behaviour of ferrite and martensite.

Once the basics of the Hy-MFC model were established, it was possible to distinguish the different stages during the tensile test, as shown in Figure 5.14.(b):

- Step 1 ($\sim 0 - 100$ MPa): Both phases deform elastically as long as the stress of the DP composite is below the yield stress of ferrite.
- Step 2 ($\sim 100 - 400$ MPa): The martensitic phase remains in the elastic domain while the ferrite begins to deform plastically (close to iso-deformation). The composite strain hardening remains very high because of the martensite, which limits the deformation of the ferrite. GNDs start to appear at this stage as the deformation gradient increases between the two phases. This stage is very short as it ends when the martensite reaches the first local microplastic yield stress.
- Step 3: As deformation proceeds, the iso-deformation gradually switches to the iso-work law. Additionally, as the deformation gradient between the phases increases, the number of GNDs formed at the interfaces to accommodate this deformation increases until saturation and relaxation phenomena occur. However, as the quantity of SSDs increases, the dislocation annihilation effect becomes more effective and tends towards global saturation of the dislocation density. This saturation results in a decrease of the macroscopic work-hardening rate of the material.

Cette thèse est accessible à l'adresse : http://theses.insa-lyon.fr/publication/2020LYSEI120/these.pdf
© [A. MATHEVON], [2020], INSA Lyon, tous droits réservés

5.3.3.4 Hybrid model parameters

The model parameters were validated using literature data for different steels. Steels with low micro-alloying element contents were selected to avoid precipitation and focus on microstructures without bainite and without additional tempering treatment. Three key microstructural parameters are required to be able to predict the mechanical properties of the steels, *i.e.*:

- $f_{\alpha'}$, the fraction of martensite that can be obtained during the thermal cycle using a phase-transformation model or optical quantification.
- D_α^0, the initial ferritic grain size, which is highly dependent on the hot-rolling thermal cycle.
- C_C^m, the mass concentration of carbon within martensite. It can be estimated from a mass balance assuming that ferrite no longer contains carbon:

$$C_C^m = \frac{C_C^0}{f_{\alpha'}} \tag{5.22}$$

  where C_C^0 is the total carbon content of the steel (expressed in wt%). Note that the C_C^m concentration should be limited to 0.6 wt% in view of the experimental results, which reveal saturation of the mechanical properties and brittle behaviour of martensite for high C concentrations. In addition, the substitutional elements are supposed to be homogeneously distributed in the steel, although it could be possible to study their partitioning in the case of longer heat treatment.

The parameters constituting the intrinsic properties of ferrite and martensite were calibrated on single-phase steels and are summarized in Table 5.2.

For the calibration of the Hy-MFC model, three parameters were adjusted by Allain *et al.* [ALL 15]:

- ϵ_0=0.05 is the average deformation within the initial ferrite imposed by the martensitic transformation.
- β_{GND}=18 is the parameter characterizing the saturation of the number of GNDs with the appearance of the relaxation phenomenon during storage.
- L_f is the characteristic length over which the GNDs will disperse from the martensite/ferrite interfaces. For steels processed in the intercritical domain, this length L_f appears to be sensitive to the size of the martensitic islands. Moreover, it is possible to correlate the size of martensitic islands with the ferritic grain size. The best calibration led to the following formula [ALL 15]:

$$L_f = 0.0225 D_\alpha^0 \frac{f_{\alpha'}^{\frac{1}{3}}}{1 - f_{\alpha'}^{\frac{1}{3}}} + 0.288\ \mu\text{m} \tag{5.23}$$

Cette thèse est accessible à l'adresse : http://theses.insa-lyon.fr/publication/2020LYSEI120/these.pdf
© [A. MATHEVON], [2020], INSA Lyon, tous droits réservés

Parameter	Symbol	Unit	Value
Ferrite model			
Forest hardening coefficient	α_T	-	$0.38\ *^1$
Taylor factor	M_T	-	$2.77\ *^1$
Shear modulus	μ	GPa	$79.3\ *^1$
Burgers vector in α-Fe	b_{111}	m	$2.48 \times 10^{-10}\ *^1$
Maximum number of dislocations	n_0^f	-	$6.2\ *^1$
Latent coefficient hardening	k^f	m^{-1}	$2.82 \times 10^7\ *^1$
Dynamical recovery parameter	f^f	-	$1.3\ *^1$
Mean shear-band spacing	λ^f	m	$2.23 \times 10^{-8}\ *^1$
Martensite model			
Young's modulus	Y	GPa	$210\ *^2$
Composite interaction parameter	β	GPa	$50\ *^2$
Avrami parameter	σ_{min}	MPa	$320\ *^2$
Avrami parameter	m	-	$1.8\ *^2$
Local yield strength constant	K_0	MPa	**570**
Local yield strength constant	K_1	$MPa.mm^{0.5}$	**24**
Local yield strength constant	K_2	$MPa.wt\%^{-1.34}$	**6053**
Interaction law model			
Initial mean deformation in ferrite	ϵ_0	–	$0.05\ *^3$
GND relaxation process parameter	L_f	μm	$0.0225 D_\alpha^0 \frac{f_{\alpha'}^{\frac{1}{3}}}{1-f_{\alpha'}^{\frac{1}{3}}} + 0.288\ *^3$
GND relaxation process parameter	β_{GND}	–	$18\ *^3$

Table 5.2: Values of the key parameters used in the different mechanical models. Similar values used by $*^1$ [BOU 08], $*^2$ [ALL 12] and $*^3$ [ALL 15]

5.4 Model validation and discussion

As described in Section 5.2, the use of two DP states after austenitization treatment containing different martensite fractions (see Table 5.1) in addition to the fully martensitic state allowed us to validate the hybrid transition law developed in this work.

Comparison between the iso-work law and the hybrid law

Figure 5.15 presents a comparison of the two transition laws applied to two ternary Fe-C-1.7Mn grades. The iso-work law leads to a clear underestimation of strain hardening for small deformations. This effect is amplified by the martensite C content, which is explained by an increase in the intrinsic mechanical properties of martensite and thus in the mechanical incompatibility between the two phases. The hybrid law proposed in this work thus better reproduces the strain hardening.

The EBSD observations shown in Figure 5.16 reveal a significant misorientation of ferrite grains in contact with martensite islands for an overall deformation of only 4.5%. This highlights the effect of martensite on ferrite, which prevents the ferrite from reaching

Cette thèse est accessible à l'adresse : http://theses.insa-lyon.fr/publication/2020LYSEI120/these.pdf
© [A. MATHEVON], [2020], INSA Lyon, tous droits réservés

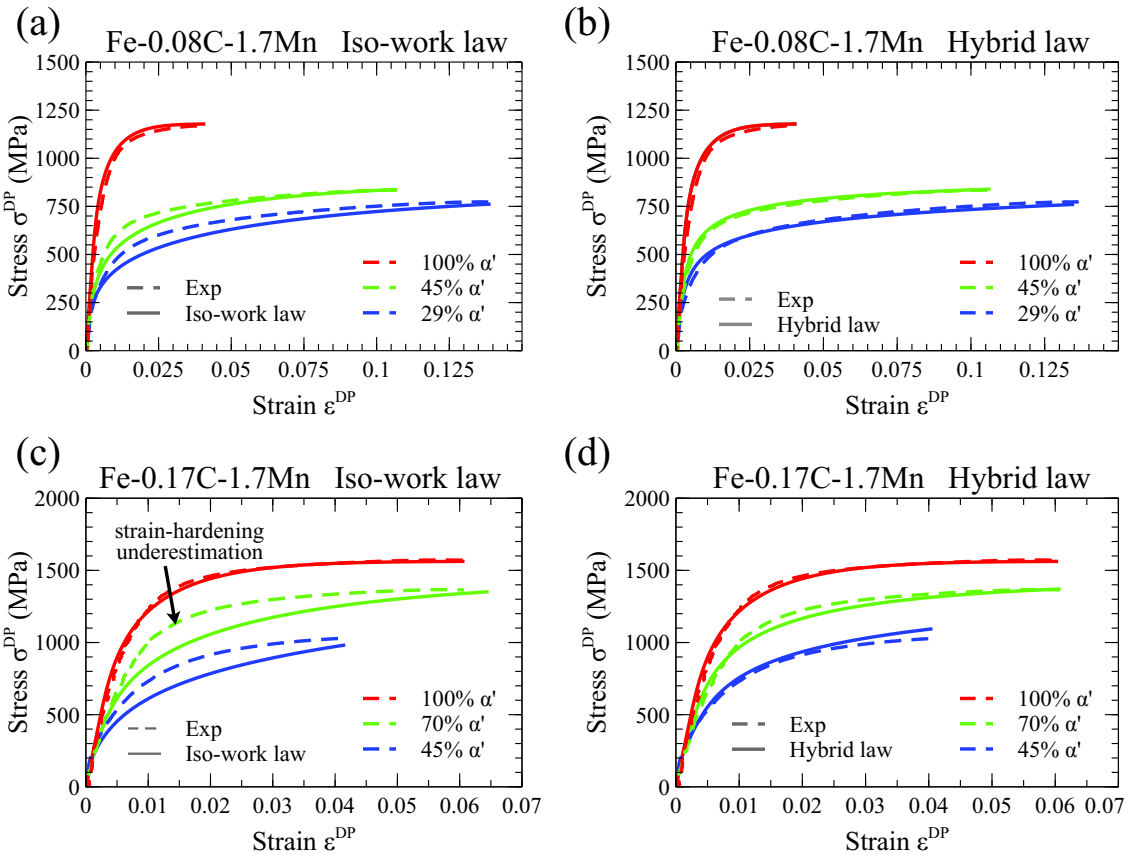

Figure 5.15: Comparison between experimental and simulated tensile curves with iso-work law for (a) the Fe-0.08C-1.7Mn steel and (c) the Fe-0.17C-1.7Mn steel. Comparison between the experimental and simulated tensile curves with new hybrid law for (a) the Fe-0.08C-1.7Mn steel and (c) the Fe-0.17C-1.7Mn steel.

the deformation predicted by the iso-work law hypothesis. Additionally, many examples of fracture/decohesion were observed in the ferritic grains and possibly within martensite, justifying the hybrid law (transition between iso-strain to iso-work).

Application of the Hy-MFC model to the industrial DP steels

Figure 5.17 compares the Hy-MFC model with tensile tests of industrial steels. Good agreement was attained for all martensite fractions and chemical compositions.

It is important to note that the model poorly accounts for strain-hardening saturation for the DP1000 steel containing 28% martensite. Indeed, the chemical composition of martensite is approximately 0.6 wt% C, which is the limit of the martensite calibration properties (see Section 5.3.3.4). Moreover, martensite exhibits brittle behaviour during tensile tests for such a chemical composition, explaining the strain-hardening saturation and the need to introduce an additional phenomenon in this case.

Nevertheless, as most industrial steels undergo an additional tempering treatment that softens the properties of martensite, the concentration of carbon in solid solution within the martensite will be lower, enabling us to more closely approach the assumptions of the

Cette thèse est accessible à l'adresse : http://theses.insa-lyon.fr/publication/2020LYSEI120/these.pdf
© [A. MATHEVON], [2020], INSA Lyon, tous droits réservés

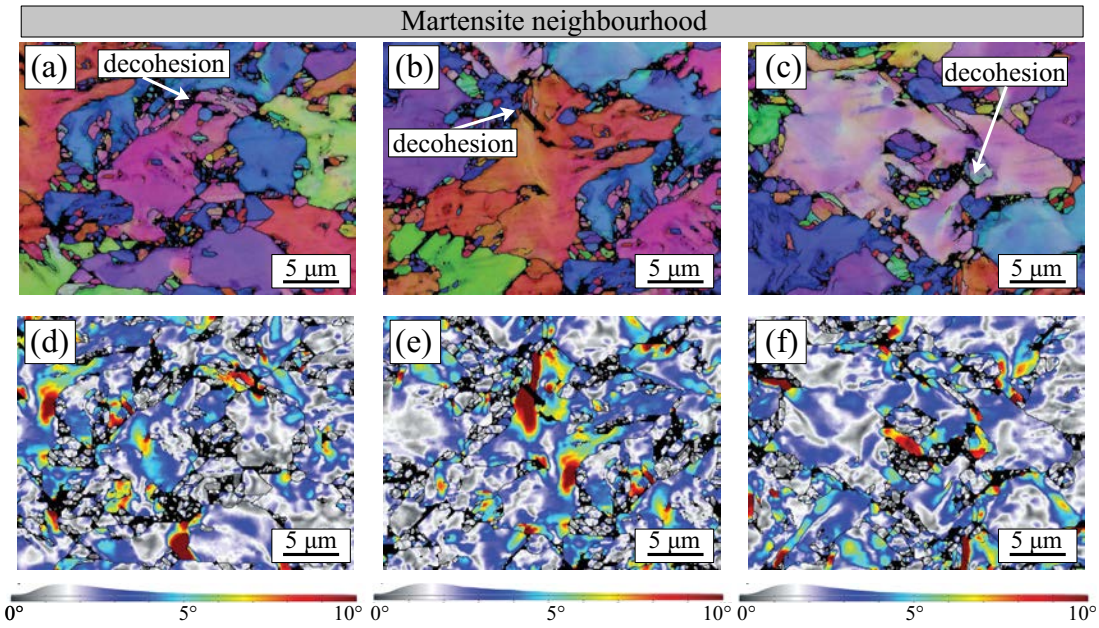

Figure 5.16: (a-c) IPFZ colour maps and (d-f) KAM maps of EBSD observation of DP600 steel containing 41% martensite at 4.5% global strain.

established model.

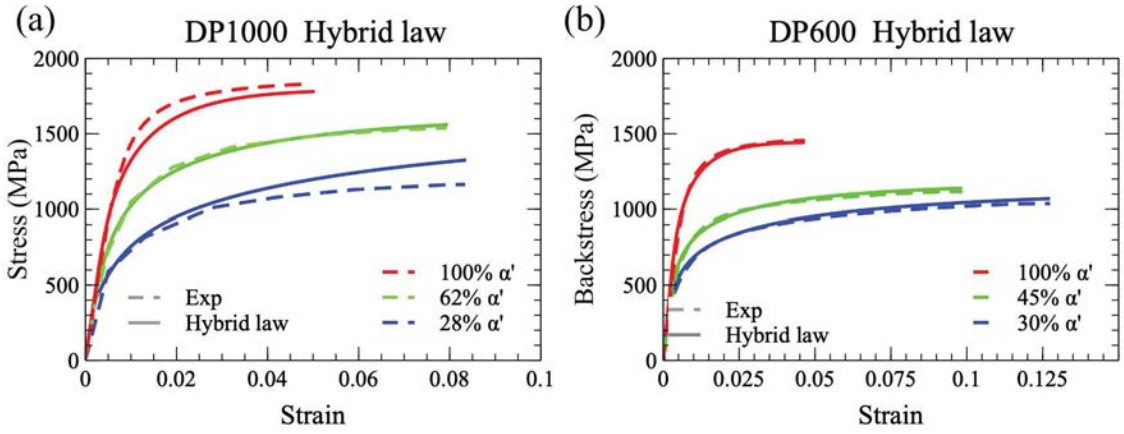

Figure 5.17: Comparison of experimental and simulated tensile curves with new hybrid law for (a) DP1000 and (c) DP600.

5.5 Conclusions

The Hy-MFC physical model developed in this work was designed to reproduce and predict the mechanical properties of DP steels based on microstructural parameters (*i.e.* chemical composition, martensite fraction, and grain size). The wide range of steels available for this study allowed us to overcome the difficulty of calibrating a model from literature

Cette thèse est accessible à l'adresse : http://theses.insa-lyon.fr/publication/2020LYSEI120/these.pdf
© [A. MATHEVON], [2020], INSA Lyon, tous droits réservés

data obtained under varying experimental conditions (cooling rate, quenching conditions) and with uncontrolled microstructure features (grain size, fraction and topology of the different phases). It was thus possible to study the effect of the key parameters through precise control of the different microstructural parameters while avoiding the problems of partial tempering, which can affect the final mechanical properties. The development of the model involved three main steps:

- For the fully ferritic phase, the model of Bouaziz *et al.* [BOU 08] (including all model parameters) was used.
- For the fully martensitic phase, a new dependence of the mechanical properties on the prior austenite grain size was proposed and calibrated on all the studied steels. Calibration of the effect of carbon on the properties of martensite was also proposed, leading to excellent agreement for all the studied steels. Finally, it was demonstrated that manganese contributes only through solid-solution hardening.
- A set of hypotheses allowing the interaction between ferrite and martensite to be reproduced led to an excellent description of the overall mechanical behaviour of the composite. This interaction was based on the addition of GNDs within the ferrite, stemming from the martensitic volume variation and the deformation incompatibility between the two phases. In addition, a new scale transition law was proposed, assuming a linear transition between an iso-strain and iso-work law, which resulted in a more accurate description of the strain hardening of the composite for low deformation in bi-percolant microstructures.

A complete validation of the Hy-MFC model was performed for a wide range of chemical compositions, grain sizes, and martensite fractions.

Finally, EBSD observations of selected areas for different deformations helped us to identify the effect of the neighbourhood of ferrite grains on their deformation. Local misorientation zones were observed within the ferritic grains in contact with martensitic islands. The numerous decohesion and high-misorientation zones within the ferrite grains indicated the primordial effect of the composite on the microstructure, validating the hypothesis of adding GNDs to accommodate the deformation incompatibility between the phases.

Cette thèse est accessible à l'adresse : http://theses.insa-lyon.fr/publication/2020LYSEI120/these.pdf
© [A. MATHEVON], [2020], INSA Lyon, tous droits réservés

Cette thèse est accessible à l'adresse : http://theses.insa-lyon.fr/publication/2020LYSEI120/these.pdf
© [A. MATHEVON], [2020], INSA Lyon, tous droits réservés

Chapter 6

Tempering of DP steels: microstructural evolutions and mechanical properties

Previously, physically based models have been used to predict the mechanical properties of Dual-Phase steels taking into account their key microstructural parameters (grain size, phase fraction and chemical composition). Industrially, martensite tempering is induced in the microstructure as a result of the galvanizing step process in the zinc bath ($\simeq$400 °C) or is added in some cases to increase the steel's formability. Nevertheless, tempering has a strong softening effect on the intrinsic properties of martensite as well as on the mechanical behaviour of the DP steels.

For this reason, this study is based on the extension of the "composite" mean-field model detailed in Chapter 5 while relying on the approach developed by Cupertino *et al.* [MAL 17] relative to the modelling of the intrinsic properties of tempered martensite.

The aim of the studies presented in this chapter is thus to develop a prediction model enabling to reproduce the tensile curve of a tempered DP microstructure for a wide range of physical parameters of the microstructure (grain size, phase fraction and chemical composition) and for different tempering heat treatments (including different tempering times and temperatures).

First of all, a characterization of the microstructural evolutions and mechanical properties of fully martensitic steels was performed during isothermal tempering between 100 °C and 550 °C. To this end, the tempering kinetics of the investigated steels were followed using ThermoElectric Power (TEP) and hardness measurements. From the obtained kinetics, time-temperature equivalences could be performed and led to the determination of the activation energies of the mechanisms controlling the tempering phenomenon of martensite in the investigated temperature range. Then an extended "composite" mean-field model of the mechanical properties was proposed using several JMAK laws reproducing the identified mechanisms and based on the measured activation energies.

Cette thèse est accessible à l'adresse : http://theses.insa-lyon.fr/publication/2020LYSEI120/these.pdf
© [A. MATHEVON], [2020], INSA Lyon, tous droits réservés

Contents

Cette thèse est accessible à l'adresse : http://theses.insa-lyon.fr/publication/2020LYSEI120/these.pdf
© [A. MATHEVON], [2020], INSA Lyon, tous droits réservés

6.1 Literature review

Dual-Phase steel production usually requires a galvanizing step in a zinc bath or an additional treatment to improve the formability properties. This supplementary heat treatment leads to microstructure evolutions, in particular within martensite. Several phenomena such as carbon segregation on defects and dislocations, cementite precipitation and reduction of the martensite internal defects result in a marked decrease in the steel ultimate strength while strongly increasing its toughness. Microstructural evolutions that may occur during the tempering stage will first be detailed hereafter before considering available approaches to model the mechanical properties of tempered martensite.

6.1.1 Microstructural evolutions during martensite tempering

6.1.1.1 Tempering stages

The metastable martensite formed after quenching progressively evolves towards an equilibrium state. Speich *et al.* [SPE 72] proposed a detailed description of the phenomena which may occur during the tempering of binary Fe-C steels with a negligible fraction of retained austenite according to the tempering temperature. This is illustrated in Figure 6.1 which highlights several tempering stages detailed hereafter:

- **Stage 0: Carbon segregation.** This phenomenon is expected to occur at very low temperatures (60-120 °C) and is associated with a redistribution of the carbon atoms in solid solution towards lower energy sites (such as dislocations or lath boundaries). Here, it has to be pointed out that carbon segregation on dislocations and lath boundaries is also expected during cooling if the M_S temperature is sufficiently high (that is to say if the carbon content is low) leading to an auto-tempering effect. This is illustrated in Figure 6.2 which clearly shows that increasing the M_S temperature or the specimen thickness has a marked influence on auto-tempering during the quench. Depending on the values of these parameters, three phenomena linked to carbon diffusion may occur : (i) carbon precipitation (especially, for the highest M_S temperatures and specimen thicknesses), (ii) carbon segregation on lath boundaries and (iii) carbon segregation on dislocations.
- **Stage 1: Intermediate carbide precipitation.**

  During stage 1 observed typically between 100 °C and 250 °C, various intermediate metastable carbides (ε, η, Hägg) are expected to precipitate depending on the steel chemistry:
  - ε carbides ($Fe_{2-4}C$, hexagonal) uniformly distributed in martensite may precipitate. In fact, ε precipitation is expected only for carbon compositions higher than 0.2 wt%. In this case, the amount of carbon in solution (without being segregated to the defects of the microstructure) is high enough to enable the precipitation [SPE 72].
  - η carbides (Fe_2C, orthorhombic): η carbides (as ε carbides) considerably decrease the martensite tetragonality [WAT 06].
  - Hägg carbides (χ, Fe_5C_2): χ precipitation is expected at higher temperature

Cette thèse est accessible à l'adresse : http://theses.insa-lyon.fr/publication/2020LYSEI120/these.pdf
© [A. MATHEVON], [2020], INSA Lyon, tous droits réservés

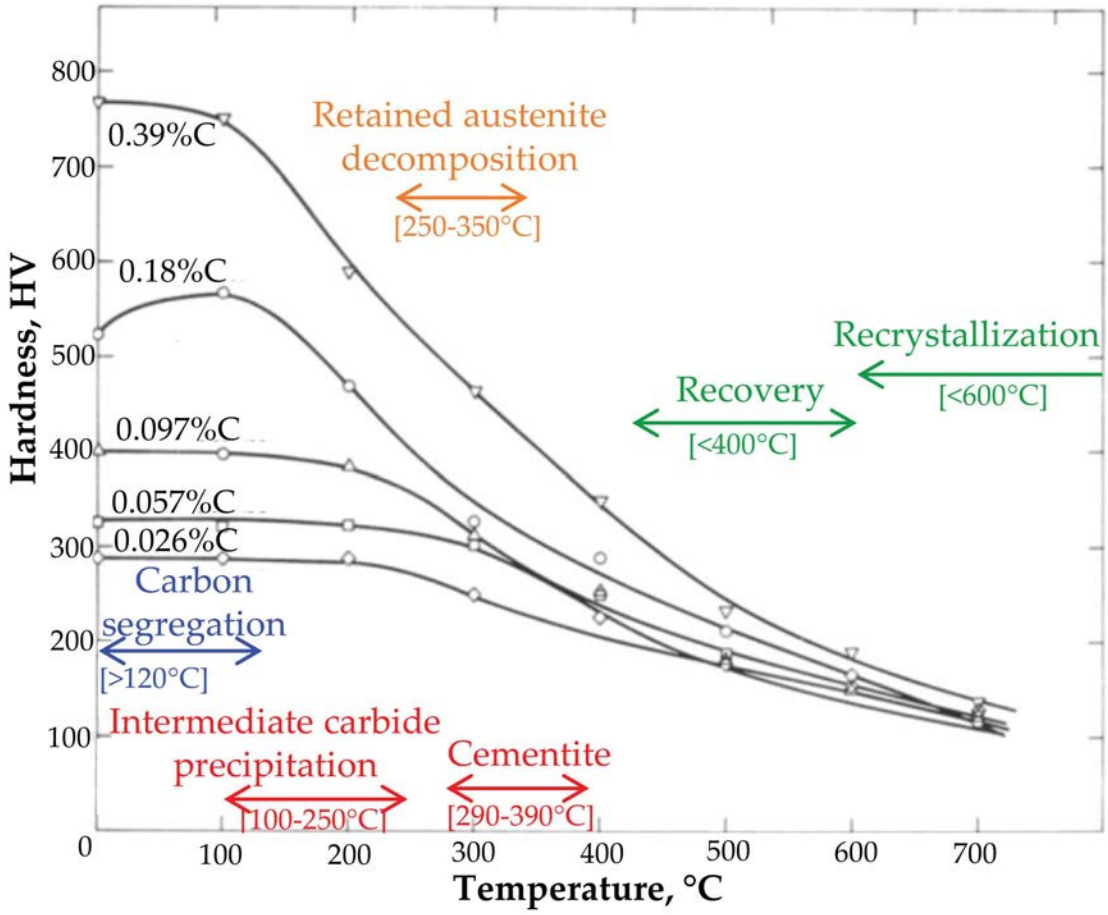

Figure 6.1: Various stages of martensite tempering as a function of the tempering temperature for binary Fe-C steels with different carbon contents [SPE 72].

between 220 and 300 °C, after ε and η precipitations [WAT 06] [SCH 07]. In addition, it serves as a precursor for the cementite precipitation [NAR 14].

- **Stage 2: Cementite precipitation (θ, Fe_3C, orthorhombic).** Cementite precipitation occurs at higher temperature (between 300 and 400 °C) after dissolution of the intermediate carbides. Initially, cementite precipitates with a plate-like morphology inside martensite laths or interfaces. Then, at higher temperatures, cementite spheroidizes and coarsens to reach its equilibrium state [MAS 14].
- **Stage 3: Recovery/Recrystallization.** Recovery takes place for temperatures superior to 400 °C and ferrite recrystallization may occur above 600 °C depending on steel chemistry. Marceaux *et al.* [MAR 20b] has observed that the achievement of the equilibrium amount of cementite during continuous heating at 1 °C/s requires to reach 650 °C. This indicates that a part of carbon is trapped in the defects of the microstructure up to very high temperatures.

Table 6.1 summarizes the activation energies and the temperature ranges commonly observed for the different phenomena involved in martensite tempering.

Cette thèse est accessible à l'adresse : http://theses.insa-lyon.fr/publication/2020LYSEI120/these.pdf
© [A. MATHEVON], [2020], INSA Lyon, tous droits réservés

Phenomenon	Temperature range	Activation energy
C segregation	60-120°C	80 kJ/mol [CHE 88] 100.6 kJ/mol [WAT 06]
Precipitation of ε and η-carbides	120-195°C 150-180°C	120-200 kJ/mol [CHE 88] 123.8 kJ/mol [WAT 06] 105-120 kJ/mol [MIT 88] [MOR 01]
Hägg carbides precipitation	220-300°C	136 kJ/mol [WAT 06]
Cementite precipitation	290-390°C 300-350°C	176.1 kJ/mol [WAT 06] 163-212 kJ/mol [MIT 88] [MOR 01]

Table 6.1: Temperature range and activation energy data for the martensite tempering.

6.1.1.2 Influence of alloying elements

Kinetics of the different phenomena occurring during the martensite tempering can be modified when adding alloying elements [GRA 77] [MIY 07].

First, the phenomenon of carbon segregation on dislocations and lath boundaries may be slightly influenced by the addition of alloying elements (such as Mn, Cr and Si) since these elements are known to decrease the carbon mobility in iron [VAS 18]. As a consequence, the segregation kinetics of carbon to defects may be slightly delayed with the addition of these elements. Moreover, the addition of alloying elements can modify the M_S temperature of the steel leading to a more or less important auto-tempering during quenching.

Cementite precipitation is also expected to be greatly influenced by the addition of substitutional elements (such as Mn, Cr and Si), as these elements are known to retard the growth and coarsening rate of cementite [MIY 07]. This leads to a delayed softening of the mechanical properties (hardness, yield strength, UTS) of martensite compared to those of the corresponding binary alloys [GRA 77]. This retardation in the growth and coarsening of cementite is considered to be mainly due to the partitioning of the substitutional elements between ferrite and cementite. For example, Cr, Mn, V and Mo are assumed to enrich cementite during tempering, while Ni, Co, Si and Al are supposed to be rejected in ferrite [MIY 07]. So, the kinetics controlling the growth and coarsening of cementite is not only governed by carbon diffusion but also by the partitioning of these elements which is managed by the slow diffusion of substitutional elements in ferrite.

Here, it has be pointed out that the retarded decrease in hardness or tensile strength due to the addition of substitutional element can be partly explained by the fact that the finer and more numerous cementite carbides observed in the microstructures due to this addition lead to a higher resistance to grain growth in the ferrite matrix [GRA 77] and thus, to a delay in the recovery-recrystallization phenomenon.

Cette thèse est accessible à l'adresse : http://theses.insa-lyon.fr/publication/2020LYSEI120/these.pdf
© [A. MATHEVON], [2020], INSA Lyon, tous droits réservés

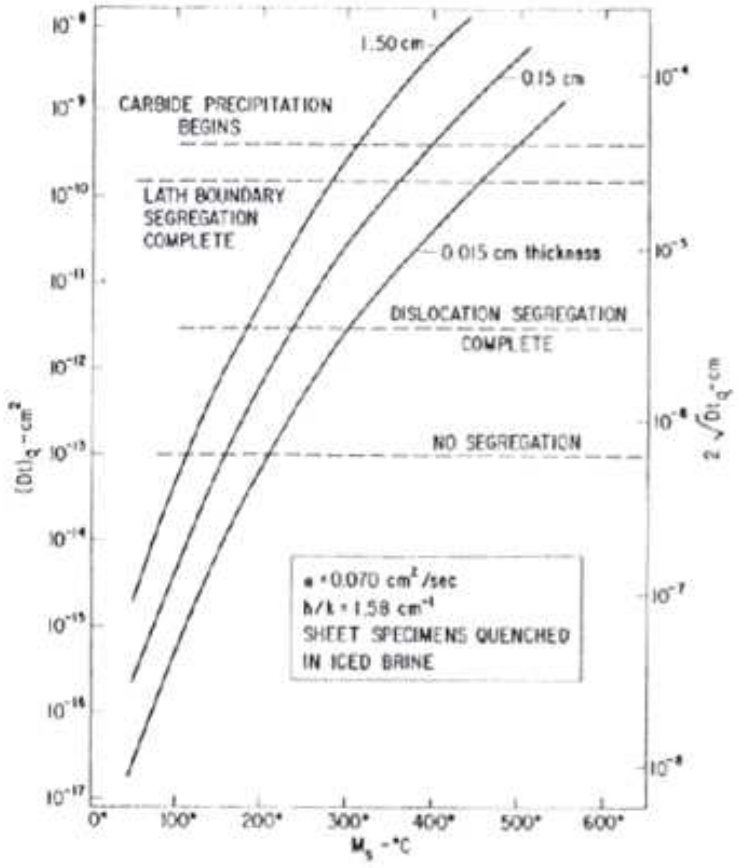

Figure 6.2: Effect of Ms temperature and specimen thickness on carbon diffusion for specimens quenched in iced brine [SPE 69].

6.1.1.3 Tempering of Dual-Phase microstructure

Tempering of martensite in the case of two-phase steels seems to be similar to the one occurring in purely martensitic steels: [HER 11]. However, it is important to note that the composition and morphology of martensite in the case of two-phase steels are strongly influenced by the intercritical process defining the ferritic and martensitic phase fraction and the martensite carbon content. Furthermore, as the M_S temperature in the case of two-phase steels is reduced due to the carbon enrichment of martensite, the possible self-tempering within martensite is limited.

It has also to be pointed out that the martensitic phase transformation can induce the appearance of residual stresses and of dislocations within ferrite close to the martensitic islands. This is why, DP steel tempering results also in ferrite tempering which induces a relaxation of residual stresses and a decrease in dislocation density. Moreover, at high temperature (∼400 °C), carbides may be formed in ferrite thanks to carbon released from the martensite tempering [WAT 03]. The evolution of ferrite mechanical properties remains nevertheless negligible compared to the important softening observed in martensite.

Cette thèse est accessible à l'adresse : http://theses.insa-lyon.fr/publication/2020LYSEI120/these.pdf
© [A. MATHEVON], [2020], INSA Lyon, tous droits réservés

6.1.2 Modelling of the mechanical properties of tempered martensite

This part aims at describing the few approaches developed in the literature to follow the mechanical properties of martensite during tempering which are the result of the combination of several phenomena strongly dependent on the chemical composition.

6.1.2.1 JMAK and time-temperature equivalence

The phenomena occurring during martensite tempering and the resulting mechanical properties (hardness, YS, UTS) can be described using a Johnson-Mehl-Avrami-Kolmogorov (JMAK) law which requires the determination of three parameters: Q (the activation energy), n (the Avrami coefficient) and b_0 (a rate constant). This type of law has already been presented in this work, notably in Chapter 2 for the modelling of the recrystallization kinetics (see Section 2.1.3.3).

With regard to the activation energy (Q) of the JMAK law, it can be determined experimentally using a time-temperature equivalence on transformation kinetics carried out at different temperatures. This equivalence is based on the assumption that the diffusion length associated with a single phenomenon must be identical for the two time-temperature pairs used (t_A, T_A) and (t_B, T_B):

$$\begin{cases} t_A = t_0 \exp\left(\frac{Q}{RT_A}\right) \\ t_B = t_0 \exp\left(\frac{Q}{RT_B}\right) \end{cases} \tag{6.1}$$

It is thus possible thereafter to define an equivalent time t_B^{eq} at the reference temperature T_B for a measurement carried out using a heat treatment at the temperature T_A for a time t_A. This time can be calculated with the following expression:

$$t_B^{eq} = \exp\left[\frac{Q}{R}\left(\frac{1}{T_B} - \frac{1}{T_A}\right)\right] t_A \tag{6.2}$$

6.1.2.2 Hollomon-Jaffe approach

Although all the phenomena are not understood, Hollomon and Jaffe [HOL 45] proposed an equation to reproduce the evolution of hardness as a function of time and tempering temperature. They found the following relationship between the tempering conditions (T, t) and the hardness:

$$R_c = H_c - 0.00457T[13 + \log(t)] \tag{6.3}$$

where R_c is the Rockwell C hardness, H_c is a characteristic hardness parameter, T is the tempering temperature in Kelvin and t is the tempering time in seconds.

Cupertino *et al.* [MAL 17] used this type of approach to reproduce the hardness, yield strength, ultimate tensile strength and uniform elongation of different steels during tempering. They defined a Hollomon-Jaffe law for each variable. This model enables to accurately extrapolate the properties for new tempering parameters. However, this type of modelling has an important drawback since the different constants are highly sensitive

Cette thèse est accessible à l'adresse : http://theses.insa-lyon.fr/publication/2020LYSEI120/these.pdf
© [A. MATHEVON], [2020], INSA Lyon, tous droits réservés

to the chemical composition of the steel, fundamentally limiting the extrapolation ability of the model for different chemical compositions.

6.1.2.3 Continuous Composite Approach with tempered martensite

To reproduce the tensile curves of fully martensitic steels, Cupertino *et al.* [MAL 17] proposed to use a simplified version of the Continuous Composite Approach presented in the preceding chapter [ARL 13]. In their model, the elasto-plastic transition used to simulate the plastic behaviour and hardening mechanisms of martensite is given by the following formula for $\sigma^m > \sigma_{min}$ (Combinaison of Equation 5.10 and Equation 5.11 with $\beta = \infty$ and $\sigma_0^m = 0$):

$$\frac{d\sigma^m}{d\epsilon^m} = Y \exp\left[-\left(\frac{\sigma_l - \sigma_{min}}{\Delta}\right)^m\right] \tag{6.4}$$

where σ^m and ϵ^m are respectively the martensite stress and strain, Y is the Young's modulus. n and σ_{min} are the 2 constants of the composite law. In addition, the parameter (noted Δ) is that controlling the width of the local distribution of yield strength as in the previous chapter. However, the dependence of Δ with the chemical composition of the steel is different. Moreover, Cupertino *et al.* substitutes the nominal carbon content of the steel by the amount of carbon in solid solution as follows:

$$\Delta = 130 + 1997 C_{C,ss}\left(1 + \frac{\mathrm{C^0_{Mn}}}{3.5}\right) \tag{6.5}$$

To take into account the martensite softening during tempering and its effect on the tensile behaviour, the decrease in the carbon concentration in solid solution ($C_{C,ss}$) due to the carbon departure from the solid solution is described by a Hollomon-Jaffe law physically corresponding to cementite precipitation:

$$\frac{C_C^0 - C_{C,ss}}{C_C^0} = 0.000103T[13 + \log(t)] - 0.655 \tag{6.6}$$

where C_C^0 is the nominal carbon content for the considered fully martensitic steels.

Cupertino *et al.* [MAL 17] showed that this equation is likely to reproduce rather well the decrease in mechanical properties of tempered martensite resulting from the decrease in the carbon content in solid solution and subsequently in the width of the yield strength local distribution as long as the tempering temperature is lower than 400 °C. For higher temperatures (above 400 °C) , these authors highlighted that a second mechanism has to be taken into account to account for the acceleration of the mechanical property degradation observed in this temperature range and that it could be associated with the martensite recovery phenomenon observed in Fe-C binaries. To this end, they defined a second Hollomon-Jaffe law and applied it to the σ_{min} parameter controlling the beginning of the elasto-plastic transition:

$$\sigma_{min} = \sigma_{min,c} - 0.1T[13 + \log(t)] \tag{6.7}$$

Cette thèse est accessible à l'adresse : http://theses.insa-lyon.fr/publication/2020LYSEI120/these.pdf
© [A. MATHEVON], [2020], INSA Lyon, tous droits réservés

where $\sigma_{min,c}$ is a constant depending on the steel chemical composition.

Figure 6.3 illustrates the model ability to reproduce the evolution of martensite mechanical property during tempering for a wide range of tempering conditions. The addition of two Hollomon-Jaffe laws to describe the phenomena occurring at low and high tempering temperatures gives a physical basis to the model although the different constants involved in the laws required an adjustment according to the chemical composition.

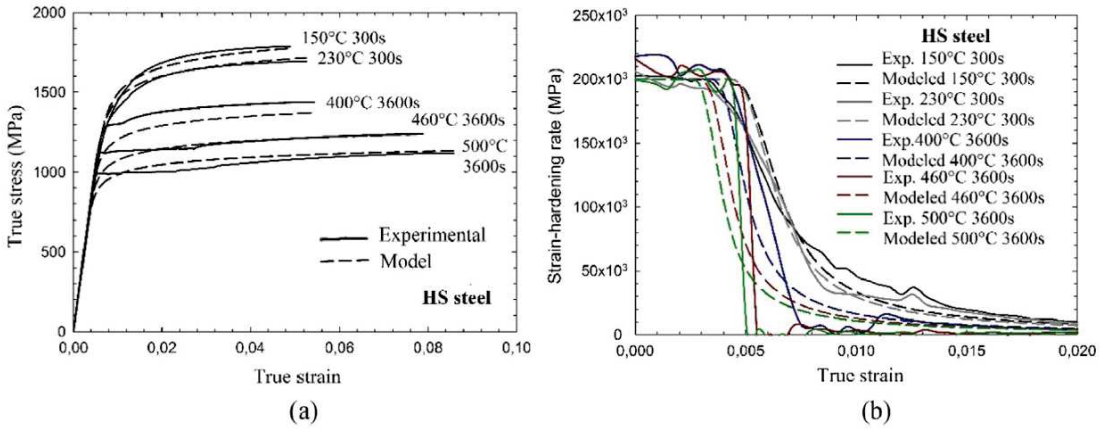

Figure 6.3: Experimental and modelled: (a) tensile curves and (b) strain-hardening evolution. The modelled curves were obtained with the Cupertino model including two Hollomon-Jaffe laws [MAL 17]. The model was applied to a steel with the following composition (in wt.%) : 0.21% C, 2.22% Mn, 1.44% Si, 0.04% Al, 0.21% Cr.

6.1.3 Conclusion: Objective of the present chapter

The martensite mechanical properties depend mainly on its carbon composition in solid solution which according to the study of Speich *et al.* for low carbon steels will evolve as a result of 3 phenomena (carbon segregation on defects, cementite precipitation and recovery). The carbon concentration can therefore be expressed as follows:

$$\mathrm{C}_{C,ss}(t) = C^0_{C,\alpha'} - \Delta C_{C,ss\to\perp}(t) - \Delta C_{C,ss\to\theta}(t) - \Delta C_{C,\perp\to\theta}(t) \tag{6.8}$$

where $C_{C,ss}(t)$ and $C^0_{C,\alpha'}(t=0)$ are respectively the martensite carbon content in solid solution during tempering and the carbon content enrichment of austenite at the quenching phase. The terms $\Delta C_{C,ss\to\perp}$ and $\Delta C_{C,ss\to\theta}$ represent respectively the carbon content left from the solid solution to segregate on the martensite defects and to be precipitated as cementite. Finally, the term $\Delta C_{C,\perp\to\theta}$ corresponds to the carbon content previously segregated on the defects that was precipitated as cementite during the recovery.

The general methodology used in this chapter is summarized in Figure 6.4 and includes three steps.

In a first step, a characterization of the microstructural evolutions and mechanical properties of fully martensitic steels was performed during isothermal tempering between 100 °C and 550 °C. From the hardness and TEP kinetics, time-temperature equivalences

Cette thèse est accessible à l'adresse : http://theses.insa-lyon.fr/publication/2020LYSEI120/these.pdf
© [A. MATHEVON], [2020], INSA Lyon, tous droits réservés

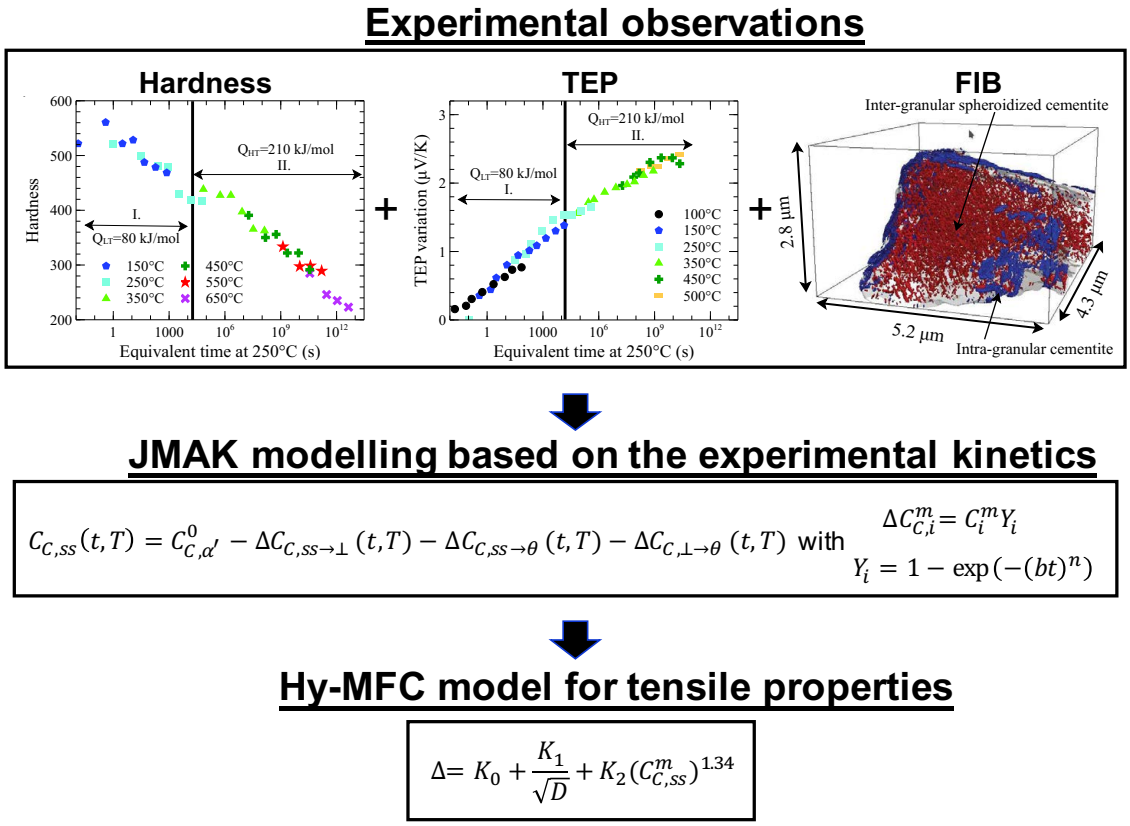

Figure 6.4: Schematics used to integrate a physical basis to the Hy-MFC tensile property prediction model. An evaluation of the JMAK parameters of the different phenomena controlling the tempering was performed using hardness, TEP and FIB monitoring.

could be performed and led to the determination of the activation energies of the phenomena responsible for the TEP and hardness evolutions. Then, using complementary techniques (DSC, TEM and FIB/SEM), these phenomena could be identified.

In a second step, taking into account the experimental kinetics and assuming that they are mainly governed by the carbon departure from the solid solution in the investigated temperature range, a JMAK modelling was proposed to predict the evolution of the carbon in solid solution during tempering. Several contributions were considered: that of the carbon atoms which segregate to the defects (dislocations, lath boundaries), that of the carbon atoms which precipitate directly from the carbon in solid solution and that of the carbon atoms, which were initially trapped by the defects and which are progressively released due to recovery phenomena and may precipitate.

In a third step, this evolution of the carbon content in solid solution was introduced in the mechanical property prediction model developed in Chapter 5 to take into account the martensite tempering. This led us to consider that the width Δ of the local yield strength distribution evolves during tempering as it is related to the carbon content in solution in the steel. However, considering that the evolution of carbon content in solid solution during tempering is modelled using JMAK laws calibrated on experimental kinetics, this

Cette thèse est accessible à l'adresse : http://theses.insa-lyon.fr/publication/2020LYSEI120/these.pdf
© [A. MATHEVON], [2020], INSA Lyon, tous droits réservés

allows to introduce an additional physical basis in the model for predicting martensite properties compared to Cupertino *et al.*. [MAL 17].

The model was fist tested on fully martensitic steels and it was then applied to two-phase microstructures with different martensite volume fractions.

6.2 Materials and experimental procedures

The experimental investigations presented in this chapter were carried out mainly on the four ternary Fe-C-Mn steels. Table 6.2 recalls their chemical composition and gives an estimation of the M_S temperatures of the ternary steels after a full austenitization followed by a water-quench. These temperatures were calculated using the empirical relations for the M_S prediction given in Table 4.1. For each steel, the average calculated value is reported in Table 6.2.

The tempering treatments were performed in salt baths after full or partial austenitization of the steels. The full autenistization was obtained by a 3 min salt bath heat treatment at 850 °C followed by a water quench. For the experimental part of this chapter, the tempering kinetics of the fully martensitic steels were followed using Vickers hardness and ThermoElectric Power (TEP) measurements during isothermal heat treatments in the range 100-550 °C. This was done in order to identify the mechanisms responsible for the martensite tempering and to determine the associated activation energies for various steel compositions. DSC experiments, tensile tests and microstructural characterization (TEM, FIB tomography) were also performed in order to analyze more precisely the results obtained with the other techniques.

Steel grades	Chemical composition (in wt.%)							M_S temperature (°C)
	C	Mn	Cr	Si	Nb	Ti	N	
Ternary steels	0.17	0.5	-	-	-	-	-	440
	0.17	1.7	-	-	-	-	-	395
	0.17	2.5	-	-	-	-	-	366
	0.08	1.7	-	-	-	-	-	430
DP1000	0.17	1.7	0.4	0.3	0.03	0.03	0.006	360

Table 6.2: Chemical composition and Ms temperature of the ternary and industrial steels investigated in this chapter

The DP1000 steel was only used in the preliminary work (see Section 6.3.1) of this chapter

6.3 Experimental characterization of the microstructural evolutions and mechanical properties of fully martensitic steels during isothermal tempering between 100-550 °C

This section aims at characterizing and quantifying the microstructural evolutions and mechanical properties of fully martensitic steels during isothermal treatments performed

Cette thèse est accessible à l'adresse : http://theses.insa-lyon.fr/publication/2020LYSEI120/these.pdf
© [A. MATHEVON], [2020], INSA Lyon, tous droits réservés

between 100-550 °C.

First, in order to investigate the possible martensite auto-tempering during water-quench which was clearly identified by Speich [SPE 69] (see Figure 6.2) and its impact on the tensile behaviour of fully martensitic steels, a preliminary work was performed on the industrial DP1000 steel using samples with different thicknesses to vary the cooling rate during the quenching step.

Second, the tempering kinetics of the ternary Fe-C-Mn steels were followed during isothermal treatments by hardness and TEP, in order to highlight the influence of manganese and carbon on tempering and thus to extract the parameters controlling the evolution of the carbon content in solid solution. Additional experiments based on TEM observations, FIB-SEM tomography, DSC and tensile tests were also performed.

6.3.1 Preliminary work: study of the martensite auto-tempering during the water-quench of DP1000 steel samples with different thicknesses

This preliminary work was performed on the DP1000 steel for which the M_S temperature is sufficiently high (of the order of 360 °C) to enable auto-tempering during the cooling step from the austenitization domain. This phenomenon is likely to lead to carbon segregation to the dislocations and/or to grain boundaries.

For this preliminary study, TEP samples with different thicknesses (between 0.3 and 1.5 mm) were prepared and fully austenitized for 3 min at 850 °C before being water-quenched and subsequently tempered for 1 min at 400 °C to promote cementite precipitation. The TEP value of each sample was measured directly after quench or after quench followed by the tempering treatment of 1 min at 400 °C as illustrated in Figure 6.5.(a).

As can be seen, the TEP value measured after quench gradually increases with an increase in the sample thickness (that is to say, with a decrease in the cooling rate). This can be attributed to the fact that the amount of carbon remaining in solid solution (or not segregated to defects) is lower in the case of thicker samples for which the cooling rate is lower. As carbon in solid solution has a negative effect on TEP while it has no strong influence when it is segregated to the defects, this explains that the TEP value after water-quench is higher for thicker samples.

By contrast, the TEP value measured after 1 min at 400 °C is almost the same for all samples regardless of their thickness. Consequently, the TEP variation between the two considered states plotted in Figure 6.5.(b) decreases with increasing the sample thickness. This TEP difference is supposed to reflect the amount of carbon, initially in solid solution after water-quench, which precipitated to form cementite particles. This amount appears to decrease with increasing the sample thickness. This is consistent with the fact that the amount of carbon in solid solution after water-quench is considered to be lower for thicker samples, thus inducing a lower TEP variation during tempering for 1 min at 400 °C.

Here, it has to be pointed out that one cannot exclude that some carbon atoms initially segregated to the dislocations or grain boundaries during cooling precipitate to form cementite particles. However, these atoms are not expected to lead to a TEP variation as only the carbon atoms initially in solid solution and leaving the solid solution can be

Cette thèse est accessible à l'adresse : http://theses.insa-lyon.fr/publication/2020LYSEI120/these.pdf
© [A. MATHEVON], [2020], INSA Lyon, tous droits réservés

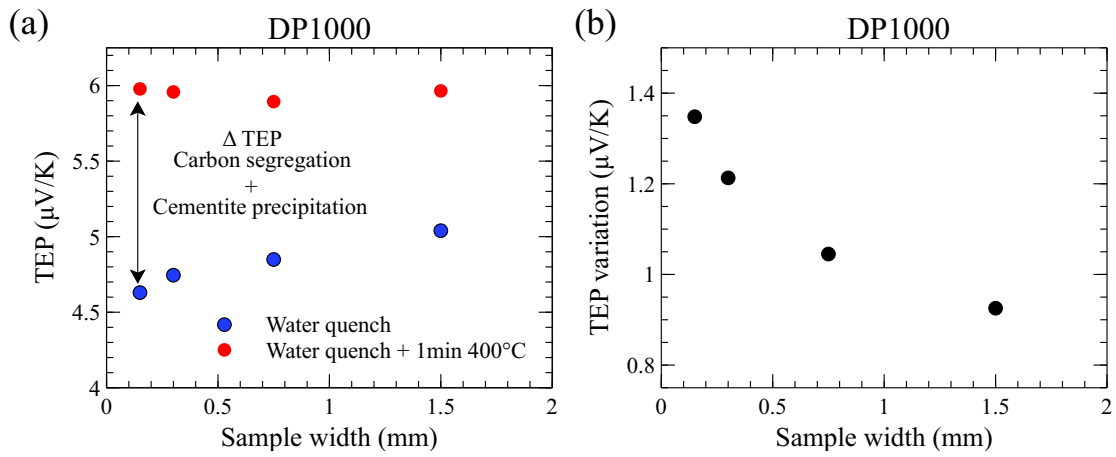

Figure 6.5: (a) TEP evolution as a function of sample thickness after water quench with or without additional tempering for 1 min at 400 °C. (b) Evolution of the TEP difference between the two tempering states as a function of sample thickness. This figure highlights the auto-tempering phenomenon during the quench of DP1000 steel according to the thickness of the sample (*i.e.* cooling speed).

detected by TEP.

As a conclusion, these results support the presence of auto-tempering during tempering due to the relatively high M_S temperature of the investigated steel.

In parallel, in order to show the possible influence of the auto-tempering conditions (due to the use of different cooling rates) on the tensile properties, tensile test were carried out after water-quench on tensile specimens with different thicknesses. The corresponding tensile curves are shown in Figure 6.6 and suggest that the difference in the relative proportion of carbon in solid solution or segregated to defects of the different samples has no strong influence on the tensile behaviour after quench.

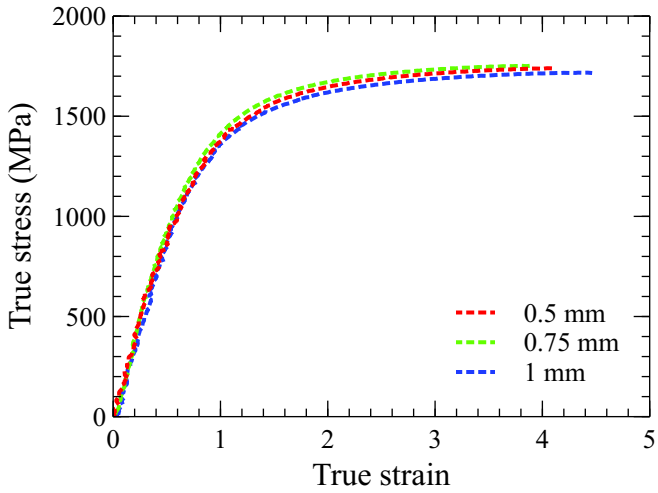

Figure 6.6: Evolution of tensile properties for fully martensitic DP1000 steel as a function of the sample thickness after water quench. The segregation of a carbon fraction previously in solid solution on the martensite defects has a negligible effect on the tensile properties of martensite.

Cette thèse est accessible à l'adresse : http://theses.insa-lyon.fr/publication/2020LYSEI120/these.pdf
© [A. MATHEVON], [2020], INSA Lyon, tous droits réservés

The results of this preliminary study support the idea that the tensile properties of fresh martensite are governed by two populations of carbon atoms: the carbon atoms in solid solution and those segregated to the defects. However, as their contribution on strengthening is very similar which is consistent with the conclusion of Hutchinson *et al.* [HUT 11], it does not seem necessary to distinguish these two types of populations of carbon atoms in a mechanical property prediction model. This is why, in the following, these two populations will not be considered separately and a carbon concentration, denoted $C_{C,ss+\perp}$, will be affected to the sum of the concentrations associated with these two populations.

$$\begin{cases} \mathrm{C}_{C,ss+\perp} = \mathrm{C}_{C,ss} + \mathrm{C}_{C,ss\rightarrow\perp} \\ \mathrm{C}_{C,ss+\perp} = C^{0}_{C,\alpha'} - \Delta C_{C,ss\rightarrow\theta} - \Delta C_{C,\perp\rightarrow\theta} \end{cases} \tag{6.9}$$

6.3.2 Tempering of the Fe-C-Mn ternary steels: Analysis of the influence of the Mn and C content

6.3.2.1 Tempering of the Fe-0.17C-1.7Mn steel

The aim of this section is to present, in a detailed manner, the procedures and the experimental results which were obtained during the tempering of the Fe-0.17C-1.7Mn steel. Namely, this steel was used, in this work, as reference material enabling to highlight in the following sections the respective influence of the Mn content and that of the C content on tempering.

In order to understand and characterize the phenomena involved in the martensite tempering of this steel, its tempering kinetics were followed during isothermal treatments at different temperatures between 150 °C and 550 °C using both hardness and TEP measurements after different treatment times. For the TEP kinetics, the TEP variation between each tempered state and the initial as-quenched state was plotted as a function of time.

Figure 6.7 illustrates that the increase in tempering time and temperature leads to a global decrease in hardness (except for the lowest ageing times at 150 °C where hardness slightly increases). This hardness decrease is associated with a gradual TEP increase which can be interpreted, at first sight, by a departure of carbon atoms from the solid solution and/or by a decrease in the dislocation density (mainly for the highest tempering temperatures where recovery phenomena could come into play). Namely, these two phenomena are assumed to lead to a TEP increase. However, in steels, carbon is known to have a predominant effect on TEP compared to the dislocations.

As detailed in Section 6.1.2.1, a time-temperature equivalence has been carried out on the hardness and TEP kinetics obtained at different temperatures using a reference temperature of 250 °C. In order to be able to match the different kinetics along a single master curve reflecting the microstructural evolutions during tempering, it was necessary to use two different activation energies (see Figure 6.8): one of about 80 kJ/mol for the lowest temperatures (T < 300 °C) and another one of about 210 kJ/mol for the highest temperatures. The first activation energy corresponds to that for carbon diffusion in iron, while the second one is close to that for self-diffusion of iron. Here, it has to be pointed

Cette thèse est accessible à l'adresse : http://theses.insa-lyon.fr/publication/2020LYSEI120/these.pdf
© [A. MATHEVON], [2020], INSA Lyon, tous droits réservés

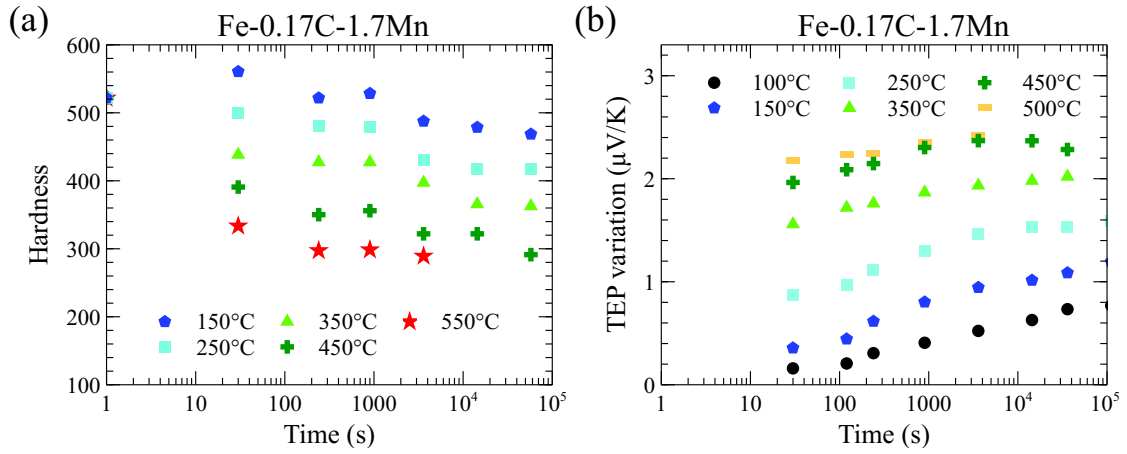

Figure 6.7: Isothermal tempering kinetics of the Fe-0.17C-1.7Mn followed by: (a) hardness and (b) TEP within the tempering temperature range from 150 °C to 550 °C.

out here that the same activation energies were obtained using the hardness and TEP kinetics.

These results suggest that tempering in the investigated temperature range involves two distinct stages associated with several metallurgical mechanisms which have to be identified.

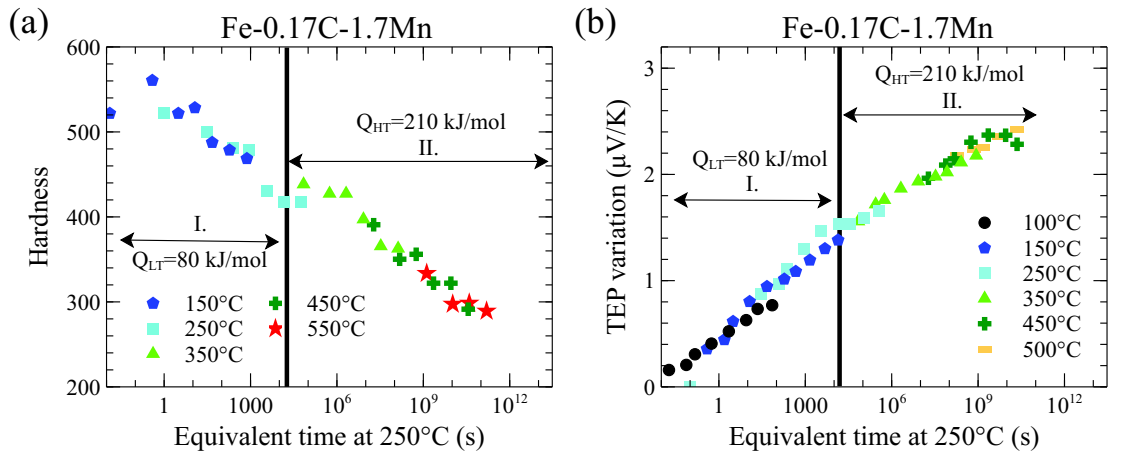

Figure 6.8: Master curve at 250 °C of the Fe-0.17C-1.7Mn steel obtained by applying a time-temperature equivalence on the tempering kinetics followed by : (a) hardness and (b) TEP. For the lowest tempering temperatures, an activation energy of 80 kJ/mol was used, while at higher temperatures, the activation energy was of 210 kJ/mol.

Analysis of the first tempering stage:

If we consider the kinetics of Figure 6.8, the first tempering stage is observed mainly at low temperature (T < 300 °C) and ends after about 1h at 250 °C. In this stage mainly governed by carbon diffusion, hardness first increases slightly before decreasing while TEP regularly increases and tends to stabilize before the beginning of the second stage. These observations (notably the hardness increase already observed in the literature in Figure 6.1)

Cette thèse est accessible à l'adresse : http://theses.insa-lyon.fr/publication/2020LYSEI120/these.pdf
© [A. MATHEVON], [2020], INSA Lyon, tous droits réservés

suggest that tempering in this stage begins with the segregation of a given amount of carbon to the defects of the microstructure (dislocations and/or lath boundaries) as this phenomenon was probably not completed during the cooling step.

Then, for longer tempering times, the significant hardness drop supports the beginning of cementite precipitation, as no intermediate carbide precipitation is expected in the present case due to the carbon content of the steel (lower than 0.2wt.%). This precipitation is supposed to be due to the carbon atoms remaining in solution after segregation to the defects and is linked to the carbon diffusion. In order to confirm this interpretation, TEM observations were performed at the end of the first tempering stage (1h at 250 °C) (see Figure 6.9.(a)). They clearly showed an intra-lath precipitation of plate-like cementite particles (θ carbides) as was expected. Figure 6.9.(b) underlines the possibility that a cementite fraction may precipitate during the 1h treatment at 250 °C in view of the precipitation spike obtained with DSC analysis at 280 °C with a heating rate of 10 °C/min.

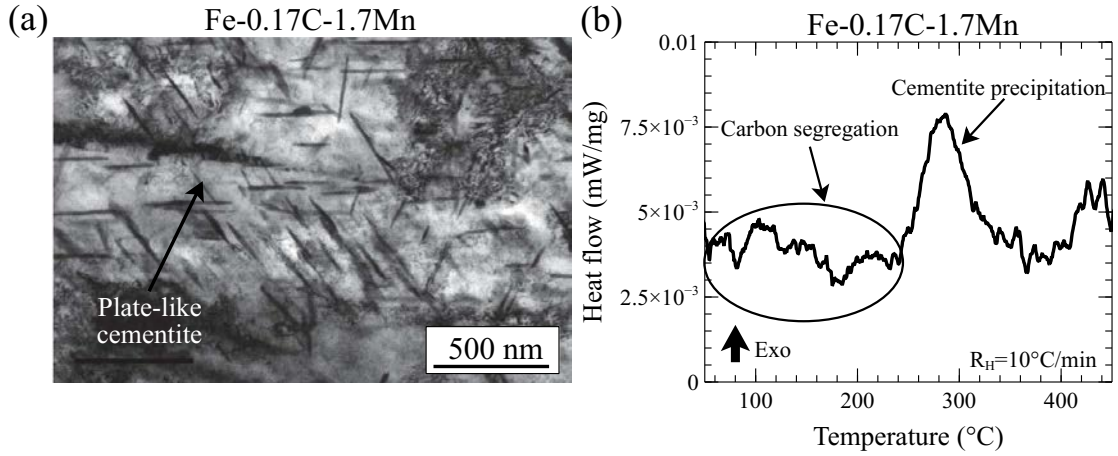

Figure 6.9: (a) TEM micrograph showing intra-lath θ-carbides formed in the Fe-0.17C-1.7 Mn steel tempered for 1h at 250 °C (end of the first tempering stage). (b) DSC analysis of the Fe-0.17C-1.7Mn steel.

With the aim of quantifying the carbon content in solid solution which precipitated in the form of cementite after 1h tempering at 250 °C, a FIB/SEM experiment. SEM observations during the FIB experiment show, similarly to TEM observations an intra-lath precipitation of plate-like cementite (see Figure 6.10.(a)). The treatment of the FIB volume by a Trainable WEKA segmentation after applying a VSNR2 filter allowed the precipitated cementite fraction during the tempering to be quantified. This measurement reveals a volume fraction of approximately 1.3% plate-like cementite which can be observed in Figure 6.10.(b). This observation allows us to estimate that the carbon, which left the solid solution during the cementite precipitation is of about 0.084 wt.%. This carbon content represents about 50% of the nominal composition of this grade.

Analysis of the second tempering stage:

For tempering temperatures above 300 °C and less than 550 °C, hardness presents a second sharp decrease while TEP keeps increasing. In this temperature domain, the measured activation energy is much higher ($\approx$ 210 kJ/mol) and indicates that other phenomena have to be considered during tempering. Unfortunately, due to a lack of time,

Cette thèse est accessible à l'adresse : http://theses.insa-lyon.fr/publication/2020LYSEI120/these.pdf
© [A. MATHEVON], [2020], INSA Lyon, tous droits réservés

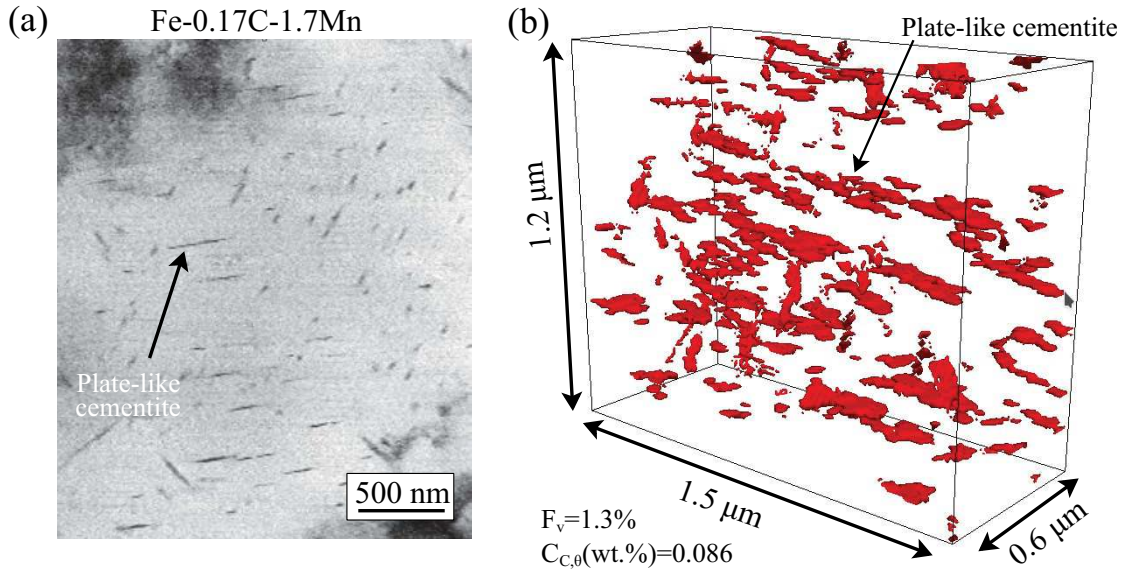

Figure 6.10: (a) SEM image of the cementite precipitation state within martensite tempered for 1h at 250 °C (Fe-0.17C-1.7Mn steel). (b) 3D view of the cementite precipitate segmentation resulting in a precipitated carbon content of 0.084 wt.% (≃49% of total carbon content).

no detailed TEM investigations could be performed in this temperature domain but a FIB/SEM experiment on the Fe-0.17C-1.7Mn grade tempered for 1 hour at 450 °C provided an opportunity to study and compare the fraction of precipitated cementite with the state tempered for 1 hour at 250 °C. Referring to the studies found in the literature above 300 °C, several phenomena are expected to occur more or less simultaneously:

- Substitutional element partitioning leading to a potential cementite enrichment in Mn and Cr.
- Beginning of the recovery phenomena responsible for : (i) the rearrangement of the martensite defects, (ii) a decrease in the dislocation density and (iii) a possible release of the segregated carbon atoms from the defects which could lead to a further cementite precipitation.
- start of cementite spheroidization.

The SEM observations of this sample reveal the presence of two types of precipitates: (i) spheroidized intra-lath cementite precipitates and (ii) inter-lath cementite precipitates. It appears that the intra-lath cementite precipitates observed at 250 °C had time to spheroidize during tempering at 450 °C (see Figure 6.11.(a)), while keeping a similar volume fraction. Indeed, volume segmentation leads to a volume fraction of 1.1% for intra-lath cementite. In parallel, Figure 6.11.(b) presents the new class of inter-lath precipitate not present at lower temperature. The formation of inter-lath cementite can be associated with the amount of carbon segregated to the microstructure defects during quenching and the first stage of tempering that would be released as these defects disappear during recovery. After quantification, a non-negligible volume fraction of approximately 1% is measured. These two types of precipitates allow to reach a precipitated carbon content of about 0.14 wt.% representing 85% of the nominal carbon content of the steel (see Figure 6.11.(c)).

Cette thèse est accessible à l'adresse : http://theses.insa-lyon.fr/publication/2020LYSEI120/these.pdf
© [A. MATHEVON], [2020], INSA Lyon, tous droits réservés

However, it is necessary to underline that a precise quantification of cementite is difficult due to image noises and the representativeness of the studied volume compared to the global microstructure. Nevertheless, these FIB/SEM experiments allowed us to observe a precipitation of plate-like cementite of the order of 50% of the nominal carbon composition during the first stage. The second stage leads to the spheroidization of the carbides precipitated at low temperatures and to the precipitation of inter-lath cementite with a proportion of about 50% of the nominal composition.

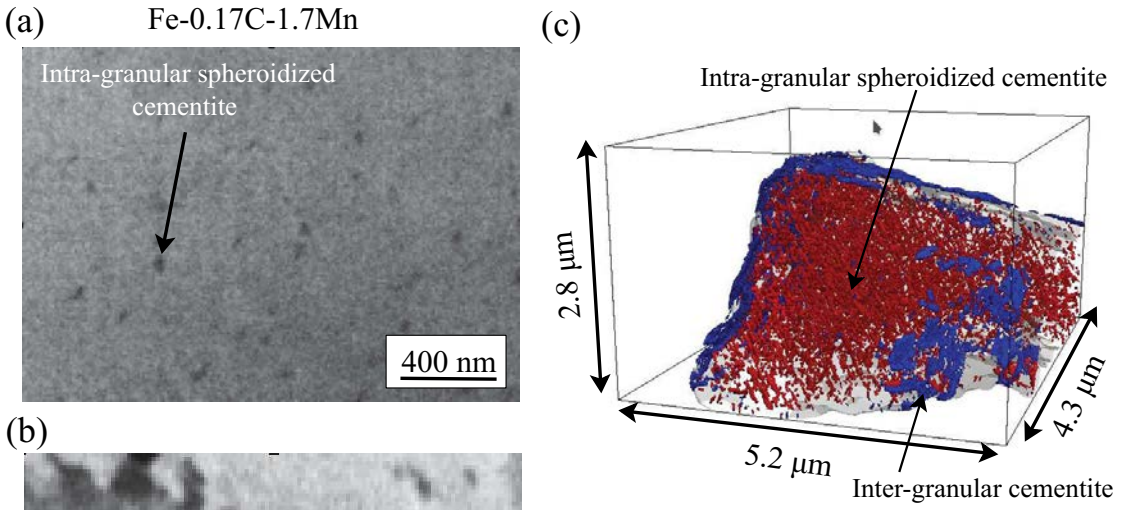

Cementite	Intra granular	Inter granular	Total
F_V (%)	1.1	1	2.1
$C_{C,\theta}$ (wt.%)	0.074	0.067	0.141

Figure 6.11: SEM image within martensite tempered for 1h at 450 °C (Fe-0.17C-1.7Mn steel): (a) intra-lath cementite precipitation state and (b) inter-lath cementite precipitation state. (b) 3D view of the cementite precipitates segmentation resulting in a precipitated carbon content of 0.14 wt.% ($\simeq$ 83% of total carbon content).

6.3.2.2 Analysis of the influence of the Mn content

After having determined the tempering kinetics of the ternary Fe-0.17C-1.7Mn steel between 150 °C and 550 °C and analyzed the two tempering stages identified in this temperature domain, the effect of the Mn content for a carbon content of 0.17wt.% will be discussed in the following section.

Influence of the Mn content on the tempering kinetics

In order to identify the possible influence of the Mn content on the tempering kinetics, the Fe-0.17C-xMn steels (with x = 0.5, 1.7 and 2.5) were submitted to the same procedure

Cette thèse est accessible à l'adresse : http://theses.insa-lyon.fr/publication/2020LYSEI120/these.pdf
© [A. MATHEVON], [2020], INSA Lyon, tous droits réservés

than that used for the Fe-0.17C-1.7Mn steel in the preceding section.

In particular, the same type of time-temperature equivalence was applied leading to the hardness and TEP master curves shown in Figure 6.12.(a-b) for the three Mn contents considered in this study. For all steels, two activation energies had to be applied in order to obtain a unique master curve. Table 6.3 summarizes the activation energies which were used for the two tempering stages of each steel. In the first tempering stage, the same activation energy was determined for all steels. However, in the case of the second tempering stage, the activation energy was found to increase slightly with increasing the manganese content of the steel. This suggests that tempering seems to be not strongly affected by the Mn content in the first tempering stage, while it is delayed in the second tempering stage with a higher manganese content.

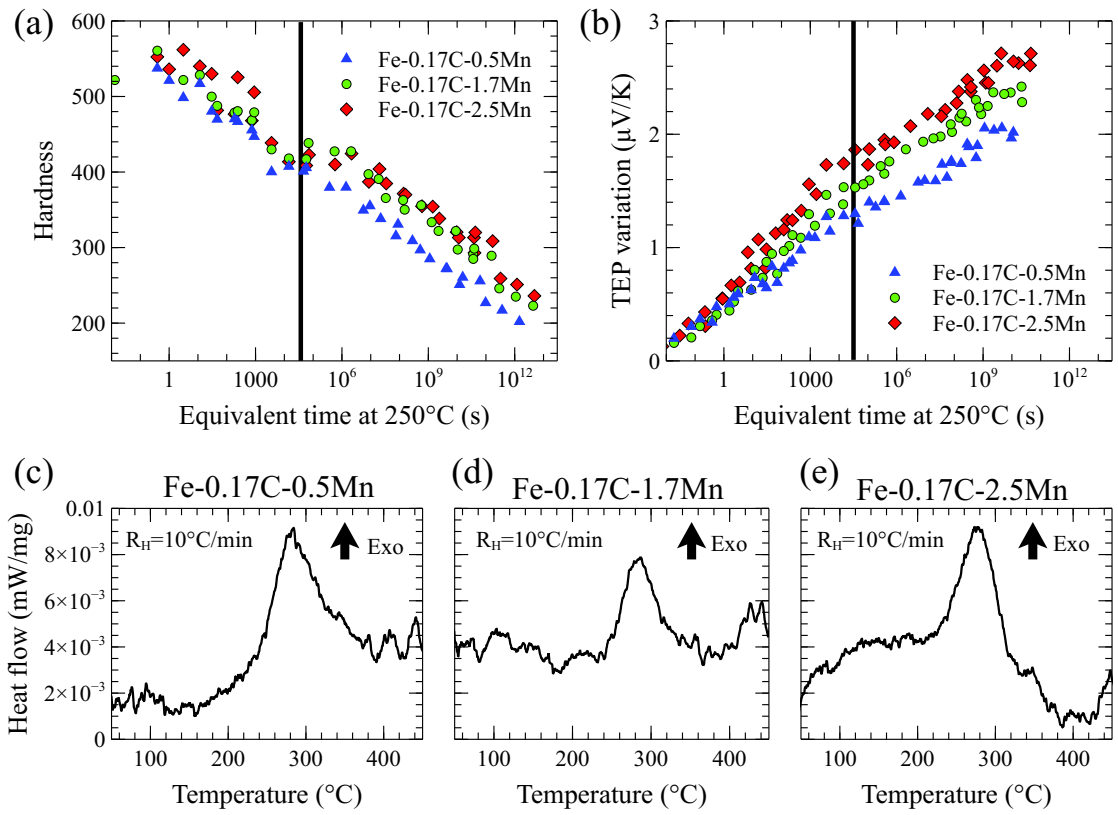

Figure 6.12: Influence of the Mn content on the master curves at 250 °C obtained by applying a time-temperature equivalence on the tempering kinetics followed by: (a) hardness and (b) TEP. DSC analysis of the steels: (c) Fe-0.17C-0.5Mn, (e) Fe-0.17C-1.7Mn and (f) Fe-0.17C-2.5Mn

Cette thèse est accessible à l'adresse : http://theses.insa-lyon.fr/publication/2020LYSEI120/these.pdf
© [A. MATHEVON], [2020], INSA Lyon, tous droits réservés

Steel grades	Activation energy for low tempering (kJ/mol)	Activation energy for high tempering (kJ/mol)
Fe-0.17C-0.5Mn	80 ± 5	199 ± 5
Fe-0.17C-1.7Mn	80 ± 5	210 ± 5
Fe-0.17C-2.5Mn	80 ± 5	211 ± 5

Table 6.3: Activation energy determined for the two tempering stages of the ternary Fe-0.17C-xMn steels

These conclusions are supported by the hardness evolutions shown in Figure 6.12.(a). While the hardness curves of the three steels are superimposed in the first tempering stage regardless of the Mn content, this is absolutely not the case in the second tempering stage where the hardness drop is retarded for the steels with a high Mn content (1.7 or 2.5 wt.%) compared to the steel with a 0.5% Mn content. These observations are also consistent with the results of the literature which clearly highlighted that the addition of alloying elements (such as Mn) has a marked influence on the loss of mechanical properties during tempering above 200 °C [GRA 77] due to the fact that the growth and coarsening rate of cementite is notably affected by the presence of substitutional elements which tend to partition [MIY 07]. This is particularly the case of Mn which tends to enrich cementite. This results in much finer and more numerous cementite particles which could retard the recovery and recrystallization phenomena and thus, the martensite softening.

The analysis of the TEP kinetics is much more complex as one has to keep in mind that the measured TEP variations for given tempering conditions depend on the chemical composition of each steel (which influences directly the electrical resistivity of the steel and subsequently the influence coefficients of the elements in solid solution such as C). In addition, it is necessary to recall here that the M_S temperature of the three studied steels is not identical (see Table 6.2) and decreases with increasing the Mn content. This is why, the self-tempering during cooling due to carbon segregation to the defects could be reduced with an increase in the Mn content, leading to a greater amount of carbon atoms in solid solution after quench (not segregated to the defects). Consequently, during the first tempering stage, higher TEP variations could be measured in the steels with a higher Mn content as observed experimentally in Figure 6.12.(b). This interpretation is also confirmed by the DSC curves of the three steels (see Figure 6.12.(c-e)) which provide evidence that the segregation of carbon atoms to the dislocations is much less marked in the case of the Fe-0.17C-0.5Mn steel.

Influence of the Mn content on the mechanical behaviour (hardness, tensile behaviour)

Figure 6.13.(a-b) show isochronal hardness curves of the studied ternary steels for two tempering times (30 s and 1h). They highlight the low influence of the Mn content after quench and confirm that Mn hardly impacts hardness at low tempering temperatures (T $<$ 250 °C) while this element has a rather strong impact at higher tempering temperatures even for a short tempering time. It is particularly noticeable between 0.5 wt.% and 1.7 wt.% Mn.

Cette thèse est accessible à l'adresse : http://theses.insa-lyon.fr/publication/2020LYSEI120/these.pdf
© [A. MATHEVON], [2020], INSA Lyon, tous droits réservés

The low influence of Mn after water-quench is also observed on the tensile curves of the steels as shown in Figure 6.13.(c). It can be attributed to the solid solution strengthening of manganese on the tensile behaviour of quenched martensite.

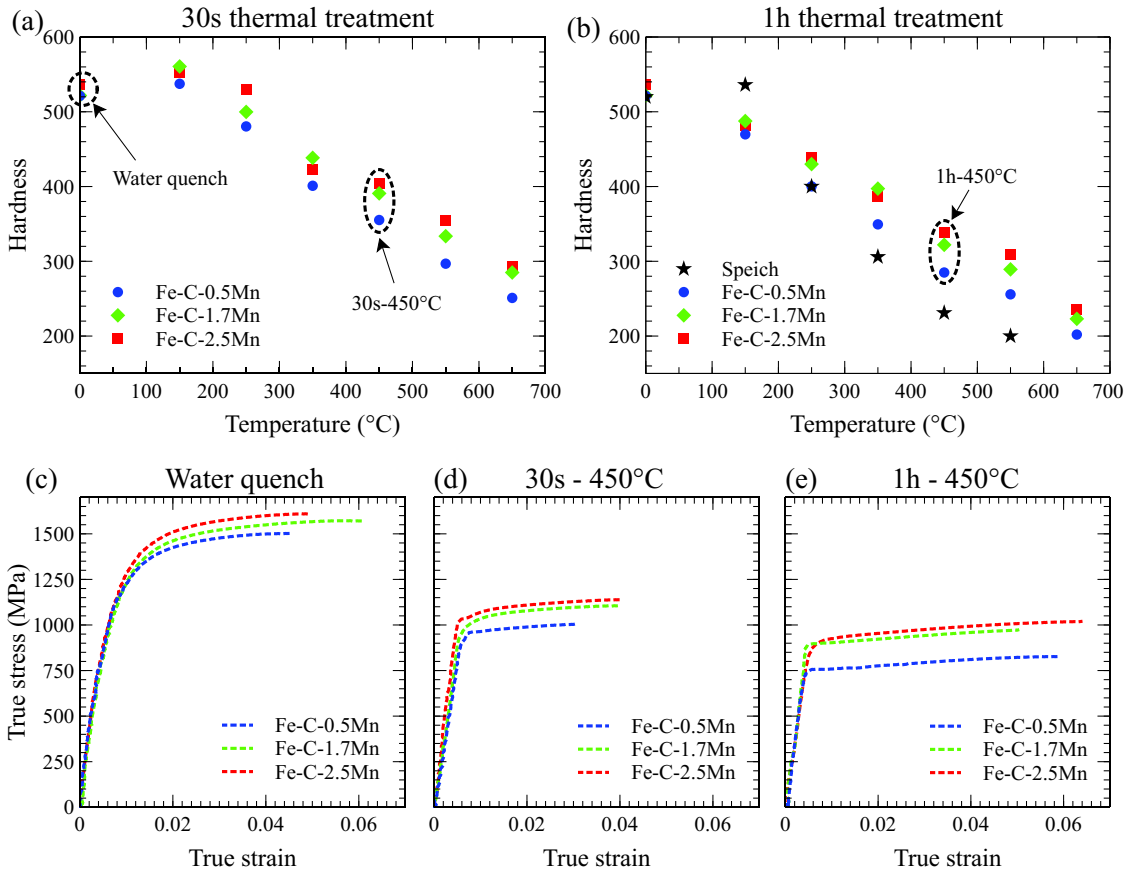

Figure 6.13: Isochronal hardness curves for a tempering temperature range between 150 °C and 650 °C on the three Fe-0.17C-xMn steels (with x = 0.5, 1.7 and 2.5) and a tempering time of : (a) 30s and (b) 1h. The experimental data from Speich [SPE 69] on a binary Fe-0.18C steel were added. Tensile curves of the fully martensitic Fe-0.17C-xMn steels: (c) after quench, (d) after tempering for 30s at 450 °C and (e) after tempering for 1h at 450 °C.

By contrast, after tempering for 30s and 1h at 450 °C, manganese has a strong impact on the tensile curves and tend to retard the drop in mechanical strength as its concentration in the steel increases. This statement is illustrated by Figure 6.13.(d-e) which presents a marked difference between 100 and 200 MPa for the steels with 0.5 and 1.7 wt.% Mn for a tempering at 450 °C. This difference appears to increase with increasing the tempering time.

An other important point is that hardness is closely related to the tensile behaviour, in particular to the ultimate tensile strength (UTS). This is illustrated in Figure 6.14 which shows a linear relationship between the UTS and hardness values of all studied ternary Fe-C-Mn steels.

Cette thèse est accessible à l'adresse : http://theses.insa-lyon.fr/publication/2020LYSEI120/these.pdf
© [A. MATHEVON], [2020], INSA Lyon, tous droits réservés

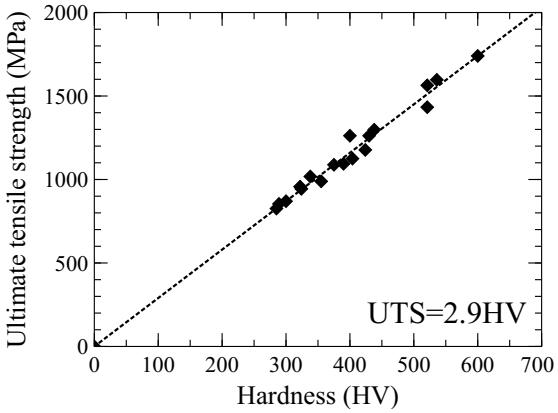

Figure 6.14: Curve of the ultimate tensile strength as a function of the Hv hardness of the steels with the following relationship: UTS=2.9HV

6.3.2.3 Analysis of the influence of the carbon content (Fe-xC-1.7Mn steels)

After having analyzed the influence of the manganese content, the effect of the carbon content on tempering was investigated using always the same procedure which was applied here to the Fe-xC-1.7Mn steels (with x = 0.08 or 0.17 wt.%).

Figure 6.15.(a-b) presents the master curves at 250 °C obtained thanks to a time-temperature equivalence on the tempering kinetics of the two studied steels. For the two tempering stages, the same activation energies were used for the two steels supporting the idea that carbon (contrary to manganese) has no influence on the tempering kinetics and probably, on the phenomena responsible for tempering in the two tempering stages. Nevertheless, it is interesting to note that as expected and contrary to manganese, carbon has a very marked effect on the hardness of quenched martensite. On the other hand, during tempering, the difference in hardness of the two steels tends to decrease as far as the quantity of carbon in solid solution is reduced, as the two steels tend to reach the same carbon content after a prolonged tempering. As can be seen in Figure 6.15.(c-e), the same conclusions can be drawn from the tensile curves of the two steels. While they are very different directly after water-quench, they tend to become very similar with increasing the tempering time at 450 °C, as most of the carbon has left the solid solution in the two steels. Concerning the TEP kinetics, the magnitude of the TEP variations is higher with increasing the carbon content. This is consistent with the fact that the TEP kinetics reflect mainly the departure of the carbon atoms from the solid solution (notably during the first tempering stage and probably also during the second tempering stage).

6.3.3 JMAK modelling phenomena during tempering

Comparative study of the phenomena responsible for the decrease in martensite mechanical properties revealed 3 stages (carbon segregation on defects, intra-lath cementite precipitation from carbon in solid solution and inter-lath cementite precipitation from the carbon released by the defects due to recovery). Nevertheless, the preliminary study showed that the phenomenon of carbon segregation had only a negligible effect on the mechanical prop-

Cette thèse est accessible à l'adresse : http://theses.insa-lyon.fr/publication/2020LYSEI120/these.pdf
© [A. MATHEVON], [2020], INSA Lyon, tous droits réservés

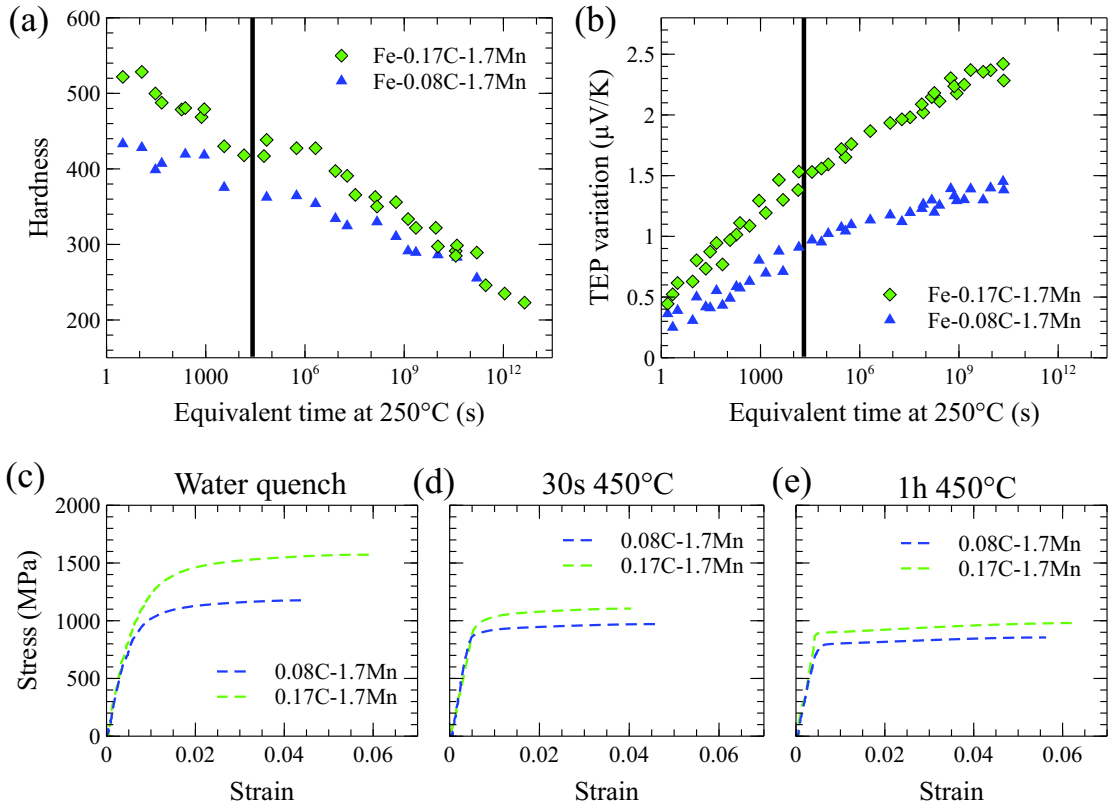

Figure 6.15: Influence of the C content on the master curves at 250 °C obtained by applying a time-temperature equivalence on the tempering kinetics of the Fe-xC-1.7Mn steels followed by : (a) hardness and (b) TEP. Tensile curves of the fully martensitic Fe-xC-1.7Mn steels: (c) after quench, (d) after tempering for 30s at 450 °C and (e) after tempering for 1h at 450 °C.

erties of martensite and was thus neglected in the following. The modelling of the two other phenomena occurring during tempering was carried out using the classical JMAK formalism:

$$Y(t,T) = 1 - \exp(-(bt)^n) \tag{6.10}$$

$$b = b_0 \exp\left(-\left(\frac{Q}{RT}\right)\right) \tag{6.11}$$

JMAK modelling of the TEP $\Delta S(t,T)$ signal evolution allows to calibrate the parameters of the two phenomena occurring during tempering with the following assumptions:

$$\Delta S(t,T) = \Delta S_{ss\to\perp} + \Delta S_{ss\to\theta} + \Delta S_{\perp\to\theta} \tag{6.12}$$

where $\Delta S_{ss\to\perp}$ corresponds to the TEP signal which is subtracted during JMAK modelling since the effect on hardness was negligible. $\Delta S_{ss\to\theta}$ and $\Delta S_{\perp\to\theta}$ represent respectively the evolution of the TEP associated with cementite precipitation and recovery.

Cette thèse est accessible à l'adresse : http://theses.insa-lyon.fr/publication/2020LYSEI120/these.pdf
© [A. MATHEVON], [2020], INSA Lyon, tous droits réservés

For each phenomenon, the evolution of the TEP is associated with a JMAK Y_i law and a carbon fraction ΔC_i associated with the phenomenon:

$$\Delta S_i = \Delta C_{C,i} Y_i \tag{6.13}$$

During the experimental characterization of the different stages of tempering, 2 stages were highlighted with an activation energy of 80 kJ/mol for low temperature tempering and another of ≃210 kJ/mol for high temperature tempering. Two JMAK models were therefore calibrated to reproduce the TEP evolution normalized during tempering (see Figure 6.16) by assuming a carbon content of 50% on the steel nominal composition for the 2 stages following the FIB observations performed. The parameters of the two JMAK models are defined in Table 6.4.

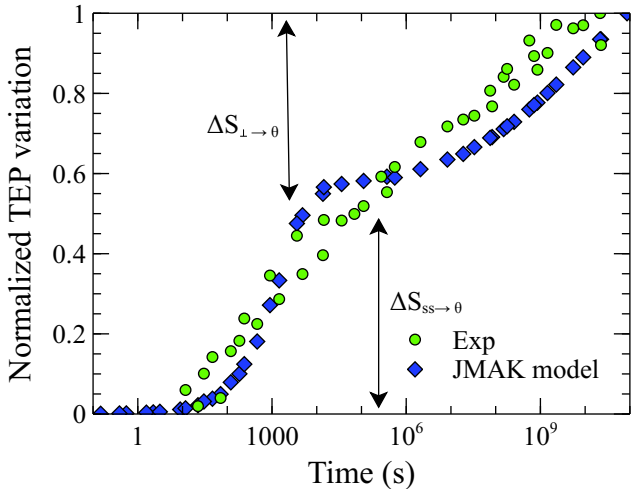

Figure 6.16: Calibration result of the two JMAK laws to reproduce the normalized experimental TEP variation.

JMAK law	b_0 (s^{-1})	Activation energy (kJ/mol)	n
$Y_{ss\to\theta}$ low temperature	6x10^4	80	0.75
$Y_{\perp\to\theta}$ high temperature	1x10^{11}	$190 + 22\left[1 - \exp\left(-(1.3C_{Mn}^{m})^{1.3}\right)\right]$	0.25

Table 6.4: Temperature range and activation energy data for the martensite tempering.

The activation energies were extracted from hardness and TEP evolution kinetics using activation energies experimentally measured as a function of the chemical composition of manganese ternary steels. Figure 6.17 illustrates the evolution of activation energy for high-temperature tempering ($Q_{\perp\to\theta}$) as a function of manganese content calibrated from experimental data.

Cette thèse est accessible à l'adresse : http://theses.insa-lyon.fr/publication/2020LYSEI120/these.pdf
© [A. MATHEVON], [2020], INSA Lyon, tous droits réservés

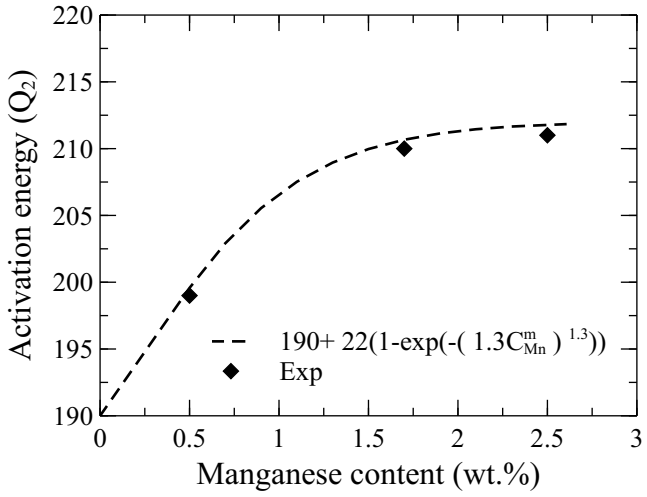

Figure 6.17: Comparison between the evolution law of the activation energy $Q_{\perp\to\theta}$ with the experimental measurements obtained with time-temperature equivalence.

6.4 Modelling of the mechanical properties of 100% martensitic steels during isothermal tempering in the range of [100 -550] °C

With the characterization of the phenomena occurring during the martensite tempering over a wide range of chemical composition and grain size, an extension of the model for predicting the mechanical properties of martensite developed in Chapter 5 is proposed here to take into account the tempering phenomena. A comparison of the (Hy-MFC) model with the experimental tensile curves for fully martensitic steels tempered under different conditions was performed. It allowed us to validate the ability of the model to reproduce the effect of temperature and tempering time on a wide range of chemical composition for ternary Fe-C-Mn steels.

6.4.1 Mechanical model for predicting the tensile curve of fresh martensite

The model chosen in order to reproduce the elasto-plastic transition of martensite is the composite continuous approach (CCA) developed in Section 5.3.2. It enables to describe the macroscopic stress of martensite as a function of the local spectrum density $F(\sigma_l)$ using the following relation:

$$\frac{d\sigma^m}{d\epsilon^m} = \frac{1}{\frac{1}{Y} + \frac{F(\sigma_l)}{\beta}} \left(1 - F\left(\sigma_l\right)\right) \tag{6.14}$$

where Y is the Young's modulus and σ_l is the local stress, while σ_m and ϵ_m are the macroscopic stress and strain of martensite. Thereafter $\beta = 50$ GPa is chosen to control the interaction between the different phases.

Cette thèse est accessible à l'adresse : http://theses.insa-lyon.fr/publication/2020LYSEI120/these.pdf
© [A. MATHEVON], [2020], INSA Lyon, tous droits réservés

In order to capture the Bauschinger effect on martensitic steels, the stress spectrum is defined using an Avrami-like law with 3 adjustable parameters modified to take into account the tempering:

$$\begin{aligned} &\text{if } \sigma^m < \sigma_0^m + \sigma_{min} \text{ then } F\left(\sigma^m\right) = 0 \\ &\text{else } F\left(\sigma^m\right) = 1 - exp\left[-\left(\frac{\sigma^m - \left(\sigma_{min} + \sigma_0^m\right)}{\Delta}\right)^m\right] \end{aligned} \tag{6.15}$$

where:

- σ_0^m is the contribution of Peierls force and the friction stress due to solid solution hardening and depends on the chemical composition of the steel as follows:

$$\sigma_0^m = 52 + 33C_{Mn}^0 + 80C_{SI}^0 + 60C_{Cr}^0 + 80C_{Mo}^0 \tag{6.16}$$

- $\sigma_{min} = 320$ MPa is the constant of Avrami's law controlling respectively the martensite yield strength.
- m=1.8 is the constant of Avrami's law controlling the rate of martensite strain-hardening.
- The width of the local yield strength distribution Δ controls the magnitude of the strain hardening between yield strength and tensile strength.

$$\Delta = K_0 + \frac{K_1}{\sqrt{D_\gamma}} + K_2(C_C^m)^{1.34} \tag{6.17}$$

where D_γ is the diameter of the austenitic grains before quenching and C_C^m the carbon content in austenite after phase transformation during intercritical annealing.

6.4.2 Model modifications to account for the martensite tempering

Implementation of the evolution of the carbon content in solid solution

To take into account the martensite tempering within the mechanical martensite prediction model, two assumptions were included:

- The first one consists in modifying the constant m required to adjust the strain-hardening rate according to the tempering conditions. For low tempering temperature ranges below 300 °C where significant hardening is observed, $m = 1.8$ is applied. On the contrary, to reproduce the decrease in hardening for tempering above 300 °C, $m = 3$ is used.
- The second is to include the evolution of the carbon content in solid solution $C_{C,ss+\perp}$ according to the experimentally measured JMAK parameters (see Table 6.4). The local yield strength distribution can therefore be expressed as follows:

$$\Delta = K_0 + \frac{K_1}{\sqrt{D_\gamma}} + K_2(\%C_{C,ss+\perp}^m)^{1.34} \tag{6.18}$$

where $C_{C,ss+\perp}$ represents the carbon content in solid solution and segregated to the defects within the martensite. Namely, as shown in Section 6.3.1, carbon atoms in

Cette thèse est accessible à l'adresse : http://theses.insa-lyon.fr/publication/2020LYSEI120/these.pdf
© [A. MATHEVON], [2020], INSA Lyon, tous droits réservés

solid solution or segregated to defects have almost the same role on the mechanical properties. The evolution of the carbon content in solid solution and segregated to defects is thus assumed to evolve by the following relationship:

$$C^m_{C,ss+\perp} = C^m_C(1 - 0.5(Y_{ss\rightarrow\theta} + Y_{\perp\rightarrow\theta})) \tag{6.19}$$

where $Y_{ss\rightarrow\theta}$ and $Y_{\perp\rightarrow\theta}$ are the two JMAK laws reproducing the carbon departure from the solid solution during the two tempering stages defined in Section 6.3.3 with $Y_i = 1 - \exp[-(bt)^n]$. The coefficient 0.5 has been fixed in relation to the carbon fraction precipitated during each of the tempering stage measured by FIB. This hypothesis is also based on the fact that almost all the carbon is assumed to be precipitated for a tempering of 1h at 550 °C.

The mechanical properties of the fully martensitic Fe-0.17C-1.7Mn steel are modelled and compared to the tensile curves obtained after quenching and after different tempering conditions. Figure 6.18.(a-c) shows the evolution of the JMAK parameters $Y_{ss\rightarrow\theta}$ and $Y_{\perp\rightarrow\theta}$ as well as the solid solution carbon content required for the prediction of the mechanical properties.

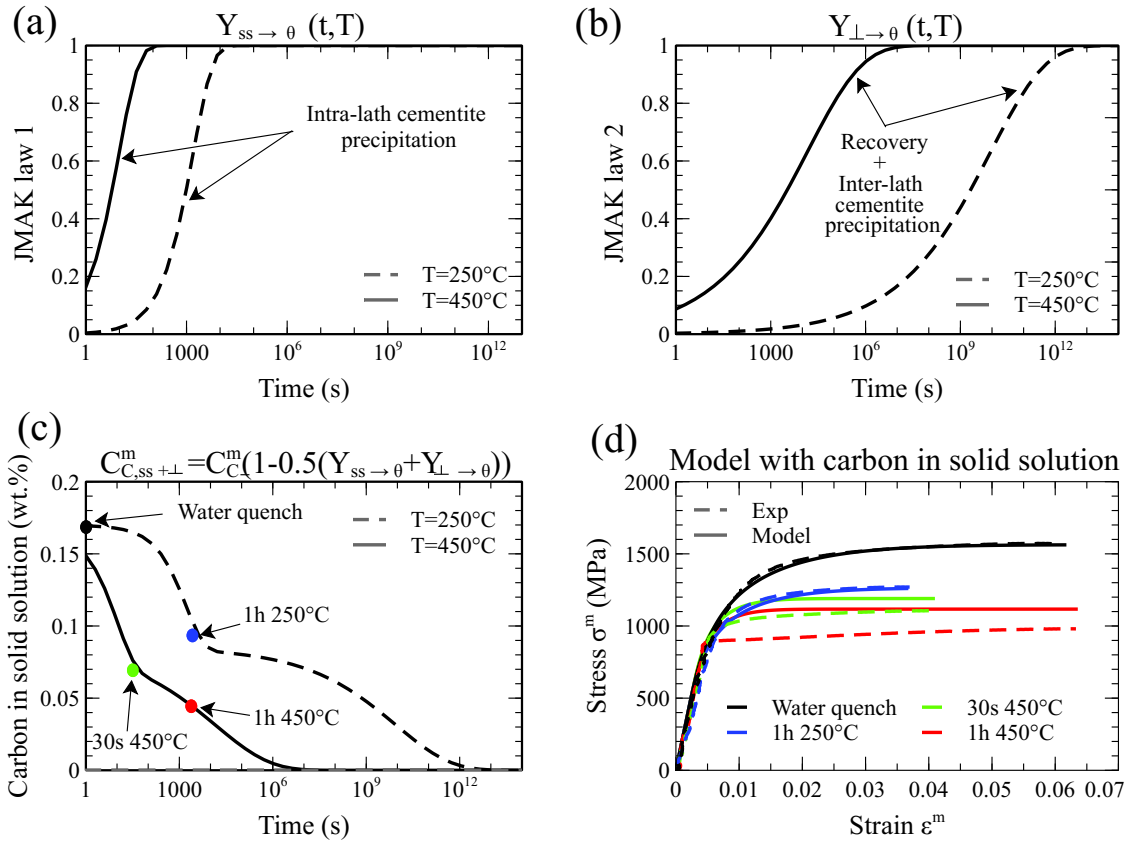

Figure 6.18: Kinetics of the JMAK laws: (a) $Y_{ss\rightarrow\theta}$ and (b) $Y_{\perp\rightarrow\theta}$ for two temperatures. (c) Evolution of the carbon content in solid solution for the two considered temperatures. (d) Comparison between experimental and modelled tensile curves of Fe-0.17C-1.7Mn steel with only the introduction of carbon in solid solution in the expression of Δ.

Cette thèse est accessible à l'adresse : http://theses.insa-lyon.fr/publication/2020LYSEI120/these.pdf
© [A. MATHEVON], [2020], INSA Lyon, tous droits réservés

For short times (t <10000s at 250 °C and t <10s at 450 °C), a fast increase of the $Y_{ss\rightarrow\theta}$ law is observed (see Figure 6.18.(a)). It corresponds to the first drop of the carbon content in solid solution visible in Figure 6.18.(c) and due to the intra-lath cementite precipitation evidenced by TEM (see Figure 6.9).

For longer times, an increase in the $Y_{\perp\rightarrow\theta}$ law is detected (see Figure 6.18.(b)). It is associated with the second drop of the carbon content in solid solution shown in Figure 6.18.(c) and it can be attributed to the inter-lath cementite precipitation resulting from the recovery phenomena in the steel according to the FIB/SEM experiment of Figure 6.11.

Figure 6.18.(d) shows the ability of the model to reproduce the softening of the mechanical properties of martensite for temperatures below 300 °C. However, at higher temperature, a softening more important than expected by the model is observed experimentally, supporting the idea that the carbon release from the solid solution is not the only phenomenon to consider to explain the tensile behaviour for high tempering temperature.

Additional softening term when restoring microstructural defects

In order to take into account the reorganization and disappearance of internal defects of martensite (decrease in dislocation density, lath boundaries), a term was added in the Δ parameter for high temperature tempering.

$$\Delta = K_0 + \frac{K_1}{\sqrt{D_\gamma}} + K_2(\%C^m_{C,ss+\perp})^{1.34} - K_3 Y_{\perp\rightarrow\theta} \tag{6.20}$$

Finally the modification of the mechanical properties due to tempering can be summarized in 3 steps:

1. A partial segregation of the carbon atoms on the different microstructure defects during quenching and for tempering temperatures below 150 °C. This step is neglected during the simulation by assuming that the segregated carbon atoms have the same hardening role as in solid solution.
2. Intra-lath cementite precipitation of the carbon atoms in solid solution non-segregated on the defects is then observed for tempering temperatures below 300 °C leading to a decrease in the intrinsic mechanical properties of the martensite. The reduction of the parameter $C^m_{C,ss+\perp}$ through the JMAK law $Y_{ss\rightarrow\theta}$ for low tempering promotes a decrease of the Δ parameter (see Figure 6.18.(c)). Since Δ controls the width of the stress spectrum, this leads to a decrease of the mechanical properties and heterogeneity within the martensite.
3. For higher tempering temperatures, a change in activation energy close to the self-diffusion of iron (210 kJ/mol) is observed, supporting the start of rearrangement of the microstructure. As the density of dislocations and defects within the microstructure decreases, a reduction in the amount of carbon involved in the hardening of the steel, described by the $Y_{\perp\rightarrow\theta}$ JMAK law, for high temperatures is observed (see Figure 6.18.(c)). The decrease in the amount of carbon involved in hardening is not sufficient, leading to the necessity of an additional term within Equation 6.20. This term reflects the effect of the presence of defects and a high dislocation density within the martensite that is lowered as the microstructure is reorganized.

Cette thèse est accessible à l'adresse : http://theses.insa-lyon.fr/publication/2020LYSEI120/these.pdf
© [A. MATHEVON], [2020], INSA Lyon, tous droits réservés

	Parameter	Symbol	Unit	Value used
Martensite model	Young's modulus	Y	GPa	210*
	Composite interaction parameter	β	GPa	50*
	Avrami parameter	σ_{min}	MPa	320*
	Avrami parameter	m	-	1.8*
	Local yield strength constant	K_0	MPa	570
	Local yield strength constant	K_1	MPa.mm$^{0.5}$	24
	Local yield strength constant	K_2	MPa.wt%$^{-1.34}$	6053
	Local yield strength constant	K_3	MPa	450

Table 6.5: Values of the key parameters used in the Hy-MFC mechanical models for tempered martensite. Values used by Allain *et al.* [ALL 12]

6.4.3 Comparison of the experimental and modelled tensile curves for the ternary Fe-C-Mn steels

A prediction capability validation of the mechanical properties for tempered martensite was carried out on all the Fe-C-Mn ternary steels of this study including all the modifications presented in the previous section. Figure 6.19 illustrates the excellent agreement obtained between the tensile curves of the four Fe-C-Mn grades for fresh martensite as well as for the three considered tempering conditions. For each grade, a softening is observed for the mechanical properties of the tempered martensite and it is all the more marked as T and t are increased. The tempering temperature appears here as the key parameter with a very important effect on the properties of the martensite when the temperature is above 300 °C.

The dependence of the activation energy $Q_{\perp\rightarrow\theta}$ (for the second tempering stage) according to the manganese composition enables to reproduce the mechanical properties of different steels and in particular the marked softening of the Fe-0.17C-0.5Mn steel.

Lastly, the type of industrial tempering in the range of 30s to 450 °C leads to an important softening of the mechanical properties for tempered martensite which is properly reproduced by the model. Nevertheless it is interesting to note that the experimental ultimate elongation of tempered martensite is improved only for high tempering times and temperatures.

Although the prediction model reproduces the mechanical properties of each ternary Fe-C-Mn steel, it is interesting to understand the role of each element on the final properties of the steel.

Figure 6.20.(a) highlights that the mechanical properties of fresh martensite are slightly increased with increasing the manganese content of the steel due to the manganese strengthening effect by solid solution. After a tempering for 1h at 450 °C, the influence of the manganese content is much more marked since a significant difference of 150 MPa is observed between the steels containing 0.5wt.% Mn and 1.7 wt.% Mn as evidenced in Figure 6.20.(b). It can be attributed to a potential solute drag effect of manganese within the microstructural defects (dislocations, lath boundaries) slowing down their rearrangement or to a decrease in the growth and coarsening rate of cementite due to manganese

Cette thèse est accessible à l'adresse : http://theses.insa-lyon.fr/publication/2020LYSEI120/these.pdf
© [A. MATHEVON], [2020], INSA Lyon, tous droits réservés

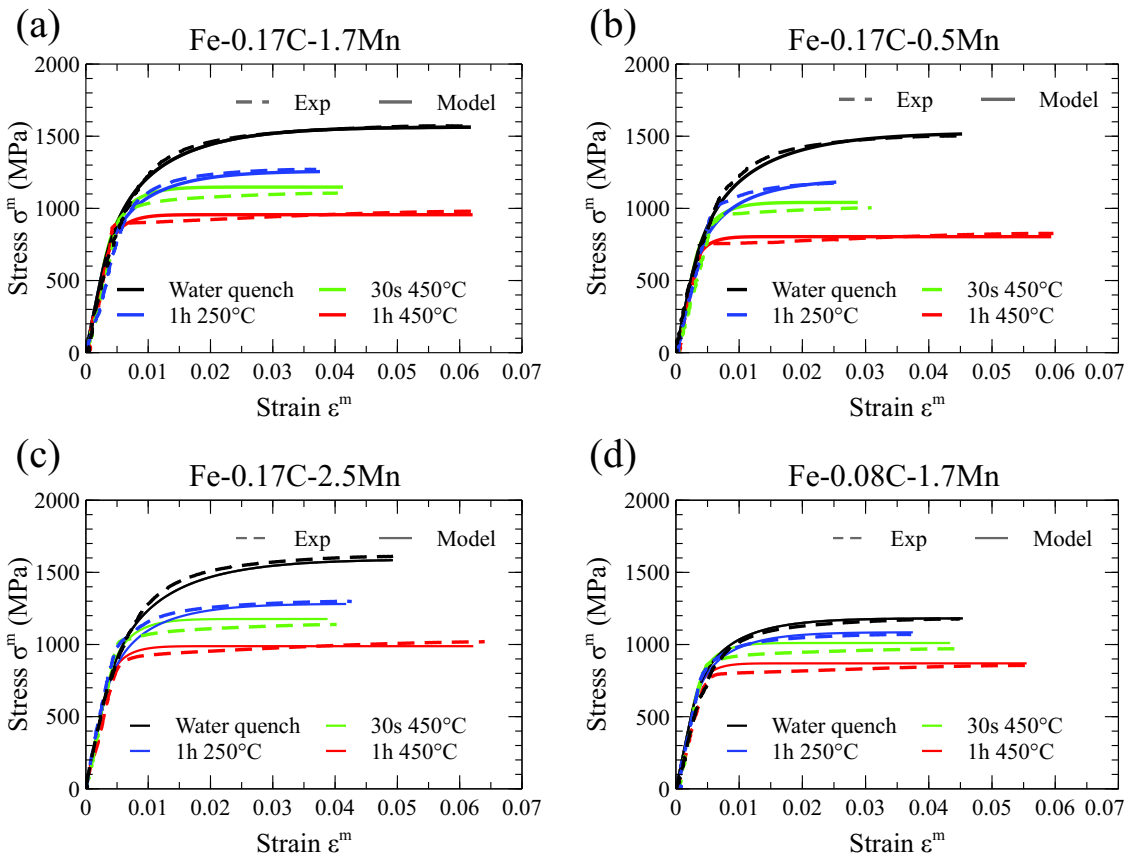

Figure 6.19: Experimental and modelled tensile curves for a fully martensitic steel water quenched or tempered at different temperatures and times: (a) Fe-0.17C-1.7Mn, (b) Fe-0.17C-0.5Mn, (c) Fe-0.17C-2.5Mn and (d) Fe-0.08C-1.7Mn

partitioning, leading to finer precipitates which could retard the recovery phenonema and subsequently, the martensite softening.

With regard to the carbon effect, Figure 6.20.(c) shows that it is very marked in the case of fresh martensite and it is mainly responsible for the martensite intrinsic heterogeneity. For a tempering time of 1h at 450 °C (see Figure 6.20.(d)), the martensite heterogeneity is reduced during carbon precipitation and defect rearrangement. The role of the carbon content on the properties of tempered martensite thus regularly decreases with the progress of the martensite tempering phenomenon.

6.5 Modelling the steel mechanical properties in a two-phase state during isothermal tempering in the range [100-550]°C

After having modified the mechanical model presented in Chapter 5 for the prediction of the tensile properties of fully martensitic steels in order to take into account the tempering stage, the model was validated on fully martensitic steels tempered under various

Cette thèse est accessible à l'adresse : http://theses.insa-lyon.fr/publication/2020LYSEI120/these.pdf
© [A. MATHEVON], [2020], INSA Lyon, tous droits réservés

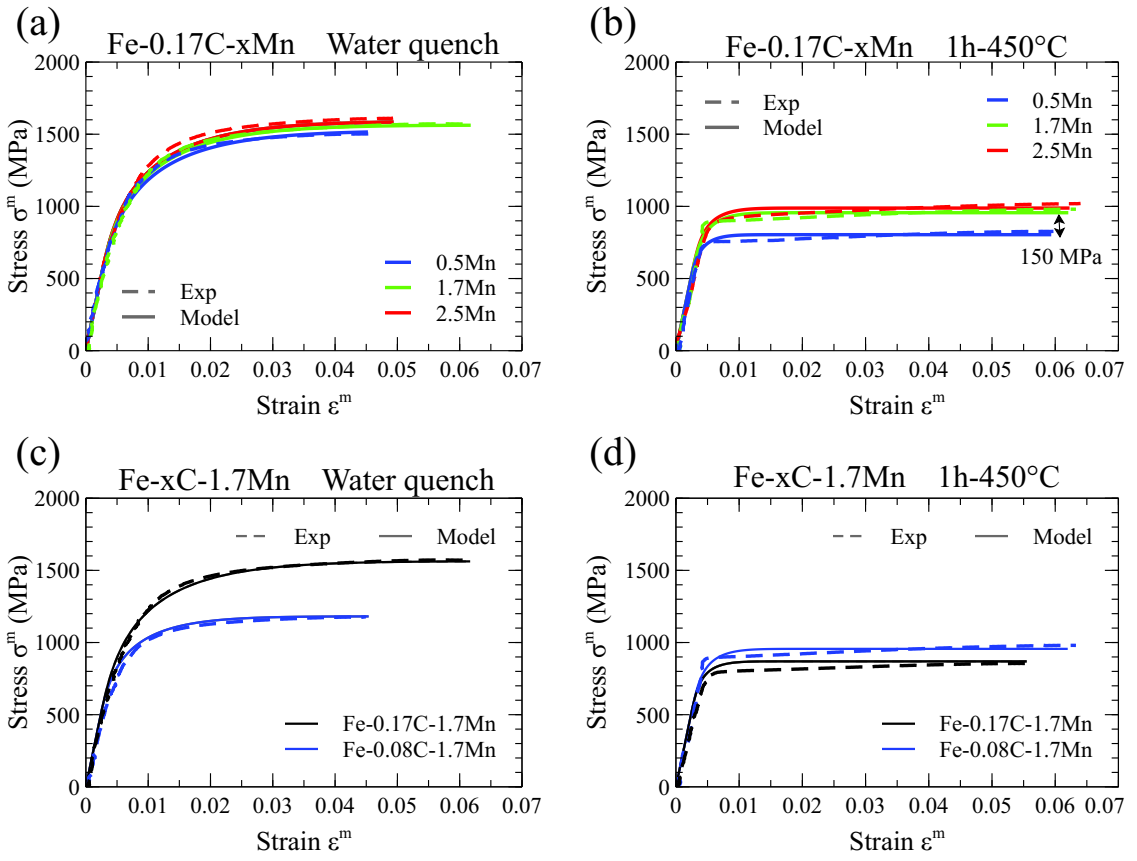

Figure 6.20: Comparison of the manganese content effect on the experimental and modelled tensile properties of fully martensitic Fe-0.17C-xMn steel (a) after water quench and (b) after tempering for 1h at 450 °C. Comparison of the carbon content effect on the experimental and modelled tensile properties of fully martensitic Fe-xC-1.7Mn steel (c) after water quench and (d) after tempering for 1h at 450 °C.

conditions of time and temperature (see Section 6.4). The aim of this section is to apply the preceding model in the case of two-phase microstructures obtained from the ternary steels of this study tempered in the temperature range between 100 °C and 550 °C. In this case, the model is applied by considering that the carbon content of martensite is that of austenite calculated with the following equation:

$$C_C^m = \frac{C_C^0}{f_{\alpha'}} \tag{6.21}$$

Figure 6.21 shows the mechanical properties and the good agreement obtained on two DP steels containing globally 70% of martensite for two different manganese contents. In both cases, a decrease in the mechanical properties of the DP steel is noted with the increase in tempering temperatures, due to the softening of the mechanical properties of martensite. Here, it is important to note that once the calibration of the model for the prediction of the mechanical properties of martensite has been completed, its extension in the case of a two-phase model is possible without any modification of these parameters.

The mechanical property prediction model is also able to reproduce the effect of the

Cette thèse est accessible à l'adresse : http://theses.insa-lyon.fr/publication/2020LYSEI120/these.pdf
© [A. MATHEVON], [2020], INSA Lyon, tous droits réservés

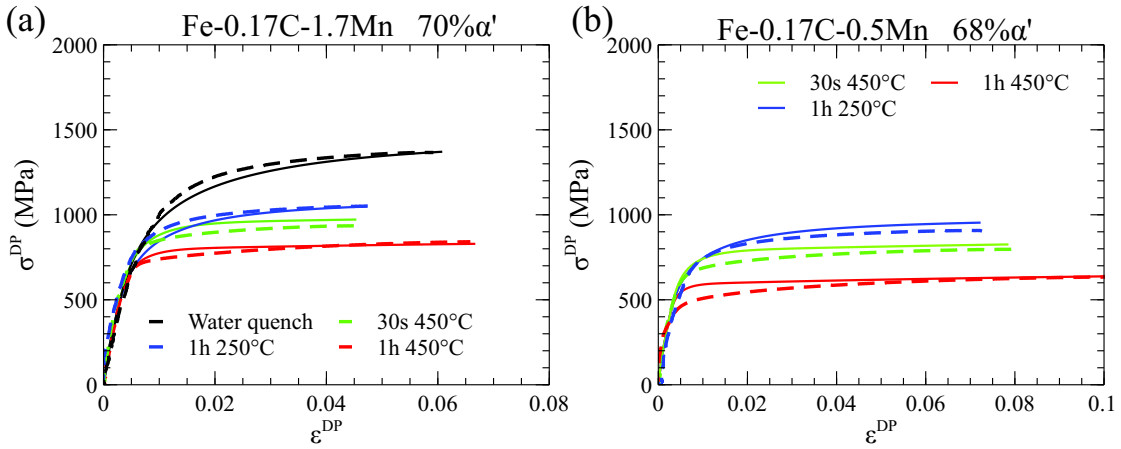

Figure 6.21: Experimental and modelled tensile curves for a DP steel with 70%α' water quenched or tempered at different temperatures and times: (a) Fe-0.17C-1.7Mn, (b) Fe-0.17C-0.5Mn

martensite fraction on the global properties of a two-phase steel as shown in Figure 6.22. It illustrates the effect of the increase in the martensite fraction which leads to an increase in the ultimate tensile strength of the steel while reducing its ultimate elongation.

Here, it has to be noted that an extension of the model in the case of high carbon and silicon steels is proposed in Annex A.

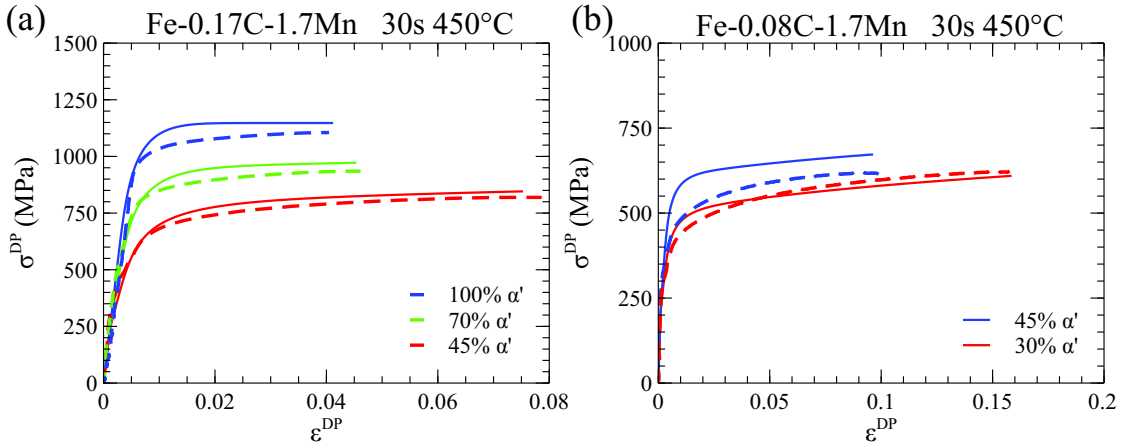

Figure 6.22: Effect of the martensite fraction on the experimental and modelled tensile properties of a steel tempered 30s at 450 °C: (a) Fe-0.17C-1.7Mn and Fe-0.08C-1.7Mn

6.6 Conclusions

A characterization of the microstructural evolutions and mechanical properties of 100% martensitic steels during isothermal tempering (100-550 °C) was performed. Using a monitoring of the microstructural property evolutions of tempered martensite by hardness and TEP, three main mechanisms during the tempering stage were identified using a time-

Cette thèse est accessible à l'adresse : http://theses.insa-lyon.fr/publication/2020LYSEI120/these.pdf
© [A. MATHEVON], [2020], INSA Lyon, tous droits réservés

temperature equivalence.

At very low temperature (<150 °C) and during the quenching, a segregation of part of the carbon on the intrinsic defects of the martensite takes place without effect on the mechanical properties.

Thereafter, the first drop in mechanical properties results from the intra-lath cementite precipitation of part of the carbon atoms remaining in solid solution after quench with an activation energy of 80 kJ/mol. This result was highlighted by TEM and FIB/SEM observations as well as DSC experiments.

Lastly, the second drop in mechanical properties (observed mainly at tempering temperatures higher than 300 °C) was attributed to a rearrangement of the microstructural defects present in fresh martensite leading to a decrease in their density and to a progressive release of the carbon atoms trapped by the defects. As highlighted by FIB/SEM tomography, these phenomena are accompanied by an inter-lath cementite precipitation which was not observed at tempering temperatures lower than 300 °C. At the end of this stage, almost all the carbon atoms of the steel are assumed to be precipitated.

Assuming that the mechanical properties of martensite during tempering between 100 °C and 550 °C are mainly governed by the carbon departure from the solid solution or from the microstructural defects and that the measured TEP variations during tempering are mainly due to the carbon contribution on TEP, the TEP master curve obtained by Time-Temperature-Equivalence at 250 °C was modelled using two JMAK laws accounting for the decrease in the carbon content due to the : (i) intra-lath cementite precipitation and (ii) inter-lath cementite precipitation.

Then, from the JMAK laws determined from the experimental study, the influence of the carbon content on the tensile properties of martensite could be taken into account in the mechanical model for martensite developed in Chapter 5, in which the carbon content influences the width of the yield strength distribution. This width tends to decrease when the martensite carbon content decreases.

The model was first tested on fully martensitic steels tempered under various conditions. It was found to reproduce very well the experimental tensile curves as long as the tempering temperature is lower than 300 °C. At higher temperature, in order to obtain a better prediction of the tensile properties during tempering, an additional term had to be introduced in the width of the yield strength distribution to account for the recovery phenomena which may take place at high temperature and contribute also to the martensite softening.

After having validated the model on fully martensitic steels, it was introduced in the "composite" mean-field model for the prediction of the tensile behaviour of Dual-Phase steels. It was then applied with success on different two-phase microstructures tempered under various conditions, thus validating the ability of the model to predict mechanical properties for several tempered two-phase steels.

Cette thèse est accessible à l'adresse : http://theses.insa-lyon.fr/publication/2020LYSEI120/these.pdf
© [A. MATHEVON], [2020], INSA Lyon, tous droits réservés

Cette thèse est accessible à l'adresse : http://theses.insa-lyon.fr/publication/2020LYSEI120/these.pdf
© [A. MATHEVON], [2020], INSA Lyon, tous droits réservés

Conclusions and Perspectives

Conclusions

This PhD-work aimed at understanding and modelling the microstructural evolutions and the mechanical properties during the thermal cycle of cold-rolled Dual-Phase steels. The thermal cycle of DP steels can be divided into three major stages in which the microstructural evolutions will occur: (i) intercritical annealing leading to recrystallisation (Chapter 2) and austenite formation (Chapter 3), (ii) quenching during which austenite is transformed into martensite (Chapter 4) and (iii) tempering which softens the mechanical properties of the martensite (Chapter 6). In parallel, Chapters 5 and 6 aimed at understanding and modelling the mechanisms controlling the mechanical properties of Dual-Phase steels.

For each stage of the thermal cycle, the choice of the models used to predict the characteristics of the steel was governed by the best compromise between reliability, versatility and computation time. Throughout the PhD thesis, a large part of the modelling selection has been oriented towards physically based mean-field models. Contrary to entirely empirical models which are generally applicable to a restricted area of applications, mean-field models take into account industrial process parameters (cycle parameters, steel chemistry and reduction ratio). On the other hand, many full-field models have been developed to model recrystallization, phase transformation and mechanical properties of steels allowing a detailed understanding of the involved phenomena. Nevertheless, they generally present very high computation times and a difficulty to integrate all industrial process parameters in a simple way.

A calibration of microstructural and mechanical models on ternary steels from laboratory grades with different carbon and manganese contents was carried out before their validation on two industrial grades and data from the literature.

Chapter 2 presents a microstruturally-based recrystallization model (denoted MiReX model) developed to accurately reproduce recrystallization kinetics of cold-rolled ferritic-pearlitic DP steels. It takes into account the reduction ratio of the steel sheet, the pinning effect of the precipitates that may form before or during recrystallization and the solute drag of substitutional elements (Mn, Si, Cr, Mo, Nb) within the interfaces. In this model, the effect of each type of alloying element segregated within the interfaces on the retardation of the recrystallization kinetics was taken into account thanks to a slowdown coefficient depending on the diffusion coefficient of the element and its affinity to be segregated at grain boundaries. The data (diffusion coefficient, binding energy to grain boundaries) of

Cette thèse est accessible à l'adresse : http://theses.insa-lyon.fr/publication/2020LYSEI120/these.pdf
© [A. MATHEVON], [2020], INSA Lyon, tous droits réservés

each element were extracted from the literature when they were available. The kinetics predicted by the MiReX model were performed without any adjustable parameters and compared to a wide range of experimental kinetics.

It was observed that Mn and Cr due to their rather high concentration in DP steels play a major role on the recrystallization kinetics which is significantly delayed compared to that of binary Fe-C steels. Contrary to silicon, molybdenum, niobium and titanium may have a strong influence on recrystallization due to their low diffusion coefficient and their high binding energy to grain boundaries even in low chemical content. In the case of micro-alloyed steels, a coupling with a precipitation modelling sofware was performed to reproduce the effect of the (Ti,Nb)C precipitates. It was highlighted that Ti and Nb have a crucial role in kinetics both in solid solution and as precipitates due to their pinning effect on the grain boundaries. Lastly, the MiReX model was used to predict recrystallization during continuous heating and to analyze the possibility of interaction of this phenomenon with austenite formation.

The development of a physically based model for the prediction of $\alpha \rightarrow \gamma$ and $\gamma \rightarrow \alpha$ phase transformations in **Chapter 3** has been proposed using the Gibbs energy minimization (GEM) concept. The model's novelty is based on the integration of the different phases (ferrite, austenite, cementite) within a single diffusion profile. This choice avoids the necessity to apply given equilibrium conditions at the interfaces. This numerical approach respects mass balance and leads to drastic reduction in the computation times compared to existing models.

First, the stasis in the transformation kinetics caused by the dissolution and enrichment of cementite on austenite formation kinetics was discussed and compared to DICTRA in the case of a Fe-C-Mn steel. Subsequently, complex cycles reproducing industrial cycles allowed us to confirm the ability of the GEM model to reproduce the austenite formation kinetics during heating and isothermal holding. The comparison with experimental kinetics underlined the model's ability to reproduce both the holding temperature and the chemical composition effect on austenite formation kinetics of Fe-C-Mn steels. The requirement to introduce chromium into the simulation in order to stabilize the cementite for the prediction of transformation kinetics in the case of an industrial grade was highlighted.

Finally, the model was tested on a cyclic thermal cycle and on decarburization tests which allowed us to prove the model's reversibility for $\gamma \rightarrow \alpha$ transformations.

Following the development of predictive models for the M_S temperature in recent years based on thermodynamic models and taking into account the grain size effect, **Chapter 4** studied the case of two-phase steels. Indeed, it is now possible to predict the M_S temperature and the austenite-to-ferrite kinetics with accuracy for fully austenitic steels, but very few studies have examined the case of the two-phase steels on the martensitic transformation, even though most new-generation high-strength steels include several phases and high contents of alloying elements. As the experimental M_S temperature drop for two-phase steel cannot be totally explained after intrecritical annealing by the carbon austenite enrichment and by the grain austenite refinement, it was assumed that the substitutional enrichment at the austenite/ferrite interface level can be partly responsible for

Cette thèse est accessible à l'adresse : http://theses.insa-lyon.fr/publication/2020LYSEI120/these.pdf
© [A. MATHEVON], [2020], INSA Lyon, tous droits réservés

the M_S fall. A coupling with GEM model was thus used to predict the interface enrichment to finally predict successfully the M_S temperature of Dual-Phase steels. These hypotheses make it possible to support the model thermodynamic foundations applied to the (100%γ) states when the exact chemical elements profile is known within the material, allowing thus its extension for two-phase states and other applications than DP steels.

Chapter 5 involved the development of a mechanical model (Hy-MFC) to reproduce the mechanical properties of DP steels based on microstructural parameters (*i.e.* chemical composition, martensite fraction, and grain size).

For the fully martensitic phase, a new dependence of the mechanical properties on the prior austenite grain size enabled calibration of the model on all the studied steels. Calibration of the effect of carbon on the properties of martensite was also proposed, leading to excellent agreement for all the studied steels. Finally, it was demonstrated that manganese contributes only through solid-solution hardening.

EBSD observations of selected areas for different deformations allowed us to detect local decohesion and misorientation zones in the ferrite grains close to martensite. They indicated the primordial effect of the composite on the microstructure, validating the hypothesis of adding geometrically necessary dislocations to accommodate the martensite dilatation during quenching and the deformation incompatibility between the phases. The interaction law was based on the addition of GNDs within the ferrite, stemming from the martensitic volume variation and the deformation incompatibility between the two phases. In addition, a new scale transition law was proposed, assuming a linear transition between an iso-strain and iso-work law, which resulted in a more accurate description of the strain hardening of the composite for low deformation in bi-percolant microstructures.

A characterization of the microstructural evolutions and mechanical properties of 100% martensitic steels during isothermal tempering (100-550 °C) was performed in **Chapter 6**. Using a monitoring of the microstructural evolution of tempered martensite by hardness and TEP, three main mechanisms during the tempering stage were identified using a time-temperature equivalence. At very low temperature (<150 °C) and during the quenching, a segregation of part of the carbon on the intrinsic defects of the martensite takes place without effect on the mechanical properties. Thereafter, the first drop in mechanical properties is due to an intra-lath cementite precipitation of a carbon fraction with an activation energy of 80 kJ/mol. The second drop is attributed to a rearrangement of the microstructure defects and the decrease in dislocation density associated with an activation energy close to the iron self-diffusion of 210 kJ/mol. This reorganization allows the carbon trapped in the defects to precipitate in order to reach the fraction predicted by the thermodynamic equilibrium for tempering above 500 °C.

Then, an extended "composite" mean-field model of the mechanical properties was proposed using several JMAK laws reproducing the different mechanisms identified using experimental activation energies. First a validation of the model in the case of fully martensitic ternary Fe-C-Mn steels tempered under various conditions was performed. Finally, the introduction of the mechanical property model for tempered martensite within the complete prediction model for two-phase steels has validated its ability to predict

Cette thèse est accessible à l'adresse : http://theses.insa-lyon.fr/publication/2020LYSEI120/these.pdf
© [A. MATHEVON], [2020], INSA Lyon, tous droits réservés

mechanical properties for several tempered two-phase steels. This last step ensures the physical basis of the model which does not need any adjustment parameters to combine all the physical parameters of the microstructure (*i.e.* chemical composition, martensite fraction and grain size) in addition to the time and temperature of the applied tempering.

Perspectives

To continue this study, several ways of exploration can be proposed to complete and deepen the characterization and modelling of microstructural evolutions during the thermal treatments of AHSS. Main ideas are developed below:

Coupling of the different models on an industrial thermal route

Presently, all the models have been developed within a global architecture allowing the different models for the prediction of microstructural evolutions and mechanical properties of DP steels to be coupled. Figure 6.23.(a) presents the approach to be followed for the coupling of the different models. For all the different models, the steel chemical composition and the thermal cycle parameters are necessary for the prediction of the different phenomena. An example of the results that can be obtained from the different models is detailed here in the case of a Fe-0.17C-1.7Mn steel.

The first step during continuous heating involves the determination of the recrystallization kinetics prior to the austenite formation based on the steel chemical composition and reduction ratio. Complete recrystallization ensures homogeneous microstructure while a strong interaction with the phase transformation phenomenon can be observed when recrystallization was not able to occur. In the studied example a heating rate of 5 °C/s leads to an almost complete recrystallization at the beginning of the austenite formation resulting in a weak interaction as shown in Figure 6.23.(b).

The phase transformation model is based on the half-spacing of the pearlitic zones generally related to the microstructure refinement as well as the enrichment of alloying elements in the cementite resulting from the coiling process. The phase transformation model is able to predict the austenite fraction obtained at the end of the intercritical heating for 3 min at different temperatures followed by quenching (100 $\%\alpha'$, 67 $\%\alpha'$ and 50 $\%\alpha'$ for respectively 850 °C, 780 °C and 760 °C) on the Fe-0.17C-1.7Mn steel (see Figure 6.23.(c)).

From the phase transformation model, it is possible to determine the austenite fraction at the end of the intercritical annealing and to estimate both the austenitic grain diameter from the initial grain size and the enrichment of the different substitutional elements at the interface. These different parameters are necessary to assess the evolution of the martensite start temperature (M_S) as a function of the applied thermal cycle and the chemical composition. Figure 6.23.(c) presents the results obtained in the case of the Fe-0.17C-1.7Mn steel where a decrease in M_S is noted due to the grain size refinement and the additional enrichment in alloying elements when the austenite fraction decreases.

Finally, the tensile properties of DP steels after quenching or tempering are defined from the Hy-MFC model using the chemical composition of the steel, the initial ferritic grain size and the parameters of the tempering process. Figure 6.23.(d-e) presents the results

Cette thèse est accessible à l'adresse : http://theses.insa-lyon.fr/publication/2020LYSEI120/these.pdf
© [A. MATHEVON], [2020], INSA Lyon, tous droits réservés

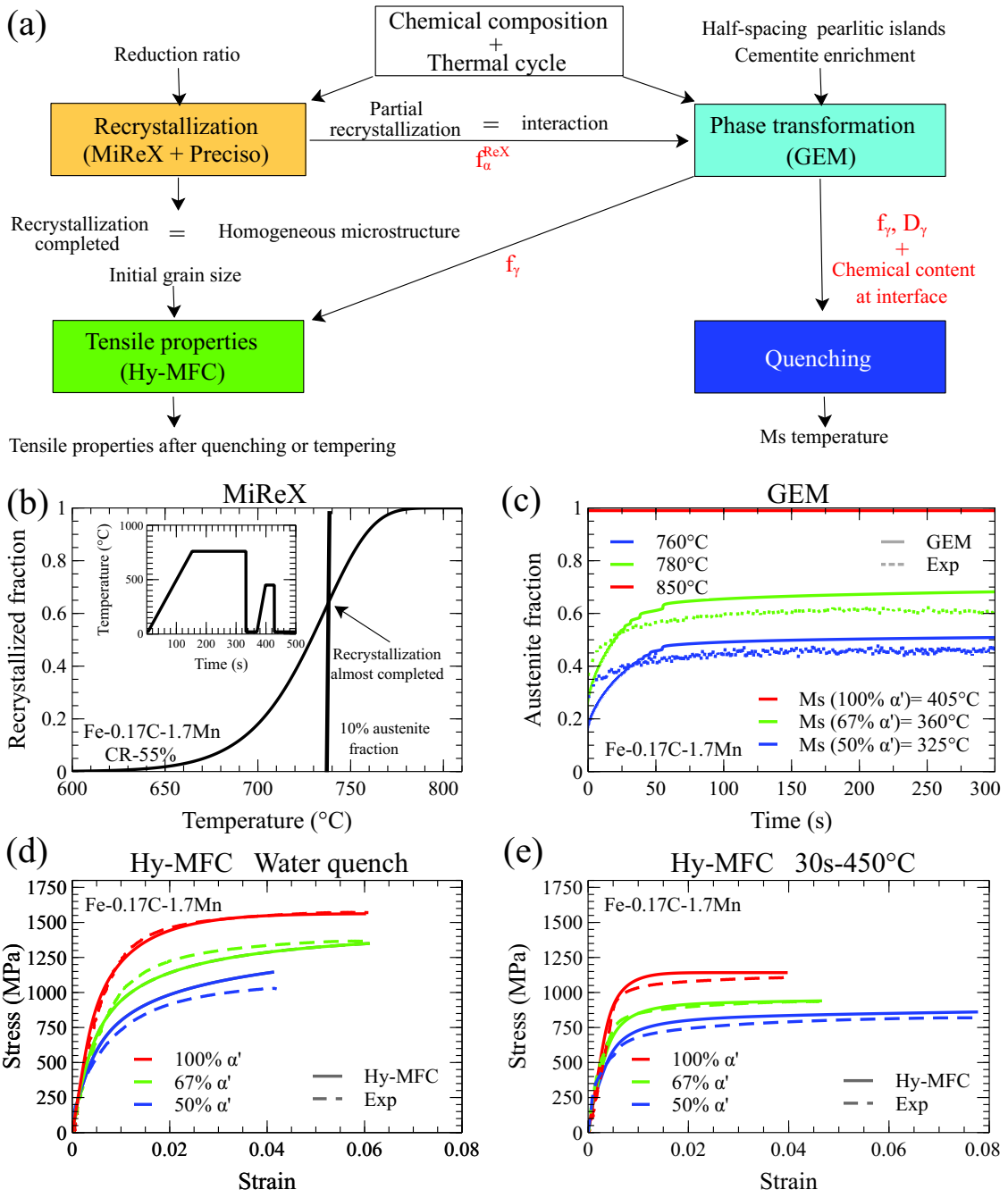

Figure 6.23: (a) Overview of the coupling approach of the different models developed in the thesis. (b) Presentation of the recrystallization kinetics in the case of the Fe-0.17C-1.7Mn steel during continuous heating with a 5 °C/s heating rate. (c) Comparaison of the experimental and modelled austenitic formation kinetics during the intercritical annealing and M_S temperature for different martensite fractions. (d-e) Comparison of the tensile properties of quenched and tempered DP steels for different martensite fractions.

Cette thèse est accessible à l'adresse : http://theses.insa-lyon.fr/publication/2020LYSEI120/these.pdf
© [A. MATHEVON], [2020], INSA Lyon, tous droits réservés

obtained for the Fe-0.17C-1.7Mn steel with different martensite fractions calculated by the GEM model of quenched or tempered DP steels. In both cases, a good agreement is obtained on the final properties of the steel despite the small error made on the estimation of the austenite fraction.

In the future, a more complete validation of this approach and the results of the different models on an industrial production line for a wide range of chemical composition will be necessary in order to set the limits of use and explore the additional difficulties encountered during the transition from laboratory to industrial scale. The coupling principle could be extended in the case of thermal cycles containing a slow cooling rate at high temperature allowing ferrite growth.

Model extension to other families of AHSS steels

During this PhD, the guideline for all the models developed was based on the classical thermal cycle of Dual-Phase steels composed of intercritical annealing followed by a quenching and tempering stage. The development of models for predicting microstructural evolutions (recrystallization and phase transformation) on a physical basis has already been tested on a wide range of chemical composition as well as on results from the literature. Nevertheless, this study was limited to an initial ferrito-pearlitic microstructure which could be extended to partially bainitic or martensitic microstructures modifying the intrinsic physical parameters of the system. Moreover, Dual-Phase steels present a quenching step which allows to obtain a fraction of residual austenite and bainite close to 0. The mechanisms of bainite formation are not yet fully understood, leading to many questions on how to model the formation of bainite during cooling. A consideration could be conducted on the way to introduce bainite within the GEM phase transformation model.

Concerning the prediction of the mechanical properties of AHSS steels, it is necessary to follow 2 essential steps: (i) the description of the intrinsic behaviour of each material phase and (ii) the interaction law between the different phases and the homogenization method of the mechanical properties.

For each phase, it is necessary to understand its mechanical behaviour during a tensile test to define the appropriate model used to reproduce the hardening of the different phases. In addition, as for adding the effect of the prior austenitic grain size on the martensite mechanical properties, the integration of different parameters such as chemical composition, grain size, dislocation density can be introduced in the case of austenite and bainite. In addition, TRIP and TWIP effects playing a major role in the achievement of the high mechanical properties of these steels could be added. Finally, a further investigation of the tempering process effects on metastable phases such as martensite and bainite will be necessary to be able to predict the mechanical properties of all AHSS steels.

An in-depth work is required for the characterization of the failure mechanisms in AHSS steels comprising more than 2 phases such as TRIP steels. The scale transition between intrinsic and macroscopic behaviour is currently based on a law of interaction between each phase which may bel more complex than a simple law (iso-strain, iso-stress or iso-work) depending on the complexity of the microstructure and the difference in mechanical properties between each one. Finally, a homogenization method based on a rule of mix-

Cette thèse est accessible à l'adresse : http://theses.insa-lyon.fr/publication/2020LYSEI120/these.pdf
© [A. MATHEVON], [2020], INSA Lyon, tous droits réservés

tures taking into account the volume fraction may allow the prediction of the mechanical properties of complex steel. More local finite element models based on real microstructures can also be used to validate the strong assumptions for the scale transition of mean-field models.

Optimization of thermal cycles

After coupling the different models and validating them industrially on production lines, a reverse optimization of the heat treatments and manufacturing processes can be envisaged.

Numerous metallurgical routes exist for the manufacture of the various desired products. However, once the models have been developed, it is possible to adapt the existing metallurgical routes to the production constraints of each line by adjusting the chemical compositions and thermal cycle parameters according to the desired properties of the final product. In the same idea, it is possible to consider an optimization of the total energy consumption during steel production by adjusting the heating and cooling power of the production lines according to the chemical compositions and the rolling process.

In a concern of production gain and reduction of the steel manufacturing cost, a rationalization of the number of input products according to the desired output product range allows to delay as much as possible the differentiation steps between products. This rationalization allows in particular the reduction of the number of products to be stocked.

The last step is the optimization of the production line control by adjusting the manufacturing process parameters for each coil in order to reach the targeted mechanical properties (SmartLine). This project is currently in progress at Marcegaglia in Italy, introducing almost all the models developed during this thesis for Dual-Phase steels.

Cette thèse est accessible à l'adresse : http://theses.insa-lyon.fr/publication/2020LYSEI120/these.pdf
© [A. MATHEVON], [2020], INSA Lyon, tous droits réservés

Cette thèse est accessible à l'adresse : http://theses.insa-lyon.fr/publication/2020LYSEI120/these.pdf
© [A. MATHEVON], [2020], INSA Lyon, tous droits réservés

Appendix A

Model extension for high C and high Si steels

The model calibration was performed in the case of ternary Fe-C-Mn steels containing no silicon and with a carbon content lower than 0.17C wt.%. Nevertheless silicon is generally added in industrial steels for its delaying effect on cementite precipitation. Moreover, Speich *et al.* [SPE 72] observed the formation of ϵ carbides in cementite for carbon concentrations higher than 0.2C wt.%. The experimental results of Cupertino *et al.* [MAL 17] will therefore be used to calibrate the model for high carbon and silicon steel grades before applying it to the two industrial DP steels studied in this thesis.

A.1 Modifications of the model to take into account the martensite tempering for high C and Si steels

Although a detailed characterization of the microstructural phenomena occurring with the addition of a high silicon content or on high carbon steels was not possible, several modifications were made based on the experimental results of Cupertino *et al.* [MAL 17].

Using available knowledge from the literature, it is nevertheless reasonable to assume that tempering for high C and Si steels occurs in 3 stages:

- Precipitation of *epsilon* carbides occurs at low temperature (T<250 °C). According to the literature results, when the nominal carbon composition of martensite exceeds 0.2 wt.%, epsilon carbides could be experimentally observed. Although the amount of carbon that can be segregated to the defects is important, starting from this carbon content of 0.2 wt.%, the precipitation of epsilon carbide becomes possible energetically.
- Intra-lath cementite precipitation occurs at low temperature (T<300 °C) with the dissolving of previously formed ϵ carbides.
- Inter-lath cementite precipitation when the carbon segregated on the defects is released during recovery between 300 °C and 550 °C.

This time, three JMAK models have been used to reproduce all the phenomena occurring during martensite tempering. The parameters of these different models are summa-

Cette thèse est accessible à l'adresse : http://theses.insa-lyon.fr/publication/2020LYSEI120/these.pdf
© [A. MATHEVON], [2020], INSA Lyon, tous droits réservés

rized in Table A.1.

JMAK law	b_0 (s^-1)	Activation energy (kJ/mol)	n
$Y_{ss\to\epsilon}$ epsilon carbide	6x10^6	80	1
$Y_{ss+\epsilon\to\theta}$ low temperature	6x10^4	$80 + 13.3C_{SI}$	0.75
$Y_{\perp\to\theta}$ high temperature	1x10^{11}	$190 + 22(1 - \exp(-(1.3C^m_{Mn})^{1.3})) + 5C_{SI}$	0.25

Table A.1: Activation energies and JMAK parameters for the martensite tempering.

The silicon addition to the steel leads to a modification of the activation energies associated with the cementite precipitation. Indeed, the retarding effect of silicon on the precipitation and growth of cementite is well known and leads to an increase in activation energy at low temperature mainly related to carbon precipitation. Moreover, it is also responsible for a slight increase in activation energy for high temperature tempering, since it can in the same way as manganese segregate within the microstructure defects and delay their rearrangement by a solute drag effect.

The following hypothesis proposes an empirical relation of the fraction of epsilon carbide that can be formed as a function of the carbon content within the martensite:

$$\begin{array}{l} \text{if } \mathrm{C}^m_C < 0.16 \text{ then } f_{eps} = 0 \\ \text{else } f_{eps} = \frac{C^m_C - 0.16}{C^m_C} \end{array} \tag{A.1}$$

Since ϵ carbides are not a stable thermodynamic phase, they are dissolved when cementite appears, leading to the following JMAK law:

$$Y_{ss\to\epsilon} = 1 - \exp(-(bt)^n) - Y_{ss+\epsilon\to\theta} \tag{A.2}$$

Once the different phenomena have been explained, it is therefore possible to define the amount of carbon atomes in solid solution or segregated to the defects with the following formula:

$$C^m_{C,ss+\perp} = C^m_C(1 - f_{eps}Y_{ss\to\epsilon} - 0.5(Y_{ss+\epsilon\to\theta} + Y_{\perp\to\theta})) \tag{A.3}$$

In the same way, the width of the local yield strength distribution Δ is expressed as below:

$$\Delta = K_0 + \frac{K_1}{\sqrt{D_\gamma}} + K_2(\%C^m_{C,ss+\perp})^{1.34} - 450Y_{\perp\to\theta} \tag{A.4}$$

Figure A.1 shows the evolution of the JMAK law parameters as a function of tempering conditions. The Fe-0.21C-2.22Mn-1.44Si steel studied experimentally by Cupertino [MAL 17] has a sufficiently high carbon content to present a non-negligible fraction of ϵ carbides (f_{eps}=0.23). For the two considered temperatures, Figure A.1.(a) highlights the rapid precipitation of epsilon carbides that are not retarded by the silicon addition

Cette thèse est accessible à l'adresse : http://theses.insa-lyon.fr/publication/2020LYSEI120/these.pdf
© [A. MATHEVON], [2020], INSA Lyon, tous droits réservés

in the steel. Then for longer times the cementite precipitation delayed by the silicon addition takes place leading initially to the dissolution of the ϵ carbides before reaching a precipitated carbon fraction of approximately 0.5. These two steps are clearly observed in Figure A.1.(c) with a first drop of carbon in solid solution due to the epsilon carbide precipitation followed by a second due to the cementite precipitation. Finally, the microstructure rearrangement and the inter-lath cementite precipitation occurs at higher temperature as for ternary steels (see Figure A.1.(c)). These evolutions of the intrinsic parameters of the microstructure enable to reproduce the tensile curves of Fe-0.21C-2.22Mn-1.44Si steel for different tempering conditions as shown in Figure A.1.(d).

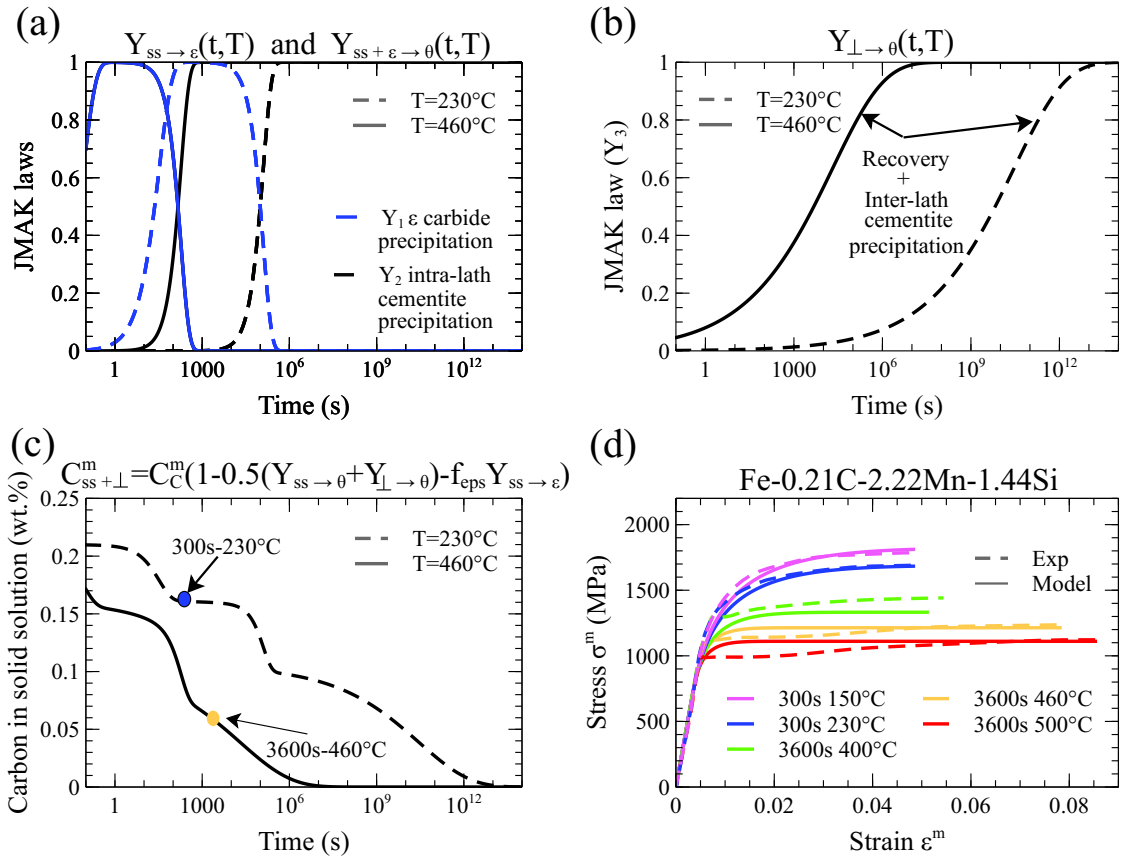

Figure A.1: Kinetics of the JMAK laws: (a) $Y_{ss\to\epsilon}$ and $Y_{ss\to\theta}$ and (b) $Y_{\perp\to\theta}$ for two temperatures. (c) Evolution of the carbon content in solid solution for the two considered temperatures. (d) Comparison between experimental and modelled tensile curves for a Fe-0.21C-2.22Mn-1.44Si steel [MAL 17].

A.2 Comparison of experimental and modelled tensile curves for high C or Si steels

A validation of the model extension was carried out on steels with high carbon or silicon content. Figure A.2 and Figure A.1.(d) show the good agreement obtained for three grades studied by Cupertino *et al.* for a wide range of tempering time and temperature. The

Cette thèse est accessible à l'adresse : http://theses.insa-lyon.fr/publication/2020LYSEI120/these.pdf
© [A. MATHEVON], [2020], INSA Lyon, tous droits réservés

integration of ϵ carbide precipitation in the case of the two high carbon steels allows to reproduce the significant softening of the mechanical properties for tempering temperatures below 250 °C. In contrast, the Fe-0.1C-2.46Mn-0.2Si steel shows almost no softening at similar tempering temperatures since the carbon content does not allow the formation of ϵ carbides. The silicon addition allows in comparison with ternary Fe-C-Mn steels to delay the different tempering phases and the decrease in the martensite mechanical properties. Finally, Figure A.2.(c) presents the results obtained for the DP1000 grade which validates the model's ability to reproduce the tempering properties of martensite in the case of an industrial micro-alloyed grade. The strain hardening rate in the case of quenched martensite and for low tempering temperatures is globally well reproduced by the CCA model assuming internal heterogeneity of the martensite. On the other hand, for high tempering temperatures above 400 °C, a change in stain hardening rate is observed with a more constant hardening close to that observed in ferrite. For the sake of simplicity, only the n constant has been increased to reproduce the overall pattern, although a gradual transition to the ferrite model used in Chapter 5 would ideally be worthwhile despite its complexity.

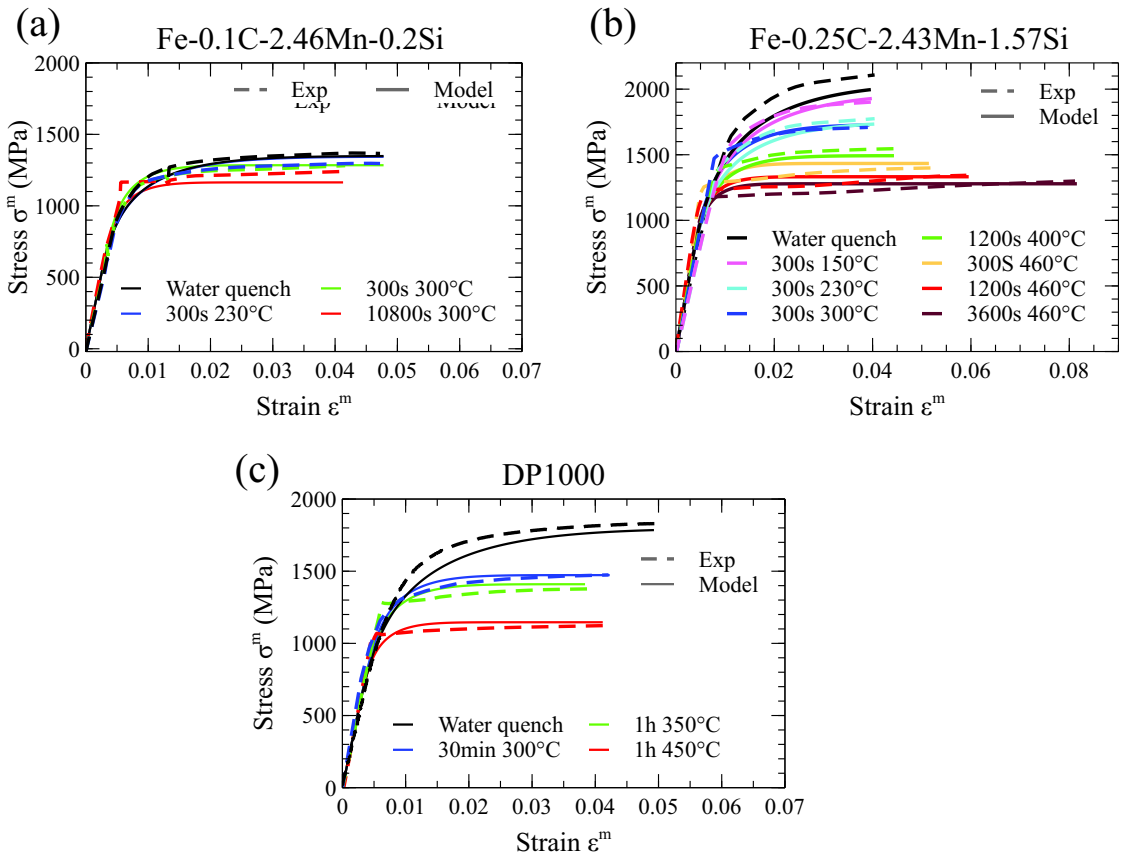

Figure A.2: Experimental and modelled tensile curves for a fully martensitic steel water quenched or tempered at different temperatures and times: a) Fe-0.25C-2.43Mn-1.57Si [MAL 17], b) Fe-0.1C-2.5Mn [MAL 17] and c) DP1000

Cette thèse est accessible à l'adresse : http://theses.insa-lyon.fr/publication/2020LYSEI120/these.pdf
© [A. MATHEVON], [2020], INSA Lyon, tous droits réservés

List of Abbreviations

AHSS	Advanced high strength steel
AUST.SS	Austenitic stainless steel
BIW	Vehicle body-in-white
CCA	Continuous composite approach
CCT	Continuous cooling transformation
CP	Complex steel
CPFEM	Crystal plasticity finite element method
CR	Cold-rolled steel
DSC	Differential scanning calorimetry
DFF	Direct flame furnace
DP	Dual-phase steel
EBSD	Electron backscattered diffraction
EDS	Energy dispersive spectroscopy
FE	Finite element
FEG	Field emission gun
FFT	Fast fourier transform
FIB	Focused ion beam
GA	Galvanization process with additional annealing treatment
GB	Grain boundary
GEM	Gibbs energy minimization
GI	Galvanization process
HSS	High strength steel
IF	Interstitial free steel
IPFZ	Inverse Pole Figure in direction Z
JMAK	Johnson-Mehl-Avrami-Kolmogorov law
KAM	Kernel average misorientation
L-IP	Lighweight steels with induced plasticity
MART	Fully martensitic steel
Q&P	Quenching and partitioning steel
REX	Recrystallized steel
RFT	Radiant tube furnace

Cette thèse est accessible à l'adresse : http://theses.insa-lyon.fr/publication/2020LYSEI120/these.pdf
© [A. MATHEVON], [2020], INSA Lyon, tous droits réservés

RVE	Representative volume element
SEM	Scanning electron microscope
SSD	Statiscially stored dislocations
TEM	Transmission electron microscope
TEP	Thermo-electrical power
TRIP	Transformation induced plasticity steel
TTT	Time temperature transformation
TWIP	Twinning induced plasticity steel
UTS	Ultimate tensile test
WH	Work hardening
YS	Yield strength
YPE	Yield point elongation

Cette thèse est accessible à l'adresse : http://theses.insa-lyon.fr/publication/2020LYSEI120/these.pdf
© [A. MATHEVON], [2020], INSA Lyon, tous droits réservés

References

[ÅGR 82] Ågren J.
Computer simulations of the austenite/ferrite diffusional transformations in low alloyed steels. *Acta Metallurgica*, vol. 30, n° 4, 1982, p. 841–851.

[ÅGR 86] Ågren J.
A revised expression for the diffusivity of carbon in binary FeC austenite. *Scripta Metallurgica*, vol. 20, n° 11, 1986, p. 1507–1510.

[AGR 06] AGREN J., BRECHET Y., HUTCHINSON C., Al. E.
Thermodynamics and phase transformations: the selected works of Mats Hillert. 2006.

[AKB 94] Akbay T., Reed R. C., Atkinson C.
Modelling reaustenitisation from ferrite/cementite mixtures in FeC steels. *Acta Metallurgica Et Materialia*, vol. 42, n° 4, 1994, p. 1469–1480.

[ALA 07] Al-Abbasi F. M., Nemes J. A.
Characterizing DP-steels using micromechanical modeling of cells. *Comput. Mater. Sci.*, vol. 39, n° 2, 2007, p. 402–415.

[ALL 12] Allain S., Bouaziz O., Takahashi M., Maizières A., Romaine-bp V., Cedex M.-l.-m.
Toward a New Interpretation of the Mechanical Behaviour of As- quenched Low Alloyed Martensitic Steels. *Mater. Sci. Eng. A*, vol. 52, n° 4, 2012, p. 717–722.

[ALL 15] Allain S., Bouaziz O., Pushkareva I., Scott C. P.
Towards the microstructure design of DP steels: a generic size-sensitive mean-field mechanical model. *Mater. Sci. Eng. A*, vol. 637, 2015, p. 222–234.

[ALU 09] aluminium W.
Global Aluminium Recycling: A Cornerstone of Sustainable Development. rapport, 2009.

[AND 65] Andrews K.
Empirical formulae for the calculation of some transformation temperatures. *J. Iron Steel Inst.*, , 1965, p. 721–727.

[AND 92] Andersson J. O., Ågren J.
Models for numerical treatment of multicomponent diffusion in simple phases. *Journal of Applied Physics*, vol. 72, n° 4, 1992, p. 1350–1355.

[AND 02] Andersson J. O., Helander T., Hoglund L., Shi P., Sundman B.
Computational tools for materials science. *Calphad*, vol. 26, 2002, p. 273–312.

Cette thèse est accessible à l'adresse : http://theses.insa-lyon.fr/publication/2020LYSEI120/these.pdf
© [A. MATHEVON], [2020], INSA Lyon, tous droits réservés

[ARL 13] Arlazarov A., Bouaziz O., Hazotte A., Gouné M., Allain S.
Characterization and modeling of manganese effect on strength and strain hardening of martensitic carbon steels. *ISIJ International*, vol. 53, n° 6, 2013, p. 1076–1080.

[ASA 75] Asaro R.
Elastic-plastic memory and kinematic-type hardening. *Acta Metall.*, vol. 23, n° 10, 1975, p. 1255–1265.

[ASS 19] steel association W.
WORLD STEEL IN FIGURES 2019. rapport, 2019.

[AUT] Autosteel
Autosteel.

[AZI 11] Azizi-Alizamini H., Militzer M., Poole W. J.
Austenite formation in plain low-carbon steels. *Metallurgical and Materials Transactions A*, vol. 42, n° 6, 2011, p. 1544–1557.

[BAR 14] Barbier D.
Extension of the martensite transformation temperature relation to larger alloying elements and contents. *Adv. Eng. Mater.*, vol. 16, n° 1, 2014, p. 122–127.

[BAR 15] Barbier D., Germain L., Hazotte A., Goune M., Chbihi A.
Microstructures resulting from the interaction between ferrite recrystallization and austenite formation in dual-phase steels. *J. Mater. Sci.*, vol. 50, 2015, p. 374–381.

[BAU 19] Baude M., Baudry M., Dussud F.-X.
Chiffres clés du climat France, Europe et Monde. rapport, 2019, Commissariat général au développement durable.

[BEL 18] Bellavoine M., Dumont M., Drillet J., Hébert V., Maugis P.
Combined Effect of Heating Rate and Microalloying Elements on Recrystallization During Annealing of Dual-Phase Steels. *Metall. Mater. Trans. A*, vol. 49, 2018, p. 2865–2875.

[BER 04] Berbenni S., Favier V., Lemoine X., Berveiller M.
Micromechanical modeling of the elastic-viscoplastic behavior of polycrystalline steels having different microstructures. *Mater. Sci. Eng. A*, vol. 372, n° 1-2, 2004, p. 128–136.

[BER 09] Bernacki M., Resk H., Coupez T., Logé R. E.
Finite element model of primary recrystallization in polycrystalline aggregates using a level set framework. *Model. Simul. Mater. Sc.*, vol. 17, 2009, Page 64006, {IOP} Publishing.

[BHA 01] Bhadeshia H.
Bainite in steels. *IOM Communication*, 2001.

[BLE 05] Bleck W., Phiu-On K.
Microalloying of cold-formable multi phase steel grades. *Materials Science Forum*, vol. 500, 2005, p. 97–114.

[BOH 09a] Bohemen S. M. C. V., Sietsma J.
Effect of composition of athermal martensite formation in plain carbon steels. *Mater. Sci. Eng.*, vol. 25, 2009, p. 1009–1012.

Cette thèse est accessible à l'adresse : http://theses.insa-lyon.fr/publication/2020LYSEI120/these.pdf
© [A. MATHEVON], [2020], INSA Lyon, tous droits réservés

[BOH 09b] Bohemen S. M. C. V., Sietsma J.
Martensite formation in partially and fully austenitic plain carbon steels. *Metall. Mater. Trans. A*, vol. 40A, 2009, p. 1059–1068.

[BOH 10] Bohemen S. V., Sietsma J.
The kinetics of bainite and martensite formation in steels during cooling. *Mater. Sci. Eng. A*, vol. 527, 2010, p. 6672–6676.

[BOH 12] Bohemen S. M. C. V.
Bainite and martensite start temperature calculated with exponential carbon dependence. *Mater. Sci. Techno.*, vol. 28, 2012, p. 487–495.

[BOH 14] Bohemen S. V., Sietsma J.
Kinetics of martensite formation in plain carbon steels: critical assessment of possible influence of austenite grain boundaries and autocatalysis. *Mater. Sci. Eng.*, vol. 30, n° 9, 2014, p. 1024–1033.

[BOH 17] van Bohemen S., Morsdorf L.
Predicting the Ms temperature of steels with a thermodynamic based model including the effect of the prior austenite grain size. *Acta Mater.*, vol. 125, 2017, p. 401–415, Pergamon.

[BOS 07] Bos C., Sietsma J.
A mixed-mode model for partitioning phase transformations. *Scripta Materialia*, vol. 57, 2007, p. 1085–1088.

[BOS 09] Bos C., Sietsma J.
Application of the maximum driving force concept for solid-state partitioning phase transformations in multi-component system. *Acta Materialia*, vol. 57, 2009, p. 136–144.

[BOU 01] Bouaziz O., Kandel M., Lecomte C.
Physical modelling of microstructure and mechanical properties of dual-phase steel. *Le Journal de Physique IV*, vol. 11, n° PR4, 2001, p. 223–231.

[BOU 02] Bouaziz O., Buessler P.
Mechanical behaviour of multiphase materials : an intermediate mixture law without fitting parameter. *Rev. Met. Paris*, vol. 99, n° 1, 2002, p. 71–77.

[BOU 08] Bouaziz O., Aouafi A., Allain S.
Effect of grain refinement on the mechanical behaviour of ferritic steels: evolution of isotropic hardening and kinematic hardening. *Mater. Sci. Forum*, vol. 584-586, 2008, p. 605–609.

[BOU 13] Bouaziz O., Zurob H., Huang M.
Driving force and logic of development of advanced high strength steels for automotive applications. *Steel Research International*, vol. 84, n° 10, 2013, p. 937–947.

[BRE 70] Breinan E., Ansell G.
Influence of Austenite Strength Upon the Austenite-Martensite Transformation in Alloy Steels. *Metall. Mater. Trans. A*, vol. 1, n° 6, 1970, p. 1513–1520.

[BRO 83] Brofman P., Ansell G.
On the effect of fine grain size on the Ms temperature in Fe-27Ni-0.025 C alloys. *Metall. Mater. Trans. A*, vol. 14, n° 9, 1983, p. 1929–1931.

Cette thèse est accessible à l'adresse : http://theses.insa-lyon.fr/publication/2020LYSEI120/these.pdf
© [A. MATHEVON], [2020], INSA Lyon, tous droits réservés

[CAH 62] Cahn J. W.
The impurity-drag effect in grain boundary motion. *Acta Metallurgica*, vol. 10, n° 9, 1962, p. 789–798.

[CAL 10] Calcagnotto M., Ponge D., Demir E., Raabe D.
Orientation gradients and geometrically necessary dislocations in ultrafine grained dual-phase steels studied by 2D and 3D EBSD. *Materials Science and Engineering A*, vol. 527, n° 10-11, 2010, p. 2738–2746, Elsevier B.V.

[CAP 02] Capdevila C., Caballero F. G., de Andrés C. G.
Determination of martensite-start temperature in steels: Bayesian neural network model. *ISIJ Int.*, vol. 42, n° 8, 2002, p. 894–902.

[CAP 03] Capdevila C., Caballero F. G., García de Andrés C.
Analysis of effect of alloying elements on martensite start temperature of steels. *Mater. Sci. Techno.*, vol. 19, n° 5, 2003, p. 581–586.

[CAR 44] Carapella L. A.
Computing A or Ms (transformation temperature on quenching) from analysis. *Metal Progress*, , n° 46, 1944, Page 108.

[CHA 19] Chantrenne P., Perez M., Ollat M., Massardier V., Fabregue D., Philippe R.
Diffusion model for austenite formation kinetics during inter-critical annealing of Dual-Phase steels. *Modelling and Simulation in Materials Science and Engineering*, , 2019, p. 0–12.

[CHB 14a] Chbihi A., Barbier D., Germain L., Hazotte A., Gouné M.
Interactions between ferrite recrystallization and austenite formation in high-strength steels. *Journal of Materials Science*, vol. 49, n° 10, 2014, p. 3608–3621.

[CHB 14b] Chbihi A., Barbier D., Germain L., Hazotte A., Gouné M.
Interactions between ferrite recrystallization and austenite formation in high-strength steels. *J. Mater. Sci.*, vol. 49, 2014, p. 3608–3621.

[CHE 88] Cheng L., Brakman C., Korevaar B., Mittemejer E.
The tempering of iron-carbon martensite; dilatometric and calorimetric analysis. *Metallurgical Transactions A*, vol. 19, n° 10, 1988, p. 2415–2426.

[CHE 89] Chen H. C., Cheng G. H.
Effect of martensite strength on the tensile strength of dual phase steels. *Journal of Materials Science*, vol. 24, n° 6, 1989, p. 1991–1994.

[CHE 11] Chen H., Appolaire B., Van Der Zwaag S.
Application of cyclic partial phase transformations for identifying kinetic transitions during solid-state phase transformations: Experiments and modeling. *Acta Materialia*, vol. 59, n° 17, 2011, p. 6751–6760.

[CHE 13a] Chen H., Gamsjäger E., Schider S., Khanbareh H., Van Der Zwaag S.
In situ observation of austenite-ferrite interface migration in a lean Mn steel during cyclic partial phase transformations. *Acta Materialia*, vol. 61, n° 7, 2013, p. 2414–2424.

Cette thèse est accessible à l'adresse : http://theses.insa-lyon.fr/publication/2020LYSEI120/these.pdf
© [A. MATHEVON], [2020], INSA Lyon, tous droits réservés

[CHE 13b] Chen H., Kuziak R., Van Der Zwaag S.
Experimental evidence of the effect of alloying additions on the stagnant stage length during Cyclic partial phase transformations. *Metallurgical and Materials Transactions A: Physical Metallurgy and Materials Science*, vol. 44, n° 13, 2013, p. 5617–5621.

[CHE 13c] Chen H., Van Der Zwaag S.
Analysis of ferrite growth retardation induced by local Mn enrichment in austenite created by prior interface passages. *Acta Materialia*, vol. 61, n° 4, 2013, p. 1338–1349, Acta Materialia Inc.

[CHE 14a] Chen H., Van Der Zwaag S.
Predicting the effect of Mo, Ni, and Si on the bainitic stasis. *Metallurgical and Materials Transactions A: Physical Metallurgy and Materials Science*, vol. 45, n° 8, 2014, p. 3429–3437.

[CHE 14b] Chen H., Xu X., Xu W., Van Der Zwaag S.
Predicting the austenite fraction after intercritical annealing in lean steels as a function of the initial microstructure. *Metallurgical and Materials Transactions A: Physical Metallurgy and Materials Science*, vol. 45, n° 4, 2014, p. 1675–1679.

[CHE 14c] Chen H., Zwaag S. V. D.
A general mixed-mode model for the austenite-to-ferrite transformation kinetics in Fe-C-M alloys. *Acta Materialia*, vol. 72, 2014, p. 1–12, Acta Materialia Inc.

[CHE 16] Chen H., Zhu B., Militzer M.
Phase field modeling of cyclic austenite-ferrite transformations in Fe-C-Mn alloys. *Metallurgical and Materials Transactions A*, vol. 47, 2016, p. 3373–3881.

[CHO 09] Choi K. S., Liu W. N., Sun X., Khaleel M. A.
Influence of martensite mechanical properties on failure mode and ductility of dual-phase steels. *Metall. Mater. Trans. A*, vol. 40, n° 4, 2009, p. 796–809.

[CHR 81a] Christian J.
The theory of transformation in metals and alloys. Pergamon édition, 1981.

[CHR 81b] Christian J. W.
The theory of transformations in metals and alloys. *Pergamon*, , 1981.

[COA 72] Coates D. E.
Diffusion-controlled precipitate growth in ternary systems I. *Metallurgical Transactions*, vol. 3, n° 5, 1972, p. 1203–1212.

[COA 73] Coates D. E.
Diffusional growth limitation and hardenability. *Metallurgical Transactions*, vol. 4, n° 10, 1973, p. 2313–2325.

[DAN 16] Danoix F., Sauvage X., Huin D., Germain L., Gouné M.
A direct evidence of solute interactions with a moving ferrite/austenite interface in a model Fe-C-Mn alloy. *Scr. Mater.*, vol. 121, 2016, p. 61–65, Elsevier B.V.

[DAV 78] Davies R. G.
Influence of martensite composition and content on the properties of dual phase steels. *Metallurgical Transactions A*, vol. 9, n° 5, 1978, p. 671–679.

[DEL 07] Delince M., Bréchet Y., Embury J. D., Geers M. G., Jacques P. J., Pardoen T.

Cette thèse est accessible à l'adresse : http://theses.insa-lyon.fr/publication/2020LYSEI120/these.pdf
© [A. MATHEVON], [2020], INSA Lyon, tous droits réservés

Structure-property optimization of ultrafine-grained dual-phase steels using a microstructure-based strain hardening model. *Acta Mater.*, vol. 55, n° 7, 2007, p. 2337–2350.

[DOH 97] Doherty R. D., Hughes D. A., Humphreys F. J., Jonas J. J., Jensen D. J., Kassner M. E., Rollett A. D.
Current issues in recrystallization: a review. *Materials Science and Engineering: A*, vol. 238, n° 2, 1997, p. 219–274.

[EIC 53] Eichman G., Hull F.
-. *Transaction American Society of Metallurgy*, vol. 45, 1953, p. 77–104.

[ELD 77] Eldis G. T.
A critical review of data sources for isothermal transformation and continuous cooling transformation diagrams. *Hardenability Concepts with Applications to Steel*, , 1977, p. 126–157.

[EPA 12] EPA
Light-Duty vehicle mass reduction and cost analysis: midsize crossover utility vehicle. *U.S. Environmental Protection Agency*, , 2012.

[EST 84] Estrin Y., Mecking H.
A unified phenomenological description of work hardening and creep based on one-parameter models. *Acta Metall.*, vol. 32, n° 1, 1984, p. 57–70.

[Eur 15] European Environment Agency
Monitoring CO2 emissions from new passenger cars and vans in 2014. rapport n° 7, 2015, European Environment Agency.

[FIL 14] Fillafer A., Krempaszky C., Werner E.
On strain partitioning and micro-damage behavior of dual-phase steels. *Mater. Sci. Eng. A*, vol. 614, 2014, p. 180–192, Elsevier.

[FIS 14] Fischer F. D., Svoboda J., Petryk H.
Thermodynamic extremal principles for irreversible processes in materials science. *Acta Materialia*, vol. 67, n° 153, 2014, p. 1–20, Acta Materialia Inc.

[Fri 69] Fridberg J, Törndahl LE H. M.
Diffusion in iron. *Jernkontorets Ann*, vol. 153, n° 6, 1969, p. 263–276.

[FUR 04] Furuhara T., Kobasyahi K., Maki T.
Control of cementite precipitation in lath martensite by rapid heating and tempering. *ISIJ International*, vol. 44, n° 11, 2004, p. 1937–1944.

[GAM 07] Gamsjäger E.
A note on the contact conditions at migrating interfaces. *Acta Materialia*, vol. 55, n° 14, 2007, p. 4823–4833.

[GAR 05] Gardey B., Bouvier S., Bacroix B.
Correlation between the macroscopic behavior and the microstructural evolutions during large plastic deformation of a dual-phase steel. *Metall. Mater. Trans. A*, vol. 36, n° 11, 2005, p. 2937–2945.

[GAR 08] García-Junceda A., Capdevila C., Caballero F. G., de Andrés C. G.
Dependence of martensite start temperature on fine austenite grain size. *Scripta Mater.*, vol. 58, n° 2, 2008, p. 134–137.

Cette thèse est accessible à l'adresse : http://theses.insa-lyon.fr/publication/2020LYSEI120/these.pdf
© [A. MATHEVON], [2020], INSA Lyon, tous droits réservés

[GHO 94] Ghosh G., Olson G. B.
Kinetics of F.C.C. to B.C.C. heterogeneous martensitic nucleation-I. The critical driving force for athermal nucleation. *Acta Metall. Mater.*, vol. 42, n° 10, 1994, p. 3361–3370.

[GOU 12] Gouné M., Maugis P., Drillet J.
A Criterion for the Change from Fast to Slow Regime of Cementite Dissolution in Fe-C-Mn Steels. *Journal of Materials Science and Technology*, vol. 28, n° 8, 2012, p. 728–736.

[GOU 15] Goune M., Danoix F., Agren J., Bréchet Y., Hutchinson C., Zwaag S. V. D., Zurob H.
Overview of the current issues in austenite to ferrite transformation and the role of migrating interfaces therein for low alloyed steels. *Materials Science and Engineering R*, vol. 92, 2015, p. 1–38.

[GRA 47] Grange R. A., Holt W. S., Tkac E. T.
Transformation of Austenite in an Aluminum-chromium-molybdenum. *Steel. Trans. AIME*, vol. 172, 1947, p. 452–466.

[GRA 77] Grange R., Hribal C., Porter L.
Hardness of tempered martensite in carbon and low-alloy steels. *Metallurgical Transactions A*, vol. 8, n° 11, 1977, p. 1775–1785.

[GRA 19] Graux A., Cazottes S., De Castro D., San Martín D., Capdevila C., Cabrera J. M., Molas S., Schreiber S., Mirković D., Danoix F., Bugnet M., Fabrègue D., Perez M.
Precipitation and grain growth modelling in Ti-Nb microalloyed steels. *Materiala*, vol. 5, 2019, Page 100233.

[HAL 51] Hall E. O.
The deformation and ageing of mild steel: II characteristics of the Lüders deformation. *Proc. Phys. Soc. B*, vol. 64, n° 9, 1951, Page 742.

[HE 14] He B. B., Zhu K., Huang M. X.
On the nanoindentation behaviour of complex ferritic phases. *Phil. Mag. Let.*, vol. 94, n° 7, 2014, p. 439–446.

[HER 11] Hernandez V., Nayak S., Zhou Y.
Tempering of martensite in dual-phase steels and its effects on softening behaviorp. *Metallurgical and Materials Transactions A*, vol. 42, n° 10, 2011, Page 3115.

[HIL 76] Hillert M., Sundman B.
A treatment of the solute drag on moving grain boundaries and phase interfaces in binary alloys. *Acta Metallurgica*, vol. 24, n° 8, 1976, p. 731–743.

[HIL 96] Hildebrand T., Rüesgsegger P.
A new method for the model-independent assessment of thickness in three-dimensional images. *J. of Microscopy*, vol. 185, 1996, p. 67–75.

[HIL 98] Hillert M.
Phase diagrams and phase transformations, their thermodynamic basis. *Cambridge*, , 1998.

Cette thèse est accessible à l'adresse : http://theses.insa-lyon.fr/publication/2020LYSEI120/these.pdf
© [A. MATHEVON], [2020], INSA Lyon, tous droits réservés

[HIL 99] Hillert M.
Solute drag, solute trapping and diffusional dissipation of Gibbs energy. *Acta Materialia*, vol. 47, n° 18, 1999, p. 4481–4505.

[HIL 07] Hillert M.
Phase equilibria, phase diagrams and phase transformations: their thermodynamic basis. Cambridge University Press, 2007.

[HIL 15] Hilditch T. B., de Souza T., Hodgson P. D.
Properties and automotive applications of advanced high-strength steels (AHSS). Elsevier Ltd, 2015.

[HOL 45] Hollomon J.
Time-temperature relations in tempering steel. Trans. AIME, 1945, vol. 162, p. 223-249. *Transaction American Society of Metallurgy*, vol. 162, 1945, p. 223–249.

[HUA 04] Huang J., Poole W. J., Militzer M.
Austenite formation during intercritical annealing. *Metallurgical and Materials Transactions A*, vol. 35A, 2004, p. 3363–3375.

[HUM 12] Humphreys F. J., Hatherly M.
Recrystallization and related annealing phenomena. *Elsevier*, , 2012.

[HÜP 99] Hüper T., Endo S., Ishikawa N., Koichi O.
Effect of Volume Fraction of Constituent Phases on the Stress-Strain Relationship of Dual Phase Steels. *Mater. Sci.*, vol. 39, n° 3, 1999, p. 288–294.

[HUT 04] Hutchinson C. R., Fuchsmann A., Zurob H. S., Brechet Y.
A novel experimental approach to identifying kinetic transitions in solid state phase transformations. *Scripta Materialia*, vol. 50, n° 2, 2004, p. 285–290.

[HUT 11] Hutchinson B., Hagström J., Karlsson O., Lindell D., Tornberg M., Lindberg F., Thuvander M.
Microstructures and hardness of as-quenched martensites (0.1-0.5%C). *Acta Materialia*, vol. 59, n° 14, 2011, p. 5845–5858.

[HUT 18] Hutchinson B., Bate P., Lindell D., Malik A., Barnett M., Lynch P.
Plastic yielding in lath martensites - An alternative viewpoint. *Acta Mater.*, vol. 152, 2018, p. 239–247, Elsevier Ltd.

[IRM 72] Irmer V., Feller-Kniepmeier M.
Diffusion of manganese in α-iron single crystals of different purity. *J. Phys. Chem. Solids.*, vol. 33, 1972, p. 2141–2148.

[JAC 07] Jacques P. J., Furnemont Q., Lani F., Pardoen T., Delannay F.
Multiscale mechanics of TRIP-assisted multiphase steels: I. Characterization and mechanical testing. *Acta Mater.*, vol. 55, n° 11, 2007, p. 3681–3693.

[JIA 95] Jiang Z., Guan Z., Lian J.
Effects of microstructural variables on the deformation behaviour of dual-phase steel. *Mater. Sci. Eng. A*, vol. 190, n° 1-2, 1995, p. 55–64.

[KAD 11] Kadkhodapour J., Schmauder S., Raabe D., Ziaei-Rad S., Weber U., Calcagnotto M.
Experimental and numerical study on geometrically necessary dislocations and non-

Cette thèse est accessible à l'adresse : http://theses.insa-lyon.fr/publication/2020LYSEI120/these.pdf
© [A. MATHEVON], [2020], INSA Lyon, tous droits réservés

homogeneous mechanical properties of the ferrite phase in dual phase steels. *Acta Mater.*, vol. 59, n° 11, 2011, p. 4387–4394, Acta Materialia Inc.

[KHA 90] Khan S. A., Bhadeshia H. K. D.
Kinetics of martensitic transformation in partially bainitic 300M steel. *Materials Science and Engineering A*, vol. 129, n° 2, 1990, p. 257–272.

[KIM 12] Kim J. H., Kim D., Barlat F., Lee M. G.
Crystal plasticity approach for predicting the Bauschinger effect in dual-phase steels. *Mater. Sci. Eng. A*, vol. 539, 2012, p. 259–270, Elsevier B.V.

[KOF 10] Koffler C., Rohde-Brandenburger K.
On the calculation of fuel savings through lightweight design in automotive life cycle assessments. *International Journal of Life Cycle Assessment*, vol. 15, n° 1, 2010, p. 128–135.

[KOI 59] Koistinen D. P., Marburger R. E.
A general equation prescribing the extent of the austenite-martensite transformation in pure iron-carbon alloys and plain carbon steels. *Acta Mater.*, vol. 7, 1959, p. 59–60.

[KOR 84] Korzekwa D. A., Matlock D. K., Krauss G.
Dislocation substructure as a function of strain in a dual-phase steel. *Metall. Mater. Trans. A*, vol. 15, n° 6, 1984, p. 1221–1228.

[KRA 99] Krauss G.
Martensite in steel: strength and structure. *Materials Science and Engineering A*, vol. 273, 1999, p. 40–57.

[KRE 09] Krebs B.
Caractérisation et prévision des structures en bandes dans les aciers Dual-Phase : lien avec les propriétés d'endommagement. Thèse de doctorat, Université Paul Verlaine, 2009.

[KRI 97] Krielaart G. P., Sietsma J., Zwaag S. V. D.
Interface Conditions. *Materials Science and Engineering*, vol. 237, 1997, p. 216–223.

[KUA 16] Kuang W., Wang H., Zhang J., Liu F.
Application of the thermodynamic extremal principle to diffusion-controlled phase-transformations in multi-component substitutional alloys: Modeling and applications. *Acta Materialia*, vol. 120, 2016, p. 415–425, Elsevier Ltd.

[KUA 18] Kuang W., Wang H., Li X., Zhang J., Zhou Q., Zhao Y.
Application of the thermodynamic extremal principle to diffusion-controlled phase transformations in Fe-C-X alloys: Modeling and applications. *Acta Materialia*, vol. 159, 2018, p. 16–30, Elsevier Ltd.

[KUL 13] Kulakov M., Poole W. J., Militzer M.
The Effect of the Initial Microstructure on Recrystallization and Austenite Formation in a DP600 Steel. *Metall. Mater. Trans. A*, vol. 44A, 2013, p. 3564–3576.

[KUN 82] Kung C. Y., Rayment J. J.
An examination of the validity of existing empirical formulae for the calculation of Ms temperature. *Metall. Mater. Trans. A*, vol. 13, 1982, p. 328–331.

Cette thèse est accessible à l'adresse : http://theses.insa-lyon.fr/publication/2020LYSEI120/these.pdf
© [A. MATHEVON], [2020], INSA Lyon, tous droits réservés

[KWO 10] KWON O., LEE K. Y., KIM G. S., Chin K. G.
New trends in advanced high strength steel developments for automotive application. *Materials Science Forum*, vol. 638, 2010, p. 136–141.

[LAI 14] Lai Q.
Optimisation de la microstructure d'aciers ferrito-martensitiques à 3.5% pds Mn: des transformations de phases à la micro-mécanique. Thèse de doctorat, 2014.

[LAI 16] Lai Q., Gouné M., Perlade A., Pardoen T., Jacques P., Bouaziz O., Bréchet Y.
Mechanism of Austenite Formation from Spheroidized Microstructure in an Intermediate Fe-0.1C-3.5Mn Steel. *Metallurgical and Materials Transactions A: Physical Metallurgy and Materials Science*, vol. 47, n° 7, 2016, p. 3375–3386.

[LAM 14] Lamontagne A.
Etude des mécanismes physiques responsables des évolutions microstructurales des aciers perlitiques au cours du tréfilage et du vieillissement post-tréfilage. Thèse de doctorat, 2014.

[LAN 07] Lani F., Furnémont Q., Van Rompaey T., Delannay F., Jacques P. J., Pardoen T.
Multiscale mechanics of TRIP-assisted multiphase steels: II. Micromechanical modelling. *Acta Mater.*, vol. 55, n° 11, 2007, p. 3695–3705.

[LEE 05] Lee S. J., Lee Y. K.
Effect of austenite grain size on martensitic transformation of a low alloy steel. *Mater. Sci. Forum*, vol. 475, 2005, p. 3169–3172.

[LEI 84] Lei T. C., Shen H. P.
A new expression for the strength of martensite plus ferrite dual-phase steels. *American Society for Metals*, , 1984, p. 341–350.

[LEW 14] Lewis A. M., Kelly J. C., Keoleian G. A.
Vehicle lightweighting vs. electrification: Life cycle energy and GHG emissions results for diverse powertrain vehicles. *Applied Energy*, vol. 126, 2014, p. 13–20, Elsevier Ltd.

[LI 90a] Li Z., Gu H.
Bauschinger effect and residual phase stresses in two ductile-phase steels. Part I. The influence of phase stresses on the Bauschinger effect. *Metall. Mater. Trans. A*, vol. 21 A, n° 3, 1990, p. 717–724.

[LI 90b] Li Z., Gu H.
Bauschinger effect and residual phase stresses in two ductile-phase steels: Part II. The effect of microstructure and mechanical properties of the constituent phases on Bauschinger effect and residual phase stresses. *Metall. Mater. Trans. A*, vol. 21, n° 2, 1990, p. 725–732.

[LI 13] Li P., Li J., Meng Q., Hu W., Xu D.
Effect of heating rate on ferrite recrystallization and austenite formation of cold-roll dual phase steel. *J. Alloys Compd.*, vol. 578, 2013, p. 320–327, Elsevier B.V.

[LIA 91] Lian J., Jiang Z., Liu J.
Theoretical model for the tensile work hardening behaviour of dual-phase steel. *Mater. Sci. Eng. A*, vol. 147, n° 1, 1991, p. 55–65.

Cette thèse est accessible à l'adresse : http://theses.insa-lyon.fr/publication/2020LYSEI120/these.pdf
© [A. MATHEVON], [2020], INSA Lyon, tous droits réservés

[LIE 02] Liedl U., Traint S., Werner E. A.
An unexpected feature of the stress-strain diagram of dual-phase steel. *Comput. Mater. Sci.*, vol. 25, n° 1-2, 2002, p. 122–128.

[LIU 09] Liu D., Yu J.
Otsu method and K-means. *Ninth International Conference on Hybrid Intelligent Systems*, vol. 1, 2009, p. 344–349.

[LIU 12] Liu G., Müller D. B.
Addressing sustainability in the aluminum industry: A critical review of life cycle assessments. *Journal of Cleaner Production*, vol. 35, 2012, p. 108–117.

[LIU 13] Liu Z. Q., Miyamoto G., Yang Z. G., Furuhara T.
Direct measurement of carbon enrichment during austenite to ferrite transformation in hypoeutectoid Fe-2Mn-C alloys. *Acta Materialia*, vol. 61, n° 8, 2013, p. 3120–3129.

[LOG 08] Loge R., Bernacki M., Resk H., Delannay L., Digonnet H., Chastel Y., Coupez T.
Linking plastic deformation to recrystallization in metals using digital microstructures. *Phil. Mag.*, vol. 88, 2008, p. 3691–3712.

[LÜ 11] Lü Y., Molodov D. A., Gottstein G.
Recrystallization kinetics and microstructure evolution during annealing of a cold-rolled Fe-Mn-C alloy. *Acta Materialia*, vol. 59, n° 8, 2011, p. 3229–3243.

[LÜC 57] Lücke K., Detert K.
A quantitative theory of grain-boundary motion and recrystallization in metals in the presence of impurities. *Acta Metallurgica*, vol. 5, n° 11, 1957, p. 628–637.

[MA 89] Ma M. T., Sun B. Z., Tomota Y.
Bauschinger Effect and Back Stress in a Dual Phase Steel. *ISIJ Int.*, vol. 29, n° 1, 1989, p. 74–77.

[MAA 16] Maalekian M., Azizi-Alizamini H., Militzer M.
Phase field modeling of microstructure banding in steels. *Metallurgical and Materials Transactions A*, vol. 47, n° 1, 2016, p. 608–622.

[MAL 11] MALEN D. E.
Fundamentals of Automobile Body Structure Design. *SAE Technical Paper*, , 2011.

[MAL 17] Malheiros L. R., Rodriguez E. A., Arlazarov A.
Mechanical behavior of tempered martensite: Characterization and modeling. *Mater. Sci. Eng. A*, vol. 706, n° May, 2017, p. 38–47, Elsevier B.V.

[MAR 82] Marder A. R.
Deformation Characteristics of Dual-Phase Steels. *Metallurgical transactions. A, Physical metallurgy and materials science*, vol. 13 A, n° 1, 1982, p. 85–92.

[MAR 20a] MARCEAUX C., HOUMMADA K., DRILLET J., HEBERT V., MAUGIS P.
Atom probe tomography study of austenite formation during heating of a high-formability steel. *Journal of Materials Science*, vol. 55, n° 22, 2020, p. 9286–9298.

[MAR 20b] MARCEAUX C., HOUMMADA K., DRILLET J., HEBERT V., MAUGIS P.

Cette thèse est accessible à l'adresse : http://theses.insa-lyon.fr/publication/2020LYSEI120/these.pdf
© [A. MATHEVON], [2020], INSA Lyon, tous droits réservés

Delaying Effect of Cementite on Recrystallization Kinetics of a Ti-Nb Microalloyed High-Formability Steel. *Metallurgical and Materials Transactions A*, , 2020.

[MAR 20c] MARCEAUX C., HOUMMADA K., DRILLET J., HEBERT V., MAUGIS P.
Effects of cementite size and chemistry on the kinetics of austenite formation during heating of a high-formability steel. *Computational Materials Science*, vol. 182, n° May, 2020.

[MAS 14] Massardier V., Goune M., Fabregue D., Selouane A., Douillard T., Bouaziz O.
Evolution of microstructure and strength during the ultra-fast tempering of Fe-Mn-C martensitic steels. *Journal of Materials Science*, vol. 49, n° 22, 2014, p. 7782–7796.

[MAT 09] Matlock D. K., Speer J. G.
Third Generation of AHSS: Microstructure Design Concepts. London, springer édition, 2009.

[MAT 12] Matlock D. K., John G. Speer, Emmanuel De Moor P. J. G.
Recent developments in advanced high strength sheet steels for automotive applications: an overview. *JESTECH*, vol. 15, n° 1, 2012, p. 1–15.

[MAT 20] Mathevon A., Massardier V., Fabrègue D., Rocabois P., Perez M.
A Microstructurally Based Model for Recrystallization in Dual-Phase Steels. *Metallurgical and Materials Transactions A: Physical Metallurgy and Materials Science*, vol. 51, n° 8, 2020, p. 4228–4241.

[MAY 12] Mayyas A. T., Qattawi A., Mayyas A. R., Omar M. A.
Life cycle assessment-based selection for a sustainable lightweight body-in-white design. *Energy*, vol. 39, n° 1, 2012, p. 412–425, Elsevier.

[MCQ 77] McQueen H. J.
The production and utility of recovered dislocation substructures. *Metallurgical Transactions A*, vol. 8, n° 6, 1977, p. 807–824.

[MEC 15] Mecozzi M. G., Bos C., Sietsma J.
A mixed-mode model for the ferrite-to-austenite transformation in a ferrite/pearlite microstructure. *Acta Materialia*, vol. 88, 2015, p. 302–313, Acta Materialia Inc.

[MIL 11] Militzer M., Azizi-Alizamini H.
Phase field modelling of austenite formation in low carbon steels. *Solid State Phenomena*, vol. 172-174, 2011, p. 1050–1059.

[MIT 88] Mittemejer E., Cheng L., Schaaf P., Brackman C., Korevaar B.
Analysis of nonisothermal transformation kinetics: tempering of iron-carbon and iron-nitrogen martensites. *Metallurgical Transactions A*, vol. 19, n° 4, 1988, p. 925–932.

[MIY 07] Miyamoto G., Oh J. C., Hono K., Furuhara T., Maki T.
Effect of partitioning of Mn and Si on the growth kinetics of cementite in tempered Fe-0.6 mass% C martensite. *Acta Materialia*, vol. 55, n° 15, 2007, p. 5027–5038.

[MOH 11] Mohanty R. R., Girina O. A., Fonstein N. M.
Effect of heating rate on the austenite formation in low-carbon high-strength steels annealed in the intercritical region. *Metallurgical and Materials transactions A*, vol. 42, n° 12, 2011, Page 3680.

Cette thèse est accessible à l'adresse : http://theses.insa-lyon.fr/publication/2020LYSEI120/these.pdf
© [A. MATHEVON], [2020], INSA Lyon, tous droits réservés

[MOR 01] Morra P., Böttger A., Mittemejer E.
Decomposition of iron-based martensite. A kinetic analysis by means of differential scanning calorimetry and dilatometry. *Journal of thermal analysis and calorimetry*, vol. 64, n° 3, 2001, p. 905–914.

[MOR 05] Morito S., Saito H., Ogawa T., Furuhara T., Maki T.
Effect of austenite grain size on the morphology and crystallography of lath martensite in low carbon steels. *Acta Materialia*, vol. 45, 2005, p. 91–94.

[MOR 15] Morsdolf L., Tasan C. C., Ponge D., Raabe D.
3D structural and atomic-scale analysis of lath martensite: effect of the transformation sequence. *Acta Materialia*, vol. 95, 2015, p. 366–377.

[MUR 19] Muransky O., Balogh L., Tran M., Hamelin C., Park J.-S., Daymond M.
On the measurement of dislocations and dislocation substructures using {EBSD} and {HRSD} techniques. *Acta Mater.*, vol. 175, 2019, p. 297–313.

[NAK 14] Nakada N., Mizutani K., Tsuchiyama T., Takaki S.
Difference in transformation behavior between ferrite and austenite formations in medium manganese steel. *Acta Materialia*, vol. 65, 2014, p. 251–258, Acta Materialia Inc.

[NAN 16] Nanda T., Singh V., Singh V., Chakraborty A., Sharma S.
Third generation of advanced high-strength steels: Processing routes and properties. *Proceedings of the Institution of Mechanical Engineers, Part L: Journal of Materials: Design and Applications*, vol. 233, n° 2, 2016, p. 209–238.

[NAR 14] Naraghi R., Selleby M., Ågren J.
Thermodynamics of stable and metastable structures in Fe-C system. *Calphad: Computer Coupling of Phase Diagrams and Thermochemistry*, vol. 46, 2014, p. 148–158, Elsevier.

[NEH 46] Nehrenberg A.
The temperature range of martensite formation. *Transaction American Society of Metallurgy*, vol. 167, 1946, p. 494–498.

[NIC 77] Nichol T. J., Judd G., Ansell G. S.
The relationship between austenite strength and the transformation to martensite in Fe-10 pct Ni-0.6 pct C alloys. *Metall. Mater. Trans. A*, vol. 8, n° 12, 1977, p. 1877–1883.

[NOR 35] Nordheim V. L., Gorter C. J.
Bemerkungen über thermokraft und widerstand. *Physica*, vol. 2, 1935, p. 383–390.

[ODQ 03] Odqvist J., Sundman B., Ågren J.
A general method for calculating deviation from local equilibrium at phase interfaces. *Acta Materialia*, vol. 51, n° 4, 2003, p. 1035–1043.

[OFF 12] Offerman S. E., Sharma H.
Following individual grains during solid-state phase transformations with 3DXRD microscopy. *Comptes Rendus Physique*, vol. 13, n° 3, 2012, p. 268–279, Elsevier Masson SAS.

Cette thèse est accessible à l'adresse : http://theses.insa-lyon.fr/publication/2020LYSEI120/these.pdf
© [A. MATHEVON], [2020], INSA Lyon, tous droits réservés

[OGA 10] Ogawa T., Maruyama N., Sugiura N., Yoshinaga N.
Incomplete recrystallization and subsequent microstructural evolution during intercritical annealing in cold-rolled low carbon steels. *ISIJ international*, vol. 50, n° 3, 2010, p. 469–475.

[OHM 01] Ohmura T., Tsuzaki K., Matsuoka S.
Nanohardness measurement of high-purity Fe-C martensite. *Scr. Mater.*, vol. 45, n° 8, 2001, p. 889–894.

[OI 00] Oi K., Lux C., Purdy G. R.
A study of the influence of Mn and Ni on the kinetics of the proeutectoid ferrite reaction in steels. *Acta Materialia*, vol. 48, n° 9, 2000, p. 2147–2155.

[OLI 07] Oliveira F. L. G., Andrade M. S., Cota A. B.
Kinetics of austenite formation during continuous heating in a low carbon steel. vol. 58, 2007, p. 256–261.

[OLL 17a] Ollat M., Massardier V., Fabregue D., Keovilay F., Buscarlet E., Perez M.
Modeling of the recrystallization and austenite formation overlapping in cold-rolled dual-phase steels during intercritical treatments. *Metall. Mater. Trans. A*, vol. 48, 2017, p. 4486–4499.

[OLL 17b] Ollat M.
Characterization and modeling of microstructural evolutions during the thermal treatment of cold-rolled Dual-Phase steels. Thèse de doctorat, 2017.

[OLL 18] Ollat M., Militzer M., Massardier V., Fabregue D., Buscarlet E., Keovilay F., Perez M.
Mixed-mode model for ferrite-to-austenite phase transformation in dual-phase steel. *Computational Materials Science*, vol. 149, 2018, p. 282–290.

[OLS 76a] Olson G. B., Cohen M.
A general mechanism of martenitic nucleation: Part I. General concepts and the FCC->HCP transformation. *Metallurgical Transactions A*, vol. 7A, 1976, p. 1897–1904.

[OLS 76b] Olson G. B., Cohen M.
A general mechanism of martenitic nucleation: Part II. FCC->HCP and other martensitic transformation. *Metallurgical Transactions A*, vol. 7A, 1976, p. 1905–1914.

[OLS 76c] Olson G. B., Cohen M.
A general mechanism of martenitic nucleation: Part III. Kinetics of martensitic nucleation. *Metallurgical Transactions A*, vol. 7A, 1976, p. 1915–1923.

[OON 03] Oono N., Nitta H., Iijima Y.
Diffusion of niobium in α-iron. *Mater. Trans.*, vol. 44, 2003, p. 2078–2083.

[OYA 08] Oyarzábal M., Martínez-de Guerenu A., Gutiérrez I.
Effect of stored energy and recovery on the overall recrystallization kinetics of a cold rolled low carbon steel. *Materials Science and Engineering A*, vol. 485, n° 1-2, 2008, p. 200–209.

[PAN 15] Panahi D., Van Landeghem H., Hutchinson C. R., Purdy G., Zurob H. S.

Cette thèse est accessible à l'adresse : http://theses.insa-lyon.fr/publication/2020LYSEI120/these.pdf
© [A. MATHEVON], [2020], INSA Lyon, tous droits réservés

New insights into the limit for non-partitioning ferrite growth. *Acta Materialia*, vol. 86, 2015, p. 286–294, Acta Materialia Inc.

[PAR 12] Pardoen T., Massart T. J.
Interface controlled plastic flow modelled by strain gradient plasticity theory. *Comptes Rendus - Mecanique*, vol. 340, n° 4-5, 2012, p. 247–260, Elsevier Masson SAS.

[PAU 12] Paul S. K., Kumar A.
Micromechanics based modeling to predict flow behavior and plastic strain localization of dual phase steels. *Comput. Mater. Sci.*, vol. 63, 2012, p. 66–74, Elsevier B.V.

[PAU 13] Paul S. K.
Real microstructure based micromechanical model to simulate microstructural level deformation behavior and failure initiation in DP 590 steel. *Mater. Design*, vol. 44, 2013, p. 397–406, Elsevier Ltd.

[PAY 44a] Payson P., Savage C. H.
Martensite reactions in alloy steels. *Transaction American Society of Metallurgy*, vol. 33, 1944, p. 261–280.

[PAY 44b] Payson P., Savage C. H.
Martensite Reactions in Alloy Steels. *Transaction American Society of Metallurgy*, vol. 33, 1944, p. 277–279.

[PEE 15] Peet M.
Prediction of martensite start temperature. *Mater. Sci. Techno.*, vol. 31, n° 11, 2015, p. 1370–1375.

[PER 03] Perlade A., Bouaziz O., Furnémont Q.
A physically based model for TRIP-aided carbon steels behaviour. *Mater. Sci. Eng. A*, vol. 356, n° 1-2, 2003, p. 145–152.

[PER 08] Perez M., Dumont M., Acevedo-Reyes D.
Implementation of classical nucleation and growth theories for precipitation. *Acta Mater.*, vol. 56, 2008, p. 2119–2132.

[PER 09] Perez M., Dumont M., Acevedo-Reyes D.
Corrigendum to "Implementation of classical nucleation and growth theories for precipitation". *Acta Mater.*, vol. 57, 2009, Page 1318, Acta Materialia Inc.

[PER 14] Perevoshchikova N., Appolaire B., Teixeira J., Aeby-gautier E., Denis S.
Investigation of the growth kinetics of austenite to ferrite in Fe-C-X alloys with a thick interface model. *Computational Materials Science*, vol. 82, 2014, p. 151–158, Elsevier B.V.

[PET 53] Petch N. J.
The cleavage strength of polycrystals. *J Iron Steel Inst. London*, vol. 174, n° 1, 1953, p. 25–33.

[PIE 13] Pierman A. P.
Micromechanical study of the influence of the microstructure and composition on the plastic flow and damage properties of Dual-Phase steels. Thèse de doctorat, 2013.

Cette thèse est accessible à l'adresse : http://theses.insa-lyon.fr/publication/2020LYSEI120/these.pdf
© [A. MATHEVON], [2020], INSA Lyon, tous droits réservés

[PIE 14] Pierman A. P., Bouaziz O., Pardoen T., Jacques P. J., Brassart L.
The influence of microstructure and composition on the plastic behaviour of dual-phase steels. *Acta Mater.*, vol. 73, 2014, p. 298–311, Acta Materialia Inc.

[POR 09] PORTER D. A., EASTERLING K. E.
Phase transformations in metals and alloys. 2009.

[PRA 07] Prahl U., Papaefthymiou S., Uthaisangsuk V., Bleck W., Sietsma J., van der Zwaag S.
Micromechanics-based modelling of properties and failure of multiphase steels. *Comput. Mater. Sci.*, vol. 39, n° 1 SPEC. ISS., 2007, p. 17–22.

[PRA 12] Prawoto Y., Jasmawati N., Sumeru K.
Effect of Prior Austenite Grain Size on the Morphology and Mechanical Properties of Martensite in Medium Carbon Steel. *J. Mater. Sci. Technol.*, vol. 28, n° 5, 2012, p. 461–466, The Chinese Society for Metals.

[PUR 11] Purdy G., Ågren J., Borgenstam A., Bréchet Y., Enomoto M., Furuhara T., Gamsjager E., Gouné M., Hillert M., Hutchinson C., Militzer M., Zurob H.
ALEMI: A ten-year history of discussions of alloying-element interactions with migrating interfaces. *Metallurgical and Materials Transactions A: Physical Metallurgy and Materials Science*, vol. 42, n° 12, 2011, p. 3703–3718.

[PUS 13] Pushkareva I., Scott C. P., Gouné M., Valle N., Redjaïmia A., Moulin A.
Distribution of carbon in martensite during quenching and tempering of dual phase steels and consequences for damage properties. *ISIJ Int.*, vol. 53, n° 7, 2013, p. 1215–1223.

[QIU 13] Qiu C., Zurob H. S., Panahi D., Brechet Y. J. M., Purdy G. R.
Quantifying the Solute Drag Effect on Ferrite Growth in Fe-C-X Alloys Using Controlled Decarburization Experiments. *Metallurgical and Materials Transactions A*, vol. 44, 2013, p. 3472–3483.

[QIU 15] Qiu C., Zurob H. S., Hutchinson C. R.
The coupled solute drag effect during ferrite growth in Fe-C-Mn-Si alloys using controlled decarburization. *Acta Materialia*, vol. 100, 2015, p. 333–343, Acta Materialia Inc.

[RAM 12] Ramazani A., Mukherjee K., Prahl U., Bleck W.
Transformation-induced, geometrically necessary, dislocation-based flow curve modeling of dual-phase steels: Effect of grain size. *Metall. Mater. Trans. A*, vol. 43, n° 10, 2012, p. 3850–3869.

[RAN 46] Range R., Stewart H.
The temperature range of martensite formation. *Transaction American Society of Metallurgy*, vol. 167, 1946, p. 467–501.

[RIO 10] Rios P. R., da Fonseca G. S.
Grain Boundary Pinning by Particles. *Mater. Sci. Forum*, vol. 638 de *Materials Science Forum* Trans Tech Publications Ltd, 2010, p. 3907–3912.

Cette thèse est accessible à l'adresse : http://theses.insa-lyon.fr/publication/2020LYSEI120/these.pdf
© [A. MATHEVON], [2020], INSA Lyon, tous droits réservés

[RUD 11] Rudnizki J., Bottger B., Prahl U., Bleck W.
Phase-field modeling of austenite formation from a ferrite plus pearlite microstructure during annealing of cold-rolled dual-phase steel. *Metallurgical and Materials Transactions A*, vol. 42, 2011, p. 2516–2525.

[RUD 12] Rudnizki J., Prahl U., Bleck W.
Phase-field modelling of microstructure evolution during processing of cold-rolled dual phase steels. *Integrating Materials and Manufacturing Innovation*, vol. 1, n° 1, 2012, p. 19–31.

[SAI 94] Saito T., Toriwaki J.
New algorithms for Euclidean distance transformation on an n-dimensional digitized picture with applications. *Pattern Recognition*, vol. 27, 1994, p. 1551–1565.

[SAL 12] Salehi M. S., Serajzadeh S.
Simulation of static recrystallization in non-isothermal annealing using a coupled cellular automata and finite element model. *Comput. Mater. Sci.*, vol. 53, 2012, p. 145–152, Elsevier B.V.

[SAS 65] Sastri A., West D.
Effect of austenitizing conditions on kinetics of martensite formation in certain medium-alloy steels. *J. Iron Steel Institute*, vol. 203, 1965, Page 138.

[SAV 07] Savran V. I., Van Leeuwen Y., Hanlon D. N., Kwakernaak C., Sloof W. G., Siestma J.
Microstructural features of austenite formation in C35 and C45 alloys. *Metallurgical and Materials Transactions A*, vol. 38A, 2007, p. 946–955.

[SAV 10] Savran V. I., Offerman S. E., Sietsma J.
Austenite nucleation and growth observed on the level of individual grains by three-dimensional X-ray diffraction microscopy. *Metallurgical and Materials Transactions A: Physical Metallurgy and Materials Science*, vol. 41, n° 3, 2010, p. 583–591.

[SCH 07] Schneider A., Inden G.
Carbon diffusion in cementite and Hagg carbide. *Computer Coupling of Phase Diagrams and Thermochemistry*, vol. 31, 2007, p. 141–147.

[SCH 16] Scholtes B., Boulais-sinou R., Settefrati A., Pino D., Poitrault I., Montouchet A., Bozzolo N., Bernacki M.
3D level set modeling of static recrystallization considering stored energy fields. *Comput. Mater. Sci.*, vol. 122, 2016, p. 57–71, Elsevier B.V.

[SIE 04] Sietsma J., van der Zwaag S.
A concise model for mixed-mode phase transformation in the solid state. *Acta Materialia*, vol. 52, 2004, p. 4143–4152.

[SIN 06] Sinclair C. W., Poole W. J., Bréchet Y.
A model for the grain size dependent work hardening of copper. *Scr. Mater.*, vol. 55, n° 8, 2006, p. 739–742.

[SIN 07] Sinclair C., Hutchinson C., Bréchet Y.
The Effect of Nb on the Recrystallization and Grain Growth of Ultra-High-Purity α-Fe: A Combinatorial Approach. *Metall. Mater. Trans. A*, vol. 38, 2007, p. 821–830.

Cette thèse est accessible à l'adresse : http://theses.insa-lyon.fr/publication/2020LYSEI120/these.pdf
© [A. MATHEVON], [2020], INSA Lyon, tous droits réservés

[SIN 12] SINGH H., KABEER B., JANSOHN W.
Mass reduction for light-duty vehicles for model years 2017-2025. *DOT HS*, vol. 811, 2012, Page 666.

[SKR 91] Skrotzki B.
The course of the volume fraction of martensite vs. temperature function Mx(T). *Journal de Physique IV*, vol. C4, 1991, p. 367–372.

[SMI 48] Smith C. S.
Grains, Phases, and Interfaces: An Interpretation of Microstructure. *Trans. Metall.*, vol. 175, 1948, p. 15–51.

[SMI 78] Smidoda K., Gottschalk W., Gleiter H.
Diffusion in migrating interfaces. *Acta Metallurgica*, vol. 26, n° 12, 1978, p. 1833–1836.

[SOT 99] Soto R., Saikaly W., Bano X., Issartel C., Rigaut G., Charai A.
Statistical and theoretical analysis of precipitates in dual-phase steels microalloyed with titanium and their effect on mechanical properties. *Acta Mater.*, vol. 47, 1999, p. 3475–3481.

[SPE 69] Speich G.
Tempering of low-carbon martensite. *Trans. American Society of Metal*, vol. 245, n° 12, 1969, p. 2553–2564.

[SPE 72] Speich G., Leslie W.
Tempering of steel. , 1972, vol. 3, no 5, p. 1043-1054. *Metallurgical Transactions*, vol. 3, n° 5, 1972, p. 1043–1054.

[SPE 79] Speich G., Miller R.
Mechanical properties of ferrite-martensite steels. *Structures and Properties of Dual-Phase Steels*, p. 145–192 1979.

[SPE 81] Speich G. R., Demarest V. A., Miller R. L.
Formation of austenite during intercritical annealing of dual-phase steels. *Metallurgical Transactions A*, vol. 12A, 1981, p. 1419–1428.

[STA 12] Stasinopoulos P., Compston P., Newell B., Jones H. M.
A system dynamics approach in LCA to account for temporal effect: a consequential energy LCI of car body-in-whites. *The International Journal of Life Cycle Assessment*, vol. 17, 2012, p. 199–207.

[STE 56] Steven W., Haynes A.
A model for predicting the Ms temperatures of steels. *J. Iron Steel Inst.*, vol. 8, 1956, p. 340–359.

[SUG 97] Sugimoto K. I., Kobayashi M., Yasuki S. I.
Cyclic deformation behavior of a transformation-induced plasticity-aided dual-phase steel. *Metall. Mater. Trans. A*, vol. 28, n° 12, 1997, p. 2637–2644.

[SUN 17] Sun W. W., Zurob H. S., Hutchinson C. R.
Coupled solute drag and transformation stasis during ferrite formation in Fe-C-Mn-Mo. *Acta Materialia*, vol. 139, 2017, p. 62–74, Elsevier Ltd.

[SUN 19] Sun X., Meng F., Liu J., McKechnie J., Yang J.
Life cycle energy use and greenhouse gas emission of lightweight vehicle: A body-in-white design. *Journal of Cleaner Production*, vol. 220, 2019, p. 1–8, Elsevier Ltd.

Cette thèse est accessible à l'adresse : http://theses.insa-lyon.fr/publication/2020LYSEI120/these.pdf
© [A. MATHEVON], [2020], INSA Lyon, tous droits réservés

[SVE 97] Sverdlin A. V., Ness A. R.
The Effects of Alloying Elements on the Heat Treatment of Steel. *Steel Heat Treatment Handbook*, , 1997, Page 45.

[SVO 02] Svoboda J., Fischer F. D., Gamsjäger E.
Influence of solute segregation and drag on properties of migrating interfaces. *Acta Materialia*, vol. 50, n° 5, 2002, p. 967–977.

[SVO 04] Svoboda J., Gamsjäger E., Fischer F. D., Fratzl P.
Application of the thermodynamic extremal principle to the diffusional phase transformations. *Acta Materialia*, vol. 52, n° 4, 2004, p. 959–967.

[TAA 19] Taalas P., Msuya J.
Global warming of 1.5ÂřC. rapport, 2019, Intergovernemental panel on climate change.

[TEM 11] Tempelman E.
Multi-parametric study of the effect of materials substitution on life cycle energy use and waste generation of passenger car structures. *Transportation Research Part D: Transport and Environment*, vol. 16, n° 7, 2011, p. 479–485, Elsevier Ltd.

[The 17a] Thermo-Calc Software
MOBFE 3 Steels/Fe-Alloys Mobility Database 3. , 2017.

[The 17b] Thermo-Calc Software
TCFE 8 Steels/Fe-alloys database version 8. , 2017.

[THO 90] Thompson S. W., Vin Col D. J., Krauss G.
Continuous cooling transformations and microstructures in a low-carbon, high-strength low-alloy plate steel. *Metallurgical Transactions A*, vol. 21, n° 6, 1990, p. 1493–1507.

[TIM 07] Timokhina I. B., Hodgson P. D., Pereloma E. V.
Transmission electron microscopy characterization of the bake-hardening behavior of transformation-induced plasticity and dual-phase steels. *Metall. Mater. Trans. A*, vol. 38, n° 10, 2007, p. 2442–2454.

[TOM 92] Tomota Y., Umemoto M., Komatsubara N., Kunishige K., Hiramatsu A., Higo Y., Nakajima N., Anan G., Miyahara M., Moriya A., Watanabe T., Nanba S.
Prediction ot Mechanical Properties of Multi-phase Steels Based on Stress-Strain Curves. *ISIJ Int.*, vol. 32, n° 3, 1992, p. 343–349.

[TSI 11] Tsipouridis P., Koll L., Krempaszky C., Werner E.
On the strength of grain and phase boundaries in ferritic-martensitic dual-phase steels. *Int. J. Mater. Res.*, vol. 102, n° 6, 2011, p. 674–686.

[TSU 16] Tsuchiyama T., Inoue T., Tobata J., Akama D., Takaki S.
Microstructure and mechanical properties of a medium manganese steel treated with interrupted quenching and intercritical annealing. *Scripta Materialia*, vol. 122, 2016, p. 36–39, Elsevier B.V.

[VAL 13] Vala H. J., Baxi A.
A review on Otsu image segmentation algorithm. *IJARCET*, vol. 2, n° 2, 2013, p. 387–389.

Cette thèse est accessible à l'adresse : http://theses.insa-lyon.fr/publication/2020LYSEI120/these.pdf
© [A. MATHEVON], [2020], INSA Lyon, tous droits réservés

[VAS 18] Vasilyev A. A., Golikov P. A.
Carbon diffusion coefficient in alloyed ferrite. *Materials Physics and Mechanics*, vol. 39, n° 1, 2018, p. 111–119.

[WAG 05] Wagner R., Voorhees R., P.W. K.
Homogeneous Second-Phase Precipitation. *Phase Trans. Mater.*, vol. 5, 2005, p. 309–407.

[WAN 99] Wang J., Van Der Wolk P. J., Van Der Zwaag S.
Effect of carbon concentration and cooling rate on continuous cooling transformations predicted by artcifial neural network. *ISIJ Int.*, vol. 39, n° 10, 1999, p. 1038–1046.

[WAN 00] Wang J., Van Der Wolk P. J., Van Der Zwaag S.
Determination of martensite start temperature in engineering steels. Part I Empirical relations describing the effect of steel chemistry. *Material Transactions*, vol. 41, n° 7, 2000, p. 761–768.

[WAT 03] Waterschoot T.
Fundamentals of aging in multiphase ferrous alloys; Static strain aging and tempering in dual phase steels. Thèse de doctorat, 2003.

[WAT 06] Waterschoot T., Verbeken K., De Cooman B. C.
Tempering kinetics of the martensitic phase in DP steel. *ISIJ Int.*, vol. 46, n° 1, 2006, p. 138–146.

[WEI 13a] Wei R., Enomoto M., Hadian R., Zurob H. S., Purdy G. R.
Growth of austenite form as-quenched martensite during intercritical annealing in an Fe-0.1C-3Mn-1.5Si alloy. *Acta Materialia*, vol. 61, 2013, p. 697–707.

[WEI 13b] Wei R., Enomoto M., Hadian R., Zurob H. S., Purdy G. R.
Growth of austenite from as-quenched martensite during intercritical annealing in an Fe-0.1C-3Mn-1.5Si alloy. *Acta Materialia*, vol. 61, n° 2, 2013, p. 697–707, Acta Materialia Inc.

[WIC 15] Wicaksono A. T.
A note on the Cahn solute drag model. , 2015.

[WIL 91] Wilkinson A., Dingley D.
Quantitative deformation studies using electron back scatter patterns. *Acta Mater.*, vol. 39, n° 12, 1991, p. 3047–3055.

[WIT 11] Witik R. A., Payet J., Michaud V., Ludwig C., Månson J. A. E.
Assessing the life cycle costs and environmental performance of lightweight materials in automobile applications. *Composites Part A: Applied Science and Manufacturing*, vol. 42, n° 11, 2011, p. 1694–1709, Elsevier Ltd.

[YAN 85a] Yang D. Z., Brown E. L., Matlock D. K., Krauss G.
Ferrite Recrystallization and Austenite Formation in Cold-Rolled Intercritically Annealed Steel. *Metall. Mater. Trans. A*, vol. 16, 1985, p. 1385–1392.

[YAN 85b] Yang D. Z., Brown E. L., Matlock D. K., Krauss G.
The formation of austenite at low intercritical annealing temperatures in a normalized 0.08C-1.45Mn-0.21Si steel. *Metallurgical Transactions A*, vol. 16, n° 8, 1985, p. 1523–1526.

Cette thèse est accessible à l'adresse : http://theses.insa-lyon.fr/publication/2020LYSEI120/these.pdf
© [A. MATHEVON], [2020], INSA Lyon, tous droits réservés

[YAN 09] Yang H. S., Bhadeshia H. K.
Austenite grain size and the martensite-start temperature. *Scripta Mater.*, vol. 60, nº 7, 2009, p. 493–495, Acta Materialia Inc.

[ZHE 13] Zheng C., Raabe D.
Interaction between recrystallization and phase transformation during intercritical annealing in a cold-rolled dual-phase steel: a cellular automaton model. *Acta Mater.*, vol. 61, 2013, p. 5504–5517.

[ZHU 12] Zhu B., Militzer M.
3D phase field modelling of recrystallization in a low-carbon steel. *Model. Simul. Mater. Sc.*, vol. 20, 2012, p. 1–17.

[ZHU 13] Zhu K., Chen H., Masse J. P., Bouaziz O., Gachet G.
The effect of prior ferrite formation on bainite and martensite transformation kinetics in advanced high-strength steels. *Acta Materialia*, vol. 61, 2013, p. 6025–6036.

[ZHU 15] Zhu B., Militzer M.
Phase-Field Modeling for Intercritical Annealing of a Dual-Phase Steel. *Metallurgical and Materials Transactions A: Physical Metallurgy and Materials Science*, vol. 46, nº 3, 2015, p. 1073–1084.

[ZUR 02] Zurob H. S., Hutchinson C. R., Brechet Y., Purdy G.
Modeling recrystallization of microalloyed austenite: Effect of coupling recovery, precipitation and recrystallization. *Acta Mater.*, vol. 50, 2002, p. 3077–3094.

[ZUR 12] Zurob H. S., Panahi D., Hutchinson C. R., Brechet Y., Purdy G. R.
Self-Consistent Model for Planar Ferrite Growth in Fe-C-X Alloys. *Metall. Mater. Trans. A*, vol. 44A, 2012, p. 3456–3471.

Cette thèse est accessible à l'adresse : http://theses.insa-lyon.fr/publication/2020LYSEI120/these.pdf
© [A. MATHEVON], [2020], INSA Lyon, tous droits réservés

FOLIO ADMINISTRATIF

THESE DE L'UNIVERSITE DE LYON OPEREE AU SEIN DE L'INSA LYON

NOM :MATHEVON DATE de SOUTENANCE : 11 /12 /2020

Prénoms : Alexandre

TITRE : Characterization and modelling of microstructural evolutions and mechanical properties during the thermal treatment of cold-rolled Dual-Phase steels

NATURE : Doctorat Numéro d'ordre : 2020LYSEI120

Ecole doctorale : 34 Matériaux Lyon

Spécialité :Matériaux

RESUME : The aim of this thesis was to contribute to the development and understanding of the physical phenomena driving the microstructural evolutions and the mechanical properties of Dual-Phase steels. In a concern of use on industrial production lines, the development of physics-based mean-field numerical tools was retained, usable for a wide range of chemical composition and thermal cycle parameters. A calibration of the models on ternary steels from laboratory castings was carried out before their validation on two industrial grades.
A model for predicting recrystallization kinetics (MiReX) was developed based on the chemical composition, the reduction ratio by cold rolling and their predicted precipitation state using a coupling with a software for predicting precipitation kinetics (Preciso).
A model for the phase transformation between ferrite and austenite, based on the minimization of the global system energy (GEM), has been proposed for isothermal and anisothermal treatments. It reproduces the kinetics of austenite formation on an industrial thermal cycle including a heating ramp and holding for quaternary systems taking into account the dissolution of the cementite.
A model for predicting the temperature of the beginning of martensitic transformation has also been developed for two-phase steels, taking into account austenitic grain size and carbon and manganese enrichment at the interface.
Finally, a new interaction law based on observations during an ex-situ tensile test has allowed the improvement of a prediction model of the mechanical properties of DP steels. A consideration of the tempering step of martensite on the mechanical properties of DP steels has been proposed after the analysis of metallurgical mechanisms involved in tempering by thermoelectric power and hardness measurements.

MOTS-CLÉS :Dual-Phase, microstructural evolutions, recrystallization, phase transformation, martensite tempering and mechanical properties modelling

Laboratoire (s) de recherche : MATEIS – UMR CNRS 5510
INSA LYON
25 avenue Jean Capelle
69621 VILLEURBANNE

Directeur de thèse: MASSARDIER Veronique (Maître de conférence), PEREZ Michel (Professeur) et FABREGUE Damien (Professeur)

Président de jury :

Composition du jury :

Cette thèse est accessible à l'adresse : http://theses.insa-lyon.fr/publication/2020LYSEI120/these.pdf
© [A. MATHEVON], [2020], INSA Lyon, tous droits réservés